UNIVERSITY OF SOUTHERN QUEENSLAND

STRUCTURAL BEHAVIOUR OF TWO-WAY FIBRE REINFORCED COMPOSITE SLABS

A Dissertation Submitted by

Da Huang

B Eng, M Tech (Cum Laude)

for the award of

Doctor of Philosophy

2004

ABSTRACT

Innovative new flooring systems utilising lightweight fibre reinforced polymer composite materials may have the significant potential to offer both economic and performance benefits for infrastructure asset owners compared to conventional concrete and steel systems. Over recent years, a range of prototype floor systems using fibre reinforced polymer composites have been developed by researchers at the University of Southern Queensland. However before such structural systems can be widely adopted by industries, fundamental understanding of their behaviour must be improved. Such work will allow for the development of new design and analysis procedures which will enable engineers to efficiently and accurately design and analyse such structures.

This dissertation presents an investigation into a new two-way fibre reinforced composite floor slab system. The proposed new two-way slab system is, in essence, a sandwich structure with an innovative hollow core made from a castable particulate filled resin system.

The key focus of this dissertation is the development of a new analysis tool to analyse the two-way fibre reinforced composite slab and facilitate subsequent parametric studies into slab configurations for concept refinement. The detailed 3D finite element analyses and experimental investigations are performed to verify the new analysis tool, and provide more detailed insight into the structural behaviour of this new two-way fibre reinforced composite slab. Comparisons with detailed 3D FEA and experiments illustrate that the simplified analysis tool is capable of providing sufficient accuracy for the preliminary analysis of a slab structure. Moreover, the 3D finite element analyses agree well with the experiments, and it is concluded that the behavioural responses of the proposed new slab structure can be reliably predicted. The experimental results show that this new slab concept exhibits quite a robust static behaviour and is likely to have a robust fatigue performance.

CERTIFICATION OF DISSERTATION

I certify that the ideas, experimental work, results, analysis, software and conclusions reported in this dissertation are entirely my own effort, except where otherwise acknowledged. I also certify that the work is original and has not been previously submitted for any other award, except where otherwise acknowledged.

_____ _____

Signature of Candidate Date

ENDORSEMENT

_____ _____

Signature of Supervisor/s Date

_____ _____

Signature of Supervisor/s Date

ACKNOWLEDGEMENTS

While undertaking and completing a PhD study is long and complex journey, the completion of this dissertation would not have been possible without the help and cooperation of a large number of significant people, to whom I wish to express my sincere gratitude.

To my supervisors, Prof. Gerard Van Erp and Dr. Tim Heldt – Thank you for your expert and invaluable guidance in many areas of this work, and for your patience and persistence in helping me complete this dissertation. Thank you for always being there and reading and commenting on so many drafts of the work. You have made the difficult task of completing this study much easier.

To the staff of FCDD, Faculty of Engineering and Surveying and the Office of Research and Higher Degrees – Thank you for your professional support, technical advice and invaluable assistance throughout my PhD candidature. I gratefully acknowledge your significant contribution in this work.

To my father, mother, sister, brother-in-law and little niece – Thank you for your love, patience, encouragement and priceless support throughout the years, which have enabled me to achieve this goal. I could not have done it without you.

To Min Wei – Thank you for your love and support through the ups and downs, and for encouraging me to pursue this goal despite all of the broken deadlines and delays. Thanks also to your family for their kindness and continual support.

To all my friends – Thank you for the years of your support and friendship, and making my candidature such an enjoyable time. Especially, thanks to my many friends, fellow postgraduates and colleagues in Toowoomba who have helped me to improve my knowledge of the English language during my PhD candidature.

To all others who have participated in this work, regardless of the magnitude of their contribution, I thank you.

Finally, I would like to acknowledge the International Postgraduate Research Scholarship (IPRS) Scheme for financial support that enabled me to undertake this study. Additional financial support provided by FCDD and the Office of Research and Higher Degrees is also gratefully acknowledged.

"*This is not the end. It is not even the beginning of the end. But it is, perhaps, the end of the beginning.*"

— Sir Winston Churchill

TABLE OF CONTENTS

ABSTRACT **i**

CERTIFICATION OF DISSERTATION **ii**

ACKNOWLEDGEMENTS **iii**

TABLE OF CONTENTS **v**

LIST OF FIGURES **x**

LIST OF TABLES **xviii**

CHAPTER 1 INTRODUCTION **1**

1.1 Introduction **1**

1.2 Background **1**

1.3 Research Objectives **2**

1.4 Scope **3**

1.5 Research Limitations **4**

1.6 Structure of Thesis **4**

CHAPTER 2 LITERATURE REVIEW IN BRIEF **6**

2.1 Introduction **6**

2.2 Review of Fibre Reinforced Polymer Composites **7**

2.2.1 FRP Composite Materials 7

2.2.2 Manufacturing Processes for FRP Composites 13

2.3 Review on FRP Composites in Civil Engineering Applications **14**

2.3.1 FRP Reinforcement for Concrete Structures 14

2.3.2 Rehabilitation of Existing Structures 15

2.3.3 New FRP Composite Civil Infrastructure 18

2.3.4 Hybrid FRP/concrete Structural Systems 25

2.4 Summary 26

CHAPTER 3 DEVELOPMENT OF A PROTOTYPE TWO-WAY FRP SLAB 29

3.1 Introduction 29

3.2 Review on FRP Floor Slab Structures 29

3.3 A New Two-way FRP Slab Concept 36

3.3.1 Prototype Two-way FRP Slab 38

3.3.2 Determination of Material Properties 41

3.4 Conclusions 44

CHAPTER 4 A NOVEL SIMPLIFIED APPROACH FOR THE ANALYSIS OF THE TWO-WAY FRP SLAB 46

4.1 Introduction 46

4.2 Review of Various Laminated Plate Theories 47

4.2.1 The Classical Laminated Plate Theory 47

4.2.2 The First-order Shear Deformation Theory 50

4.2.3 The Higher-order Shear Deformation Theory 52

4.2.4 Summary and Selection of the Appropriate Laminated Plate Theory 54

4.3 Transformed Plate Approach 56

4.3.1 Constitutive Equations of Composite Materials 56

4.3.2 Development of the Equivalent Transformed Plate 59

4.3.3 Governing Equations of the Equivalent Transformed Plate 80

4.4 Verification of the Simplified Approach **85**

4.4.1 Ritz Solution of Equivalent Transformed Plate 86

4.4.2 Finite Element Solution of Equivalent Transformed Plate 95

4.5 Conclusions **100**

CHAPTER 5 3D FINITE ELEMENT ANALYSIS OF THE TWO-WAY FRP SLAB **102**

5.1 Introduction **102**

5.2 Static Analysis **104**

5.2.1 Development of Finite Element Model 104

5.2.2 Results and Discussions 112

5.3 Natural Frequency Analysis **124**

5.3.1 Development of Finite Element Model 125

5.3.2 Results and Discussions 127

5.4 Buckling Analysis **128**

5.4.1 Development of Finite Element Model 128

5.4.2 Results and Discussions 129

5.5 Conclusions **132**

CHAPTER 6 EXPERIMENTAL INVESTIGATION OF THE TWO-WAY FRP SLAB **134**

6.1 Introduction **134**

6.2 Fabrication of the Prototype Two-way FRP Slab **135**

6.3 Test Arrangement and Instrumentation **136**

6.4 Static Analysis **140**

6.4.1 Static Loading up to 25% of 3D FEA Predicted PFR Cracking Load Test 141
6.4.1.1 Slab Loaded in Orientation 1 142
6.4.1.2 Slab Loaded in Orientation 2 144
6.4.1.3 Comparisons and Discussions 147
6.4.2 Static Loading up to 70% of 3D FEA Predicted PFR Cracking Load Test 149
6.4.3 Failure Load Test 153
6.4.4 Post Failure Behaviour Test 157
6.5 Dynamic Analysis 162
6.5.1 Natural Frequency Test 162
6.5.2 Fatigue Indication Test 166
6.6 Conclusions 171

CHAPTER 7 FINDINGS AND CONCLUSIONS 172
7.1 Review of Research 172
7.2 Major Outcomes and Key Findings 173
7.2.1 FRP Composites in Civil Engineering 173
7.2.2 Development of A Prototype Two-way FRP Slab 173
7.2.3 Development of A Novel Simplified Approach 174
7.2.4 Detailed 3D Finite Element Analysis of the Two-way FRP Slab 175
7.2.5 Experimental Investigations of the Two-way FRP Slab 176
7.3 Conclusions and Recommendations 177
7.3.1 Conclusions 177
7.3.2 Recommendations for Future Research 178

REFERENCES **179**

APPENDIX A FRP COMPOSITES IN BRIEF

APPENDIX B MODULAR MANUFACTURING APPROACH

APPENDIX C DETERMINATION OF FRP COMPOSITE MATERIAL PROPERTIES

APPENDIX D ARBITRARY TRANSFORMATION OF CONSTITUTIVE EQUATIONS

APPENDIX E TSAI-HILL FAILURE CRITERION

LIST OF FIGURES

Figure 2.1	A typical sandwich panel	11
Figure 2.2	Type of renewal strategies	16
Figure 2.3	West Gate Bridge in Australia strengthened with CFRP plates	17
Figure 2.4	Walkways on an offshore platform manufactured by pultrusion process	19
Figure 2.5	Brisbane's floating walkway: (a) View of the floating walkway; (b) Testing of fibre composite walers; (c) 18m long fibre composite truss	20
Figure 2.6	The Eyecatcher building in Basle, Switzerland	21
Figure 2.7	A prototype building structure of two-storey height using FRP planks	22
Figure 2.8	Aberfeldy footbridge, Aberfeldy, Scotland	23
Figure 2.9	A FRP footbridge in Pontresina, Switzerland	23
Figure 2.10	All-composite full-service bridge to link two separate areas of the campus at University if California, San Diego, USA	24
Figure 2.11	New FRP composite bridge: (a) Transportation and installation of new composite bridge; (b) Field testing of the bridge	26
Figure 3.1	One-way and two-way slabs	30
Figure 3.2	FRP bridge deck cross-section types considered in Ref. [54]	31
Figure 3.3	Pultruded FRP bridge deck systems	31
Figure 3.4	Construction of the bridge using H-deck slab structure	32
Figure 3.5	Demonstration bridge in Darke Country, Ohio, USA	32
Figure 3.6	Concept of square tube and plate deck system	34
Figure 3.7	Installation of the FRP composite bridge deck at the Troutville Weigh Station, Virginia, USA	34
Figure 3.8	Typical cross-section of the new FRP slab	35
Figure 3.9	New concept of FRP slab in test configuration	35
Figure 3.10	The concept of the new two-way FRP composite slab	37
Figure 3.11	Instron hydraulic testing machine	39
Figure 3.12	A completed single module	41
Figure 3.13	Testing machines: (a) MTS 810 material testing system machine; (b) Shimadzu universal testing machine	42
Figure 4.1	Undeformed and deformed geometries of an edge of a plate under the Kirchhoff-Love assumptions	48
Figure 4.2	Undeformed and deformed geometries of an edge of a plate under the assumptions of the first-order plate theory	51

Figure 4.3	Deformation of a transverse normal according the classical, first-order, and third-order plate theories	53
Figure 4.4	Transversely isotropic material	57
Figure 4.5	Tractions acting on the laminated plate	60
Figure 4.6	Geometry of an n-layered laminate	60
Figure 4.7	Representative element of the two-way FRP slab	61
Figure 4.8	Coordinate systems used in the representative element	61
Figure 4.9	Coordinate system used for outer shell (I)	62
Figure 4.10	Shell local and global coordinate systems used for top circular cell (II_t)	64
Figure 4.11	Shell local and global coordinate systems used for bottom circular cell (II_b)	70
Figure 4.12	Coordinate system used for PFR core (III)	77
Figure 4.13	3D two-way FRP slab FE model	84
Figure 4.14	2D equivalent transformed plate FE model	85
Figure 4.15	Geometry and loads of the transformed plate with all edges simply supported	86
Figure 4.16	Convergence of Ritz series solution for a central rectangular patch load	90
Figure 4.17	Convergence of a Ritz series solution for a uniformly distributed load	91
Figure 4.18	Convergence of Ritz series solution for a point load at (0.5a, 0.5b)	91
Figure 4.19	Convergence of Ritz series solution for three loading cases	92
Figure 4.20	Vertical displacement for a uniformly distributed load along x at y = 0.5b for Ritz solution ($m_{\max} = n_{\max} = 7$) and 3D FEA results	92
Figure 4.21	Vertical displacement for a uniformly distributed load along y at x = 0.5a for Ritz solution ($m_{\max} = n_{\max} = 7$) and 3D FEA results	93
Figure 4.22	Vertical displacement for a central rectangular patch load along x at y = 0.5b for Ritz solution ($m_{\max} = n_{\max} = 9$) and 3D FEA results	93
Figure 4.23	Vertical displacement for a central rectangular patch load along y at x = 0.5a for Ritz solution ($m_{\max} = n_{\max} = 9$) and 3D FEA results	94
Figure 4.24	Vertical displacement for a point load at (0.5a, 0.5b) along x at y = 0.5b for Ritz solution ($m_{\max} = n_{\max} = 11$) and 3D FEA results	94
Figure 4.25	Vertical displacement for a point load at (0.5a, 0.5b) along y at x = 0.5a for Ritz solution ($m_{\max} = n_{\max} = 11$) and 3D FEA results	95
Figure 4.26	Vertical displacement for SSSS along x at y = 0.5b for 2D and 3D FEA results	97

Figure 4.27	Vertical displacement for SSSS along y at $x = 0.5a$ for 2D and 3D FEA results	97
Figure 4.28	Vertical displacement for CCCC along x at $y = 0.5b$ for 2D and 3D FEA results	98
Figure 4.29	Vertical displacement for CCCC along y at $x = 0.5a$ for 2D and 3D FEA results	98
Figure 4.30	Vertical displacement for CCSS along x at $y = 0.5b$ for 2D and 3D FEA results	99
Figure 4.31	Vertical displacement for CCSS along y at $x = 0.5a$ for 2D and 3D FEA results	99
Figure 5.1	Slab with symmetric axis system: (a) All edges simply support; (b) All edges clamped; (c) Two opposite edges simply supported and the other two edges clamped	104
Figure 5.2	3D FE model of fibre laminate skins and circular tubes using four nodes plate elements	105
Figure 5.3	3D FE model of the PFR core using eight nodes brick elements	105
Figure 5.4	Typical mesh used for the two-way FRP slab	106
Figure 5.5	Separate parts of the two-way FRP slab with different material properties for the static analysis	107
Figure 5.6	The boundary condition of CCSS imposed on the model	109
Figure 5.7	Uplifting at the four corners of the slab	109
Figure 5.8	Definition of the point contact type beam element	110
Figure 5.9	Plot of load-deflection diagram for FE model of the slab with SSSS including and excluding point contact elements	111
Figure 5.10	Deflection shape of the two-way FRP slab: (a) SSSS; (b) CCCC; (c) CCSS	112
Figure 5.11	Ply strain at fibre direction in laminates: (a) SSSS; (b) CCCC; (c) CCSS	113
Figure 5.12	Ply strain at normal to fibre direction in laminates: (a) SSSS; (b) CCCC; (c) CCSS	113
Figure 5.13	Strain at X-direction in PFR core: (a) SSSS; (b) CCCC; (c) CCSS	114
Figure 5.14	Strain at Z-direction in PFR core: (a) SSSS; (b) CCCC; (c) CCSS	114
Figure 5.15	Sub-model of the centre part of the two-way FRP slab	115
Figure 5.16	Comparison of the two-way FRP slab stiffness for three boundary conditions	116
Figure 5.17	Ply strain at fibre direction in the sub-model: (a) SSSS; (b) CCCC; (c) CCSS	116

Figure 5.18	Ply strain at normal to fibre direction in the sub-model: (a) SSSS; (b) CCCC; (c) CCSS	117
Figure 5.19	Ply strain in fibre direction and location of the first ply failure: (a) SSSS (at failure load 310 kN); (b) CCCC (at failure load 400 kN); (c) CCSS (at failure load 340 kN)	119
Figure 5.20	Ply strain normal to fibre direction and location of the first ply failure: (a) SSSS (at failure load 310 kN); (b) CCCC (at failure load 400 kN); (c) CCSS (at failure load 340 kN)	120
Figure 5.21	PFR core shear strain in XY-direction: (a) SSSS; (b) CCCC; (c) CCSS	121
Figure 5.22	PFR core shear strain in YZ-direction: (a) SSSS; (b) CCCC; (c) CCSS	121
Figure 5.23	Maximum shear strain in the PFR core versus load for SSSS	122
Figure 5.24	Maximum shear strain in the PFR core versus load for CCCC	122
Figure 5.25	Maximum shear strain in the PFR core versus load for CCSS	123
Figure 5.26	Separate parts of the two-way FRP slab with average material properties for the natural frequency analysis	126
Figure 5.27	First vibration model of the two-way FRP slab: (a) SSSS; (b) CCCC; (c) CCSS	127
Figure 5.28	First local buckling occurred in the fibre laminate of the two-way FRP slab with SSSS	130
Figure 5.29	First local buckling occurred in the fibre laminate of the two-way FRP slab with CCCC	130
Figure 5.30	First local buckling occurred in the fibre laminate of the two-way FRP slab with CCSS	130
Figure 5.31	Predicted first local buckling load in comparison with predicted PFR core cracking load of the two-way FRP slab with SSSS	131
Figure 6.1	Modules assembly of the slab	136
Figure 6.2	Reinforcement lamination of the slab	136
Figure 6.3	Completed prototype two-way FRP slab	136
Figure 6.4	View of the prototype two-way FRP slab in test configuration	137
Figure 6.5	Detailed test setup configuration for the prototype Two-way FRP slab: (a) Top view: (b) Section A-A; (c) Section B-B	138
Figure 6.6	Combination of steel plates and rubber matting underneath the loading platen	138
Figure 6.7	Comparison of the centre deflection at between top and bottom surface of the slab	139
Figure 6.8	Location of strain gauges on: (a) Top surface of the slab; (b) Bottom surface of the slab	139

Figure 6.9 View of the two-way FRP slab loaded in different cross-section orientations: (a) Orientation 1; (b) Orientation 2 141
Figure 6.10 Load-deflection behaviour for the first test of the Test 2 142
Figure 6.11(a) Strain from strain gauge B1-L for the first test of Test 2 compared with 3D FEA prediction 143
Figure 6.11(b) Strain from strain gauge B1-T for the first test of Test 2 compared with 3D FEA prediction 143
Figure 6.11(c) Strain from strain gauge B2-L for the first test of Test 2 compared with 3D FEA prediction 143
Figure 6.11(d) Strain from strain gauge B2-T for the first test of Test 2 compared with 3D FEA prediction 143
Figure 6.11(e) Strain from strain gauge B3-L for the first test of Test 2 compared with 3D FEA prediction 143
Figure 6.11(f) Strain from strain gauge B3-T for the first test of Test 2 compared with 3D FEA prediction 143
Figure 6.11(g) Strain from strain gauge T2-L for the first test of Test 2 compared with 3D FEA prediction 144
Figure 6.11(h) Strain from strain gauge T2-T for the first test of Test 2 compared with 3D FEA prediction 144
Figure 6.11(i) Strain from strain gauge T3-L for the first test of Test 2 compared with 3D FEA prediction 144
Figure 6.11(j) Strain from strain gauge T3-T for the first test of Test 2 compared with 3D FEA prediction 144
Figure 6.12 Load-deflection behaviour for the second test of the Test 2 145
Figure 6.13(a) Strain from strain gauge T1-L for the second test of Test 2 compared with 3D FEA prediction 146
Figure 6.13(b) Strain from strain gauge T1-T for the second test of Test 2 compared with 3D FEA prediction 146
Figure 6.13(c) Strain from strain gauge T2-L for the second test of Test 2 compared with 3D FEA prediction 146
Figure 6.13(d) Strain from strain gauge T2-T for the second test of Test 2 compared with 3D FEA prediction 146
Figure 6.13(e) Strain from strain gauge T3-L for the second test of Test 2 compared with 3D FEA prediction 146
Figure 6.13(f) Strain from strain gauge T3-T for the second test of Test 2 compared with 3D FEA prediction 146
Figure 6.13(g) Strain from strain gauge B2-L for the second test of Test 2 compared

with 3D FEA prediction 147
Figure 6.13(h) Strain from strain gauge B2-T for the second test of Test 2 compared with 3D FEA prediction 147
Figure 6.13(i) Strain from strain gauge B3-L for the second test of Test 2 compared with 3D FEA prediction 147
Figure 6.13(j) Strain from strain gauge B3-T for the second test of Test 2 compared with 3D FEA prediction 147
Figure 6.14 Stiffness comparisons for the slab loaded in two different cross-section orientations: (a) Experiment; (b) 3D slab FEA; (c) Ritz solution; (d) 2D equivalent transformed plate FEA 148
Figure 6.15 Load-deflection curve for static loading up to 200 kN 150
Figure 6.16(a) Strain from strain gaugeB1-L for static load up to 200 kN test compared with 3D FEA prediction 151
Figure 6.16(b) Strain from strain gaugeB1-T for static load up to 200 kN test compared with 3D FEA prediction 151
Figure 6.16(c) Strain from strain gaugeB2-L for static load up to 200 kN test compared with 3D FEA prediction 151
Figure 6.16(d) Strain from strain gaugeB2-T for static load up to 200 kN test compared with 3D FEA prediction 151
Figure 6.16(e) Strain from strain gaugeB3-L for static load up to 200 kN test compared with 3D FEA prediction 152
Figure 6.16(f) Strain from strain gaugeB3-T for static load up to 200 kN test compared with 3D FEA prediction 151
Figure 6.16(g) Strain from strain gaugeT2-L for static load up to 200 kN test compared with 3D FEA prediction 151
Figure 6.16(h) Strain from strain gaugeT2-T for static load up to 200 kN test compared with 3D FEA prediction 151
Figure 6.16(i) Strain from strain gaugeT3-L for static load up to 200 kN test compared with 3D FEA prediction 151
Figure 6.16(j) Strain from strain gaugeT3-T for static load up to 200 kN test compared with 3D FEA prediction 151
Figure 6.17 Load-deflection curve for the failure test of the slab 154
Figure 6.18(a) Strain from strain gauge B1-L for the failure test compared with 3D FEA predication 155
Figure 6.18(b) Strain from strain gauge B1-T for the failure test compared with 3D FEA predication 155
Figure 6.18(c) Strain from strain gauge B2-L for the failure test compared with

	3D FEA predication	155
Figure 6.18(d)	Strain from strain gauge B2-T for the failure test compared with 3D FEA predication	155
Figure 6.18(e)	Strain from strain gauge B3-L for the failure test compared with 3D FEA predication	155
Figure 6.18(f)	Strain from strain gauge B3-T for the failure test compared with 3D FEA predication	155
Figure 6.18(g)	Strain from strain gauge T2-L for the failure test compared with 3D FEA predication	156
Figure 6.18(h)	Strain from strain gauge T2-T for the failure test compared with 3D FEA predication	156
Figure 6.18(i)	Strain from strain gauge T3-L for the failure test compared with 3D FEA predication	156
Figure 6.18(j)	Strain from strain gauge T3-T for the failure test compared with 3D FEA predication	156
Figure 6.19	Load-deflection curve for the post failure behaviour test of the slab	158
Figure 6.20	Debonding between fibre laminate skins and PFR core at the bottom surface of the slab	159
Figure 6.21	Transverse slab section after punching shear failure	160
Figure 6.22	Magnified views of the transverse slab section after punching shear failure	160
Figure 6.23	Longitudinal slab section after punching shear failure	161
Figure 6.24	Magnified views of the longitudinal slab section after punching shear failure	161
Figure 6.25	Test setup and instrumentation for natural frequency test of the slab	162
Figure 6.26	Accelerometer attached to the testing slab	163
Figure 6.27	Electrical responses recorded from attached accelerometer for a number of excitations	163
Figure 6.28	Part of electrical response recorded from attached accelerometer for one excitation	164
Figure 6.29	Results of power spectral density analysis for the signal shown in Figure 6.27	165
Figure 6.30	An identified structural response for the excitation shown in Figure 6.27 with the filtering bandpass of 135 Hz to 145 Hz	165
Figure 6.31	Sample of the two-way FRP slab fatigue loading	168
Figure 6.32	Sample of the deflection at the centre of the slab	168
Figure 6.33	Sample of longitudinal strain at gauge B1-L	168

Figure 6.34 Sample of transverse strain at gauge B1-T 168
Figure 6.35 Load-deflection curves from interrupted fatigue cycling 169
Figure 6.36(a) Strain at gauge B1-L from interrupted fatigue cycling 169
Figure 6.36(b) Strain at gauge B1-T from interrupted fatigue cycling 169
Figure 6.36(c) Strain at gauge B2-L from interrupted fatigue cycling 169
Figure 6.36(d) Strain at gauge B2-T from interrupted fatigue cycling 169
Figure 6.36(e) Strain at gauge B3-L from interrupted fatigue cycling 170
Figure 6.36(f) Strain at gauge B3-T from interrupted fatigue cycling 170
Figure 6.36(g) Strain at gauge T2-L from interrupted fatigue cycling 170
Figure 6.36(h) Strain at gauge T2-T from interrupted fatigue cycling 170
Figure 6.36(i) Strain at gauge T3-L from interrupted fatigue cycling 170
Figure 6.36(j) Strain at gauge T3-T from interrupted fatigue cycling 170

LIST OF TABLES

Table 2.1	Typical properties of various reinforced fibres	9
Table 2.2	Typical properties of various polymer matrix resins	11
Table 2.3	Typical average properties of various core materials	13
Table 3.1	Material properties of E-glass/vinylester of unidirectional lamina	43
Table 3.2	Material properties of vinylester/SLG of PFR core	44
Table 5.1	Summary of 3D FEA results for the first ply failure prediction	118
Table 5.2	Summary of 3D FEA results for PFR cracking load prediction	124
Table 5.3	First natural frequency of the two-way FRP slab	128
Table 5.4	Calculated buckling factors	131
Table 6.1	Strain comparison for the slab loaded in two different orientations	148
Table 6.2	Comparison of test results between two tests of the two-way FRP slab	157

Chapter 1

INTRODUCTION

1.1 Introduction

The focus of this PhD thesis is on research into the analysis and structural behaviour of a new two-way fibre reinforced composite floor slab. The principles of this new slab structure were developed by Fibre Composite Design and Development, a research centre at the University of Southern Queensland, Toowoomba.

This study is the first investigation into the behaviour of this new slab structure. It uses a combination of analytical, numerical and experimental techniques to quantify and examine the behavioural response of such two-way fibre composite slabs.

1.2 Background

Fibre reinforced polymers (FRPs), have great potential for use in civil infrastructure applications. They offer a number of advantages over conventional materials, such as:

- superior strength-to-weight ratio;
- superior stiffness-to-weight ratio;
- superior electromagnetic properties;
- high degree of chemical inertness;
- excellent fatigue damage tolerance ;
- flexible custom design characteristics.

However, the commercial uptake of these new materials has been very slow to date. High cost, insufficient knowledge of long-term material durability and the absence of adequate established standards for design, maintenance, and repair have been major reasons for this limited usage in civil infrastructure. Most existing composite infrastructure applications have been built either to demonstrate the suitability of the material for a specific type of application, or to further the understanding of fibre reinforced composites behaviour in civil infrastructure in general.

Even though there is significant research and design data available for aerospace, marine and automotive application, this is of limited suitability in civil engineering due to the different service environments and loading situations.

In order to improve understanding of composite materials and their behaviour in civil engineering applications, a major research program was initiated at the University of Southern Queensland in the mid 1990's. The ultimate objective of this program is to develop fibre composite structures that are more suitable to the civil engineering market. To date, a range of new concepts has been developed and used successfully in real civil applications (Van Erp and Ayers 2004). A relatively new development with significant commercial potential, which has resulted from this research program, is a novel two-way fibre composite floor slab structure. The structural analysis and behaviour of this new floor slab structure has been the main focus of this PhD study.

1.3 Research Objectives

The new two-way floor slab system is, in essence, a sandwich structure with an innovative hollow core made of a castable filled resin system. Due to the geometric complexity of the core, a 3-dimensional finite element analysis is required to accurately analyse this new slab structure. However, a 3D finite element analysis is very time consuming, which is a potential impediment to wider industry adoption of this new structural concept. This situation has lead to the formulation of the current PhD study which has as its primary aim **the development of a more efficient analytical and/or numerical approach for the analysis of this new two-way floor slab structure**. An additional aim of this study is to initiate a numerical and

experimental investigation of this new structure in order to verify the accuracy of the newly developed analysis method, and to obtain and analyse the first round of numerical and experimental data. Hence, the overall objectives of this study have been formulated as:

1. Develop and verify a practical analysis technique (analytical and/or numerical) capable of analysing the structural behaviour of the new slab structure within the range of expected applications and design conditions.
2. Conduct an investigation into the structural behaviour of this new type of floor structure, including generation of the most detailed numerical and experimental data for this concept to date.

1.4 Scope

Consistent with the above objectives, the scope of this research program has been formulated as follows:

- Review the fundamental characteristics of fibre reinforced polymer materials within a civil engineering context.
- Review the development of FRP structures for civil engineering applications, in particular for FRP floor slab or bridge deck systems.
- Develop the FCDD laboratory slab concept into a test structure, suitable for use in the experimental program.
- Determine the material properties of all fibre composite materials used in the experimental slab structure.
- Develop and quantify a practical analysis technique capable of analysing the structural behaviour of the new slab structure.
- Undertake a numerical and experimental investigation with the purpose of validating the analysis technique referred to above and understanding the structural behaviour of this new two-way floor structure.
- Draw conclusions as the appropriateness of the analysis and design techniques.

1.5 Research Limitations

Due to the complexity and magnitude of this project, a number of constraints were applied to this study in order to retain appropriate focus. These are as follows:

- The selection of the appropriate fibre composite materials was based on previous research conducted at the University of Southern Queensland. Effects of the different fibre composite material systems on the behavioural response of this new floor system were not quantified by this study.
- Both theoretical and numerical investigations for analysis of the two-way FRP slab were limited to the linear elastic range.
- Three boundary conditions were considered in the finite element analysis of the two-way FRP slab to investigate the effects of overall performance of the slab due to the different edge supported condition types.
- The dimensions of the prototype slab were chosen to suit the available testing infrastructure in the laboratory of the University of Southern Queensland. Only one slab geometry was investigated.
- Slab testing was limited to single span with all edges simply supported and central patch loading. All experiments were performed at ambient temperature.
- Experimental study of fatigue effects of cyclic loading on the slab was limited to a preliminary investigation. Other long-term effects (i.e. creep) of the slab were not investigated.
- Investigations into the effect of geometric parameters and the optimisation of the two-way FRP slab structure were not considered in the present study.

1.6 Structure of Thesis

After the introduction given in this chapter, Chapter 2 provides a brief literature review on fibre reinforced polymer composite materials and their usage in civil and structural engineering. A brief overview of fibre reinforced polymer composites is presented in summarised form. A review of existing structural applications with fibre reinforced polymers and composite construction are also presented to examine the relevant previous research in this area.

The development of the prototype two-way FRP slab is described in Chapter 3. This chapter starts with a review of FRP composite floor slab structures, followed by a detailed description of the proposed two-way FRP slab concept. The FRP materials used for the construction of the prototype slab are presented together with the results of the materials testing. The modular manufacturing process adopted for the production of the prototype two-way FRP slab is introduced.

A novel simplified approach for the analysis of the two-way FRP slab is presented in Chapter 4. A brief review of various plate theories is provided following which the adopted plate theory used in the analysis is explained. The detailed analytical procedure is described and numerical verification of this simplified approach is presented.

Chapter 5 presents detailed 3D finite element analyses of the two-way FRP slab to investigate the structural behaviour of the slab numerically. The results obtained from these analyses were also used in Chapter 4 to verify the simplified approach developed, and in Chapter 6 to be compared with experimental findings.

Chapter 6 presents experimental studies of the two-way FRP slab. The production of a prototype slab is described together with the manufacturing method described in Chapter 3 and the associated Appendix. Testing arrangements and instrumentation for flexural, natural frequency, and cyclic load tests on the slab specimen are also presented. The experimental results are compared with the analytical and finite element results and the findings discussed.

Finally, Chapter 7 summarizes the main findings of this PhD project. Conclusions regarding the analytical and numerical models developed and the performance of the new two-way FRP slab are presented. Recommendations for future investigations expanding the present research work are also provided.

Chapter 2

LITERATURE REVIEW IN BRIEF

2.1 Introduction

Simply stated, a composite is a material which is composed of two or more distinct phases to create an end product for a specific purpose. Fibre reinforced composites are a two-phase material in which one phase acts as a reinforcement of a second phase, which holds the fibres in place. The second phase is called the matrix.

Fibrous composite materials have a long history of usage. Early Egyptians used natural fibre composite papyrus to make boats, sails, baskets, and ropes as early as 4000 B.C. (Herakovich 1998). Around 1300 B.C., straw was used by the Israelites as reinforcement for mud bricks, a practice that is still in use today (Jones 1998). Ancient Egyptians also made containers of coarse fibres drawn from heat-softened glass, and French scientist Reaumur considered the potential of forming fine glass fibres as early as the 18th century (Hartman et al. 1994). It was not until 1939 that continuous glass fibres were produced commercially (Knox 1982). Two more decades passed before the so-called advanced fibres were produced: boron (late 1950s) and carbon (1960s). Although manufactured composites have been used for thousands of years, the high technology era of composites began in 1964 when carbon fibre exhibiting sufficiently high strength and stiffness was produced at the Royal Aircraft Establishment in England (Kim 1995). Thus, from the earliest applications of natural fibre composites by the Egyptians to the introduction of advanced fibre composites in the second half of the 20th century, roughly 6000 years

have passed. Without doubt, the progress in the use of fibrous composite in the latter half the 20th century has been much greater than that during the preceding 6000 years.

Today, fibre reinforced composite materials have been successfully utilised in a diverse range of engineering applications. The applications over the past quarter-century have been primarily in specialty areas such as aerospace structures, automobile industry, athletic equipment, and the military. Recent advances in civil engineering have created interesting possibilities for replacing conventional structural forms with components made from fibre reinforced composite materials. A significant number of civil engineers have become very interested in building large-scale structures using fibre reinforced composite materials.

This chapter outlines the background of fibre reinforced polymer (FRP) composites for the project. It firstly provides a brief overview of FRP composites. It then discusses the use of FRP composites in a range of civil engineering applications. At the conclusion of this chapter, some remarks on the usage of FRP composites into civil engineering are presented.

2.2 Review of Fibre Reinforced Polymer Composites

The purpose of this section is to provide background information on fibre reinforced polymer composites. It starts with a general overview of fibre reinforced composite materials, and continues with a brief discussion of the constituents of FRP composites. Finally the most common manufacturing processes for FRP composites are briefly mentioned.

2.2.1 FRP Composite Materials

Fibre reinforced composite materials consist of fibres of high strength and modulus embedded, in and bonded to, a matrix with distinct interfaces between them. In this form, both fibres and matrix retain their physical and chemical identities; yet produce a combination of properties that cannot be achieved with either of the constituents

acting alone. In general, the fibres are the principal load-carrying elements, whereas the surrounding matrix keeps them in the desired location and orientation. The matrix acts as a load transfer medium between the fibres, and protects them from environmental and chemical attack. The matrix material in a composite may be a polymer, a metal, or a ceramic. Depending on the matrix used, composite materials are classified as polymer matrix composites (PMCs), metal matrix composites (MMCs), or ceramic matrix composites (CMCs) (Mallick 1997).

The materials used in this study are termed fibre reinforced polymer (FRP) composites, which form part of PMCs. FRP composites are the most common fibre reinforced composite materials used in civil applications. The three main constituent materials used to create fibre reinforced composite structures are: reinforcing fibres, polymer matrix resins, and core materials. The remainder of this section will briefly examine each of these constituent materials. A more detailed review of fibre reinforced polymer composites is included in Appendix A.

(a) Reinforcing Fibres

Fibres are one of the principal constituents in FRP composites. They normally occupy the largest volume fraction in a composite laminate and share the major portion of the load acting on a composite structure. Proper selection of the type, amount, and orientation of fibres is very important, because it influences the following characteristics of a composite laminate (Schwartz 1997a):

- Specific gravity
- Tensile strength and modulus
- Compressive strength and modulus
- Fatigue strength and fatigue failure mechanisms
- Electric and thermal conductivities
- Cost

A wide variety of reinforcing fibres are commercially available for use in advanced composites. These include glass, carbon, aramid, polyester, polyethylene, quartz, boron and ceramics fibres etc. The three most commonly used fibres in civil

engineering applications are glass, carbon and aramid fibres, and their typical properties are summarized in Table 2.1. Detailed discussions of these three fibre types and associated reinforcement forms are provided in Appendix A. The use of other fibres is not widespread in civil applications due to either their cost or performance. A discussion of these alternative fibres can be found in Schwartz (1997a), Marzullo (1998), Matthews et al (1994), and Kumar et al (1997).

Table 2.1 Typical properties of various reinforcing fibres[74, 116]

Reinforcing Fibres	Density (kg/m^3)	Modulus (GPa)	Tensile Strength (MPa)	Strain to failure (%)
Glass				
E-glass	2540	72.4	3448	4
S-glass	2460	86.9	4482	5.2
Carbon-PAN				
HS (T-300)	1760	231	3650	1.4
HS (AS-4)	1800	248	4070	1.65
HM (HMS-4)	1800	345	2480	0.7
UHM (GY-70)	1960	483	1520	0.38
Carbon-Pitch				
Amoco P-25	1900	160	1400	0.9
Amoco P-55	2000	380	1900	0.5
Amoco P-100	2150	725	2200	0.32
Aramid				
Kevlar 29	1440	65	2800	4
Kevlar 49	1450	131	3620	2.8
Kevlar 149	1470	179	3450	-

(b) Polymer Matrix Resins

The matrix plays a vital role in a FRP composite. It is the binder that holds the reinforcement in place, it transfers external loads to the reinforcement, it provides a barrier against adverse environments, and it protects the surface of the fibres from mechanical abrasion. The selection of a matrix also has a major influence on the interlaminar shear as well as on in-plane shear properties of the composite materials.

Moreover, the matrix redistributes the load to surrounding fibres when an individual fibre fractures and provides lateral support against the possibility of fibre buckling under compression loading, thus influencing to some extent the compressive strength of the fibre reinforced composite.

Polymer matrix resins can be classified into two primary groups: thermoplastics and thermosets. Thermoplastics are polymers that can be repeatedly softened by increasing the temperature and hardened by decreasing the temperature. Thermosets are polymers which readily cross-link during curing. Thermoset resins, in contrast to thermoplastic resins, set at room temperature or above and cannot be reshaped by subsequent heating. In general, thermosetting polymers contain two or more ingredients, namely, a resinous matrix and a curing agent known as a catalyst or hardener. Solidification of the composite matrix starts when the resin and the curing agent are mixed, which causes a reaction between the resin and its curing agent.

Well known thermoplastics include acrylic, nylon, polystyrene, polyethylene and polyetheretherketone (Matthews et al 1994). From the perspective of civil engineering, thermoplastic resins have found little application in primary structural composites to date compared to thermoset resins, and are not discussed further in this study. Greater details on various types of thermoplastic resins can be found in Schwartz (1997a), Åström (1997), Matthews et al (1994), Juska et al (1997) and Berglund (1998).

Thermoset resins form the most widely used class of matrix materials in polymer-based composites because of their ease in processing and low cost. The most common thermosets used in civil engineering applications are polyesters, vinylesters, and epoxies. Vinylesters have high strength and polyesters have moderate strength. Epoxy resins can be considered high performance resins in the sense that their strength is superior to that of other thermosets, however they are more expensive. A comparison of these three classical thermoset resins and their typical properties is given in Table 2.2. Further discussions of polyesters, vinylesters and epoxies, and other thermosetting resin systems can be found in Appendix A.

Table 2.2 Typical properties of various polymer matrix resins[15, 65, 101]

	Density (Mg/m^3)	Tensile Modulus (GPa)	Tensile Strength (MPa)	Compression Strength (MPa)	Tensile Elongation (%)	Approximate Cost (AUD$/kg)
Polyester	1.2-1.5	2.8-3.4	40-90	100-120	1.4-3.3	2.50-4.00
Vinylester	1.0-1.2	3.3-3.6	70-80	105-125	5.0-6.0	4.00-6.00
Epoxy	1.1-1.4	2.6-6.0	35-100	90-115	2.6-6.0	7.00-50.00*

*The cost of epoxy resins is proportional to the performance of the resin, which varies over a broad range.

(c) Core Materials

The primary disadvantage associated with fibre composite materials is that of relatively high cost when compared to conventional civil engineering materials (Simpson et al. 1999). In order to use fibre reinforced laminates more economically, the sandwich concept has been widely utilized in fibre composite industries.

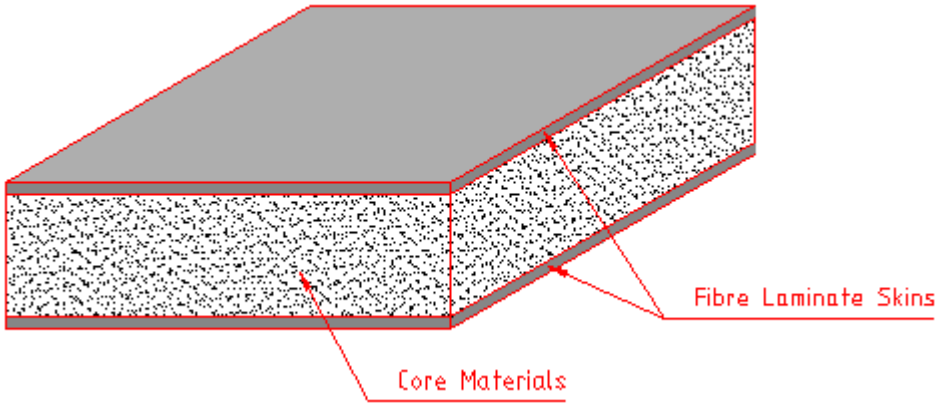

Figure 2.1 A typical sandwich panel

A sandwich structure (Figure 2.1) consists of two high performance fibre composite skins separated by a "thick", low-density and inexpensive (compared to the fibre composites) core material. Apart from providing the spacing for the laminates and reducing the structural cost, the primary function of a core in sandwich structures is that of stabilizing the laminate skins and carrying most of the shear loads through the

thickness. Especially when using lightweight, thin laminate skins, the core must be capable of carrying compressive loading without premature failure. This helps to prevent the thin skins from wrinkling, and failing in a buckling mode. In order to perform this job efficiently, the core material should have adequate rigidity.

Most core materials available on the market today have been designed for either aerospace or marine applications. The weight savings required by such applications have resulted in the development of lightweight core materials which are quite expensive, such as foams and honeycomb structures (refer Appendix A). However, weight is normally not the critical issue for civil engineering applications, cost and load carrying capacity are far more important. Other important issues include damage tolerance and ability to carry high concentrated loads. The core materials used by aerospace or marine industries generally fail to meet these requirements. Recently, a new core material has been developed at the University of Southern Queensland (Ayers et al. 1999 and Ayers 2001). This new core material, which is known as a Particulate Filled Resin (PFR) core, has been specifically designed for civil engineering applications.

The following discussion will describe the PFR core material in more detail. Further discussions on other commonly used sandwich core materials including woods, foams and honeycombs, their characteristics and applications are presented in Appendix A. A comparison of the structural property of various core materials is summarized in Table 2.3.

- **Particulate Filled Resin (PFR)**

PFR core material is a particulate-reinforced composite system formed by the combination of a hollow ceramic microsphere filler material with a polymer resin binder (polyester, vinylester or epoxy). It offers unique advantages in terms of low cost and excellent structural performance. The properties of this filled resin system depend heavily on the type and amount of filler and base resin used and therefore a wide range of properties and densities are achievable.

PFRs possess attractive mechanical properties compared with other core materials such as relatively high tensile strength, high compressive strength, high shear rigidity,

and relatively high shear strength. The flexibility of shape is another significant advantage for PFR cores. Complex shapes can be formed easily using a casting procedure. PFR cores also possess good capacity to distribute concentrated loads into the laminate, exceptional durability, and good damage tolerance. Due to the high level of structural performance and low material and processing cost, PFR core materials are seen to offer significant potential in the development of economical solutions for fibre composites in civil engineering. Detailed information on this type of core material can be found in publications by Ayers et al. (1999) and Ayers (2001).

Table 2.3 Typical average properties of various core materials[7, 26, 30, 66, 91]

	Density (kg/m^3)	Tensile Strength (MPa)	Compressive Strength (MPa)	Compressive Modulus (MPa)	Shear Strength (MPa)	Shear Modulus (MPa)
Balsa wood	90-220	7.0-20.6	5.4-21.9	1850-6840	1.6-4.5	96-237
PU Foams	20-400	0.1-8.96	0.1-13.8	–	0.14-3.1	1.56-103.5
Linear PVC Foam	50-80	1.2-1.8	0.4-0.9	37-56	0.5-1.2	15-21
Cross-linked PVC Foam	40-200	0.5-6.0	0.5-4.6	26-223	0.4-3.5	12-77
SAN Foam	50-200	1.0-6.8	0.4-3.44	22.8-86.0	0.66-1.97	11.7-45.2
Aluminium Honeycomb	33-118	–	0.79-7.65	–	0.69-5.18	14-63
Nomex Honeycomb	32-64	–	0.77-2.95	–	0.63-1.67	27-61
PFR Core*	924	25.29	81.72	6127	13.89	1753

*44% SLG filler by volume from Envirospheres (Section 3.4) in vinylester resin

2.2.2 Manufacturing Processes for FRP Composites

The choice of manufacturing process for FRP composites depends on a number of factors including the type of matrix and fibres used, the temperature required to form and cure the part, the required final shape, the number of products, the cost effectiveness of the process. Therefore, the designer needs to understand the advantages, limitations, cost, and typical uses of various manufacturing processes.

Common manufacturing processes for FRP composites which have potential for application in civil engineering include:

- Wet Layup
- Bag Moulding
- Resin Transfer Moulding
- Filament Winding
- Pultrusion

Detailed discussions of these processes are presented in Appendix A. Discussion of other manufacturing methods for FRP composites that are not mentioned within this chapter can be found in Ball (1994), Åström (1997), Schwartz (1997b) and Barbero (1999).

2.3 Review on FRP Composites in Civil Engineering Applications

The introduction of FRP composites in infrastructure and other civil engineering applications has been a very rapid process in comparison to other civil engineering materials. FRP composite materials have hitherto been utilised predominately in the aerospace, marine and automotive industries. However, since the 1970s, there has been a growing awareness amongst civil/structural engineers of the unique mechanical and in-service properties of these materials together with their customised fabrication technologies. A number of demonstration projects have been successfully constructed in recent years. This section will briefly review some of these developments and applications.

2.3.1 FRP Reinforcement for Concrete Structures

FRP reinforcing bars (rebars) have been used for reinforcing concrete structures since 1990s. FRP rebars resist oxidation and corrosion from seawater, de-icing salts and the caustic environment of concrete. However, to date there has only been limited and specialized use of FRP reinforcement for concrete structures, mainly in

hospitals and military installations. The first major use of FRP composite rebars was for a vehicular bridge, the McKinleyville Bridge, located in West Virginia, USA, which was completed in 1996. The bridge has a 54 m long concrete deck over steel stringers accommodating two lanes of vehicular traffic. The reinforcement of the concrete is exclusively made of composite rebars with E-glass fibres (Barbero 1998). Another example is the Oppegard footbridge Oslo, Norway, which was built in 1997 on a golf course. It has a span of about 10 m and consists of twin-arched beams, with glass fibre reinforced polymer (GFRP) main and shear reinforcement.

Since concrete has a relatively high compression strength and, for most practical purposes, negligible tensile strength it is advantageous to pre-stress concrete before the actual load is applied. In this case, applied loads only reduce the amount of compressive stress without producing tensile stress. Currently, high strength steel tendons are generally used for pre-stressing concrete. Even though concrete cracks can be prevented by the prestress, concrete is porous and water and chemicals may still reach the prestressed tendons, particularly in a caustic environment. Due to their superior durability, FRP prestressing tendons show great potential to replace conventional steel tendons. The first prestressed concrete bridge to be built using glass reinforced prestressing strand was a small footbridge in Dusseldorf, Germany which was completed in 1980. This bridge was essentially designed as a reinforced concrete bridge allowing some of the tendons to be removed for testing. During the past twenty years, a number of concrete structures have been built worldwide utilizing prestressed FRP tendons (Hollaway and Head 2001). However, due to the high material cost of FRP composites compared to steel, the use of FRP reinforcement for concrete structures is currently limited to special applications where the cost disadvantage is out-weighted by other benefits.

2.3.2 Rehabilitation of Existing Structures

The use of FRP composite materials for strengthening and rehabilitation of existing structures has quickly gained momentum in Europe, North America, and Asia due to its many inherent advantages over conventional methods of strengthening, not least in terms of durability and whole of life costs (Luke et al. 2000). In the US, for the seven-year period between 1990 and 1996, 17% of the Federal-aid highway funds

were spent on rehabilitation and replacement of existing bridges whereas only 4.5% was spent for construction of new bridges (Hollaway and Head 2001). The UK spends more on maintenance and upgrading of existing RC structures than on new buildings. In the European Union nearly 84,000 reinforced and prestressed concrete bridges require maintenance, repair and strengthening with an annual budget of £215M, excluding traffic management cost (Leeming 1996). Therefore, the development of effective, durable and cost-efficient methods using FRP composite materials is attracting great attention in the construction industry worldwide.

The use of FRP composites in infrastructure renewal can be classified into different classes of rehabilitation and new structural systems (Hollaway and Head 2001). In general, the use of FRP composites for rehabilitation of existing structures can be thought of as a partial or complete skin designed to either protect and/or improve the response of the encapsulated element. Within the scope of rehabilitation of concrete structures, it is essential that differentiation is made between repair, strengthening and retrofit which are often erroneously used interchangeably but in fact refer to three different structural conditions (Figure 2.2). In 'repairing' a structure, the composite material is used to fix a structural or functional deficiency such as a cracked or a severely degraded structural component. In contrast, the 'strengthening' of structures is specific to those cases wherein the addition or application of the composite would enhance the existing designed performance level. The term 'retrofit' is specifically used to relate to seismic upgrade of facilities, such as in the use of composite jackets for the confinement of columns.

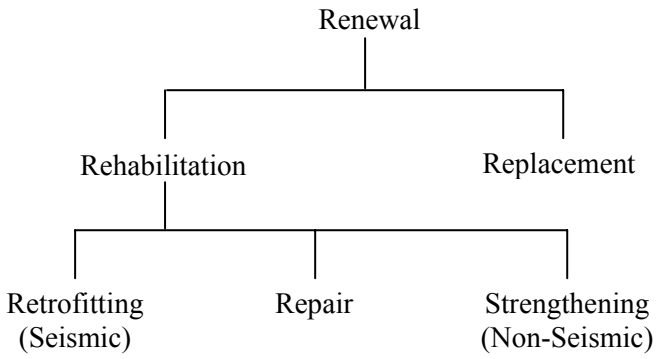

Figure 2.2 Type of renewal strategies[61]

- **Repair and Strengthening**

In recent years FRP composite systems externally bonded to reinforced concrete, prestressed concrete, cast iron, steel and timer structures as a means for repair and strengthening have gained popularity worldwide. The fibre reinforcement may be a cured composite plate bonded to the structure, or a room-temperature cure prepreg directly applied to the structure. Numerous research studies have revealed that FRP composite systems bonded to various structural members can significantly increase their stiffness and load capacity beyond what can be achieved through conventional methods. FRP composite plate bonding has shown to be a cost effective alternative to other traditional methods of strengthening such as the use of steel plates (Burgoyne 1999, Clarke 1999, Karbhari and Seible 2000).

Figure 2.3 West Gate Bridge in Australia strengthened with CFRP plates[130]

There are numerous examples of repair and strengthening projects that have been undertaken since the early 1990's (Hollaway and Leeming 1999, Shaw and Drewett 2000, Karbhari and Seible 2000, Luke et al. 2000, Meier 2000, Hollaway and Head 2001, Hollaway and Cadei 2002). One of the world's largest CFRP (carbon fibre reinforced polymer) strengthening programs was undertaken in Melbourne, Australia in 2001 (Van Erp and Ayers 2004). The 650 m long West Gate Bridge is one of the city's busiest transport corridors. The construction of additional approach lanes to the bridge required the placement of an additional traffic lane within the existing roadway. It was found that strengthening of the structure was required to accommodate the new lanes. Strengthening of the bridge was achieved through a

combination of external post-tensioning using longitudinal steel tendons, as well as the application of bonded CFRP strips and sheets (Figure 2.3). CFRP was used for both flexural, shear and torsional strengthening. The overall project cost was of the order of A$10 million. The scale and complexity of the CFRP strengthening undertaken in this project was unprecedented at the time and has demonstrated the cost effectiveness of FRP for strengthening large span concrete bridges in Australia.

- **Seismic Retrofit**

Seismic retrofit of reinforced concrete columns using conventional steel techniques, whilst effective, has been found to be time consuming, cause significant traffic disruption, rely on field welding and is susceptible to corrosion. Additionally, many of the methods increase the stiffness and strength capacity of the columns putting adjacent structural elements at the risk from higher transmitted seismic forces (Karbhari and Seible 2000). Seismic retrofitting of columns using FRP composites was developed in the early 1990s. The use of FRP composites not only provides a means of confinement, without the associated increase in stiffness, but also enables the rapid fabrication of cost effective and durable jackets with little or no traffic disruption. The available composite systems include epoxy with either carbon, aramid or glass fibre fabric materials. The Sakama River Bridge project in Japan is believed to be one of the largest seismic retrofitting projects to date using carbon fibre composites. The bridge consists of 7 m diameter hollow concrete columns varying from 30 to 60 m high. Some parts of the columns where the concrete/steel splice joints are located were jacketed by a carbon fibre wrap; 50,000 m^2 of sheet material were used to upgrade eight columns (Hollaway and Head 2001).

Due to its many advantages, the use of FRP composites will increasingly be the preferred choice for repair and rehabilitation projects involving buildings, bridges, historic monuments and other structures.

2.3.3 New FRP Composite Civil Infrastructure

A more exciting application of fibre reinforced polymer composites is in the construction of new civil infrastructure. Research conducted throughout the world has resulted in the design and construction of FRP composite bridges, buildings, and

marine structures. The following section will briefly describe and illustrate some buildings and structures that have been constructed using FRP composites.

- **Marine Structures**

Industrial platforms built entirely of pultruded fibreglass reinforced plastics are widely used because of their corrosion resistance. An area of application of special interest is offshore platforms for oil production (Figure 2.4). In this type of environment, weight savings are absolutely necessary. Fibreglass platforms weigh typically 30% of their steel counterpart, allowing for installation by a smaller crew, in less time, with less demand on space for lifting equipment, and reduced transportation cost to the site (Barbero 1998). Another major reason for using FRP composites is its superior corrosion resistance thus reducing maintenance costs.

Figure 2.4 Walkways on an offshore platform manufactured by pultrusion process[61]

Another recent example of FRP composites in marine structures is the floating RiverWalk in Brisbane, Australia (Van Erp and Ayers 2004). The RiverWalk, is a 34 km long trail along the bank of the Brisbane River. As shown in Figure 2.5a, a part of the RiverWalk has been designed as a floating walkway which is 850 m long and 5.4 m wide. This part of the walkway consists of 288 individual concrete floats connected by beams called walers. Due to the aggressive marine environment, walers

using traditional materials such as timber and steel would require replacement every 10 to 15 years which made them the weak link in the 100-year design life required for the walkway. In a bid to find a better alternative, Brisbane City Council approached Fibre Composite Design and Development (FCDD) at the University of Southern Queensland about the possible use of fibre composites for the walers. Based on a detailed set of specifications including structural performance, vandal resistance, boat impact and aesthetics, FCDD developed a revolutionary new waler beam concept using a patented combination of polymer concrete, 3-dimensional FRP reinforcement and a special filled resin system (Van Erp and Ayers 2004). The waler beam concept was designed to carry a wide range of static and dynamic loads and was extensively tested before being applied in the floating walkway (Figure 2.5b).

(a)

(b)

(c)

Figure 2.5 Brisbane's floating walkway[130]: (a) View of the floating walkway; (b) Testing of fibre composite walers; (c) 18m long fibre composite truss

In addition to the development of the new fibre composite walers, a special 18 m long fibre composite truss was also developed by FCDD for the Brisbane RiverWalk project (Figure 2.5c). This truss, of which a large part is submersed in saltwater, was designed to distribute the highly concentrated loads from a 20 m span, 5 m wide pedestrian bridge over a number of pontoons of the floating walkway. The truss has an ultimate bending moment capacity of 700 kNm, is 2.5 m deep and has a 1.4 m deep cut out to accommodate the bridge. Because of its low weight (5000 kg) and corrosion resistance, the fibre composite truss offered significant benefits in terms of construction and installation time. It provides an extremely durable and high capacity solution to a difficult engineering problem.

- **Building Structures**

Although the use of FRP composites in building structures is still in its infancy due to the high material cost and low fire resistance, a number of examples exist around the world demonstrating their use in this type of application. For example, a five-storey 15m-tall multi-functional building – Eyecatcher building (Figure 2.6) has been constructed in Basle, Switzerland in 1999. This building is made of glass-fibre-reinforced polyester building elements (Keller 1999). Another two-storey building (Figure 2.7), used as site offices, has been developed using FRP plank units manufactured and designed by Maunsell Structural Plastics, Beckenham, UK. The wall and floors are bonded together to form an integral monocoque structure (Burgoyne 1999, Hollaway and Head 2001).

Figure 2.6 The Eyecatcher building in Basle, Switzerland[81]

Figure 2.7 A prototype building structure of two-storey height using FRP planks[20]

FRP composites have also been used for the National Bank building in Atlanta, Georgia, which features a 11 m tall and all fibreglass spire at its top. The spire is mounted 312 m above ground, and it is designed to sustain a wind pressure of 550 kPa (Barbero 1998). Lightweight, moulded-in colour, and timely delivery were cited as the advantages of composite materials for this highly visible application.

- **Bridge Structures**

Another exciting application of FRP composites is in the construction of new bridge structures. Prototype bridges constructed entirely from FRP were first conceived in Europe and North America in the late 1970 and the first FRP bridge built in Europe is believed to be a 10 m span bridge constructed at Ginzi, Bulgaria, in 1981/1982. This GFRP bridge was constructed using chopped strand mat in a resin matrix and fabricated by the hand lay-up method. The second GFRP bridge to be constructed was the Miyun bridge in Beijing, China, which was completed in October 1982 (Hollaway and Head 2001). During the past twenty-five years, considerable research resources have gone into the development of composites in bridge structures and today a number of FRP composite bridges have been constructed worldwide. A wellknown example of an FRP composite bridge is the world's longest all-composite pedestrian bridge spanning the River Tay at the golf club in Aberfeldy, Scotland (Figure 2.8). The footbridge was completed in 1993 and has a main span of 63 m, width of 2.12 m and an overall length of 113 m. The deck and two A-frame towers are pultruded with fibreglass reinforcement and polyester resin, then bonded together with an epoxy adhesive. The cable stays were manufactured from Aramid fibres. The

bridge deck was designed to be modular, and was assembled without heavy machinery at the remote site (Schwartz 1997b, Barbero 1998, Hollaway and Head 2001, and Ref.[50]).

Figure 2.8 Aberfeldy footbridge, Aberfeldy, Scotland [18]

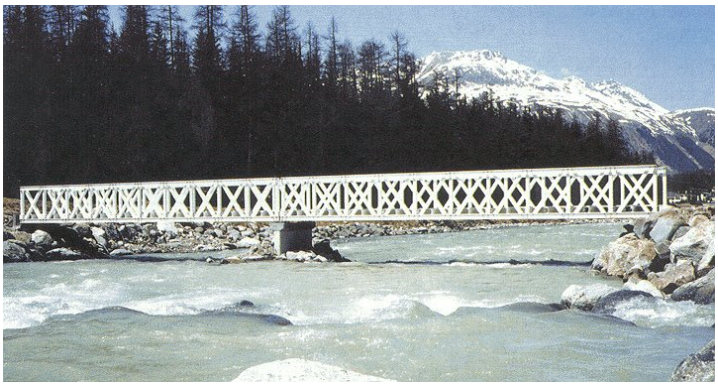

Figure 2.9 A FRP footbridge in Pontresina, Switzerland[79]

The advantage of lightweight FRP composite bridge construction is also illustrated by two footbridges which have been airlifted into position by helicopter because of the difficulty of transportation in the severe terrain in which they are situated. A 17 m long footbridge designed by Maunsell Structural Plastics weighted only 1 ton and was lowered into position in a remote area of Wales. Another two span girder bridge was erected across a river at Pontresina, Switzerland in 1997 (Figure 2.9). The Pontresina bridge weighting 2.5 tonnes is unique in that it was designed to be

removed each year before the snows melt, and then reinstalled once the danger of flooding has passed. Light weight was thus a significant factor in the design, and the two 12.5-m spans were lifted into place by helicopter (Burgoyne 1999, Keller 1999, Hollaway and Head 2001, Keller 2002). Light weight was also one of the main reasons for choosing a fibre composite solution for the Bonds Mill Bridge – the world's first drawbridge for vehicular traffic on the Stroudwater navigation canal in England, since this meant that both lifting tower and counterweight could be eliminated. The bridge was erected in 1994 and assembled from the same modular system as used for the Aberfeldy Bridge (Åström 1997, Hollaway 2000, Hollaway and Head 2001). Recently an all-composite full-service bridge designed by the University of California at San Diego (UCSD) was proposed to provide a link between the east and west part of the campus, which are separated by a ten-lane interstate freeway (Schwartz 1997b, Hollaway and Head 2001). The bridge is designed as a 137 m long dual plane fan-type cable-stayed bridge supported by a 58 m high A-frame pylon with circular legs filled with normal concrete (Figure 2.10). The bridge deck design utilizes a new FRP modular system – Hybrid Tube System (HTS) developed at the University of California, San Diego. Details of this new FRP composite bridge system can be found in Karbhari and Seible (2000), Karbhari et al. (2000), Hollaway and Head (2001).

Figure 2.10 All-composite full-service bridge to link two separate areas of the campus at University of California, San Diego, USA[61]

2.3.4 Hybrid FRP/concrete Structural Systems

The civil engineering industry is constantly striving for ways to improve design and construction technologies to obtain a more economical solution to engineering problems. It has long been recognized that, in the area of construction involving reinforced concrete beams, the region of the beam below the neutral axis is wasteful of material. Concrete is very weak in tension and the sole use of this material in this location is to position the reinforcing steel bars and to protect them from aggressive environments. However, the concrete in the tensile zone of the loaded beam will crack and allow aggressive substances to attack the steel, causing gradual degradation. On the other hand FRP composites possess excellent in-service properties, in particular, resistance to aggressive substances, and have high specific strength and stiffness. Thus, FRP composites and concrete can be jointed to form a hybrid structural system that combines the high strength/low weight characteristics of FRP composites in the tensile zone with the high compression capacity of plain concrete in the compression zone, in which these two very dissimilar materials will be used to their best advantage.

To date there are a number of research developments focussed on hybrid FRP/concrete structural systems (Triantafillou and Meier 1992, Deskovic 1993, Deskovic et al. 1995, Hall and Mottram 1998, Canning et al. 1999 and Hulatt et al. 2001). A recent example of applying the hybrid FRP/concrete concept into a real civil infrastructure is the first Australian FRP composite road bridge, which was developed by FCDD and constructed in Toowoomba, Queensland, in January 2002 (Figure 2.11). The design concept of this bridge was based on the traditional plank bridge concept, where individual beams are laterally post tensioned to create the bridge (Van Erp et al. 2002). The beams in the successful design were a box section formed using glass reinforced polyester pultruded profiles. Additional carbon fibre reinforcement was incorporated into the base of the deck to enhance stiffness. Plain concrete was used to form a compression flange on the top of the beams. An extensive series of field tests have revealed that the hybrid concept exhibits good structural performance including excellent damping and fatigue behaviour. In this hybrid concept, failure is initiated by concrete crushing and the section continues to carry additional load until the carbon fibre reinforcement in the

tensile zone fails. A major advantage of this type of failure behaviour is that the crushing of the concrete will show up in the wear surface of the bridge. This is easier to detect than failure in the carbon reinforcement underneath the bridge. Furthermore, localised crushed concrete is relatively easy to repair compared to an FRP tensile failure (Van Erp et al. 2002).

(a) (b)

Figure 2.11 New FRP composite bridge: (a) Transportation and installation of new composite bridge; (b) Field testing of the bridge

The structures outlined in the sections above are only a small portion of the structures built using FRP composites over resent years. Other examples of the usage of FRP composites in civil infrastructure can be found in Åström (1997), Schwartz (1997b), Barbero (1998), Hollaway and Head (2001), and Ref.[28]. While many of these structures probably do not represent an optimal solution to FRP composite application, they do demonstrate the viability of these materials in large structural applications.

2.4 Summary

This chapter has provided some background on fibre reinforced polymer (FRP) composites for this project including a brief overview of FRP composite materials and their usage in civil and structural engineering applications. It is clear that FRP composites are structural capable materials and that they exhibit significant potential

in a wide range of civil engineering applications. Thus, there is no doubt that FRP composites have the potential to bring about far reaching innovations in civil and structural engineering.

Although FRP composites have been used and are increasingly being used in a variety of civil engineering applications, the most significant realised potential in recent years appears to be in the area of rehabilitation of existing structures. The immediate cost and safety benefits of FRP rehabilitation technologies are clear, and adoption of the material by the construction industry is widespread (Neale 2000, Baskis et al. 2002). FRP composites in other civil applications are still in the realm of demonstrations rather than in fully commercialised products and technologies. Thus, fibre composite research conducted in civil engineering applications is occurring in the context of a relatively immature industry.

The continued use of FRP composites in civil engineering infrastructure applications is dependent, amongst other factors, on demonstration of their enhanced durability and lower whole life cycle costs as compared to conventional materials. Currently, there is a lack of a comprehensive database on the long-term response of FRP composites in civil infrastructure (Hollaway and Head 2001). As a result, a number of careful monitoring programs of structures with primary FRP load-bearing components have been set up around the world and should provide such database in the coming years.

In addition to lack of long-term durability data, the lack of design codes and standards for FRP composite materials in civil engineering structures has also been well documented as another major inhibitor to the wider usage of these materials in mainstream applications (Karbhari and Seible 2000, Baskis et al. 2002). Although Duranovic et al. (1997) have shown that the conventional technique for analysis of steel reinforced concrete sections can be adopted for those sections using FRP rebars, the design techniques for FRP reinforced concrete are different in certain respects to those in steel reinforced concrete. Over recent years there have been international efforts to develop design codes and standards for FRP composites in civil engineering. To date, a number of preliminary documents in the form of design codes and standards for FRP composites in civil construction are either published or

currently being written in Japan, Canada, the United States and Europe (Hollaway and Head 2001, Cripps 2002 and Ref. [28]). However, these documents are still under validation and several major issues have to be addressed before they become certified and accepted codes of practice. In Australia, efforts are also underway to develop an Australian Code and Practice for the structural design of fibre composites (Van Erp and Ayers 2004).

Furthermore, the education and training of engineers, constructions workers, inspectors, and owners of structures on various relevant aspects of FRP technology and practice will also be crucial in the successful application of FRP composites in civil engineering applications (Karbhari and Seible 2000, Ayers 2001). However, it should be emphasised that even with anticipated resolution of the above-described issues the initial use of FRP composites will be mainly restricted to those applications where their unique properties are crucially needed.

Chapter 3

DEVELOPMENT OF A PROTOTYPE TWO-WAY FRP SLAB

3.1 Introduction

The previous chapter has outlined the background of FRP composites associated with the proposed research work. This chapter will describe the development of the present study in more detail. It firstly reviews the relevant research on FRP slab and bridge deck systems. The chapter then moves focus to describe the proposed new two-way FRP floor slab system. Following the description of this new slab concept, the development of a prototype two-way FRP slab and the composite materials selected for the construction of this prototype slab are presented. The constituent results discussed in this chapter are key inputs into the detailed analysis procedure described in subsequent chapters.

3.2 Review on FRP Floor Slab Structures

Floor slab structures are one of the most common structural elements in civil and structural engineering. They are used widely in infrastructure such as bridge decks and pedestrian walkways. The dominant materials used for floor structures are conventional construction materials, such as steel and concrete.

In terms of their structural behaviour, floor slabs can be divided into two major types, namely, one-way slabs and two-way slabs (Warner et al. 1998 and Park et al. 2000). One-way slabs act structurally as wide beams with primary bending moments

in one direction. Consequently in a one-way slab, the main reinforcement is placed in one direction to resist the loads. Some secondary reinforcement is provided in the orthogonal direction to control cracking due to shrinkage and assist with load distribution. Two-way slabs have comparable magnitude of bending moments in both directions, and hence similar quantities of reinforcement are placed in both directions to resist the main loads and resulting bending moments (Figure 3.1).

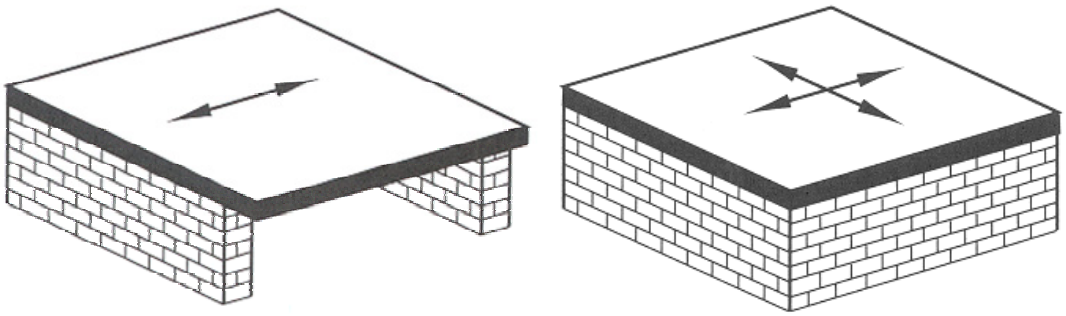

(a) One-way slab (b) Two-way slab

Figure 3.1 One-way and two-way slabs[133]

In the past few years, FRP composite slab structures have received significant attention due to their inherent advantages compared to traditional steel reinforced concrete slab. These advantages have created interesting possibilities for replacing of conventional concrete floor slabs with slab structures made out of FRP materials. Around the world, most research in FRP floor slab structures has so far focused on bridge deck applications. Thus, a brief review of published works pertaining to the analytical and experimental investigations conducted on FRP composite bridge deck systems will be presented next.

One of the earliest discussions on the use of fibre reinforced composite materials in bridge decks was presented by Henry (1985). Henry investigated FRP lattice bridge decks using finite element models of four FRP deck concepts with the following web configurations: (1) X-shaped panels with vertical members; (2) X-shaped panels only; (3) V-shaped panels; and (4) inverted V-shaped panels with vertical members (Figure 3.2). Each of these configurations had an FRP top and bottom flange thickness of 12.7-15.9mm. In this research, it was found that the design of each of

the deck concepts was controlled by the deflection limit state rather than the strength limit states, and that the deck concept with X-shaped web members appeared to have the lowest deflection when compared to other deck configurations (Zureick et al. 1995, Hayes et al. 2000). This X-shaped deck concept was selected by Plecnik and Azar (1991) for fabrication and further study. Relatively small deck panels for static and fatigue testing were fabricated using a combination of filament winding and hand layup. The testing program focused on fatigue behaviour of simply supported panels over a 2.13 m span. Loss of stiffness in the deck specimens was significant after 4,000,000 cycles of load ranging from 9.34 to 37.8 kN.

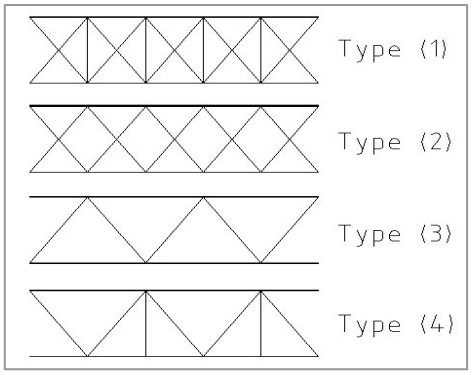

Figure 3.2 FRP bridge deck cross-section types considered in Ref. [54]

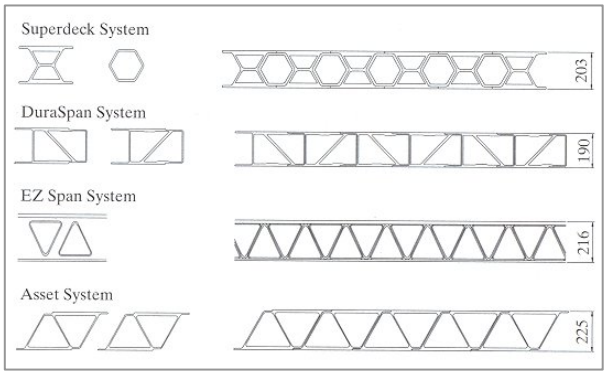

Figure 3.3 Pultruded FRP bridge deck systems[79]

More recent developments in the area of commercial FRP slabs or deck system include the superdeck system and the use of box-shaped or V-shaped cellular decks (Figure 3.3), which are constructed using assemblies of adhesively bonded pultruded structural shapes. The superdeck system, also termed H-deck system, has been used on four bridges to date in USA (GangaRao and Craigo II 1999). The cross section of this system is 203 mm deep and consists of full-depth hexagons and half-depth trapezoids with the cores oriented transverse to the traffic direction (Lopez-Anido et al. 1997a). Modelling and testing of the H-deck system was conducted before installation (Lopez-Anido et al. 1997b). The testing program included static tests up to failure and fatigue tests under a simulated wheel load. Figure 3.4 shows one of the four bridges using the H-deck system under site construction.

Figure 3.4 Construction of the bridge using H-deck slab structure[45]

Figure 3.5 Demonstration bridge in Darke Country, Ohio, USA[22]

A demonstration bridge using the DuraSpan bridge deck system (Figure 3.3) was constructed in Darke Country, Ohio, USA and opened to traffic in November 1999 (Figure 3.5). A comprehensive testing program was undertaken at the University of Delaware to validate the design of this bridge deck system including static and fatigue testing. A specimen was subjected to 10.6 million cycles of fatigue loading, which corresponds with average daily truck traffic of the demonstration bridge applied throughout a design life of 75 years. Throughout the fatigue and strength test, the connection region behaved well and showed negligible variation in structural response. This demonstration bridge is the first bridge in the world to fully rely on composite action between a FRP deck and girders to resist superimposed dead and live load (Cassity et al. 2002).

Brown and Zureick (1998) presented an extensive investigation on FRP V-shaped bridge deck systems (EZ Span System). The finite element models of the deck configurations were subjected to axle loads. The results show that orientation of the majority of the top and bottom plate fibres parallel to the long axis of the triangular elements provides the greatest resistance to deflection and the highest safety factor. Three fabrication approaches were investigated in the research which include impregnated engineered fabrics, vacuum assisted moulding of preforms and pultruded 3D braid. The conduct of this research program demonstrates the benefits of guiding the design and fabrication effort by analysis and test. The results of the program to date also show the improved performance obtained through the use of 3D braided fabric pultrusions.

In Europe an all composite bridge deck system, the ASSET system (Figure 3.3), has been developed by a consortium of seven industrial firms (Hollaway and Head 2001). This pultruded deck forms a complete FRP bridge deck system with associated parapet and street furniture fixing concepts for all situations. Detailed finite element analyses and small and large-scale laboratory testing of the ASSET profile were conducted prior to construction of the bridge structure (Hodgson 2000, Luke et al. 2002). In order to prove this advanced composite bridge deck concept, a prototype highway bridge using the ASSET system capable of carrying a 40 tons vehicle has been constructed for Oxfordshire County Council, and was officially opened in October 2002 (Ref. [40]). The bridge is being periodically monitored to document its performance under real life conditions.

The square plate tube and plate deck shown in Figure 3.6 is a pre-commercial design composed of off-the-shelf shapes typical of many of the basic pultrusion companies (Hayes et al. 2000). The square tubes comprising the core of the deck were oriented perpendicular to the support stringers. A 1.5 m × 4.5 m FRP composite bridge deck using this system has been installed at the Troutville Weigh Station, Virginia, USA in 1999 (Figure 3.7). The bridge deck was installed with strain gages and a data acquisition terminal to continuously monitor the deflection for at least a year. Both laboratory and field testings indicate that the square tube and plate design integrated into a simulated deck-girder configuration met the necessary strength performance criteria. No change in stiffness or strength of the deck system were found after 3

million cycles of a fatigue load in excess of the design wheel load (Hayes et al. 2000, Hollaway and Head 2001). A similar floor system was used by Bank et al. (2000) as the deck for a floating causeway system.

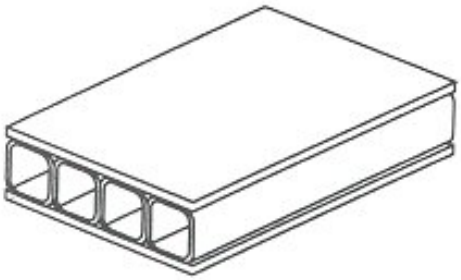

Figure 3.6 Concept of square tube and plate deck system

Figure 3.7 Installation of the FRP composite bridge deck at the Troutville Weigh Station, Virginia, USA[18]

FRP sandwich slab structures are another floor system commercially available at the present time for bridge deck applications. FRP sandwich slab structures use thin, strong and stiff fibre face sheets that carry flexural loads and a low-density, bonded core material that separate the face sheets and ensures composite action of the slab. Due to the ease with which face sheets and core materials can be changed in manufacturing, sandwich construction presents tremendous flexibility in designing for various depths and deflection requirements. Fibre face sheets of sandwich bridge decks are primarily composed of E-glass mats and/or rovings infused with a polyester or vinylester resin. Core materials for sandwich bridge deck systems are commonly rigid foams or thin-walled cellular FRP materials. An all-composite bridge using FRP sandwich bridge deck system has been designed, fabricated, tested and deployed over the NO Name Creek in Russell, Kansas, USA (GangaRao 1999). The deck is compromised of a thin layer of polymer concrete covering two layers of alternating laminates of chopped strand mat and uni-axial material that sandwiches about 0.6 m of a FRP honeycomb core. Extensive investigations on a FRP sandwich bridge deck system using a honeycomb core have also been conducted by Davalos et al. (2001).

Recently, a new concept for fibre reinforced composite slabs, based on a structural particulate filled resin (PFR) core (refer Chapter 2) was developed by researchers at the University of Southern Queensland (Davey at al. 2001). The design concept of this slab structure combines FRP composite structural shapes (circular tubes) and sandwich construction concepts. A typical cross-section of this new floor system is shown in Figure 3.8. The slab is created as a sandwich structure with a central PFR core. Circular voids are included to save materials, thus reducing cost and weight. These voids are made with a glass fibre reinforced tube. Fibres in the circular tube are oriented at +45º and -45º to resist shear forces. The PFR core is thoroughly bonded to the FRP circular tube and helps to resist local buckling. A casting process similar to that used in reinforced concrete was used for the construction of the slab. Analytical and experimental investigations have been undertaken on this new floor slab system (Figure 3.9). The preliminary results clearly indicate the potential of this type of FRP slab structure (Davey at al. 2001).

Figure 3.8 Typical cross-section of the new FRP slab[33]

Figure 3.9 New concept of FRP slab in test configuration[33]

3.3 A New Two-way FRP Slab Concept

The previous section has highlighted recent developments of FRP composite slabs and bridge deck systems. To date this development has largely focussed on one-way structural systems using pultruded elements. Although a significant number of such floor systems are available, broad industry acceptance, particularly commercial acceptance, has not been forthcoming. Despite their inherent advantages, only limited attempts have been made to develop FRP sandwich panels for civil engineering applications. One of the reasons for this limited activity has been the lack of a suitable core material (refer Section 2.2.1). However, one approach that has shown significant potential is the preliminary development work on the FRP slab undertaken by Davey et al. (2001). The findings of this preliminary work can be summarised as follows:

- PFR appears to have appropriate structural characteristics for use as a core material in civil engineering FRP sandwich panel applications;
- The material cost of PFR is approximately 10 times that of concrete. Hence, the introduction of voids to save material is highly desirable. Davey et al (2001) proposed a concept that has 45% voids (by volume);
- The bending characteristics of the sandwich slab concept are largely determined by the skin architecture, while the shear characteristics are largely determined by the core materials and geometry. It was proposed that the void former should also contribute to shear strength and stiffness;
- While epoxy PFR has good structural characteristics, there may be significant cost advantages in utilising vinyl-ester PFR systems because of their reduced cost. While detailed material choices were beyond the scope of initial developments, the issues were explored generally. Vinyl-ester PFR was found to be a viable system for concept development.

The research work undertaken by Davey et al (2001) focussed on the development of a one-way slab system. Based on the positive findings of this preliminary research work, a two-way FRP slab system was developed using the similar design philosophy.

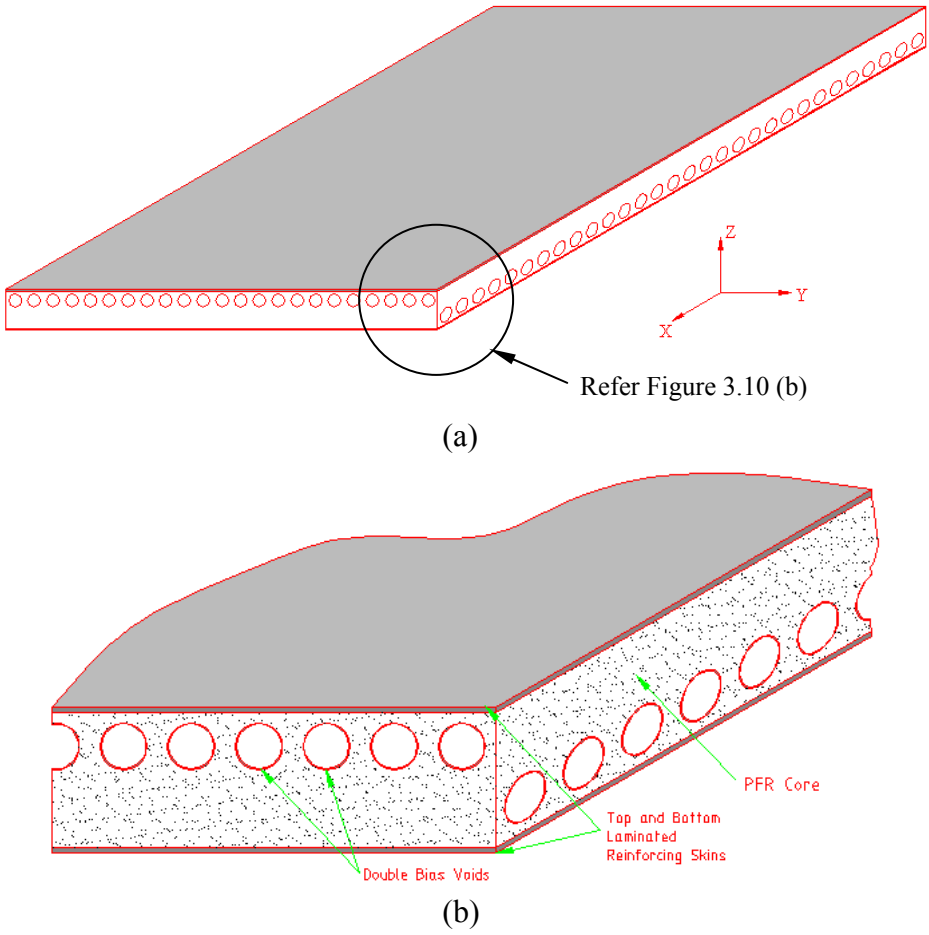

Figure 3.10 The concept of the new two-way FRP composite slab

The new two-way FRP composite slab concept is shown in Figure 3.10. It is created as a sandwich structure with a central core made from a particulate filled resin. Fibre reinforced laminates (skins) are bonded to the top and bottom of the core to provide bending moment resistance in two directions. This is achieved by placing a similar amount of reinforcing fibres parallel and perpendicular alternative to the longitudinal axis.

As for the one-way slab, circular voids are introduced in the core region of this two-way slab to save material and reduce weight. The void formers are fibre reinforced tubes with the fibres oriented at +45° and -45° to resist shear forces. The circular tubes are oriented in *x*- (longitudinal) and *y*- (transverse) direction to provide shear resistance in both directions of the two-way slab (Figure 3.10). These tubes also

provide reinforcement to the thin wall of PFR between adjacent voids. As with traditional core materials, the PFR core also has the following functions:

- restrains the compression laminate from buckling, and
- provides torsional and bearing capacity.

In addition, the core contributes significantly to the overall load carrying capacity of the two-way composite slab.

3.3.1 Prototype Two-way FRP Slab

Commercial development of the new two way FRP slab concept is beyond the scope of this investigation, however a prototype structure developed using the principles of the new concept was required to:

- Investigate the structural validity of the concept;
- Provide experimental verification of analytical and numerical results developed within the context of this investigation.

Both outcomes are important initial investigations that may subsequently facilitate development of this concept into commercial products.

Planning for this prototype required a series of practical and functional constraints to be considered, in particular the prototype geometry was largely governed by the geometry and capacity of available testing facilities. The largest facility available at the University of Southern Queensland is an Instron Hydraulic Testing Machine which has a limited span (at about 1740 mm) between the two steel columns, as shown in Figure 3.11. Consequently, the width of the prototype slab was chosen to be W_S = 1620 mm (with actual span of 1380 mm in transverse direction) such that the slab could be tested underneath the available heavy-duty testing machine. The length of slab was then selected at L_S = 2020 mm (with actual span of 1800 mm in longitudinal direction) to obtain comparable dimensions in both longitudinal and transverse directions (Park and Gamble 2000, McCormac 2001).

As shown in Figure 3.10, the overall thickness of this prototype two-way FRP composite slab is mainly determined by the diameter of the double bias reinforced circular tubes. With reference to previous investigations on fibre composite beam

and slab structures conducted by the researchers at the University of Southern Queensland (Davey 1999 and Cattell 2000), a double bias reinforced circular tube with inner diameter of 43mm was adopted for the prototype slab. In addition, a PFR core cover thickness of approximately 8mm around each tube was selected. These dimensions are similar to those used for the one-way FRP slab (Davey et al. 2001). Consequently, the thickness of the centre core is chosen to be 120mm. To make sure that strength of the prototype slab did not exceed the maximum capacity provided by the Instron Hydraulic Testing Machine, eight layers of unidirectional laminates with the stacking sequence $[0°/90°]_4$ (anti-symmetric cross-ply laminates) were selected for both top and bottom reinforcing skins. These choices resulted in an overall thickness of the proposed prototype two-way FRP slab of approximately T_S = 128.7 mm.

Figure 3.11 Instron hydraulic testing machine

The three main constituent materials in this slab are: reinforcing fibres, polymer matrix resins and core materials. In general, glass/polyester or glass/vinylester systems are most commonly used in civil applications because of their relatively low cost. The cost of glass fibres is only about 10% (by weight) that of carbon fibres often used in aerospace applications, and the cost of vinyl ester resin is less than half that of a typical structural epoxy resin (Foster et al. 2000). Hence, E-glass fibre

reinforcements in combination with a vinylester resin matrix were adopted in this study to manufacture the proposed composite slab components.

Typically, the core material occupies the majority of the total material volume of a sandwich structure, and therefore the cost of the core material per unit volume needs to be comparatively low to be cost competitive. The PFR core used in this project was a mixture of a low-cost and lightweight fly-ash based ceramic microspheres filler material (SLG) with vinylester resin. Research on this new structural core material has indicated that this type of mixture offers significant benefits in term of both cost and structural performance (Ayers and Van Erp 1999).

The details of the materials used in the production of the prototype two-way FRP slab are as follows:

- MU4500K 450 g/m^2 unidirectional E-glass fabric (Colan Pty Ltd)
- MX6000A 600 g/m^2 double bias (+45°/-45°) E-glass fabric (Colan Pty Ltd)
- Hetron 922 vinylester resin (Huntsman Chemical Company Australia Pty Ltd)
- Butanox M60 MEKP initiator (Akzo Nobel Chemicals Pty Ltd)
- E-spheres SLG filler (Envirospheres Pty Ltd)

It should be noted that all types of E-glass fabric used for the proposed composite slab were supplied in the form of mats. Hetron 922, a general-purpose vinylester resin, was cured using the initiator Butanox M60 MEKP. An initiator level of 2% was used throughout this study and found to yield a gel time of approximately 60 minutes.

Development of the prototype concept required some relatively detailed investigations to ensure that the prototype slab would meet project requirements. This included the proof of concept of a modular manufacturing approach described in Appendix B. In particular, there was considerable value in developing a modular manufacturing approach to overcome some difficulties with fabrication, including exotherm and shrinkage problems. While the modular manufacturing approach has considerable value in relation to this new two-way FRP slab concept, it is not central to the objectives of this PhD Study. Figure 3.12 shows a completed single module.

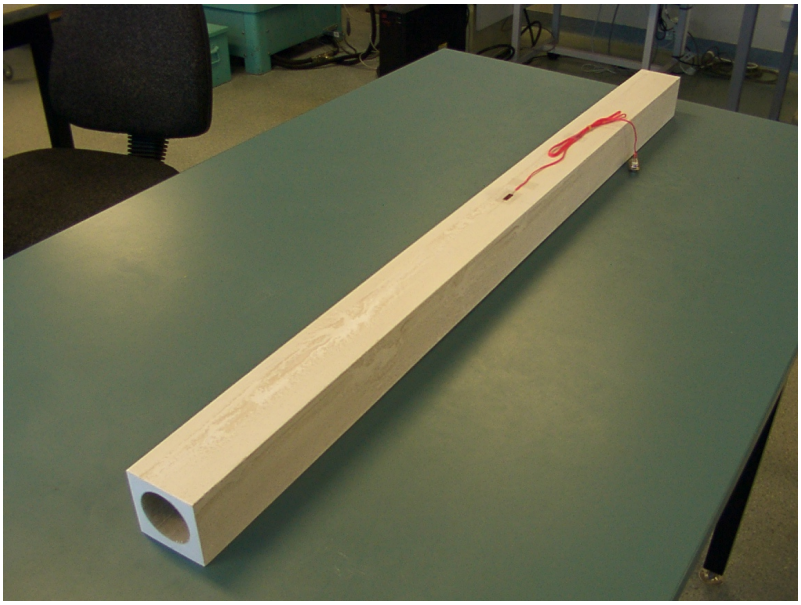

Figure 3.12 A completed single module

3.3.2 Determination of Material Properties

The determination of the mechanical characteristics of FRP materials plays an important role in the design and analysis of fibre reinforced composite structures. The accuracy of such material property data is of paramount importance, as it directly affects the prediction of structural performance. In order to establish the confidence in the predicability of the material performance, all material types used (summarised in Section 3.3.1) during the course of this research were subjected to material testing, to determine their respective mechanical properties. The data obtained from the material tests was then used in the subsequent analysis throughout this study. All tests were conducted at the University of Southern Queensland using the MTS 810 Material Testing System Machine or Shimadzu Universal Testing Machine (Figure 3.13). The specimens were prepared and tested in accordance with the relevant international standards. The details of the individual material testing program are described in Appendix C.

(a)

(b)

Figure 3.13 Testing machines: (a) MTS 810 material testing system machine; (b) Shimadzu universal testing machine

(a) E-glass Laminate

All E-glass laminate specimens were fabricated using the hand layup technique. A layer of peel ply was applied to both sides of the uncured laminate to ensure an even and uniform surface finish. The laminates were allowed to cure at room temperature for a duration of 24 hours, after which the laminates were post-cured at 80°C for a duration of 8 hours. The test results are summarised in Table 3.1. The details of the individual laminate properties test can be found in Appendix C.

Table 3.1 Material properties of E-glass/vinylester of unidirectional lamina

Density (kg/m^3)			1825		
Fibre volume fraction (%)			52.79		
Thickness per layer (mm)			0.542		
Fibre Direction	11	22	Fibre Direction	11	22
Tensile Modulus (MPa)	21222	9207	Compressive Modulus (MPa)	28221	12052
Tensile Strength (MPa)	534.87	43.12	Compressive Strength (MPa)	569.88	151.19
Ultimate Tensile Strain (%)	2.80	0.55	Ultimate Compressive Strain (%)	2.24	1.84
Shear Modulus (MPa)	3074		Poisson's Ratio (12)	0.253	
Shear Strength (MPa)	68.00		Poisson's Ratio (23)	0.041	

Note that no material testing of the MX6000A double bias E-glass mat was undertaken within this study since it can be modelled as two layers of unidirectional fibres at +45° and -45° (Coker 2002). The data obtained from the unidirectional laminate properties tests were used for the double bias fabric for subsequent analysis. In terms of the fibre volume fraction of the unidirectional laminate and the mass per unit area of the double bias used in this study, the thickness per layer of the E-glass/vinylester of double bias lamina was determined as $2 \times 0.3615 = 0.723$ mm, which agreed well with the experimental measurement of the single layer double bias laminate.

(b) PFR Core

As mentioned previously, the PFR core material used in this study consists of a vinylester resin mixed with E-spheres SLG filler. SLG filler is a flyash (power station by-product) and considerably less expensive compared with vinyl ester resin (SLG = \$0.90/kg). Thus, high percentage of SLG filler involved in the PFR core can significantly reduce the cost. However, it may also result in poor structural properties and low fluidity. Extensive research conducted by Ayers (2001) suggests that the mix ratio of filler to resin in the range of 40%-50% filler by volume provides a good balance between material properties and cost. Filler loading in excess of 50% by volume resulted in unworkable fluidity. Therefore, the ratio of SLG filler to

vinylester resin used in the proposed two-way FRP slab is 1:2 by mass, which is equivalent to 44% SLG filler by volume. The PFR core obtained with this mixed ratio was found to offer good mechanical properties and workability at relatively low cost. All testing specimens were cast into pre-fabricated moulds and the castings were allowed to cure at room temperature for a period of 24 hours, and then post-cured at 80°C for a period of 8 hours. Table 3.2 shows the summary of the results obtained from PFR core material properties tests. The details of the individual PFR core properties test are outlined in Appendix C.

Table 3.2 Material properties of vinylester/SLG of PFR core

Density (kg/m^3)	924	Compressive Strength (MPa)	81.72
Tensile Modulus (MPa)	4925	Ultimate Compressive Strain (%)	2.62
Tensile Strength (MPa)	25.29	Shear Modulus (MPa)	1871
Ultimate Tensile Strain (%)	0.66	Shear Strength (MPa)	13.89
Compressive Modulus (MPa)	6127	Poisson's Ratio	0.316

Due to the isotropic nature of the PFR core material (Ayers and Van Erp 1999, Ayers 2001), the shear modulus was determined in terms of the elastic modulus (Tensile) and Poisson's ratio. The shear strength was determined by standard shear properties test, as described in Appendix C.

3.4 Conclusions

The review of FRP floor slab structures has highlighted that the use of FRP composites in such fundamental structural elements is one of the most promising application for these materials. It has been noted that the majority of these FRP slab or bridge deck systems were constructed by adhesively assembling pultruded structural profiles and mainly behaved as a one-way floor system. Research results for a one-way FRP slab constructed using a casting process have also been published. This latter approach seems to have significant potential in terms of both structural performance and manufacturing process. The current project extends this one-way FRP slab concept and presents the first study into a new two-way FRP slab system.

This chapter has focused on the development of this new two-way FRP floor slab concept into a prototype structure. The concept and configuration of such new composite slab were discussed and identified. The selection of the appropriate materials including reinforcement, matrix, and core material was briefly addressed in terms of performance and cost. The accuracy of the structural behaviour prediction and uncertainty associated with published laminate properties prompted the testing of each of the material types used within this research to determine their respective mechanical properties for subsequent analyses. The modular approach to the slab construction was introduced and adopted to overcome the relative high volumetric shrinkage problem of the selected matrix system. Detailed investigations of the modular manufacturing approach were presented in Appendix B. Both single module and small-scale slab tests were performed and the results have aptly demonstrated the potential and feasibility of the modular approach suitable for both small and large slab structures.

The remaining chapters will present details of the analytical, numerical and experimental analyses of the proposed two-way FRP sandwich slab system, which forms the basis for fundamental understanding of the structural behaviour of this slab structure.

Chapter 4

A NOVEL SIMPLIFIED APPROACH FOR THE ANALYSIS OF THE TWO-WAY FRP SLAB

4.1 Introduction

The finite element analysis (FEA) is a powerful technique for studying the anisotropic behaviour of fibre composite structures. These days commercial finite element software capable of analysing fibre composite structures are widely available. As described in Chapter 3, the proposed two-way FRP composite slab is created as a sandwich structure with a central core being formed from PFR material and contains a number of voids. To accurately analyse this type of composite floor slab system a 3D finite element model is often adopted. However, due to the geometric complexity of the slab, the standard 3D finite element analysis is extremely demanding of computer resources, time consuming to prepare and tedious to check for error. Furthermore, any changes in geometric and material parameters in the 3D model require considerable time to modify the geometry and finite element mesh and analyse the model, which is unsuitable for the preliminary investigation of such fibre composite structures. Hence, there is a need to develop a practical simplified approach as an analysis tool prior to building a detailed finite element model to minimize design and analysis effort.

The focus of this chapter is to develop a simplified approach for the analysis of the two-way FRP composite slab. The chapter begins with a brief review of various laminate plate theories. The appropriate plate theory is then identified, and used to develop a simplified analysis technique (transformed plate approach) for the analysis

of the floor slab structure described in Chapter 3. At the conclusion of this chapter, both analytical (Ritz solution) and 2D FEA results of an equivalent transformed plate are compared with the 3D slab FEA results (discussed in Chapter 5) to verify this simplified approach.

4.2 Review of Various Laminated Plate Theories

The laminated plate theories reviewed in this section are generally termed as equivalent single-layer (ESL) laminate theories, which are based on equivalent two-dimensional theories (Reddy 1997). They are obtained from the three-dimensional elasticity theory by making assumptions concerning the variation of displacements and/or stress through the thickness of the laminate, and are used to analyse laminated composite structures (Reddy and Miravete 1995).

The ESL laminate theories are those in which a heterogeneous laminated plate is treated as a statically equivalent, single layer having a complex constitutive behaviour, reducing the 3-D continuum problem to a 2-D problem (Reddy 1997). They generally include three categories, namely classical laminated plate theory (CLPT), first-order shear deformation theory (FSDT), and higher-order shear deformation theory (HSDT). The three-dimensional elasticity theory and multiple model methods fall beyond the scope of this research, and will not be included in this review.

4.2.1 The Classical Laminated Plate Theory

Plates can be classified into two groups: *thin* plates and *thick* plates. A plate is said to be thin when the ratio of the thickness to the smaller span length is less than a commonly accepted ratio 1/20 (Reddy 1984). The small-deflection theory of bending of thin plates is known as the classical plate theory and is based on the Kichhoff-Love assumptions. The classical laminated plate theory is an extension of the classical plate theory to composite laminates. The fundamental assumptions of the Kichhoff-Love Hypothesis (see Figure 4.1) or the classical laminated plate theory (CLPT) are (Reddy 1984, 1997):

(1) Straight lines perpendicular to the midsurface before deformation remain straight after deformation.

(2) The transverse normals do not experience elongation.

(3) The transverse normals rotate such that they remain perpendicular to the midsurface after deformation.

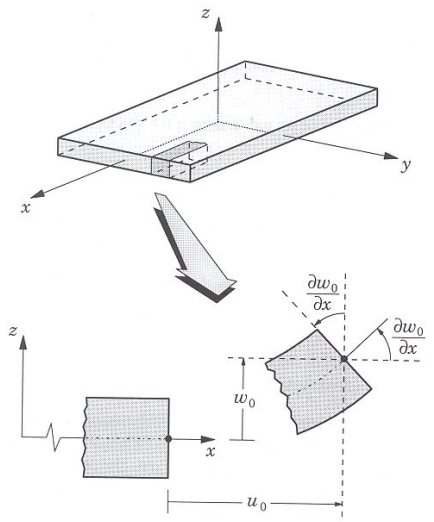

Figure 4.1 Undeformed and deformed geometries of an edge of a plate under the Kirchhoff –Love assumptions[111]

The first two assumptions imply that the transverse displacement is independent of the transverse (or thickness) coordinate and the transverse normal strain ε_z is zero. The third assumption results in zero transverse shear strains, $\gamma_{xz} = 0, \gamma_{yz} = 0$. Since the (virtual) work done by the actual internal forces of the plate in moving through the virtual displacements is the product of forces associated with the stress field and the (virtual) displacements, which result in (virtual) strains, the (virtual) work done by the transverse stresses is zero because of the zero transverse (virtual) strains. Consequently, transverse stresses σ_{xz}, σ_{yz} and σ_{zz} do not contribute to the equations of motion. This amounts to omitting the transverse stresses in the classical laminated theory, and is equivalent to, from a physical point of view, assuming that the plate is 'infinitely' rigid in the transverse direction. When plates are very thin, this assumption is reasonably accurate (Reddy and Miravete 1995). In formulating the theory, certain assumption and restrictions are also made as follows (Reddy 1997):

- The layers are perfectly bonded together (assumption).
- The material of each layer is linearly elastic and has two planes of material symmetry (restriction).
- Each layer is of uniform thickness (restriction).
- The strains and displacements are small compared with the thickness of the plate (restriction).
- The transverse shear stresses on the top and bottom surfaces of the laminate are zero (restriction).

Thus, based on the above assumptions and restrictions, the displacement field of the simplest of ESL laminate theory, the classical laminated plate theory, is of the form

$$\begin{aligned} u(x, y, z, t) &= u_0(x, y, t) - z\frac{\partial w_0}{\partial x} \\ v(x, y, z, t) &= v_0(x, y, t) - z\frac{\partial w_0}{\partial y} \\ w(x, y, z, t) &= w_0(x, y, t) \end{aligned} \tag{4.1}$$

where (u_0, v_0, w_0) are the displacements of a point on the *xy*-plane (or midplane) and *t* denotes the time. The strains associated with the displacement field (4.1) are given by

$$\begin{Bmatrix} \varepsilon_x \\ \varepsilon_y \\ \gamma_{xy} \end{Bmatrix} = \begin{Bmatrix} \varepsilon_x^0 \\ \varepsilon_y^0 \\ \gamma_{xy}^0 \end{Bmatrix} + z\begin{Bmatrix} \kappa_x \\ \kappa_y \\ \kappa_{xy} \end{Bmatrix} \tag{4.2}$$

$$\{\varepsilon^0\} = \begin{Bmatrix} \varepsilon_x^0 \\ \varepsilon_y^0 \\ \gamma_{xy}^0 \end{Bmatrix} = \begin{Bmatrix} \dfrac{\partial u_0}{\partial x} \\ \dfrac{\partial v_0}{\partial y} \\ \dfrac{\partial u_0}{\partial y} + \dfrac{\partial v_0}{\partial x} \end{Bmatrix}, \quad \{\kappa\} = \begin{Bmatrix} \kappa_x \\ \kappa_y \\ \kappa_{xy} \end{Bmatrix} = \begin{Bmatrix} -\dfrac{\partial^2 w_0}{\partial x^2} \\ -\dfrac{\partial^2 w_0}{\partial y^2} \\ -2\dfrac{\partial^2 w_0}{\partial x \partial y} \end{Bmatrix} \tag{4.3}$$

where $(\varepsilon_x^0, \varepsilon_y^0, \gamma_{xy}^0)$ are the membrane strains, and $(\kappa_x, \kappa_y, \kappa_{xy})$ are the flexural (bending) strains, known as the curvatures. Note that the transverse strains $(\varepsilon_z, \gamma_{xz}, \gamma_{yz})$ are identically zero in the classical plate theory. Once the

displacements (u_0, v_0, w_0) of the midplane are known, displacements and strains at any point (x, y, z) in the plate can be computed using Eqs. (4.1), (4.2) and (4.3).

In the classical laminated plate theory (CLPT), the in-plane displacements are assumed to vary linearly through the thickness and the transverse displacement is assumed to be constant through the thickness. The classical laminated plate theory is found to be adequate for most applications where the thickness of laminate is small, by two orders of magnitude compared to the in-plane dimensions. When the classical laminate theory is not applicable, a refined theory that accounts for the transverse shear strains can be adopted. More details of CLPT and discussions of its usage can be found in Reissner and Stavsky (1961), Dong et al. (1962), Yang et al. (1966) and Whitney and Leissa (1969a).

4.2.2 The First-order Shear Deformation Theory

Classical (Kirchhoff) plate theory has been widely used to model plate behaviour, but is adequate only for very thin laminate FRP plates. Since the ratio of the in-plane elastic modulus to the transverse shear modulus is very large for FRP plates, Kirchhoff theory, which neglects transverse shear deformation, is usually inadequate for the analysis of thick or moderately thick FRP plates. Many plate theories have been proposed to include the effect of shear deformation. The laminated version of the first-order shear deformation theory (FSDT) developed by Reissner (1945) and Mindlin (1951) is the simplest, which is also termed as Reissner-Mindlin plate theory. In the first-order shear deformation theory, the third assumption of the Kirchhoff-Love hypothesis is removed, hence the tranverse normals do not remain perpendicular to the midsurface after deformation (Figure 4.2). This amounts to including transverse shear strains in the theory. The inextensibility of transverse normals requires that the displacement w not be a function of the thickness coordinate z (Whitney 1969b, Reissner 1979, Reddy 1997).

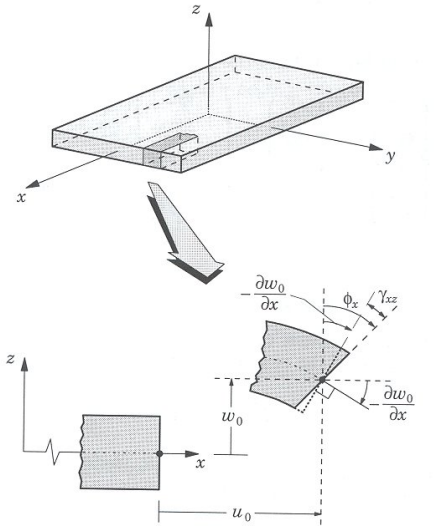

Figure 4.2 Undeformed and deformed geometries of an edge of a plate under the assumptions of the first-order plate theory[111]

Under the same assumptions and restrictions as in the classical laminated plate theory, the displacement field of the first-order shear deformation theory (or Reissner-Mindlin plate theory) is of the form

$$\begin{aligned} u(x, y, z, t) &= u_0(x, y, t) + z\psi_x(x, y, t) \\ v(x, y, z, t) &= v_0(x, y, t) + z\psi_y(x, y, t) \\ w(x, y, z, t) &= w_0(x, y, t) \end{aligned} \tag{4.4}$$

where $(u_0, v_0, w_0, \psi_x, \psi_y)$ are unknown functions to be determined. As before, (u_0, v_0, w_0) denotes the displacement of the midplane and t is the time. Here ψ_x and ψ_y are rotations of the transverse normal about the y-axis and x-axis, respectively. The strains associated with the displacement field (4.4) are given by

$$\begin{Bmatrix} \varepsilon_x \\ \varepsilon_y \\ \gamma_{yz} \\ \gamma_{xz} \\ \gamma_{xy} \end{Bmatrix} = \begin{Bmatrix} \varepsilon_x^0 \\ \varepsilon_y^0 \\ \gamma_{yz}^0 \\ \gamma_{xz}^0 \\ \gamma_{xy}^0 \end{Bmatrix} + z \begin{Bmatrix} \kappa_x \\ \kappa_y \\ \kappa_{yz} \\ \kappa_{xz} \\ \kappa_{xy} \end{Bmatrix} \tag{4.5}$$

$$\left\{\varepsilon^0\right\}=\begin{Bmatrix}\varepsilon_x^0\\ \varepsilon_y^0\\ \gamma_{yz}^0\\ \gamma_{xz}^0\\ \gamma_{xy}^0\end{Bmatrix}=\begin{Bmatrix}\dfrac{\partial u_0}{\partial x}\\ \dfrac{\partial v_0}{\partial y}\\ \dfrac{\partial w_0}{\partial y}+\psi_y\\ \dfrac{\partial w_0}{\partial x}+\psi_x\\ \dfrac{\partial u_0}{\partial y}+\dfrac{\partial v_0}{\partial x}\end{Bmatrix},\quad \left\{\kappa\right\}=\begin{Bmatrix}\kappa_x\\ \kappa_y\\ \kappa_{yz}\\ \kappa_{xz}\\ \kappa_{xy}\end{Bmatrix}=\begin{Bmatrix}\dfrac{\partial \psi_x}{\partial x}\\ \dfrac{\partial \psi_y}{\partial y}\\ 0\\ 0\\ \dfrac{\partial \psi_x}{\partial y}+\dfrac{\partial \psi_y}{\partial x}\end{Bmatrix} \tag{4.6}$$

Note that the strain ε_z is also identically zero in the first-order shear deformation theory. In addition, the strains $(\varepsilon_x, \varepsilon_y, \gamma_{xy})$ are linear through the laminate thickness, while the transverse shear strains $(\gamma_{yz}, \gamma_{xz})$ are constant in the first-order laminated plate theory. As a consequence, the transverse shear stresses will also be constant due to the constant transverse shear strains through the laminate thickness. Since the FSDT accounts for layerwise constant states of transverse shear stress, shear correction factors are required to rectify the unrealistic variation of the shear strain/stress through the thickness (Whitney 1973, Bert 1973, Wittrick 1987). The shear correction factors depend not only on the lamination and geometric parameters, but also on the loading and boundary conditions.

4.2.3 The Higher-order Shear Deformation Theory

The first-order shear deformation theory assumes a linear distribution of the in-plane normal and shear stresses over the thickness, which results in nonzero transverse shear stresses but does not reproduce the nonlinear transverse shear stresses distribution through the plate's thickness. Higher-order shear deformation theories (HSDT) can overcome the limitations of the first-order plate theory by introducing additional degrees of freedom. In both CLPT and FSDT, the inextensibility and/or straightness of transverse normals can be removed. Such extensions lead to second- and higher-order theories for plates. In principle, it is possible to expand the displacement field in terms of the thickness coordinate up to any desired level. However, due to the algebraic complexity and computational effort involved with higher-order theories in return for marginal gain in accuracy, theories higher than third order have not been attempted. The reason for expanding the displacement up

to the cubic term in the thickness coordinate is to have quadratic variation of the transverse shear strains and transverse shear stresses through each layer, and to eliminate the transverse shear stresses on the top and bottom surfaces of the laminate plate to satisfy the stress-free boundary conditions. This avoids the need for shear correction coefficients used in the first-order shear deformation theory (Reddy 1997).

There are many papers on higher-order theories and their applications. Among them, the third-order shear deformation theory (TSDT) originally developed by Reddy (1984a, b) is commonly used. This theory is based on the same assumptions as the classical and first-order plate theories, expect it releases the assumption on the straightness and normality of a transverse normal after deformation by expanding the displacements as cubic functions of the thickness coordinate. Figure 4.3 shows the comparisons of three ESL laminate theories on deformation of a transverse normal.

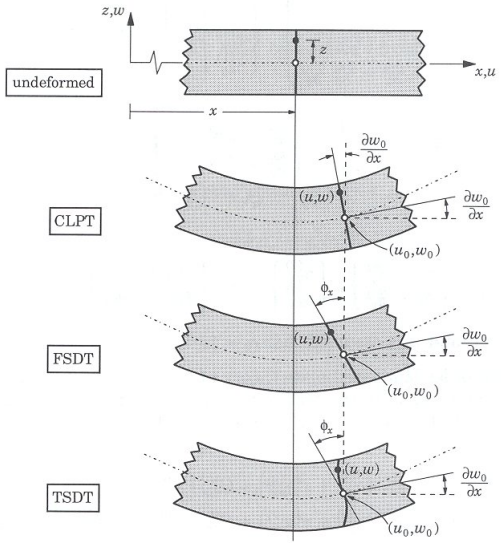

Figure 4.3 Deformation of a transverse normal according the classical, first-order, and third-order plate theories[111]

The displacement field of TSDT developed by Reddy (1984a, b) is given by

$$
\begin{aligned}
u(x, y, z, t) &= u_0(x, y, t) + z\psi_x(x, y, t) + z^3\left(-\frac{4}{3h^2}\right)\left(\psi_x + \frac{\partial w_0}{\partial x}\right) \\
v(x, y, z, t) &= v_0(x, y, t) + z\psi_y(x, y, t) + z^3\left(-\frac{4}{3h^2}\right)\left(\psi_y + \frac{\partial w_0}{\partial y}\right) \\
w(x, y, z, t) &= w_0(x, y, t)
\end{aligned}
\tag{4.7}
$$

where (u_0, v_0, w_0) and (ψ_x, ψ_y) have the same physical meaning as in the first-order theory and h denotes the total thickness of the laminated plate. The strains associated with the displacements in Eq. (4.7) are (Reddy 1984a)

$$\begin{Bmatrix} \varepsilon_x \\ \varepsilon_y \\ \gamma_{xy} \end{Bmatrix} = \begin{Bmatrix} \varepsilon_x^0 \\ \varepsilon_y^0 \\ \gamma_{xy}^0 \end{Bmatrix} + z\begin{Bmatrix} \kappa_x^{(1)} \\ \kappa_y^{(1)} \\ \kappa_{xy}^{(1)} \end{Bmatrix} + z^3\begin{Bmatrix} \kappa_x^{(3)} \\ \kappa_y^{(3)} \\ \kappa_{xy}^{(3)} \end{Bmatrix}, \quad \begin{Bmatrix} \gamma_{yz} \\ \gamma_{xz} \end{Bmatrix} = \begin{Bmatrix} \gamma_{yz}^0 \\ \gamma_{xz}^0 \end{Bmatrix} + z^2\begin{Bmatrix} \kappa_{yz}^{(2)} \\ \kappa_{xz}^{(2)} \end{Bmatrix} \tag{4.8}$$

where

$$\begin{Bmatrix} \varepsilon_x^0 \\ \varepsilon_y^0 \\ \gamma_{xy}^0 \end{Bmatrix} = \begin{Bmatrix} \dfrac{\partial u_0}{\partial x} \\ \dfrac{\partial v_0}{\partial y} \\ \dfrac{\partial u_0}{\partial y} + \dfrac{\partial v_0}{\partial x} \end{Bmatrix}, \quad \begin{Bmatrix} \kappa_x^{(1)} \\ \kappa_y^{(1)} \\ \kappa_{xy}^{(1)} \end{Bmatrix} = \begin{Bmatrix} \dfrac{\partial \psi_x}{\partial x} \\ \dfrac{\partial \psi_y}{\partial y} \\ \dfrac{\partial \psi_x}{\partial y} + \dfrac{\partial \psi_y}{\partial x} \end{Bmatrix} \tag{4.9a}$$

$$\begin{Bmatrix} \kappa_x^{(3)} \\ \kappa_y^{(3)} \\ \kappa_{xy}^{(3)} \end{Bmatrix} = -\frac{4}{3h^2}\begin{Bmatrix} \dfrac{\partial \psi_x}{\partial x} + \dfrac{\partial^2 w_0}{\partial x^2} \\ \dfrac{\partial \psi_y}{\partial y} + \dfrac{\partial^2 w_0}{\partial y^2} \\ \dfrac{\partial \psi_x}{\partial y} + \dfrac{\partial \psi_y}{\partial x} + 2\dfrac{\partial^2 w_0}{\partial x \partial y} \end{Bmatrix} \tag{4.9b}$$

$$\begin{Bmatrix} \gamma_{yz}^0 \\ \gamma_{xz}^0 \end{Bmatrix} = \begin{Bmatrix} \dfrac{\partial w_0}{\partial y} + \psi_y \\ \dfrac{\partial w_0}{\partial x} + \psi_x \end{Bmatrix}, \quad \begin{Bmatrix} \kappa_{yz}^{(2)} \\ \kappa_{xz}^{(2)} \end{Bmatrix} = -\frac{4}{h^2}\begin{Bmatrix} \dfrac{\partial w_0}{\partial y} + \psi_y \\ \dfrac{\partial w_0}{\partial x} + \psi_x \end{Bmatrix} \tag{4.9c}$$

Note that the strain ε_z is also identically zero in the TSDT.

4.2.4 Summary and Selection of the Appropriate Laminated Plate Theory

In addition to their inherent simplicity and low computational cost, the ESL models often provide a sufficiently accurate description of global response for thin to moderately thick laminate plates, including deflections, critical buckling loads, and fundamental vibration frequencies and associated mode shapes. However, the ESL models have limitations that prevent them from being used to solve the whole spectrum of composite laminate problems. First, the accuracy of the global response predicted by ESL models deteriorates as the laminate plate becomes thicker. Second,

the ESL models are often incapable of accurately describing the state of stress and strain at the ply level near geometric and material discontinuities or near regions of intense loading – areas where accurate stress are needed most. In such cases, 3-D elasticity theory such as layerwise theories or multiple model approaches are required.

The overview of various ESL laminate theories indicates that the classical laminate plate theory and the first-order shear deformation theory are the simplest equivalent single-layer theories, and they adequately describe the kinematic behaviour of most laminated plates. Higher-order theories can represent the kinematics better, may not require shear correction factors, and can yield more accurate interlaminar stress distributions. However, they involve considerably more computational effort. Therefore, such theories should be used only when necessary.

In this study, the proposed transformed plate approach for analysis of the two-way FRP slab is similar to that adopted by Timoshenko and Woinowsky-Krieger (1959) for deriving the transformed stiffness properties for stiffened and corrugated plates composed of isotropic materials. Aref and Parsons (1999) have developed such simplified method to analyse a fibre-reinforced plastic bridge system. However, their method is based on classical laminated plate theory (CLPT) and therefore most suitable for thin plate structures. Since the ratio of the in-plane elastic modulus to transverse shear modulus is very large for FRP plates, classical plate theory, which neglects transverse shear deformation, is usually inadequate for analysis of thick or moderately thick FRP plate structures.

In view of the dimensions of the proposed two-way FRP slab (refer Chapter 3), it can be considered as a moderately thick plate structure, hence both FSDT and TSDT are suitable to analyse this plate structure. However, the third-order theories only provide a slight increase in accuracy relative to the FSDT solution, at the expense of a significant in crease in computational effort (Reddy 1997). Moreover, the FSDT with transverse extensibility appears to provide the best compromise of solution accuracy, economy, and simplicity among the ESL theories. This theory also allows the determination of accurate solutions for a wide class of laminate problems. Thus, the Reissner-Mindlin plate theory (mostly used laminated version of FSDT), which is

suitable for both thin and moderately thick plate structures, will be used to develop the transformed plate approach in this study.

4.3 Transformed Plate Approach

In this section, the transformed plate approach for the analysis of the two-way FRP composite slab is described. This includes detailed derivation of the transformed plate and its governing equations. The transformed plate is essentially the homogeneous plate that is obtained by applying the assumptions used in first-order shear deformation theory to the two-way FRP composite slab. In order to homogenize the inhomogeneous sandwich slab structure, the contributions to the stiffness matrix from individual parts of the representative element are taken into account, and a transformed global stiffness matrix is obtained by adding the contributions of individual parts. This results in the transformed global stiffness matrix relating the section forces and moments to the midsurface strains and curvatures of the actual slab structure.

4.3.1 Constitutive Equations of Composite Materials

The basic building block of a composite structure is the lamina, which is a thin layer of fibres and matrix material. In general, the properties of a composite are anisotropic. That is, the properties associated with an axis passing through a point in the material depend on the orientation of the axis (Gibson 1994). Fortunately, each type of composite has characteristic materials property symmetries that make it possible to simplify the general anisotropic constitutive equations. In particular, the symmetry possessed by the unidirectional lamina makes it a so-called orthotropic material. The constitutive equations of orthotropic materials based on the lamina principal coordinates (1, 2, 3) are given by (Gibson 1994, Kerakovich 1998, Jones 1999)

$$\begin{Bmatrix} \sigma_1 \\ \sigma_2 \\ \sigma_3 \\ \tau_{23} \\ \tau_{13} \\ \tau_{12} \end{Bmatrix} = \begin{bmatrix} C_{11} & C_{12} & C_{13} & 0 & 0 & 0 \\ C_{12} & C_{22} & C_{23} & 0 & 0 & 0 \\ C_{13} & C_{23} & C_{33} & 0 & 0 & 0 \\ 0 & 0 & 0 & C_{44} & 0 & 0 \\ 0 & 0 & 0 & 0 & C_{55} & 0 \\ 0 & 0 & 0 & 0 & 0 & C_{66} \end{bmatrix} \begin{Bmatrix} \varepsilon_1 \\ \varepsilon_2 \\ \varepsilon_3 \\ \gamma_{23} \\ \gamma_{13} \\ \gamma_{12} \end{Bmatrix} \tag{4.10}$$

where C_{ij} are the stiffness coefficients in the principal material axes. In most composites (i.e., unidirectional fibrous composite) the fibre-packing arrangement is statistically random in nature (Figure 4.4), so that the properties are nearly the same in any direction perpendicular to the fibres (i.e., the properties long the 2-direction are the same as those along the 3-direction), and the material exhibits isotropic properties in the plane transverse to the fibres. Transverse isotropy results in the following relations for stiffness coefficients:

$$C_{22} = C_{33}, \quad C_{12} = C_{13}, \quad C_{55} = C_{66}, \quad C_{44} = \frac{C_{22} - C_{23}}{2} \tag{4.11}$$

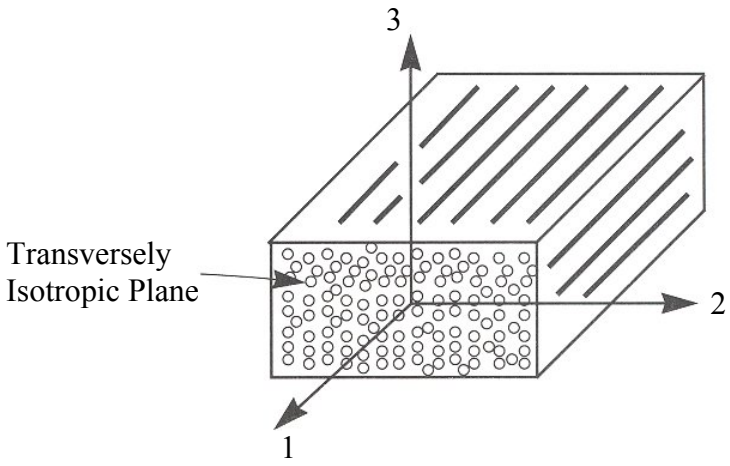

Figure 4.4 Transversely isotropic material[55]

Thus, the unidirectional fibrous composite lamina can be defined as a transversely isotropic material for which the constitutive equations can be written as

$$\begin{Bmatrix} \sigma_1 \\ \sigma_2 \\ \tau_{23} \\ \tau_{13} \\ \tau_{12} \end{Bmatrix} = \begin{bmatrix} C_{11} & C_{12} & 0 & 0 & 0 \\ C_{12} & C_{22} & 0 & 0 & 0 \\ 0 & 0 & C_{44} & 0 & 0 \\ 0 & 0 & 0 & C_{55} & 0 \\ 0 & 0 & 0 & 0 & C_{66} \end{bmatrix} \begin{Bmatrix} \varepsilon_1 \\ \varepsilon_2 \\ \gamma_{23} \\ \gamma_{13} \\ \gamma_{12} \end{Bmatrix} \tag{4.12}$$

where $C_{55} = C_{66}$, $C_{44} = \frac{C_{22} - C_{23}}{2}$ as shown in Eq. (4.11). Note that the stress σ_3 and strain ε_3 along the 3-axis (thickness direction of the lamina) have been eliminated from Eq. (4.10) due to the assumptions used in first-order shear deformation theory (refer Section 4.2.2). In most cases, the coordinate system used in

the solution of a problem (i.e., the global coordinate system (x, y, z)) does not coincide with the lamina principal coordinate system. In addition, the composite laminated plate has several layers and each layer may have different orientation. Thus, transforming constitutive relations from the lamina principal system (1, 2, 3) to the global coordinate system (x, y, z) are necessary. Upon transformation by using transformation matrix [*T*] and the transformation relation (see Appendix D), the constitutive equations for a transversely isotropic layer can be expressed in term of stresses and strains in the global coordinate system (x, y, z) as

$$\begin{Bmatrix} \sigma_x \\ \sigma_y \\ \tau_{yz} \\ \tau_{xz} \\ \tau_{xy} \end{Bmatrix} = \begin{bmatrix} \overline{C}_{11} & \overline{C}_{12} & 0 & 0 & \overline{C}_{16} \\ \overline{C}_{12} & \overline{C}_{22} & 0 & 0 & \overline{C}_{26} \\ 0 & 0 & \overline{C}_{44} & \overline{C}_{45} & 0 \\ 0 & 0 & \overline{C}_{45} & \overline{C}_{55} & 0 \\ \overline{C}_{16} & \overline{C}_{26} & 0 & 0 & \overline{C}_{66} \end{bmatrix} \begin{Bmatrix} \varepsilon_x \\ \varepsilon_y \\ \gamma_{yz} \\ \gamma_{xz} \\ \gamma_{xy} \end{Bmatrix} \tag{4.13}$$

where $\overline{C}_{ij}$ are the transformed stiffness coefficients and their definitions are listed in Appendix D.

The particular filled resin (PFR) core used in this research is considered as an isotropic material according to the extensive investigations and findings presented by Ayers (2001). An isotropic material is one whose properties are independent of direction and whose planes are all planes of symmetry. In this case the following additional relations between stiffness coefficients are created (Gibson 1994, Kerakovich 1998, Jones 1999):

$$C_{11} = C_{22}\,, \quad C_{12} = C_{23}\,, \quad C_{66} = \frac{C_{22} - C_{23}}{2} = \frac{C_{11} - C_{12}}{2} \tag{4.14}$$

Thus, based on the same assumptions used in first-order shear deformation theory, the constitutive equations of the PFR core material can be expressed as

$$\begin{Bmatrix} \sigma_1 \\ \sigma_2 \\ \tau_{23} \\ \tau_{13} \\ \tau_{12} \end{Bmatrix} = \begin{bmatrix} C_{11} & C_{12} & 0 & 0 & 0 \\ C_{12} & C_{11} & 0 & 0 & 0 \\ 0 & 0 & \dfrac{C_{11} - C_{12}}{2} & 0 & 0 \\ 0 & 0 & 0 & \dfrac{C_{11} - C_{12}}{2} & 0 \\ 0 & 0 & 0 & 0 & \dfrac{C_{11} - C_{12}}{2} \end{bmatrix} \begin{Bmatrix} \varepsilon_1 \\ \varepsilon_2 \\ \gamma_{23} \\ \gamma_{13} \\ \gamma_{12} \end{Bmatrix} \tag{4.15}$$

Due to the characteristic of isotropic materials, any local coordinate systems can be used as global coordinate system. Therefore, no transformation of coordinate system is required. In order to derive the formulations conveniently in the following section, the same symbols of stiffness coefficients as unidirectional fibrous composites are used in the constitutive equations for PFR core materials in the global coordinate system (x, y, z), which are written as

$$\begin{Bmatrix} \sigma_x \\ \sigma_y \\ \tau_{yz} \\ \tau_{xz} \\ \tau_{xy} \end{Bmatrix} = \begin{bmatrix} \overline{C}_{11} & \overline{C}_{12} & 0 & 0 & 0 \\ \overline{C}_{12} & \overline{C}_{22} & 0 & 0 & 0 \\ 0 & 0 & \overline{C}_{44} & 0 & 0 \\ 0 & 0 & 0 & \overline{C}_{55} & 0 \\ 0 & 0 & 0 & 0 & \overline{C}_{66} \end{bmatrix} \begin{Bmatrix} \varepsilon_x \\ \varepsilon_y \\ \gamma_{yz} \\ \gamma_{xz} \\ \gamma_{xy} \end{Bmatrix} \tag{4.16}$$

where

$$\overline{C}_{11} = \overline{C}_{22} = C_{11}, \quad \overline{C}_{12} = C_{12}, \quad \overline{C}_{44} = \overline{C}_{55} = \overline{C}_{66} = \frac{C_{11} - C_{12}}{2} \tag{4.17}$$

4.3.2 Development of the Equivalent Transformed Plate

In this study, the equivalent transformed plate is obtained by considering first-order shear deformation theory. The assumptions used in this theory are applied to generate the stiffness matrix that relates the section forces and moments to strains and curvatures with respect to the midsurface of the two-way FRP slab. Figure 4.5 shows the tractions acting on the faces of a differential element of the laminated plate. Stress resultants are defined to represent the forces and moments produced by these tractions. By integrating the stresses over the cross-section, the force and moment resultants per unit length of reference surface based on first-order shear deformation theory are defined as

$$\{N\} = \begin{Bmatrix} N_x \\ N_y \\ N_{xy} \end{Bmatrix} = \int_h \begin{Bmatrix} \sigma_x \\ \sigma_y \\ \tau_{xy} \end{Bmatrix} dz = \sum_{k=1}^{n} \int_{z_{k-1}}^{z_k} \begin{Bmatrix} \sigma_x \\ \sigma_y \\ \tau_{xy} \end{Bmatrix} dz \tag{4.18a}$$

$$\{M\} = \begin{Bmatrix} M_x \\ M_y \\ M_{xy} \end{Bmatrix} = \int_h \begin{Bmatrix} \sigma_x \\ \sigma_y \\ \tau_{xy} \end{Bmatrix} z dz = \sum_{k=1}^{n} \int_{z_{k-1}}^{z_k} \begin{Bmatrix} \sigma_x \\ \sigma_y \\ \tau_{xy} \end{Bmatrix} z dz \tag{4.18b}$$

$$\{Q\} = \begin{Bmatrix} Q_y \\ Q_x \end{Bmatrix} = K\int_h \begin{Bmatrix} \tau_{yz} \\ \tau_{xz} \end{Bmatrix} dz = K\sum_{k=1}^{n}\int_{z_{k-1}}^{z_k} \begin{Bmatrix} \tau_{yz} \\ \tau_{xz} \end{Bmatrix} dz \tag{4.18c}$$

where h is total thickness of the laminated plate and the parameter K called shear correction coefficient (see Section 4.2.2). The quantities (Q_x, Q_y) are called the transverse force resultants. Figure 4.6 shows the notation used in Eqs. (4.18a~c). The objective of this section is to obtain expressions for the extensional stiffness matrix [A], the bending-extensional coupling stiffness matrix [B], and the bending stiffness matrix [D] for the representative element of the two-way FRP slab shown in Figure 4.7. The element has a width of b_s in both the longitudinal or x-direction, and the transverse or y-direction, respectively. This element gives the constitutive relations for the transformed plate. The representative element is subdivided into three parts: outer shell segments (I), circular cell segments (II) and PFR core segments (III). Figure 4.8 shows the coordinate systems used in the element. The contribution of the individual parts to the global stiffness of the equivalent transformed plate is described as follows.

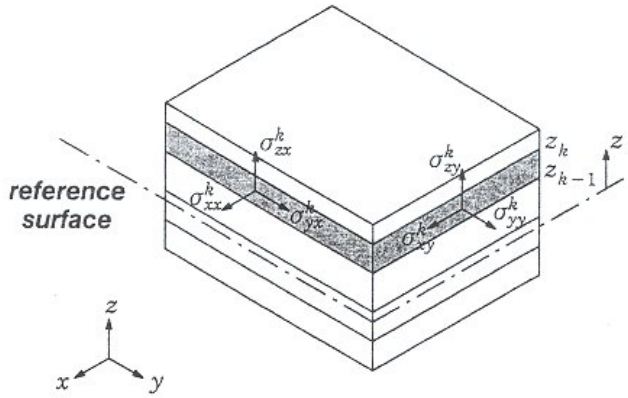

Figure 4.5 Tractions acting on the laminated plate

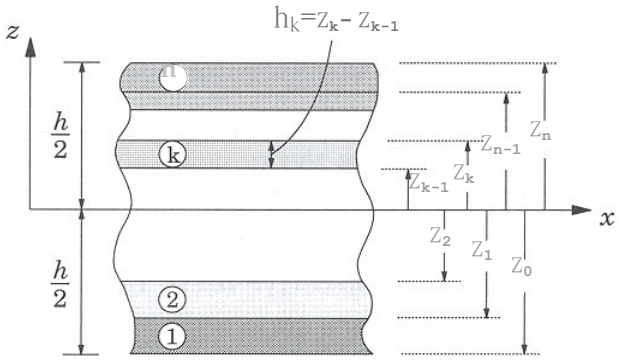

Figure 4.6 Geometry of an n-layered laminate

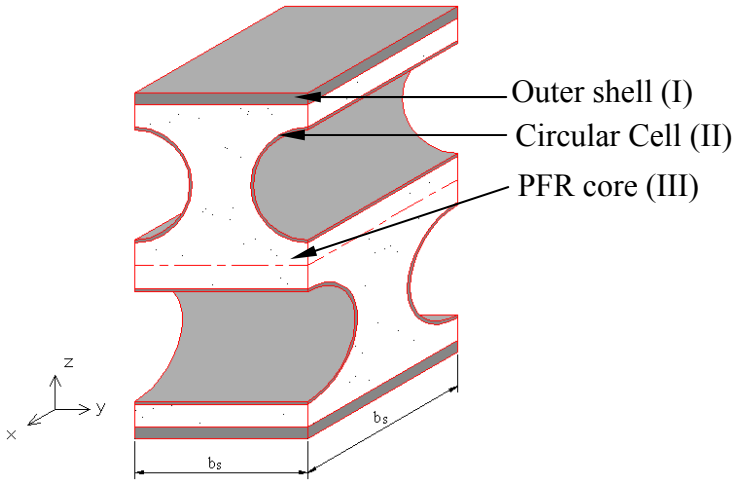

Figure 4.7 Representative element of the two-way FRP slab

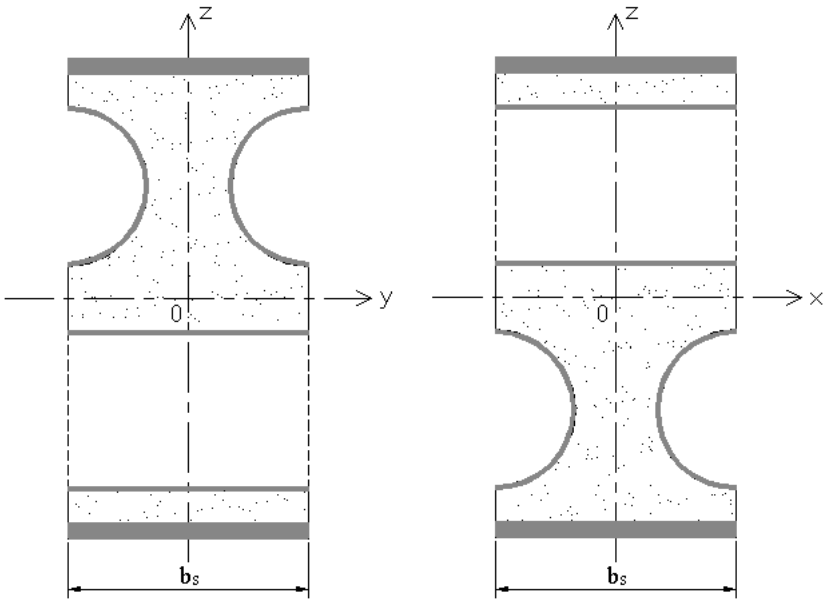

Figure 4.8 Coordinate systems used in the representative element

- **Outer Shell Segment (I)**

The outer shell segment (I) of the two-way FRP slab (Figure 4.9) is comprised of a number of unidirectional fibre laminae with different fibre orientations. Referring to Eq. (4.13), the constitutive equations of a unidirectional fibrous composite for the *k*th lamina in the global coordinate system are written as

$$\begin{Bmatrix}\sigma_x\\ \sigma_y\\ \tau_{yz}\\ \tau_{xz}\\ \tau_{xy}\end{Bmatrix}^I = \begin{bmatrix}\overline{C}_{11} & \overline{C}_{12} & 0 & 0 & \overline{C}_{16}\\ \overline{C}_{12} & \overline{C}_{22} & 0 & 0 & \overline{C}_{26}\\ 0 & 0 & \overline{C}_{44} & \overline{C}_{45} & 0\\ 0 & 0 & \overline{C}_{45} & \overline{C}_{55} & 0\\ \overline{C}_{16} & \overline{C}_{26} & 0 & 0 & \overline{C}_{66}\end{bmatrix}_k^I \begin{Bmatrix}\varepsilon_x\\ \varepsilon_y\\ \gamma_{yz}\\ \gamma_{xz}\\ \gamma_{xy}\end{Bmatrix}_k^I \tag{4.19}$$

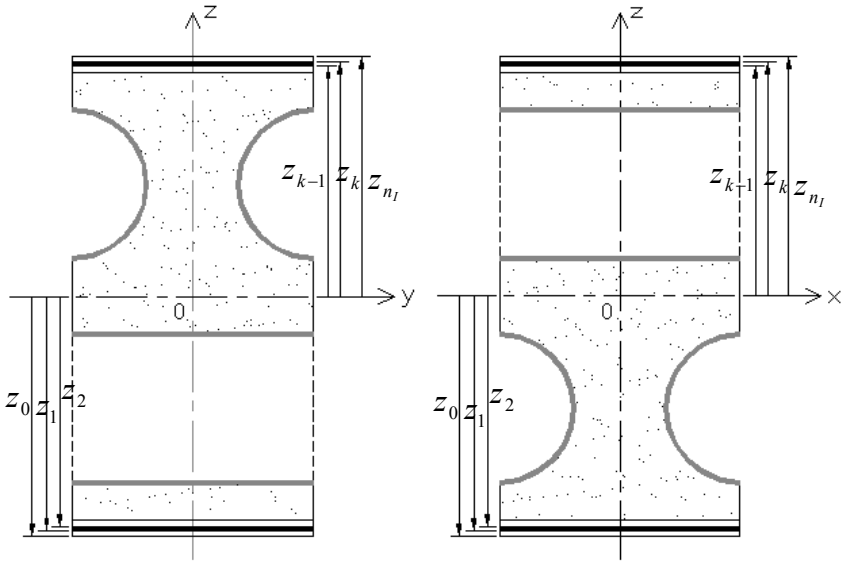

Figure 4.9 Coordinate system used for outer shell (I)

Substituting Eq. (4.19) in Eqs. (4.18a~c) and using Eqs. (4.5) and (4.6), the stress resultants of the outer shell segment (I) are

$$\begin{aligned}N_x^I &= \sum_{k=1}^{n_I}\int_{z_{k-1}}^{z_k}(\overline{C}_{11}^k\varepsilon_x^0 + \overline{C}_{12}^k\varepsilon_y^0 + \overline{C}_{16}^k\gamma_{xy}^0)dz\\ &+ \sum_{k=1}^{n_i}\int_{z_{k-1}}^{z_k}(\overline{C}_{11}^k\kappa_x + \overline{C}_{12}^k\kappa_y + \overline{C}_{16}^k\kappa_{xy})zdz\end{aligned} \tag{4.20a}$$

$$\begin{aligned}N_y^I &= \sum_{k=1}^{n_I}\int_{z_{k-1}}^{z_k}(\overline{C}_{12}^k\varepsilon_x^0 + \overline{C}_{22}^k\varepsilon_y^0 + \overline{C}_{26}^k\gamma_{xy}^0)dz\\ &+ \sum_{k=1}^{n_i}\int_{z_{k-1}}^{z_k}(\overline{C}_{12}^k\kappa_x + \overline{C}_{22}^k\kappa_y + \overline{C}_{26}^k\kappa_{xy})zdz\end{aligned} \tag{4.20b}$$

$$\begin{aligned}N_{xy}^I &= \sum_{k=1}^{n_I}\int_{z_{k-1}}^{z_k}(\overline{C}_{16}^k\varepsilon_x^0 + \overline{C}_{26}^k\varepsilon_y^0 + \overline{C}_{66}^k\gamma_{xy}^0)dz\\ &+ \sum_{k=1}^{n_i}\int_{z_{k-1}}^{z_k}(\overline{C}_{16}^k\kappa_x + \overline{C}_{26}^k\kappa_y + \overline{C}_{66}^k\kappa_{xy})zdz\end{aligned} \tag{4.20c}$$

$$M_x^I = \sum_{k=1}^{n_I}\int_{z_{k-1}}^{z_k}(\overline{C}_{11}^k\varepsilon_x^0 + \overline{C}_{12}^k\varepsilon_y^0 + \overline{C}_{16}^k\gamma_{xy}^0)zdz + \sum_{k=1}^{n_i}\int_{z_{k-1}}^{z_k}(\overline{C}_{11}^k\kappa_x + \overline{C}_{12}^k\kappa_y + \overline{C}_{16}^k\kappa_{xy})z^2dz \tag{4.20d}$$

$$M_y^I = \sum_{k=1}^{n_I}\int_{z_{k-1}}^{z_k}(\overline{C}_{12}^k\varepsilon_x^0 + \overline{C}_{22}^k\varepsilon_y^0 + \overline{C}_{26}^k\gamma_{xy}^0)zdz + \sum_{k=1}^{n_i}\int_{z_{k-1}}^{z_k}(\overline{C}_{12}^k\kappa_x + \overline{C}_{22}^k\kappa_y + \overline{C}_{26}^k\kappa_{xy})z^2dz \tag{4.20e}$$

$$M_{xy}^I = \sum_{k=1}^{n_I}\int_{z_{k-1}}^{z_k}(\overline{C}_{16}^k\varepsilon_x^0 + \overline{C}_{26}^k\varepsilon_y^0 + \overline{C}_{66}^k\gamma_{xy}^0)zdz + \sum_{k=1}^{n_i}\int_{z_{k-1}}^{z_k}(\overline{C}_{16}^k\kappa_x + \overline{C}_{26}^k\kappa_y + \overline{C}_{66}^k\kappa_{xy})z^2dz \tag{4.20f}$$

$$Q_x^I = K\sum_{k=1}^{n_I}\int_{z_{k-1}}^{z_k}(\overline{C}_{45}^k\gamma_{yz}^0 + \overline{C}_{55}\gamma_{xz}^0)dz \tag{4.20g}$$

$$Q_y^I = K\sum_{k=1}^{n_I}\int_{z_{k-1}}^{z_k}(\overline{C}_{44}^k\gamma_{yz}^0 + \overline{C}_{45}\gamma_{xz}^0)dz \tag{4.20h}$$

where n_I is total number of laminae in the outer shell. Performing the integrations in Eqs. (4.20a~h), the force and moment resultants are obtained as

$$\begin{Bmatrix} N_x \\ N_y \\ N_{xy} \end{Bmatrix}^I = \begin{bmatrix} A_{11} & A_{12} & A_{16} \\ A_{12} & A_{22} & A_{26} \\ A_{16} & A_{26} & A_{66} \end{bmatrix}^I \begin{Bmatrix} \varepsilon_x^0 \\ \varepsilon_y^0 \\ \gamma_{xy}^0 \end{Bmatrix} + \begin{bmatrix} B_{11} & B_{12} & B_{16} \\ B_{12} & B_{22} & B_{26} \\ B_{16} & B_{26} & B_{66} \end{bmatrix}^I \begin{Bmatrix} \kappa_x \\ \kappa_y \\ \kappa_{xy} \end{Bmatrix} \tag{4.21a}$$

$$\begin{Bmatrix} M_x \\ M_y \\ M_{xy} \end{Bmatrix}^I = \begin{bmatrix} B_{11} & B_{12} & B_{16} \\ B_{12} & B_{22} & B_{26} \\ B_{16} & B_{26} & B_{66} \end{bmatrix}^I \begin{Bmatrix} \varepsilon_x^0 \\ \varepsilon_y^0 \\ \gamma_{xy}^0 \end{Bmatrix} + \begin{bmatrix} D_{11} & D_{12} & D_{16} \\ D_{12} & D_{22} & D_{26} \\ D_{16} & D_{26} & D_{66} \end{bmatrix}^I \begin{Bmatrix} \kappa_x \\ \kappa_y \\ \kappa_{xy} \end{Bmatrix} \tag{4.21b}$$

$$\begin{Bmatrix} Q_y \\ Q_x \end{Bmatrix}^I = K\begin{bmatrix} A_{44} & A_{45} \\ A_{45} & A_{55} \end{bmatrix}^I \begin{Bmatrix} \gamma_{yz}^0 \\ \gamma_{xz}^0 \end{Bmatrix} \tag{4.21c}$$

where the contribution of the outer shell segment (I) to global stiffness matrixes of the equivalent transformed plate [A], [B] and [D] is given by

$$A_{ij}^I = \sum_{k=1}^{n_I}\overline{C}_{ij}^k(z_k - z_{k-1}), \quad i, j = 1, 2, 6 \tag{4.22a}$$

$$B_{ij}^{I} = \frac{1}{2}\sum_{k=1}^{n_I} \overline{C}_{ij}^{k} (z_k{}^2 - z_{k-1}{}^2), \quad i, j = 1, 2, 6 \tag{4.22b}$$

$$D_{ij}^{I} = \frac{1}{3}\sum_{k=1}^{n_I} \overline{C}_{ij}^{k} (z_k{}^3 - z_{k-1}{}^3), \quad i, j = 1, 2, 6 \tag{4.22c}$$

$$A_{ij}^{I} = \sum_{k=1}^{n_I} \overline{C}_{ij}^{k} (z_k - z_{k-1}), \quad i, j = 4, 5 \tag{4.22d}$$

- **Circular Cell Segment (II)**

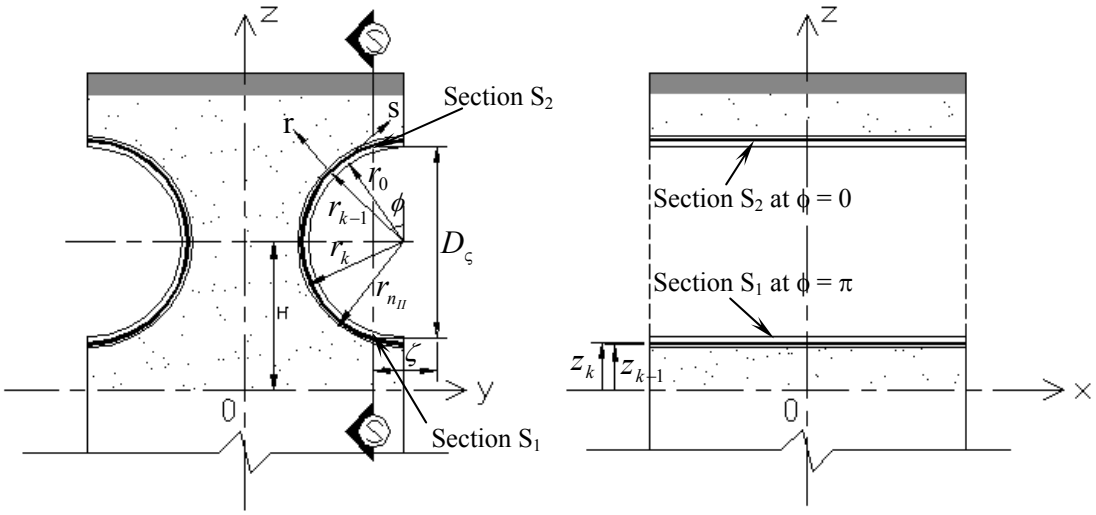

Figure 4.10 Shell local and global coordinate systems used for top circular cell (II_t)

Analogous to the outer shell segment, the circular cell segment (II) also consists of several unidirectional fibre plies with different fibre orientations. Figure 4.10 shows the top circular cell segment (II_t), which will be considered first. Using the standard procedure described in Section (4.3.1) and taking into account Eq. (4.13), the constitutive equation of the top circular cell segment can be transformed from lamina principal coordinate system (1, 2, 3) into the shell local coordinate system (x, s, r) for the kth lamina as

$$\begin{Bmatrix} \sigma_x \\ \sigma_s \\ \tau_{sr} \\ \tau_{xr} \\ \tau_{xs} \end{Bmatrix}_k^{II_t} = \begin{bmatrix} \overline{C}_{11} & \overline{C}_{12} & 0 & 0 & \overline{C}_{16} \\ \overline{C}_{12} & \overline{C}_{22} & 0 & 0 & \overline{C}_{26} \\ 0 & 0 & \overline{C}_{44} & \overline{C}_{45} & 0 \\ 0 & 0 & \overline{C}_{45} & \overline{C}_{55} & 0 \\ \overline{C}_{16} & \overline{C}_{26} & 0 & 0 & \overline{C}_{66} \end{bmatrix}_k^{II_t} \begin{Bmatrix} \varepsilon_x \\ \varepsilon_s \\ \gamma_{sr} \\ \gamma_{xr} \\ \gamma_{xs} \end{Bmatrix}_k^{II_t} \tag{4.23}$$

Then the stresses and strains are transformed from the shell local coordinate system (x, s, r) into the global coordinate system (x, y, z). The stresses at the top circular cell segment are rotated around the x-axis by an angle ϕ as shown in Figure 4.10. The details of such transformation of coordinate system are described in Appendix D. The constitutive equation of the top circular cell segment in the global coordinate system (x, y, z) can then be expressed as

$$\begin{Bmatrix} \sigma_x \\ \sigma_y \\ \tau_{yz} \\ \tau_{xz} \\ \tau_{xy} \end{Bmatrix}_k^{II_t} = \begin{bmatrix} \widetilde{C}_{11} & \widetilde{C}_{12} & \widetilde{C}_{14} & \widetilde{C}_{15} & \widetilde{C}_{16} \\ \widetilde{C}_{12} & \widetilde{C}_{22} & \widetilde{C}_{24} & \widetilde{C}_{25} & \widetilde{C}_{26} \\ \widetilde{C}_{14} & \widetilde{C}_{24} & \widetilde{C}_{44} & \widetilde{C}_{45} & \widetilde{C}_{46} \\ \widetilde{C}_{15} & \widetilde{C}_{25} & \widetilde{C}_{45} & \widetilde{C}_{55} & \widetilde{C}_{56} \\ \widetilde{C}_{16} & \widetilde{C}_{26} & \widetilde{C}_{46} & \widetilde{C}_{56} & \widetilde{C}_{66} \end{bmatrix}_k^{II_t} \begin{Bmatrix} \varepsilon_x \\ \varepsilon_y \\ \gamma_{yz} \\ \gamma_{xz} \\ \gamma_{xy} \end{Bmatrix}_k^{II_t} \tag{4.24}$$

where

$$\left[\widetilde{C}\right]_k^{II_t} = \left[T_1'\right]^{-1} \left[\overline{C}\right]_k^{II_t} \left[T_1'\right]^{-T} \tag{4.25}$$

The definitions of the transformation matrix $\left[T_1'\right]$ and the transformed stiffness coefficients $\widetilde{C}_{ij}^{\,II_t}$ $(i,\ j = 1, 2, 4, 5, 6)$ are included in Appendix D.

The relations between the resultant forces $\{N\}$, $\{Q\}$ and the moment $\{M\}$, and the midsurface strains and curvatures for the top circular cell part (II_t) are obtained by integrating $\sigma_x^{II_t}$, $\tau_{xy}^{II_t}$ and $\tau_{xz}^{II_t}$ over the face of segment II_t normal to the x-axis or oyz plane, and $\sigma_y^{II_t}$ and $\tau_{yz}^{II_t}$ over the face of segment II_t normal to the y-axis or oxz plane (Figure 4.10). Furthermore, the contributions originating from $\sigma_x^{II_t}$, $\tau_{xy}^{II_t}$ and $\tau_{xz}^{II_t}$ must be averaged over the width of the representative element to obtain moments and forces per unit length of reference surface. The relations between the shell local coordinate system (x, s, r) of top circular segment and global coordinate system (x, y, z) can be expressed as

$$\begin{cases} x = x \\ y = -r\sin\phi + \dfrac{b_s}{2} \\ z = r\cos\phi + H \end{cases} \tag{4.26}$$

where the notations used in Eq. (4.26) are shown in Figure 4.9.

Substituting Eq. (4.24) in Eqs. (4.18a~c) and using Eqs. (4.5), (4.6) and (4.26), the stress resultants $N_x^{II_t}$, $N_{xy}^{II_t}$, $M_x^{II_t}$, $M_{xy}^{II_t}$ and $Q_x^{II_t}$ acting on *oyz* plane are computed as

$$\begin{aligned} N_x^{II_t} = \frac{1}{b_s}\Bigg[& \sum_{k=1}^{n_{II}} \int_{r_{k-1}}^{r_k} \int_0^{2\pi} \left(\widetilde{C}_{11}^k \varepsilon_x^0 + \widetilde{C}_{12}^k \varepsilon_y^0 + \widetilde{C}_{14}^k \gamma_{yz}^0 + \widetilde{C}_{15}^k \gamma_{xz}^0 + \widetilde{C}_{16}^k \gamma_{xy}^0 \right) r dr d\phi \\ & + \sum_{k=1}^{n_{II}} \int_{r_{k-1}}^{r_k} \int_0^{2\pi} \left(\widetilde{C}_{11}^k \kappa_x + \widetilde{C}_{12}^k \kappa_y + \widetilde{C}_{16}^k \kappa_{xy} \right) r^2 \cos\phi dr d\phi \\ & + H \sum_{k=1}^{n_{II}} \int_{r_{k-1}}^{r_k} \int_0^{2\pi} \left(\widetilde{C}_{11}^k \kappa_x + \widetilde{C}_{12}^k \kappa_y + \widetilde{C}_{16}^k \kappa_{xy} \right) r dr d\phi \Bigg] \end{aligned} \tag{4.27a}$$

$$\begin{aligned} N_{xy}^{II_t} = \frac{1}{b_s}\Bigg[& \sum_{k=1}^{n_{II}} \int_{r_{k-1}}^{r_k} \int_0^{2\pi} \left(\widetilde{C}_{16}^k \varepsilon_x^0 + \widetilde{C}_{26}^k \varepsilon_y^0 + \widetilde{C}_{46}^k \gamma_{yz}^0 + \widetilde{C}_{56}^k \gamma_{xz}^0 + \widetilde{C}_{66}^k \gamma_{xy}^0 \right) r dr d\phi \\ & + \sum_{k=1}^{n_{II}} \int_{r_{k-1}}^{r_k} \int_0^{2\pi} \left(\widetilde{C}_{16}^k \kappa_x + \widetilde{C}_{26}^k \kappa_y + \widetilde{C}_{66}^k \kappa_{xy} \right) r^2 \cos\phi dr d\phi \\ & + H \sum_{k=1}^{n_{II}} \int_{r_{k-1}}^{r_k} \int_0^{2\pi} \left(\widetilde{C}_{16}^k \kappa_x + \widetilde{C}_{26}^k \kappa_y + \widetilde{C}_{66}^k \kappa_{xy} \right) r dr d\phi \Bigg] \end{aligned} \tag{4.27b}$$

$$\begin{aligned} M_x^{II_t} = \frac{1}{b_s}\Bigg[& \sum_{k=1}^{n_{II}} \int_{r_{k-1}}^{r_k} \int_0^{2\pi} \left(\widetilde{C}_{11}^k \varepsilon_x^0 + \widetilde{C}_{12}^k \varepsilon_y^0 + \widetilde{C}_{14}^k \gamma_{yz}^0 + \widetilde{C}_{15}^k \gamma_{xz}^0 + \widetilde{C}_{16}^k \gamma_{xy}^0 \right) r^2 \cos\phi dr d\phi \\ & + \sum_{k=1}^{n_{II}} \int_{r_{k-1}}^{r_k} \int_0^{2\pi} \left(\widetilde{C}_{11}^k \kappa_x + \widetilde{C}_{12}^k \kappa_y + \widetilde{C}_{16}^k \kappa_{xy} \right) r^3 \cos^2\phi dr d\phi \\ & + H \sum_{k=1}^{n_{II}} \int_{r_{k-1}}^{r_k} \int_0^{2\pi} \left(\widetilde{C}_{11}^k \kappa_x + \widetilde{C}_{12}^k \kappa_y + \widetilde{C}_{16}^k \kappa_{xy} \right) r^2 \cos\phi dr d\phi \Bigg] \\ + \frac{H}{b_s}\Bigg[& \sum_{k=1}^{n_{II}} \int_{r_{k-1}}^{r_k} \int_0^{2\pi} \left(\widetilde{C}_{11}^k \varepsilon_x^0 + \widetilde{C}_{12}^k \varepsilon_y^0 + \widetilde{C}_{14}^k \gamma_{yz}^0 + \widetilde{C}_{15}^k \gamma_{xz}^0 + \widetilde{C}_{16}^k \gamma_{xy}^0 \right) r dr d\phi \\ & + \sum_{k=1}^{n_{II}} \int_{r_{k-1}}^{r_k} \int_0^{2\pi} \left(\widetilde{C}_{11}^k \kappa_x + \widetilde{C}_{12}^k \kappa_y + \widetilde{C}_{16}^k \kappa_{xy} \right) r^2 \cos\phi dr d\phi \\ & + H \sum_{k=1}^{n_{II}} \int_{r_{k-1}}^{r_k} \int_0^{2\pi} \left(\widetilde{C}_{11}^k \kappa_x + \widetilde{C}_{12}^k \kappa_y + \widetilde{C}_{16}^k \kappa_{xy} \right) r dr d\phi \Bigg] \end{aligned} \tag{4.27c}$$

$$
\begin{aligned}
M_{xy}^{II_t} = \frac{1}{b_s}\Bigg[& \sum_{k=1}^{n_{II}} \int_{r_{k-1}}^{r_k} \int_0^{2\pi} \left(\widetilde{C}_{16}^k \varepsilon_x^0 + \widetilde{C}_{26}^k \varepsilon_y^0 + \widetilde{C}_{46}^k \gamma_{yz}^0 + \widetilde{C}_{56}^k \gamma_{xz}^0 + \widetilde{C}_{66}^k \gamma_{xy}^0 \right) r^2 \cos\phi \, dr d\phi \\
& + \sum_{k=1}^{n_{II}} \int_{r_{k-1}}^{r_k} \int_0^{2\pi} \left(\widetilde{C}_{16}^k \kappa_x + \widetilde{C}_{26}^k \kappa_y + \widetilde{C}_{66}^k \kappa_{xy} \right) r^3 \cos^2\phi \, dr d\phi \\
& + H \sum_{k=1}^{n_{II}} \int_{r_{k-1}}^{r_k} \int_0^{2\pi} \left(\widetilde{C}_{16}^k \kappa_x + \widetilde{C}_{26}^k \kappa_y + \widetilde{C}_{66}^k \kappa_{xy} \right) r^2 \cos\phi \, dr d\phi \Bigg] \\
& + \frac{H}{b_s}\Bigg[\sum_{k=1}^{n_{II}} \int_{r_{k-1}}^{r_k} \int_0^{2\pi} \left(\widetilde{C}_{16}^k \varepsilon_x^0 + \widetilde{C}_{26}^k \varepsilon_y^0 + \widetilde{C}_{46}^k \gamma_{yz}^0 + \widetilde{C}_{56}^k \gamma_{xz}^0 + \widetilde{C}_{66}^k \gamma_{xy}^0 \right) r \, dr d\phi \\
& + \sum_{k=1}^{n_{II}} \int_{r_{k-1}}^{r_k} \int_0^{2\pi} \left(\widetilde{C}_{16}^k \kappa_x + \widetilde{C}_{26}^k \kappa_y + \widetilde{C}_{66}^k \kappa_{xy} \right) r^2 \cos\phi \, dr d\phi \\
& + H \sum_{k=1}^{n_{II}} \int_{r_{k-1}}^{r_k} \int_0^{2\pi} \left(\widetilde{C}_{16}^k \kappa_x + \widetilde{C}_{26}^k \kappa_y + \widetilde{C}_{66}^k \kappa_{xy} \right) r \, dr d\phi \Bigg]
\end{aligned}
\tag{4.27d}
$$

$$
\begin{aligned}
Q_x^{II_t} = K\Bigg\{ \frac{1}{b_s}\Bigg[& \sum_{k=1}^{n_{II}} \int_{r_{k-1}}^{r_k} \int_0^{2\pi} \left(\widetilde{C}_{15}^k \varepsilon_x^0 + \widetilde{C}_{25}^k \varepsilon_y^0 + \widetilde{C}_{45}^k \gamma_{yz}^0 + \widetilde{C}_{55}^k \gamma_{xz}^0 + \widetilde{C}_{56}^k \gamma_{xy}^0 \right) r \, dr d\phi \\
& + \sum_{k=1}^{n_{II}} \int_{r_{k-1}}^{r_k} \int_0^{2\pi} \left(\widetilde{C}_{15}^k \kappa_x + \widetilde{C}_{25}^k \kappa_y + \widetilde{C}_{56}^k \kappa_{xy} \right) r^2 \cos\phi \, dr d\phi \\
& + H \sum_{k=1}^{n_{II}} \int_{r_{k-1}}^{r_k} \int_0^{2\pi} \left(\widetilde{C}_{15}^k \kappa_x + \widetilde{C}_{25}^k \kappa_y + \widetilde{C}_{56}^k \kappa_{xy} \right) r \, dr d\phi \Bigg] \Bigg\}
\end{aligned}
\tag{4.27e}
$$

where n_{II} is the total number of plies in the circular cell segment. The resultants $N_y^{II_t}$, $M_y^{II_t}$ and $Q_y^{II_t}$ acting on the *oxz* plane are obtained by integrating $\sigma_y^{II_t}$ and $\tau_{yz}^{II_t}$ over the section S-S (at $y = \frac{b_s}{2} - \zeta$) shown in Figure 4.10, where ζ is the distance between the section S-S and the centre of the circle void. This produces

$$
\begin{aligned}
N_y^{II_t} = & \sum_{k=1}^{n_{II}} \int_{z_{k-1}}^{z_k} \left(\widetilde{C}_{12}^k \varepsilon_x^0 + \widetilde{C}_{22}^k \varepsilon_y^0 + \widetilde{C}_{24}^k \gamma_{yz}^0 + \widetilde{C}_{25}^k \gamma_{xz}^0 + \widetilde{C}_{26}^k \gamma_{xy}^0 \right) dz \\
& + \sum_{k=1}^{n_{II}} \int_{z_{k-1}}^{z_k} \left(\widetilde{C}_{12}^k \kappa_x + \widetilde{C}_{22}^k \kappa_y + \widetilde{C}_{26}^k \kappa_{xy} \right) z \, dz \\
& + \sum_{k=1}^{n_{II}} \int_{z_{k-1}+D_\zeta}^{z_k+D_\zeta} \left(\widetilde{C}_{12}^k \varepsilon_x^0 + \widetilde{C}_{22}^k \varepsilon_y^0 + \widetilde{C}_{24}^k \gamma_{yz}^0 + \widetilde{C}_{25}^k \gamma_{xz}^0 + \widetilde{C}_{26}^k \gamma_{xy}^0 \right) dz \\
& + \sum_{k=1}^{n_{II}} \int_{z_{k-1}+D_\zeta}^{z_k+D_\zeta} \left(\widetilde{C}_{12}^k \kappa_x + \widetilde{C}_{22}^k \kappa_y + \widetilde{C}_{26}^k \kappa_{xy} \right) z \, dz
\end{aligned}
\tag{4.27f}
$$

$$
\begin{aligned}
M_y^{II_t} = & \sum_{k=1}^{n_{II}} \int_{z_{k-1}}^{z_k} \left(\widetilde{C}_{12}^k \varepsilon_x^0 + \widetilde{C}_{22}^k \varepsilon_y^0 + \widetilde{C}_{24}^k \gamma_{yz}^0 + \widetilde{C}_{25}^k \gamma_{xz}^0 + \widetilde{C}_{26}^k \gamma_{xy}^0 \right) z dz \\
& + \sum_{k=1}^{n_{II}} \int_{z_{k-1}}^{z_k} \left(\widetilde{C}_{12}^k \kappa_x + \widetilde{C}_{22}^k \kappa_y + \widetilde{C}_{26}^k \kappa_{xy} \right) z^2 dz \\
& + \sum_{k=1}^{n_{II}} \int_{z_{k-1}+D_\zeta}^{z_k+D_\zeta} \left(\widetilde{C}_{12}^k \varepsilon_x^0 + \widetilde{C}_{22}^k \varepsilon_y^0 + \widetilde{C}_{24}^k \gamma_{yz}^0 + \widetilde{C}_{25}^k \gamma_{xz}^0 + \widetilde{C}_{26}^k \gamma_{xy}^0 \right) z dz \\
& + \sum_{k=1}^{n_{II}} \int_{z_{k-1}+D_\zeta}^{z_k+D_\zeta} \left(\widetilde{C}_{12}^k \kappa_x + \widetilde{C}_{22}^k \kappa_y + \widetilde{C}_{26}^k \kappa_{xy} \right) z^2 dz
\end{aligned}
\tag{4.27g}
$$

$$
\begin{aligned}
Q_y^{II_t} = K \Bigg[& \sum_{k=1}^{n_{II}} \int_{z_{k-1}}^{z_k} \left(\widetilde{C}_{14}^k \varepsilon_x^0 + \widetilde{C}_{24}^k \varepsilon_y^0 + \widetilde{C}_{44}^k \gamma_{yz}^0 + \widetilde{C}_{45}^k \gamma_{xz}^0 + \widetilde{C}_{46}^k \gamma_{xy}^0 \right) dz \\
& + \sum_{k=1}^{n_{II}} \int_{z_{k-1}}^{z_k} \left(\widetilde{C}_{14}^k \kappa_x + \widetilde{C}_{24}^k \kappa_y + \widetilde{C}_{46}^k \kappa_{xy} \right) z dz \\
& + \sum_{k=1}^{n_{II}} \int_{z_{k-1}+D_\zeta}^{z_k+D_\zeta} \left(\widetilde{C}_{14}^k \varepsilon_x^0 + \widetilde{C}_{24}^k \varepsilon_y^0 + \widetilde{C}_{44}^k \gamma_{yz}^0 + \widetilde{C}_{45}^k \gamma_{xz}^0 + \widetilde{C}_{46}^k \gamma_{xy}^0 \right) dz \\
& + \sum_{k=1}^{n_{II}} \int_{z_{k-1}+D_\zeta}^{z_k+D_\zeta} \left(\widetilde{C}_{14}^k \kappa_x + \widetilde{C}_{24}^k \kappa_y + \widetilde{C}_{46}^k \kappa_{xy} \right) z dz \Bigg]
\end{aligned}
\tag{4.27h}
$$

where D_ζ is the distance between the midline of the S_1 section and S_2 section shown in Figure 4.10. It should be noted that the transformed stiffness coefficients $\widetilde{C}_{ij}^{\ k}$ $(i, j = 1, 2, 4, 5, 6)$ in Eqs. (4.27a~h) are a function of the angle ϕ. Due to the arbitrary selection of section S-S, it can be chosen at $y = \frac{b_s}{2}$, that is $\zeta = 0$. In this case, the S_1 section corresponds to angle $\phi = \pi$ and the following relations are produced

$$
\begin{aligned}
& \widetilde{C}_{12} = \overline{C}_{12}, \quad \widetilde{C}_{22} = \overline{C}_{22}, \quad \widetilde{C}_{26} = -\overline{C}_{26}, \quad \widetilde{C}_{44} = \overline{C}_{44}, \quad \widetilde{C}_{45} = -\overline{C}_{45} \\
& \widetilde{C}_{14} = \widetilde{C}_{24} = \widetilde{C}_{25} = \widetilde{C}_{46} = 0
\end{aligned}
\tag{4.28a}
$$

The S_2 section corresponds to angle $\phi = 0$ and yields

$$
\begin{aligned}
& \widetilde{C}_{12} = \overline{C}_{12}, \quad \widetilde{C}_{22} = \overline{C}_{22}, \quad \widetilde{C}_{26} = \overline{C}_{26}, \quad \widetilde{C}_{44} = \overline{C}_{44}, \quad \widetilde{C}_{45} = \overline{C}_{45} \\
& \widetilde{C}_{14} = \widetilde{C}_{24} = \widetilde{C}_{25} = \widetilde{C}_{46} = 0
\end{aligned}
\tag{4.28b}
$$

Thus, substituting Eqs. (4.28a, b) in Eqs. (4.27f~h), the resultants $N_y^{II_t}$, $M_y^{II_t}$ and $Q_y^{II_t}$ acting on the *oxz* plane can be simplified by considering section S-S at $y = \frac{b_s}{2}$ ($\zeta = 0$). In order to produce symmetrical [*A*], [*B*] and [*D*] matrices, the terms which

involve $\widetilde{C}_{12}$, $\widetilde{C}_{26}$ and $\widetilde{C}_{45}$ in Eqs. (4.27f~h) are replaced with the corresponding terms in Eqs. (4.27a~e). While this is a simplification and not strictly (mathematically) correct, the off-diagonal terms in the stiffness matrix generally make a relatively minor contribution to response. Hence the error that results from this assumption is unlikely to produce significant affect on calculated results.

By performing the integration in Eq. (4.27a~h) and taking into account Eqs. (4.28a, b), the forces and moments resultants of the top circular cell segment (II_t) are obtained as

$$\begin{Bmatrix} N_x \\ N_y \\ N_{xy} \end{Bmatrix}^{II_t} = \begin{bmatrix} A_{11} & A_{12} & A_{16} \\ A_{12} & A_{22} & A_{26} \\ A_{16} & A_{26} & A_{66} \end{bmatrix}^{II_t} \begin{Bmatrix} \varepsilon_x^0 \\ \varepsilon_y^0 \\ \gamma_{xy}^0 \end{Bmatrix} + \begin{bmatrix} B_{11} & B_{12} & B_{16} \\ B_{12} & B_{22} & B_{26} \\ B_{16} & B_{26} & B_{66} \end{bmatrix}^{II_t} \begin{Bmatrix} \kappa_x \\ \kappa_y \\ \kappa_{xy} \end{Bmatrix} \tag{4.29a}$$

$$\begin{Bmatrix} M_x \\ M_y \\ M_{xy} \end{Bmatrix}^{II_t} = \begin{bmatrix} B_{11} & B_{12} & B_{16} \\ B_{12} & B_{22} & B_{26} \\ B_{16} & B_{26} & B_{66} \end{bmatrix}^{II_t} \begin{Bmatrix} \varepsilon_x^0 \\ \varepsilon_y^0 \\ \gamma_{xy}^0 \end{Bmatrix} + \begin{bmatrix} D_{11} & D_{12} & D_{16} \\ D_{12} & D_{22} & D_{26} \\ D_{16} & D_{26} & D_{66} \end{bmatrix}^{II_t} \begin{Bmatrix} \kappa_x \\ \kappa_y \\ \kappa_{xy} \end{Bmatrix} \tag{4.29b}$$

$$\begin{Bmatrix} Q_y \\ Q_x \end{Bmatrix}^{II_t} = K \begin{bmatrix} A_{44} & A_{45} \\ A_{45} & A_{55} \end{bmatrix}^{II_t} \begin{Bmatrix} \gamma_{yz}^0 \\ \gamma_{xz}^0 \end{Bmatrix} \tag{4.29c}$$

where the contribution of the top circular cell segment (II_t) to the global stiffness matrices of the equivalent transformed plate [A], [B] and [D] is given by

$$\begin{aligned} A_{11}^{II_t} &= \frac{\pi}{b_s}\sum_{k=1}^{n_{II}} \overline{C}_{11}^k (r_k^{\,2} - r_{k-1}^{\,2}), \quad A_{12}^{II_t} = \frac{\pi}{2b_s}\sum_{k=1}^{n_{II}} \overline{C}_{12}^k (r_k^{\,2} - r_{k-1}^{\,2}), \quad A_{16}^{II_t} = 0 \\ A_{22}^{II_t} &= 2\sum_{k=1}^{n_{II}} \overline{C}_{22}^k (z_k - z_{k-1}), \quad A_{26}^{II_t} = 0, \quad A_{66}^{II_t} = \frac{\pi}{2b_s}\sum_{k=1}^{n_{II}} (\overline{C}_{55}^k + \overline{C}_{66}^k)(r_k^{\,2} - r_{k-1}^{\,2}) \end{aligned} \tag{4.30a}$$

$$\begin{aligned} B_{11}^{II_t} &= \frac{\pi H}{b_s}\sum_{k=1}^{n_{II}} \overline{C}_{11}^k (r_k^{\,2} - r_{k-1}^{\,2}), \quad B_{12}^{II_t} = \frac{\pi H}{2b_s}\sum_{k=1}^{n_{II}} \overline{C}_{12}^k (r_k^{\,2} - r_{k-1}^{\,2}) \\ B_{16}^{II_t} &= \frac{\pi}{3b_s}\sum_{k=1}^{n_{II}} \overline{C}_{16}^k (r_k^{\,3} - r_{k-1}^{\,3}), \quad B_{22}^{II_t} = \frac{1}{2}\sum_{k=1}^{n_{II}} \overline{C}_{22}^k [(z_k^{\,2} - z_{k-1}^{\,2}) + (z_k + D_\zeta)^2 - (z_{k-1} + D_\zeta)^2] \\ B_{26}^{II_t} &= \frac{\pi}{12b_s}\sum_{k=1}^{n_{II}} (3\overline{C}_{26}^k + 2\overline{C}_{45}^k)(r_k^{\,3} - r_{k-1}^{\,3}), \quad B_{66}^{II_t} = \frac{\pi H}{2b_s}\sum_{k=1}^{n_{II}} (\overline{C}_{55}^k + \overline{C}_{66}^k)(r_k^{\,2} - r_{k-1}^{\,2}) \end{aligned} \tag{4.30b}$$

$$D_{11}^{II_t} = \frac{\pi}{b_s}\sum_{k=1}^{n_{II}} \overline{C}_{11}^{k}[\frac{1}{4}(r_k{}^4 - r_{k-1}{}^4) + H^2(r_k{}^2 - r_{k-1}{}^2)]$$

$$D_{12}^{II_t} = \frac{\pi}{b_s}\sum_{k=1}^{n_{II}} \overline{C}_{12}^{k}[\frac{3}{16}(r_k{}^4 - r_{k-1}{}^4) + \frac{H^2}{2}(r_k{}^2 - r_{k-1}{}^2)]$$

$$D_{16}^{II_t} = \frac{2\pi H}{3b_s}\sum_{k=1}^{n_{II}} \overline{C}_{16}^{k}(r_k{}^3 - r_{k-1}{}^3),\quad D_{26}^{II_t} = \frac{\pi H}{6b_s}\sum_{k=1}^{n_{II}}(3\overline{C}_{26}^{k} + 2\overline{C}_{45}^{k})(r_k{}^3 - r_{k-1}{}^3) \qquad (4.30c)$$

$$D_{22}^{II_t} = \frac{1}{3}\sum_{k=1}^{n_{II}} \overline{C}_{22}^{k}[(z_k{}^3 - z_{k-1}{}^3) + (z_k + D_\zeta)^3 - (z_{k-1} + D_\zeta)^3]$$

$$D_{66}^{II_t} = \frac{\pi}{b_s}\sum_{k=1}^{n_{II}}[\frac{1}{16}(\overline{C}_{55}^{k} + 3\overline{C}_{66}^{k})(r_k{}^4 - r_{k-1}{}^4) + \frac{H^2}{2}(\overline{C}_{55}^{k} + \overline{C}_{66}^{k})(r_k{}^2 - r_{k-1}{}^2)]$$

$$A_{44}^{II_t} = 2\sum_{k=1}^{n_{II}} \overline{C}_{44}^{k}(z_k - z_{k-1}),\quad A_{45}^{II_t} = 0$$

$$A_{55}^{II_t} = \frac{\pi}{2b_s}\sum_{k=1}^{n_{II}}(\overline{C}_{55}^{k} + \overline{C}_{66}^{k})(r_k{}^2 - r_{k-1}{}^2) \qquad (4.30d)$$

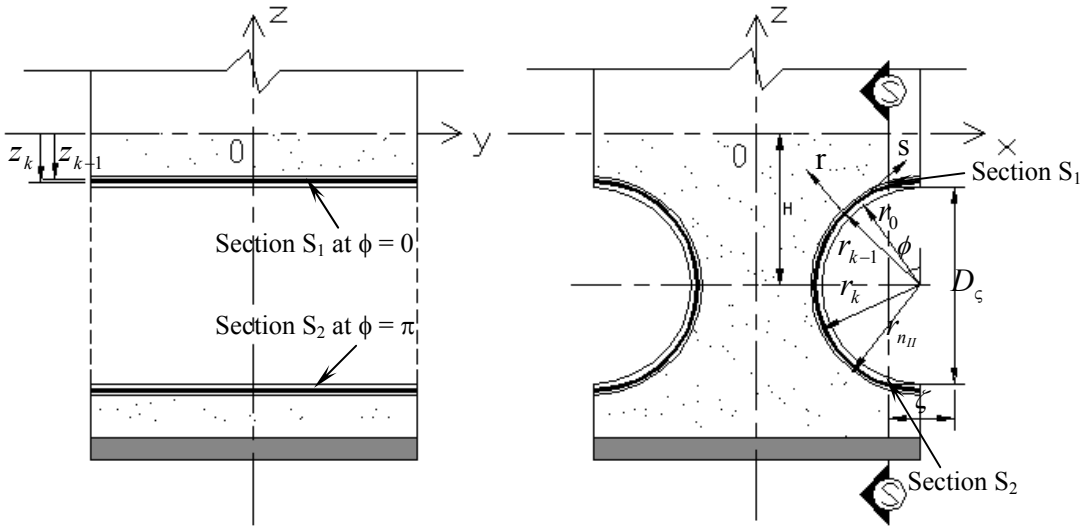

Figure 4.11 Shell local and global coordinate systems used for bottom circular cell (II_b)

For the bottom circular cell segment (II_b) shown in Figure 4.11, the constitutive equation can be transformed from the lamina principal coordinate system (1, 2, 3) into the shell local coordinate system (*x*, *s*, *r*) for the *k*th lamina by using the same procedure as applied for top circular cell segment (II_t), which results in

$$\begin{Bmatrix} \sigma_x \\ \sigma_s \\ \tau_{sr} \\ \tau_{xr} \\ \tau_{xs} \end{Bmatrix}_k^{II_b} = \begin{bmatrix} \overline{C}_{11} & \overline{C}_{12} & 0 & 0 & \overline{C}_{16} \\ \overline{C}_{12} & \overline{C}_{22} & 0 & 0 & \overline{C}_{26} \\ 0 & 0 & \overline{C}_{44} & \overline{C}_{45} & 0 \\ 0 & 0 & \overline{C}_{45} & \overline{C}_{55} & 0 \\ \overline{C}_{16} & \overline{C}_{26} & 0 & 0 & \overline{C}_{66} \end{bmatrix}_k^{II_b} \begin{Bmatrix} \varepsilon_x \\ \varepsilon_s \\ \gamma_{sr} \\ \gamma_{xr} \\ \gamma_{xs} \end{Bmatrix}_k^{II_b} \tag{4.31}$$

Then, the stresses and strains are transformed from the shell local coordinate system (x, s, r) into the global coordinate system (x, y, z). The stresses at the bottom circular cell segment are rotated around the y-axis by an angle ϕ as shown in Figure 4.11. The details of this coordinate system transformation are described in Appendix D as well. Thus, the constitutive equation of the bottom circular cell segment in the global coordinate system (x, y, z) can be obtained as

$$\begin{Bmatrix} \sigma_x \\ \sigma_y \\ \tau_{yz} \\ \tau_{xz} \\ \tau_{xy} \end{Bmatrix}_k^{II_b} = \begin{bmatrix} \widetilde{C}_{11} & \widetilde{C}_{12} & \widetilde{C}_{14} & \widetilde{C}_{15} & \widetilde{C}_{16} \\ \widetilde{C}_{12} & \widetilde{C}_{22} & \widetilde{C}_{24} & \widetilde{C}_{25} & \widetilde{C}_{26} \\ \widetilde{C}_{14} & \widetilde{C}_{24} & \widetilde{C}_{44} & \widetilde{C}_{45} & \widetilde{C}_{46} \\ \widetilde{C}_{15} & \widetilde{C}_{25} & \widetilde{C}_{45} & \widetilde{C}_{55} & \widetilde{C}_{56} \\ \widetilde{C}_{16} & \widetilde{C}_{26} & \widetilde{C}_{46} & \widetilde{C}_{56} & \widetilde{C}_{66} \end{bmatrix}_k^{II_b} \begin{Bmatrix} \varepsilon_x \\ \varepsilon_y \\ \gamma_{yz} \\ \gamma_{xz} \\ \gamma_{xy} \end{Bmatrix}_k^{II_b} \tag{4.32}$$

where

$$\left[\widetilde{C}\right]_k^{II_b} = \left[T_2'\right]^{-1} \left[\overline{C}\right]_k^{II_b} \left[T_2'\right]^{-T} \tag{4.33}$$

The transformation matrix $\left[T_2'\right]$ and the transformed stiffness coefficients $\widetilde{C}_{ij}^{\ II_b}$ $(i,\ j = 1, 2, 4, 5, 6)$ are defined in Appendix D.

The relations between the resultant forces $\{N\}$, $\{Q\}$ and moment $\{M\}$, and the midsurface strains and curvatures for the bottom circular cell part (II_b) are obtained by integrating $\sigma_x^{II_b}$ and $\tau_{xz}^{II_b}$ over the face of segment II_b normal to the x-axis or oyz plane, and $\sigma_y^{II_b}$, $\tau_{xy}^{II_b}$ and $\tau_{yz}^{II_b}$ over the face of segment II_b normal to the y-axis or oxz plane (Figure 4.11). Averaging over the width of the representative element is again required when computing $N_y^{II_b}$, $N_{xy}^{II_b}$, $M_y^{II_b}$, $M_{xy}^{II_b}$ and $Q_y^{II_b}$ from $\sigma_y^{II_b}$, $\tau_{xy}^{II_b}$ and $\tau_{yz}^{II_b}$. The relations between the shell local coordinate system (x, s, r) of bottom circular segment and global coordinate system (x, y, z) can be expressed as (Figure 4.10)

$$\begin{cases} x = -r\sin\phi + \dfrac{b_s}{2} \\ y = y \\ z = r\cos\phi - H \end{cases} \tag{4.34}$$

Substituting Eq. (4.32) in Eqs. (4.18a~c) and using Eqs. (4.5), (4.6) and (4.34), the stress resultants acting on *oxz* plane are given by

$$\begin{aligned} N_y^{II_b} = \frac{1}{b_s}\Bigg[& \sum_{k=1}^{n_{II}} \int_{r_{k-1}}^{r_k} \int_0^{2\pi} \left(\widetilde{C}_{12}^k \varepsilon_x^0 + \widetilde{C}_{22}^k \varepsilon_y^0 + \widetilde{C}_{24}^k \gamma_{yz}^0 + \widetilde{C}_{25}^k \gamma_{xz}^0 + \widetilde{C}_{26}^k \gamma_{xy}^0 \right) r dr d\phi \\ & + \sum_{k=1}^{n_{II}} \int_{r_{k-1}}^{r_k} \int_0^{2\pi} \left(\widetilde{C}_{12}^k \kappa_x + \widetilde{C}_{22}^k \kappa_y + \widetilde{C}_{26}^k \kappa_{xy} \right) r^2 \cos\phi dr d\phi \\ & - H \sum_{k=1}^{n_{II}} \int_{r_{k-1}}^{r_k} \int_0^{2\pi} \left(\widetilde{C}_{12}^k \kappa_x + \widetilde{C}_{22}^k \kappa_y + \widetilde{C}_{26}^k \kappa_{xy} \right) r dr d\phi \Bigg] \end{aligned} \tag{4.35a}$$

$$\begin{aligned} N_{xy}^{II_b} = \frac{1}{b_s}\Bigg[& \sum_{k=1}^{n_{II}} \int_{r_{k-1}}^{r_k} \int_0^{2\pi} \left(\widetilde{C}_{16}^k \varepsilon_x^0 + \widetilde{C}_{26}^k \varepsilon_y^0 + \widetilde{C}_{46}^k \gamma_{yz}^0 + \widetilde{C}_{56}^k \gamma_{xz}^0 + \widetilde{C}_{66}^k \gamma_{xy}^0 \right) r dr d\phi \\ & + \sum_{k=1}^{n_{II}} \int_{r_{k-1}}^{r_k} \int_0^{2\pi} \left(\widetilde{C}_{16}^k \kappa_x + \widetilde{C}_{26}^k \kappa_y + \widetilde{C}_{66}^k \kappa_{xy} \right) r^2 \cos\phi dr d\phi \\ & - H \sum_{k=1}^{n_{II}} \int_{r_{k-1}}^{r_k} \int_0^{2\pi} \left(\widetilde{C}_{16}^k \kappa_x + \widetilde{C}_{26}^k \kappa_y + \widetilde{C}_{66}^k \kappa_{xy} \right) r dr d\phi \Bigg] \end{aligned} \tag{4.35b}$$

$$\begin{aligned} M_y^{II_b} = & \frac{1}{b_s}\Bigg[\sum_{k=1}^{n_{II}} \int_{r_{k-1}}^{r_k} \int_0^{2\pi} \left(\widetilde{C}_{12}^k \varepsilon_x^0 + \widetilde{C}_{22}^k \varepsilon_y^0 + \widetilde{C}_{24}^k \gamma_{yz}^0 + \widetilde{C}_{25}^k \gamma_{xz}^0 + \widetilde{C}_{26}^k \gamma_{xy}^0 \right) r^2 \cos\phi dr d\phi \\ & + \sum_{k=1}^{n_{II}} \int_{r_{k-1}}^{r_k} \int_0^{2\pi} \left(\widetilde{C}_{12}^k \kappa_x + \widetilde{C}_{22}^k \kappa_y + \widetilde{C}_{26}^k \kappa_{xy} \right) r^3 \cos^2\phi dr d\phi \\ & - H \sum_{k=1}^{n_{II}} \int_{r_{k-1}}^{r_k} \int_0^{2\pi} \left(\widetilde{C}_{12}^k \kappa_x + \widetilde{C}_{22}^k \kappa_y + \widetilde{C}_{26}^k \kappa_{xy} \right) r^2 \cos\phi dr d\phi \Bigg] \\ & - \frac{H}{b_s}\Bigg[\sum_{k=1}^{n_{II}} \int_{r_{k-1}}^{r_k} \int_0^{2\pi} \left(\widetilde{C}_{12}^k \varepsilon_x^0 + \widetilde{C}_{22}^k \varepsilon_y^0 + \widetilde{C}_{24}^k \gamma_{yz}^0 + \widetilde{C}_{25}^k \gamma_{xz}^0 + \widetilde{C}_{26}^k \gamma_{xy}^0 \right) r dr d\phi \\ & + \sum_{k=1}^{n_{II}} \int_{r_{k-1}}^{r_k} \int_0^{2\pi} \left(\widetilde{C}_{12}^k \kappa_x + \widetilde{C}_{22}^k \kappa_y + \widetilde{C}_{26}^k \kappa_{xy} \right) r^2 \cos\phi dr d\phi \\ & - H \sum_{k=1}^{n_{II}} \int_{r_{k-1}}^{r_k} \int_0^{2\pi} \left(\widetilde{C}_{12}^k \kappa_x + \widetilde{C}_{22}^k \kappa_y + \widetilde{C}_{26}^k \kappa_{xy} \right) r dr d\phi \Bigg] \end{aligned} \tag{4.35c}$$

$$
\begin{aligned}
M_{xy}^{II_b} = \frac{1}{b_s}\Bigg[& \sum_{k=1}^{n_{II}} \int_{r_{k-1}}^{r_k} \int_0^{2\pi} \left(\widetilde{C}_{16}^k \varepsilon_x^0 + \widetilde{C}_{26}^k \varepsilon_y^0 + \widetilde{C}_{46}^k \gamma_{yz}^0 + \widetilde{C}_{56}^k \gamma_{xz}^0 + \widetilde{C}_{66}^k \gamma_{xy}^0 \right) r^2 \cos\phi \, dr d\phi \\
& + \sum_{k=1}^{n_{II}} \int_{r_{k-1}}^{r_k} \int_0^{2\pi} \left(\widetilde{C}_{16}^k \kappa_x + \widetilde{C}_{26}^k \kappa_y + \widetilde{C}_{66}^k \kappa_{xy} \right) r^3 \cos^2\phi \, dr d\phi \\
& - H \sum_{k=1}^{n_{II}} \int_{r_{k-1}}^{r_k} \int_0^{2\pi} \left(\widetilde{C}_{16}^k \kappa_x + \widetilde{C}_{26}^k \kappa_y + \widetilde{C}_{66}^k \kappa_{xy} \right) r^2 \cos\phi \, dr d\phi \Bigg] \\
- \frac{H}{b_s}\Bigg[& \sum_{k=1}^{n_{II}} \int_{r_{k-1}}^{r_k} \int_0^{2\pi} \left(\widetilde{C}_{16}^k \varepsilon_x^0 + \widetilde{C}_{26}^k \varepsilon_y^0 + \widetilde{C}_{46}^k \gamma_{yz}^0 + \widetilde{C}_{56}^k \gamma_{xz}^0 + \widetilde{C}_{66}^k \gamma_{xy}^0 \right) r \, dr d\phi \\
& + \sum_{k=1}^{n_{II}} \int_{r_{k-1}}^{r_k} \int_0^{2\pi} \left(\widetilde{C}_{16}^k \kappa_x + \widetilde{C}_{26}^k \kappa_y + \widetilde{C}_{66}^k \kappa_{xy} \right) r^2 \cos\phi \, dr d\phi \\
& - H \sum_{k=1}^{n_{II}} \int_{r_{k-1}}^{r_k} \int_0^{2\pi} \left(\widetilde{C}_{16}^k \kappa_x + \widetilde{C}_{26}^k \kappa_y + \widetilde{C}_{66}^k \kappa_{xy} \right) r \, dr d\phi \Bigg]
\end{aligned}
\tag{4.35d}
$$

$$
\begin{aligned}
Q_y^{II_b} = K\Bigg\{ \frac{1}{b_s}\Bigg[& \sum_{k=1}^{n_{II}} \int_{r_{k-1}}^{r_k} \int_0^{2\pi} \left(\widetilde{C}_{14}^k \varepsilon_x^0 + \widetilde{C}_{24}^k \varepsilon_y^0 + \widetilde{C}_{44}^k \gamma_{yz}^0 + \widetilde{C}_{45}^k \gamma_{xz}^0 + \widetilde{C}_{46}^k \gamma_{xy}^0 \right) r \, dr d\phi \\
& + \sum_{k=1}^{n_{II}} \int_{r_{k-1}}^{r_k} \int_0^{2\pi} \left(\widetilde{C}_{14}^k \kappa_x + \widetilde{C}_{24}^k \kappa_y + \widetilde{C}_{46}^k \kappa_{xy} \right) r^2 \cos\phi \, dr d\phi \\
& - H \sum_{k=1}^{n_{II}} \int_{r_{k-1}}^{r_k} \int_0^{2\pi} \left(\widetilde{C}_{14}^k \kappa_x + \widetilde{C}_{24}^k \kappa_y + \widetilde{C}_{46}^k \kappa_{xy} \right) r \, dr d\phi \Bigg]\Bigg\}
\end{aligned}
\tag{4.35e}
$$

The resultants $N_x^{II_b}$, $M_x^{II_b}$ and $Q_x^{II_b}$ acting on *oyz* plane are obtained by integrating $\sigma_x^{II_b}$ and $\tau_{xz}^{II_b}$ over the section S-S (at $x = \frac{b_s}{2} - \zeta$) shown in Figure 4.11, which results in

$$
\begin{aligned}
N_x^{II_b} = & \sum_{k=1}^{n_{II}} \int_{z_{k-1}}^{z_k} \left(\widetilde{C}_{11}^k \varepsilon_x^0 + \widetilde{C}_{12}^k \varepsilon_y^0 + \widetilde{C}_{14}^k \gamma_{yz}^0 + \widetilde{C}_{15}^k \gamma_{xz}^0 + \widetilde{C}_{16}^k \gamma_{xy}^0 \right) dz \\
& + \sum_{k=1}^{n_{II}} \int_{z_{k-1}}^{z_k} \left(\widetilde{C}_{11}^k \kappa_x + \widetilde{C}_{12}^k \kappa_y + \widetilde{C}_{16}^k \kappa_{xy} \right) z \, dz \\
& + \sum_{k=1}^{n_{II}} \int_{z_{k-1}+D_\zeta}^{z_k+D_\zeta} \left(\widetilde{C}_{11}^k \varepsilon_x^0 + \widetilde{C}_{12}^k \varepsilon_y^0 + \widetilde{C}_{14}^k \gamma_{yz}^0 + \widetilde{C}_{15}^k \gamma_{xz}^0 + \widetilde{C}_{16}^k \gamma_{xy}^0 \right) dz \\
& + \sum_{k=1}^{n_{II}} \int_{z_{k-1}+D_\zeta}^{z_k+D_\zeta} \left(\widetilde{C}_{11}^k \kappa_x + \widetilde{C}_{12}^k \kappa_y + \widetilde{C}_{16}^k \kappa_{xy} \right) z \, dz
\end{aligned}
\tag{4.35f}
$$

$$
\begin{aligned}
M_x^{II_b} = & \sum_{k=1}^{n_{II}} \int_{z_{k-1}}^{z_k} \left(\widetilde{C}_{11}^k \varepsilon_x^0 + \widetilde{C}_{12}^k \varepsilon_y^0 + \widetilde{C}_{14}^k \gamma_{yz}^0 + \widetilde{C}_{15}^k \gamma_{xz}^0 + \widetilde{C}_{16}^k \gamma_{xy}^0 \right) z dz \\
& + \sum_{k=1}^{n_{II}} \int_{z_{k-1}}^{z_k} \left(\widetilde{C}_{11}^k \kappa_x + \widetilde{C}_{12}^k \kappa_y + \widetilde{C}_{16}^k \kappa_{xy} \right) z^2 dz \\
& + \sum_{k=1}^{n_{II}} \int_{z_{k-1}+D_\zeta}^{z_k+D_\zeta} \left(\widetilde{C}_{11}^k \varepsilon_x^0 + \widetilde{C}_{12}^k \varepsilon_y^0 + \widetilde{C}_{14}^k \gamma_{yz}^0 + \widetilde{C}_{15}^k \gamma_{xz}^0 + \widetilde{C}_{16}^k \gamma_{xy}^0 \right) z dz \\
& + \sum_{k=1}^{n_{II}} \int_{z_{k-1}+D_\zeta}^{z_k+D_\zeta} \left(\widetilde{C}_{11}^k \kappa_x + \widetilde{C}_{12}^k \kappa_y + \widetilde{C}_{16}^k \kappa_{xy} \right) z^2 dz
\end{aligned}
\tag{4.35g}
$$

$$
\begin{aligned}
Q_x^{II_b} = K \Bigg[& \sum_{k=1}^{n_{II}} \int_{z_{k-1}}^{z_k} \left(\widetilde{C}_{15}^k \varepsilon_x^0 + \widetilde{C}_{25}^k \varepsilon_y^0 + \widetilde{C}_{45}^k \gamma_{yz}^0 + \widetilde{C}_{55}^k \gamma_{xz}^0 + \widetilde{C}_{56}^k \gamma_{xy}^0 \right) dz \\
& + \sum_{k=1}^{n_{II}} \int_{z_{k-1}}^{z_k} \left(\widetilde{C}_{15}^k \kappa_x + \widetilde{C}_{25}^k \kappa_y + \widetilde{C}_{56}^k \kappa_{xy} \right) z dz \\
& + \sum_{k=1}^{n_{II}} \int_{z_{k-1}+D_\zeta}^{z_k+D_\zeta} \left(\widetilde{C}_{15}^k \varepsilon_x^0 + \widetilde{C}_{25}^k \varepsilon_y^0 + \widetilde{C}_{45}^k \gamma_{yz}^0 + \widetilde{C}_{55}^k \gamma_{xz}^0 + \widetilde{C}_{56}^k \gamma_{xy}^0 \right) dz \\
& + \sum_{k=1}^{n_{II}} \int_{z_{k-1}+D_\zeta}^{z_k+D_\zeta} \left(\widetilde{C}_{15}^k \kappa_x + \widetilde{C}_{25}^k \kappa_y + \widetilde{C}_{56}^k \kappa_{xy} \right) z dz \Bigg]
\end{aligned}
\tag{4.35h}
$$

where the parameters ζ and D_ζ shown in Figure 4.10 have the same meaning as in Eqs. (4.27f~h). The transformed stiffness coefficients $\widetilde{C}_{ij}^{\ k}$ $(i, j = 1, 2, 4, 5, 6)$ in Eqs. (4.35a~h) are again a function of the angle ϕ. If we choose the section S-S at $x = \dfrac{b_s}{2}$, that is $\zeta = 0$, the S_1 section corresponds to angle $\phi = 0$ for this case and produces the following relations

$$
\begin{aligned}
& \widetilde{C}_{11} = \overline{C}_{11}, \quad \widetilde{C}_{12} = \overline{C}_{12}, \quad \widetilde{C}_{16} = \overline{C}_{16}, \quad \widetilde{C}_{45} = \overline{C}_{45}, \quad \widetilde{C}_{55} = \overline{C}_{55} \\
& \widetilde{C}_{14} = \widetilde{C}_{15} = \widetilde{C}_{25} = \widetilde{C}_{56} = 0
\end{aligned}
\tag{4.36a}
$$

and the S_2 section corresponds to angle $\phi = \pi$ and yields

$$
\begin{aligned}
& \widetilde{C}_{11} = \overline{C}_{11}, \quad \widetilde{C}_{12} = \overline{C}_{12}, \quad \widetilde{C}_{16} = -\overline{C}_{16}, \quad \widetilde{C}_{45} = -\overline{C}_{45}, \quad \widetilde{C}_{55} = \overline{C}_{55} \\
& \widetilde{C}_{14} = \widetilde{C}_{15} = \widetilde{C}_{25} = \widetilde{C}_{56} = 0
\end{aligned}
\tag{4.36b}
$$

The resultants $N_x^{II_b}$, $M_x^{II_b}$ and $Q_x^{II_b}$ in Eqs. (4.35f~h) therefore can be simplified by substituting the relations given in Eqs. (4.36a, b). Again, the terms which involve $\widetilde{C}_{12}$, $\widetilde{C}_{16}$ and $\widetilde{C}_{45}$ in Eqs. (4.35f~h) are replaced with the corresponding terms in Eqs. (4.35a~e) to produce symmetrical [*A*], [*B*] and [*D*] matrices.

By performing the integration in Eq. (4.35a~h) and taking into account Eqs. (4.26a, b), the forces and moments resultants of bottom circular cell segment (II_b) can be obtained as

$$\begin{Bmatrix} N_x \\ N_y \\ N_{xy} \end{Bmatrix}^{II_b} = \begin{bmatrix} A_{11} & A_{12} & A_{16} \\ A_{12} & A_{22} & A_{26} \\ A_{16} & A_{26} & A_{66} \end{bmatrix}^{II_b} \begin{Bmatrix} \varepsilon_x^0 \\ \varepsilon_y^0 \\ \gamma_{xy}^0 \end{Bmatrix} + \begin{bmatrix} B_{11} & B_{12} & B_{16} \\ B_{12} & B_{22} & B_{26} \\ B_{16} & B_{26} & B_{66} \end{bmatrix}^{II_b} \begin{Bmatrix} \kappa_x \\ \kappa_y \\ \kappa_{xy} \end{Bmatrix} \tag{4.37a}$$

$$\begin{Bmatrix} M_x \\ M_y \\ M_{xy} \end{Bmatrix}^{II_b} = \begin{bmatrix} B_{11} & B_{12} & B_{16} \\ B_{12} & B_{22} & B_{26} \\ B_{16} & B_{26} & B_{66} \end{bmatrix}^{II_b} \begin{Bmatrix} \varepsilon_x^0 \\ \varepsilon_y^0 \\ \gamma_{xy}^0 \end{Bmatrix} + \begin{bmatrix} D_{11} & D_{12} & D_{16} \\ D_{12} & D_{22} & D_{26} \\ D_{16} & D_{26} & D_{66} \end{bmatrix}^{II_b} \begin{Bmatrix} \kappa_x \\ \kappa_y \\ \kappa_{xy} \end{Bmatrix} \tag{4.37b}$$

$$\begin{Bmatrix} Q_y \\ Q_x \end{Bmatrix}^{II_b} = K \begin{bmatrix} A_{44} & A_{45} \\ A_{45} & A_{55} \end{bmatrix}^{II_b} \begin{Bmatrix} \gamma_{yz}^0 \\ \gamma_{xz}^0 \end{Bmatrix} \tag{4.37c}$$

where the contribution of the bottom circular cell segment (II_b) to the global stiffness matrices of the equivalent transformed plate [A], [B] and [D] is given by

$$\begin{aligned} A_{11}^{II_b} &= 2\sum_{k=1}^{n_{II}} \overline{C}_{11}^k (z_k - z_{k-1}), \quad A_{12}^{II_b} = \frac{\pi}{2b_s} \sum_{k=1}^{n_{II}} \overline{C}_{12}^k (r_k^{\,2} - r_{k-1}^{\,2}), \quad A_{16}^{II_b} = 0 \\ A_{22}^{II_b} &= \frac{\pi}{b_s} \sum_{k=1}^{n_{II}} \overline{C}_{22}^k (r_k^{\,2} - r_{k-1}^{\,2}), \quad A_{26}^{II_b} = 0, \quad A_{66}^{II_b} = \frac{\pi}{2b_s} \sum_{k=1}^{n_{II}} (\overline{C}_{44}^k + \overline{C}_{66}^k)(r_k^{\,2} - r_{k-1}^{\,2}) \end{aligned} \tag{4.38a}$$

$$\begin{aligned} B_{11}^{II_b} &= \frac{1}{2} \sum_{k=1}^{n_{II}} \overline{C}_{11}^k [(z_k^{\,2} - z_{k-1}^{\,2}) + (z_k + D_\zeta)^2 - (z_{k-1} + D_\zeta)^2], \quad B_{12}^{II_b} = -\frac{\pi H}{2b_s} \sum_{k=1}^{n_{II}} \overline{C}_{12}^k (r_k^{\,2} - r_{k-1}^{\,2}) \\ B_{16}^{II_b} &= \frac{\pi}{12b_s} \sum_{k=1}^{n_{II}} (3\overline{C}_{16}^k + 2\overline{C}_{45}^k)(r_k^{\,3} - r_{k-1}^{\,3}), \quad B_{22}^{II_b} = -\frac{\pi H}{b_s} \sum_{k=1}^{n_{II}} \overline{C}_{22}^k (r_k^{\,2} - r_{k-1}^{\,2}) \\ B_{26}^{II_b} &= \frac{\pi}{3b_s} \sum_{k=1}^{n_{II}} \overline{C}_{26}^k (r_k^{\,3} - r_{k-1}^{\,3}), \quad B_{66}^{II_b} = -\frac{\pi H}{2b_s} \sum_{k=1}^{n_{II}} (\overline{C}_{44}^k + \overline{C}_{66}^k)(r_k^{\,2} - r_{k-1}^{\,2}) \end{aligned} \tag{4.38b}$$

$$D_{11}^{II_b} = \frac{1}{3}\sum_{k=1}^{n_{II}} \overline{C}_{11}^{k}[({z_k}^3 - {z_{k-1}}^3) + (z_k + D_\zeta)^3 - (z_{k-1} + D_\zeta)^3]$$

$$D_{12}^{II_b} = \frac{\pi}{b_s}\sum_{k=1}^{n_{II}} \overline{C}_{12}^{k}[\frac{3}{16}({r_k}^4 - {r_{k-1}}^4) + \frac{H^2}{2}({r_k}^2 - {r_{k-1}}^2)]$$

$$D_{16}^{II_b} = -\frac{\pi H}{6b_s}\sum_{k=1}^{n_{II}} (3\overline{C}_{16}^{k} + 2\overline{C}_{45}^{k})({r_k}^3 - {r_{k-1}}^3), \quad D_{26}^{II_b} = -\frac{2\pi H}{3b_s}\sum_{k=1}^{n_{II}} \overline{C}_{26}^{k}({r_k}^3 - {r_{k-1}}^3) \qquad (4.38c)$$

$$D_{22}^{II_b} = \frac{\pi}{b_s}\sum_{k=1}^{n_{II}} \overline{C}_{22}^{k}[\frac{1}{4}({r_k}^4 - {r_{k-1}}^4) + H^2({r_k}^2 - {r_{k-1}}^2)]$$

$$D_{66}^{II_b} = \frac{\pi}{b_s}\sum_{k=1}^{n_{II}} [\frac{1}{16}(\overline{C}_{44}^{k} + 3\overline{C}_{66}^{k})({r_k}^4 - {r_{k-1}}^4) + \frac{H^2}{2}(\overline{C}_{44}^{k} + \overline{C}_{66}^{k})({r_k}^2 - {r_{k-1}}^2)]$$

$$A_{44}^{II_b} = \frac{\pi}{2b_s}\sum_{k=1}^{n_{II}} (\overline{C}_{44}^{k} + \overline{C}_{66}^{k})({r_k}^2 - {r_{k-1}}^2), \quad A_{45}^{II_b} = 0$$

$$A_{55}^{II_b} = 2\sum_{k=1}^{n_{II}} \overline{C}_{55}^{k}(z_k - z_{k-1}) \qquad (4.38d)$$

Therefore, the total contributions of the circular cell segment (II) to the global matrices [*A*], [*B*] and [*D*] are

$$A_{ij}^{II} = A_{ij}^{II_t} + A_{ij}^{II_b}, \quad (i, j = 1, 2, 6) \qquad (4.39a)$$

$$B_{ij}^{II} = B_{ij}^{II_t} + B_{ij}^{II_b}, \quad (i, j = 1, 2, 6) \qquad (4.39b)$$

$$D_{ij}^{II} = D_{ij}^{II_t} + D_{ij}^{II_b}, \quad (i, j = 1, 2, 6) \qquad (4.39c)$$

$$A_{ij}^{II} = A_{ij}^{II_t} + A_{ij}^{II_b}, \quad (i, j = 4, 5) \qquad (4.39d)$$

- **PFR Core Segment (III)**

As described in Section 4.3.1, the particular filled resin (PFR) core material is generally considered as an isotropic material. The coordinate system used for computing the contribution of the PFR core segment is shown in Figure 4.12. Due to the irregularity of the PFR core part in the representative element, the PFR core segment (III) is subdivided into a number of layers to simulate a realistic shape of the PFR core segment, as shown in Figure 4.12. Each layer therefore can be treated as a single plate with thickness t_k and width b_k, where parameter k denotes the number of the layers. The accuracy of the results will increase when the number k is increased.

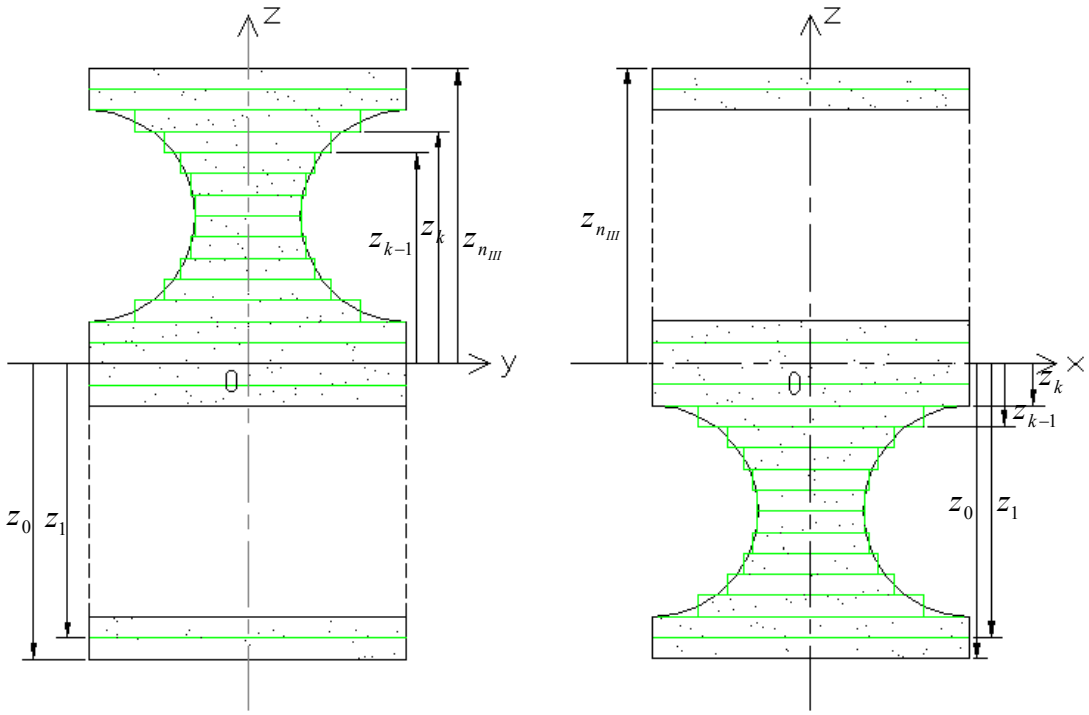

Figure 4.12 Coordinate system used for PFR core (III)

Using Eq. (4.16), the constitutive equation of PFR core segment (III) for the *k*th layer can be written as

$$\begin{Bmatrix} \sigma_x \\ \sigma_y \\ \tau_{yz} \\ \tau_{xz} \\ \tau_{xy} \end{Bmatrix}_k^{III} = \begin{bmatrix} \overline{C}_{11} & \overline{C}_{12} & 0 & 0 & 0 \\ \overline{C}_{12} & \overline{C}_{22} & 0 & 0 & 0 \\ 0 & 0 & \overline{C}_{44} & 0 & 0 \\ 0 & 0 & 0 & \overline{C}_{55} & 0 \\ 0 & 0 & 0 & 0 & \overline{C}_{66} \end{bmatrix}_k^{III} \begin{Bmatrix} \varepsilon_x \\ \varepsilon_y \\ \gamma_{yz} \\ \gamma_{xz} \\ \gamma_{xy} \end{Bmatrix}_k^{III} \tag{4.40}$$

The relations between the coefficients $\overline{C}_{ij}$ and C_{ij} are expressed in Eq. (4.17).

Analogous to the circular cell segment, σ_x^{III}, τ_{xy}^{III} and τ_{xz}^{III} are integrated over the face of segment III normal to the *x*-axis (*oyz* plane), and σ_y^{III} and τ_{yz}^{III} over the face of segment III normal to the *y*-axis (*oxz* plane) (Figure 4.12). Because the width of the *k*th layer in PFR core segment b_k can be different to the width of the representative element b_s, the stresses are integrated to obtain the total forces and moments acting over the length b_k and the result is divided by the width of the representative element

b_s to produce the average contribution per unit width. Substitution of Eq. (4.40) into Eqs. (4.18a~c) and using Eqs. (4.5) and (4.6), the stress resultants of PFR core segment (III) yields

$$N_x^{III} = \frac{1}{b_s}\sum_{k=1}^{n_{III}} b_k \left[\int_{z_{k-1}}^{z_k} \left(\overline{C}_{11}^k \varepsilon_x^0 + \overline{C}_{12}^k \varepsilon_y^0 \right) dz + \int_{z_{k-1}}^{z_k} \left(\overline{C}_{11}^k \kappa_x + \overline{C}_{12}^k \kappa_y \right) z dz \right] \tag{4.41a}$$

$$N_y^{III} = \frac{1}{b_s}\sum_{k=1}^{n_{III}} b_k \left[\int_{z_{k-1}}^{z_k} \left(\overline{C}_{12}^k \varepsilon_x^0 + \overline{C}_{22}^k \varepsilon_y^0 \right) dz + \int_{z_{k-1}}^{z_k} \left(\overline{C}_{12}^k \kappa_x + \overline{C}_{22}^k \kappa_y \right) z dz \right] \tag{4.41b}$$

$$N_{xy}^{III} = \frac{1}{b_s}\sum_{k=1}^{n_{III}} b_k \left[\int_{z_{k-1}}^{z_k} \overline{C}_{66}^k \gamma_{xy}^0 dz + \int_{z_{k-1}}^{z_k} \overline{C}_{66}^k \kappa_{xy} z dz \right] \tag{4.41c}$$

$$M_x^{III} = \frac{1}{b_s}\sum_{k=1}^{n_{III}} b_k \left[\int_{z_{k-1}}^{z_k} \left(\overline{C}_{11}^k \varepsilon_x^0 + \overline{C}_{12}^k \varepsilon_y^0 \right) z dz + \int_{z_{k-1}}^{z_k} \left(\overline{C}_{11}^k \kappa_x + \overline{C}_{12}^k \kappa_y \right) z^2 dz \right] \tag{4.41d}$$

$$M_y^{III} = \frac{1}{b_s}\sum_{k=1}^{n_{III}} b_k \left[\int_{z_{k-1}}^{z_k} \left(\overline{C}_{12}^k \varepsilon_x^0 + \overline{C}_{22}^k \varepsilon_y^0 \right) z dz + \int_{z_{k-1}}^{z_k} \left(\overline{C}_{12}^k \kappa_x + \overline{C}_{22}^k \kappa_y \right) z^2 dz \right] \tag{4.41e}$$

$$M_{xy}^{III} = \frac{1}{b_s}\sum_{k=1}^{n_{III}} b_k \left[\int_{z_{k-1}}^{z_k} \overline{C}_{66}^k \gamma_{xy}^0 z dz + \int_{z_{k-1}}^{z_k} \overline{C}_{66}^k \kappa_{xy} z^2 dz \right] \tag{4.41f}$$

$$Q_x^{III} = K \frac{1}{b_s}\sum_{k=1}^{n_{III}} b_k \int_{z_{k-1}}^{z_k} \overline{C}_{55}^k \gamma_{xz}^0 dz \tag{4.41g}$$

$$Q_y^{III} = K \frac{1}{b_s}\sum_{k=1}^{n_{III}} b_k \int_{z_{k-1}}^{z_k} \overline{C}_{44}^k \gamma_{yz}^0 dz \tag{4.41h}$$

where n_{III} is total number of the layers in the PFR core segment.

By performing the integrations in Eqs. (4.41a~h), the force and moment resultants are obtained as

$$\begin{Bmatrix} N_x \\ N_y \\ N_{xy} \end{Bmatrix}^{III} = \begin{bmatrix} A_{11} & A_{12} & 0 \\ A_{12} & A_{22} & 0 \\ 0 & 0 & A_{66} \end{bmatrix}^{III} \begin{Bmatrix} \varepsilon_x^0 \\ \varepsilon_y^0 \\ \gamma_{xy}^0 \end{Bmatrix} + \begin{bmatrix} B_{11} & B_{12} & 0 \\ B_{21} & B_{22} & 0 \\ 0 & 0 & B_{66} \end{bmatrix}^{III} \begin{Bmatrix} \kappa_x \\ \kappa_y \\ \kappa_{xy} \end{Bmatrix} \tag{4.42a}$$

$$\begin{Bmatrix} M_x \\ M_y \\ M_{xy} \end{Bmatrix}^{III} = \begin{bmatrix} B_{11} & B_{12} & 0 \\ B_{21} & B_{22} & 0 \\ 0 & 0 & B_{66} \end{bmatrix}^{III} \begin{Bmatrix} \varepsilon_x^0 \\ \varepsilon_y^0 \\ \gamma_{xy}^0 \end{Bmatrix} + \begin{bmatrix} D_{11} & D_{12} & 0 \\ D_{12} & D_{22} & 0 \\ 0 & 0 & D_{66} \end{bmatrix}^{III} \begin{Bmatrix} \kappa_x \\ \kappa_y \\ \kappa_{xy} \end{Bmatrix} \tag{4.42b}$$

$$\begin{Bmatrix} Q_y \\ Q_x \end{Bmatrix}^{III} = K \begin{bmatrix} A_{44} & 0 \\ 0 & A_{55} \end{bmatrix}^{III} \begin{Bmatrix} \gamma_{yz}^0 \\ \gamma_{xz}^0 \end{Bmatrix} \tag{4.42c}$$

where the contribution of the PFR core segment (III) to the global stiffness matrices of the equivalent transformed plate [*A*], [*B*] and [*D*] is given by

$$A_{ij}^{III} = \frac{1}{b_s} \sum_{k=1}^{n_{III}} b_k \overline{C}_{ij}^{k} (z_k - z_{k-1}), \quad i, j = 1, 2, 6 \tag{4.43a}$$

$$B_{ij}^{III} = \frac{1}{2b_s} \sum_{k=1}^{n_{III}} b_k \overline{C}_{ij}^{k} (z_k^{\,2} - z_{k-1}^{\,2}), \quad i, j = 1, 2, 6 \tag{4.43b}$$

$$D_{ij}^{III} = \frac{1}{3b_s} \sum_{k=1}^{n_{III}} b_k \overline{C}_{ij}^{k} (z_k^{\,3} - z_{k-1}^{\,3}), \quad i, j = 1, 2, 6 \tag{4.43c}$$

$$A_{ij}^{III} = \frac{1}{b_s} \sum_{k=1}^{n_{III}} b_k \overline{C}_{ij}^{k} (z_k - z_{k-1}), \quad i, j = 4, 5 \tag{4.43d}$$

Note that $B_{21}^{III} = -B_{12}^{III}$. Thus, the stress resultants (*N*'s, *M*'s and *Q*'s) associated with strains for the complete form of the equivalent transformed plate can be obtained as

$$\begin{Bmatrix} N_x \\ N_y \\ N_{xy} \end{Bmatrix} = \begin{bmatrix} A_{11} & A_{12} & A_{16} \\ A_{12} & A_{22} & A_{26} \\ A_{16} & A_{26} & A_{66} \end{bmatrix} \begin{Bmatrix} \varepsilon_x^0 \\ \varepsilon_y^0 \\ \gamma_{xy}^0 \end{Bmatrix} + \begin{bmatrix} B_{11} & B_{12} & B_{16} \\ B_{21} & B_{22} & B_{26} \\ B_{16} & B_{26} & B_{66} \end{bmatrix} \begin{Bmatrix} \kappa_x \\ \kappa_y \\ \kappa_{xy} \end{Bmatrix} \tag{4.44a}$$

$$\begin{Bmatrix} M_x \\ M_y \\ M_{xy} \end{Bmatrix} = \begin{bmatrix} B_{11} & B_{12} & B_{16} \\ B_{21} & B_{22} & B_{26} \\ B_{16} & B_{26} & B_{66} \end{bmatrix} \begin{Bmatrix} \varepsilon_x^0 \\ \varepsilon_y^0 \\ \gamma_{xy}^0 \end{Bmatrix} + \begin{bmatrix} D_{11} & D_{12} & D_{16} \\ D_{12} & D_{22} & D_{26} \\ D_{16} & D_{26} & D_{66} \end{bmatrix} \begin{Bmatrix} \kappa_x \\ \kappa_y \\ \kappa_{xy} \end{Bmatrix} \tag{4.44b}$$

$$\begin{Bmatrix} Q_y \\ Q_x \end{Bmatrix} = K \begin{bmatrix} A_{44} & A_{45} \\ A_{45} & A_{55} \end{bmatrix} \begin{Bmatrix} \gamma_{yz}^0 \\ \gamma_{xz}^0 \end{Bmatrix} \tag{4.44c}$$

where the [*A*], [*B*] and [*D*] matrices for the equivalent transformed plate are obtained by adding the contributions of the outer shell, circular cell, and PFR core parts, hence

$$A_{ij} = A_{ij}^{I} + A_{ij}^{II} + A_{ij}^{III}, \quad (i, j = 1, 2, 6) \tag{4.45a}$$

$$B_{ij} = B_{ij}^{I} + B_{ij}^{II} + B_{ij}^{III}, \quad (i, j = 1, 2, 6) \tag{4.45b}$$

$$D_{ij} = D_{ij}^{I} + D_{ij}^{II} + D_{ij}^{III}, \quad (i, j = 1, 2, 6) \tag{4.45c}$$

and

$$A_{ij} = A_{ij}^{I} + A_{ij}^{II} + A_{ij}^{III}, \quad (i, j = 4, 5) \tag{4.45d}$$

4.3.3 Governing Equations of the Equivalent Transformed Plate

As part of developing the transformed plate approach, the governing equations of the equivalent transformed plate based on first-order shear deformation theory will be derived by using Hamilton's principle which can be written as

$$\int_{t_0}^{t_1} \delta L dt = 0 \tag{4.46}$$

where δL is the first variation of the Lagrangian which can be expressed as

$$\delta L = \delta \Pi - \delta T \tag{4.47}$$

where Π and T are the total potential and kinetic energies respectively. The total potential energy is given as

$$\Pi = U + V \tag{4.48}$$

where U is strain energy of the transformed plate and V is the potential energy of the external loads distributed over the plate. The general forms of U and V can be written as

$$U = \frac{1}{2}\iiint (\sigma_x \varepsilon_x + \sigma_y \varepsilon_y + \tau_{xy}\gamma_{xy} + \tau_{yz}\gamma_{yz} + \tau_{xz}\gamma_{xz}) dxdydz \tag{4.49}$$

and

$$V = \int_R q w_0 dxdy \tag{4.50}$$

where R denotes the distributed area of the external load and q is the density of the load.

Substitution of Eqs. (4.49) and (4.50) into Eq. (4.48) and considering Eqs. (4.5), (4.6), and (4.18a~c) yields

$$\begin{aligned}\Pi = \frac{1}{2}\int_0^a\int_0^b\Bigg[& N_x\frac{\partial u_0}{\partial x} + N_y\frac{\partial v_0}{\partial y} + N_{xy}\left(\frac{\partial u_0}{\partial y} + \frac{\partial v_0}{\partial x}\right) \\ & + M_x\frac{\partial \psi_x}{\partial x} + M_y\frac{\partial \psi_y}{\partial y} + M_{xy}\left(\frac{\partial \psi_x}{\partial y} + \frac{\partial \psi_y}{\partial x}\right) \\ & + Q_y\left(\frac{\partial w_0}{\partial y} + \psi_y\right) + Q_x\left(\frac{\partial w_0}{\partial x} + \psi_x\right)\Bigg]dxdy \\ & - \int_R q w_0 dxdy\end{aligned} \tag{4.51}$$

Note that total potential energy functional Π is a function of the five displacement functions u_0, v_0, w_0, ψ_x and ψ_y. The kinetic energy T can be written as

$$T = \frac{1}{2}\int_V \rho(\dot{u}\dot{u} + \dot{v}\dot{v} + \dot{w}\dot{w})dV \tag{4.52}$$

where ρ is the material density. Substituting Eq. (4.4) in Eq. (4.52) yields

$$\begin{aligned}T = \frac{1}{2}\int_0^a\int_0^b\Bigg\{ & I_0\left[\left(\frac{\partial u_0}{\partial t}\right)^2 + \left(\frac{\partial v_0}{\partial t}\right)^2 + \left(\frac{\partial w_0}{\partial t}\right)^2\right] + 2I_1\left(\frac{\partial u_0}{\partial t}\frac{\partial \psi_x}{\partial t} + \frac{\partial v_0}{\partial t}\frac{\partial \psi_y}{\partial t}\right) \\ & + I_2\left[\left(\frac{\partial \psi_x}{\partial t}\right)^2 + \left(\frac{\partial \psi_y}{\partial t}\right)^2\right]\Bigg\}dxdy\end{aligned} \tag{4.53}$$

where I_0, I_1 and I_2 are the normal, coupled normal-rotary, and rotary inertia coefficients which are given by

$$(I_0, I_1, I_2) = \int_{-\frac{h}{2}}^{\frac{h}{2}}(1, z, z^2)\rho dz = \sum_{k=1}^{n}\int_{z_{k-1}}^{z_k}(1, z, z^2)\rho^k dz \tag{4.54}$$

where ρ^k is the material density of the kth layer.

Due to the different material densities of the three parts of the two-way FRP slab (Figure 4.7), the inertia coefficients will be calculated individually for three different parts. For outer shell segment (I), the inertia coefficients are obtained as

$$(I_0^I, I_1^I, I_2^I) = \sum_{k=1}^{n_I}\int_{z_{k-1}}^{z_k}(1, z, z^2)\rho_I^k dz \tag{4.55}$$

For circular cell (II), averaging over the width of the representative element is required when computing the inertia coefficients. By considering the top (Figure 4.10)

and bottom (Figure 4.11) circular cell segments separately and then adding their contributions together, the inertia coefficients for circular cell (II) are obtained as

$$(I_0^{II}, I_1^{II}, I_2^{II}) = \frac{2}{b_s}\sum_{k=1}^{n_{II}}\int_{r_{k-1}}^{r_k}\int_0^{2\pi}(1, r\cos\phi, r^2\cos^2\phi + H^2)\rho_{II}^k r dr d\phi \tag{4.56}$$

Note that the relationships between the shell local coordinate system (x, s, r) of circular cell segment and global coordinate system (x, y, z) are shown in Eqs. (4.26) and (4.34) for top and bottom circular cells, respectively.

As described in section 4.3.2, the PFR core segment (III) can be subdivided into a number of layers (Figure 4.12). Averaging over the width of the representative element is again required when computing the inertia coefficients for PFR core segment (III) due to the different width (b_k) of subdivided layers. Using the coordinate systems shown in Figure 4.12, these inertia coefficients are given by

$$(I_0^{III}, I_1^{III}, I_2^{III}) = \frac{1}{b_s}\sum_{k=1}^{n_{III}} b_k \int_{z_{k-1}}^{z_k}(1, z, z^2)\rho_{III}^k dz \tag{4.57}$$

The normal, coupled normal-rotary, and rotary inertia coefficients for the transformed plate therefore can be obtained by adding the contributions of the outer shell, circular cell and PFR core together as

$$\begin{aligned} I_0 &= I_0^I + I_0^{II} + I_0^{III} \\ I_1 &= I_1^I + I_1^{II} + I_1^{III} \\ I_2 &= I_2^I + I_2^{II} + I_2^{III} \end{aligned} \tag{4.58}$$

Substituting Eqs. (4.51) and (4.53) into Eq. (4.47), applying the Hamilton's principle Eq. (4.46), integrating by parts both with respect to time t and spatial coordinates (x, y, z), and setting the coefficients of the virtual displacements $(\delta u_0, \delta v_0, \delta w_0, \delta\psi_x, \delta\psi_y)$ to zero gives the following Euler-Lagrange equations of the FSDT

$$\delta u_0: \quad \frac{\partial N_x}{\partial x} + \frac{\partial N_{xy}}{\partial y} = I_0\frac{\partial^2 u_0}{\partial t^2} + I_1\frac{\partial^2\psi_x}{\partial t^2} \tag{4.59a}$$

$$\delta v_0: \quad \frac{\partial N_{xy}}{\partial x} + \frac{\partial N_y}{\partial y} = I_0\frac{\partial^2 v_0}{\partial t^2} + I_1\frac{\partial^2\psi_y}{\partial t^2} \tag{4.59b}$$

$$\delta w_0: \quad \frac{\partial Q_x}{\partial x}+\frac{\partial Q_y}{\partial y}+q=I_0\frac{\partial^2 w_0}{\partial t^2} \tag{4.59c}$$

$$\delta \psi_x: \quad \frac{\partial M_x}{\partial x}+\frac{\partial M_{xy}}{\partial y}-Q_x=I_2\frac{\partial^2 \psi_x}{\partial t^2}+I_1\frac{\partial^2 u_0}{\partial t^2} \tag{4.59d}$$

$$\delta \psi_y: \quad \frac{\partial M_{xy}}{\partial x}+\frac{\partial M_y}{\partial y}-Q_y=I_2\frac{\partial^2 \psi_y}{\partial t^2}+I_1\frac{\partial^2 v_0}{\partial t^2} \tag{4.59e}$$

and Eqs. (4.59) are subject to the following boundary conditions

$$x=0 \text{ and } x=a: \quad N_x=\widetilde{N}_x \text{ or } u_0=\widetilde{u}_0$$

$$y=0 \text{ and } y=b: \quad N_y=\widetilde{N}_y \text{ or } v_0=\widetilde{v}_0$$

$$x=0 \text{ and } x=a: \quad N_{xy}=\widetilde{N}_{xy} \text{ or } v_0=\widetilde{v}_0$$

$$y=0 \text{ and } y=b: \quad N_{xy}=\widetilde{N}_{xy} \text{ or } u_0=\widetilde{u}_0$$

$$x=0 \text{ and } x=a: \quad M_x=\widetilde{M}_x \text{ or } \psi_x=\widetilde{\psi}_x$$

$$y=0 \text{ and } y=b: \quad M_y=\widetilde{M}_y \text{ or } \psi_y=\widetilde{\psi}_y$$

$$x=0 \text{ and } x=a: \quad M_{xy}=\widetilde{M}_{xy} \text{ or } \psi_y=\widetilde{\psi}_y$$

$$y=0 \text{ and } y=b: \quad M_{xy}=\widetilde{M}_{xy} \text{ or } \psi_x=\widetilde{\psi}_x$$

$$x=0 \text{ and } x=a: \quad Q_x=\widetilde{Q}_x \text{ or } w_0=\widetilde{w}_0$$

$$y=0 \text{ and } y=b: \quad Q_y=\widetilde{Q}_y \text{ or } w_0=\widetilde{w}_0$$

where "~" denotes the known value.

Substituting Eqs. (4.44a~c) into Eqs. (4.59a~e) and using Eq. (4.6), the governing equations can be obtained in matrix form in terms of the displacement functions as

$$\begin{bmatrix} L_{11} & L_{12} & 0 & L_{14} & L_{15} \\ L_{12} & L_{22} & 0 & L_{24} & L_{25} \\ 0 & 0 & L_{33} & L_{34} & L_{35} \\ L_{14} & L_{24} & L_{34} & L_{44} & L_{45} \\ L_{15} & L_{25} & L_{35} & L_{45} & L_{55} \end{bmatrix} \begin{Bmatrix} u_0 \\ v_0 \\ w_0 \\ \psi_x \\ \psi_y \end{Bmatrix} = \begin{Bmatrix} 0 \\ 0 \\ q \\ 0 \\ 0 \end{Bmatrix} \tag{4.60}$$

where the differential operators are given as

$$
\begin{aligned}
L_{11} &= A_{11}d_{11} + 2A_{16}d_{12} + A_{66}d_{22} - I_0 d_{tt} \\
L_{12} &= A_{16}d_{11} + (A_{12} + A_{66})d_{12} + A_{26}d_{22} \\
L_{14} &= B_{11}d_{11} + 2B_{16}d_{12} + B_{66}d_{22} - I_1 d_{tt} \\
L_{15} &= B_{16}d_{11} + (B_{12} + B_{66})d_{12} + B_{26}d_{22} \\
L_{22} &= A_{66}d_{11} + 2A_{26}d_{12} + A_{22}d_{22} - I_0 d_{tt} \\
L_{24} &= B_{16}d_{11} + (B_{12} + B_{66})d_{12} + B_{26}d_{22} \\
L_{25} &= B_{66}d_{11} + 2B_{26}d_{12} + B_{22}d_{22} - I_1 d_{tt} \\
L_{33} &= -KA_{55}d_{11} - 2KA_{45}d_{12} - KA_{44}d_{22} - I_0 d_{tt} \\
L_{34} &= KA_{55}d_1 - KA_{45}d_2\,, \quad L_{35} = -KA_{45}d_1 - KA_{44}d_2 \\
L_{44} &= D_{11}d_{11} + 2D_{16}d_{12} + D_{66}d_{22} - A_{55} - I_2 d_{tt} \\
L_{45} &= D_{16}d_{11} + (D_{12} + D_{66})d_{12} + D_{26}d_{22} - A_{45} \\
L_{55} &= D_{66}d_{11} + 2D_{26}d_{12} + D_{22}d_{22} - A_{44} - I_2 d_{tt}
\end{aligned}
$$

where $d_{ij} = (\partial^2 / \partial x_i \partial x_j)$ $(x_1 = x$ and $x_2 = y)$, and $d_{tt} = (\partial^2 / \partial t^2)$.

Eqs. (4.60) describe the governing equations of the equivalent transformed plate based on the first-order shear deformation theory. It incorporates ten boundary conditions that include both natural and essential boundary conditions. By developing this simplified transformed plate approach, the problem of the 3D two-way FRP slab (Figure 4.13) has been reduced to a 2D equivalent transformed anisotropic plate (Figure 4.14). Standard analytical and numerical methods can be used to analyse this 2D plate model. In the following section, a Ritz solution and a 2D finite element solution of the equivalent transformed plate are developed and compared with 3D FEA results (discussed in detail in Chapter 5).

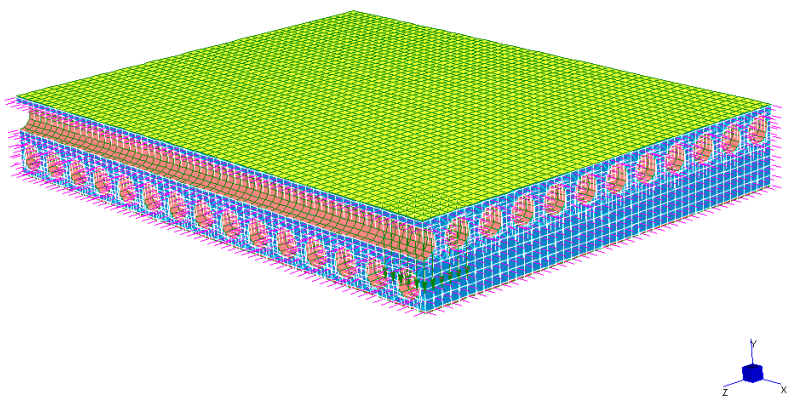

Figure 4.13 3D two-way FRP slab FE model

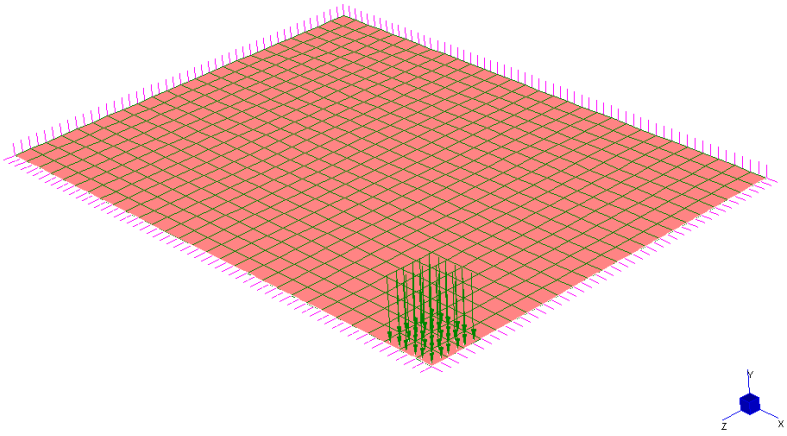

Figure 4.14 2D equivalent transformed plate FE model

4.4 Verification of the Simplified Approach

There are different methods available to solve the developed governing equations of this two-way FRP slab system, such as the Ritz approach, or incorporation with existing FEA software package. The advantages of using Ritz approach including ease of programming and "stand-alone" format (does not require FEA software package). However the Ritz approach may produce considerable errors for a plate model subjected to a load other than uniformly distributed load, and for cases where the displacement functions vary significantly from sinusoidal functions that are consistent with boundary conditions. In contrast 2D FEA approach can accommodate a wide range of loading conditions, boundary conditions and displacement functions, however, this requires FEA software with ability to use user-defined stiffness matrices.

In the remaining part of this chapter, the simplified transformed plate approach is verified by comparing both a Ritz solution and 2D finite element solution of the equivalent transformed plate developed with 3D FEA results. The following transformed stiffness properties were used in this study.

$$\left[A_{ij}\right]=\begin{bmatrix}446044 & 112833 & 0\\ 112833 & 446184 & 0\\ 0 & 0 & 161059\end{bmatrix} MPa\cdot mm\,,\quad (i\,,\ j=1,2,6) \tag{4.61a}$$

$$[A_{ij}] = \begin{bmatrix} 135160 & 0 \\ 0 & 135160 \end{bmatrix} MPa \cdot mm, \quad (i, j = 4, 5) \tag{4.61b}$$

$$[B_{ij}] = \begin{bmatrix} 4.21075\times10^{6} & 1076233 & -1541.74 \\ -678365 & -1.48399\times10^{6} & -1541.74 \\ -1541.74 & -1541.74 & 0 \end{bmatrix} MPa \cdot mm^{2}, \quad (i, j = 1, 2, 6) \tag{4.61c}$$

$$[D_{ij}] = \begin{bmatrix} 1.00895\times10^{9} & 2.16796\times10^{8} & -18646.5 \\ 2.16796\times10^{8} & 1.01336\times10^{9} & 18646.5 \\ -18646.5 & 18646.5 & 2.79346\times10^{8} \end{bmatrix} MPa \cdot mm^{3}, \quad (i, j = 1, 2, 6) \tag{4.61d}$$

The material properties for the different parts of the slab used to generate these matrices are described in Section 5.2.4.

4.4.1 Ritz Solution of Equivalent Transformed Plate

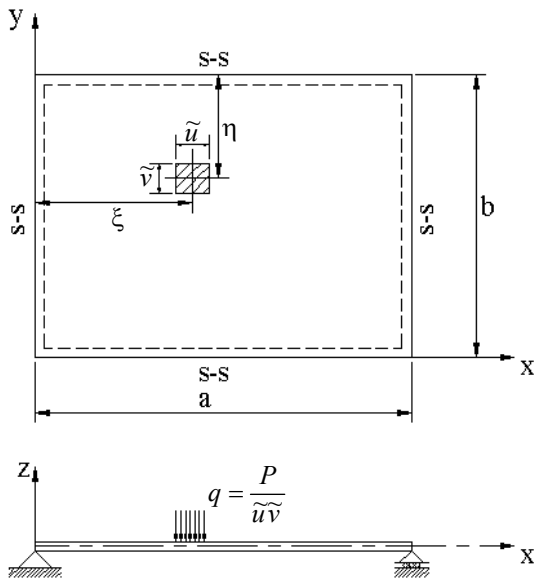

Figure 4.15 Geometry and loads of the transformed plate with all edges simply supported

In this section, the governing equations of the equivalent transformed plate are solved using the Ritz method. Figure 4.15 shows the dimensions, coordinate system and boundary conditions of the transformed plate. Since the bending-extensional coupling stiffness matrix (i.e., [*B*]) is insignificant for this case, the extension and

bending problems are separable. In the absence of bending-extensional coupling, the relation between moments and curvature from Eq. (4.44b) can be written as

$$\begin{Bmatrix} M_x \\ M_y \\ M_{xy} \end{Bmatrix} = \begin{bmatrix} D_{11} & D_{12} & D_{16} \\ D_{12} & D_{22} & D_{26} \\ D_{16} & D_{26} & D_{66} \end{bmatrix} \begin{Bmatrix} \kappa_x \\ \kappa_y \\ \kappa_{xy} \end{Bmatrix} \tag{4.62}$$

The Ritz solution can be obtained by considering the total potential energy of the system (Eq. 4.48), in which the kinetic energy T is eliminated. The bending strain energy of the transformed plate is given by

$$\begin{aligned} U = \frac{1}{2}\int_0^a \int_0^b \Bigg[& D_{11}\left(\frac{\partial \psi_x}{\partial x}\right)^2 + 2D_{12}\frac{\partial \psi_x}{\partial x}\frac{\partial \psi_y}{\partial y} + D_{22}\left(\frac{\partial \psi_y}{\partial y}\right)^2 \\ & + 2\left(D_{16}\frac{\partial \psi_x}{\partial x} + D_{26}\frac{\partial \psi_y}{\partial y}\right)\left(\frac{\partial \psi_x}{\partial y} + \frac{\partial \psi_y}{\partial x}\right) + D_{66}\left(\frac{\partial \psi_x}{\partial y} + \frac{\partial \psi_y}{\partial x}\right)^2 \\ & + KA_{44}\left(\frac{\partial w_0}{\partial y} + \psi_y\right)^2 + 2KA_{45}\left(\frac{\partial w_0}{\partial y} + \psi_y\right)\left(\frac{\partial w_0}{\partial x} + \psi_x\right) \\ & + KA_{55}\left(\frac{\partial w_0}{\partial x} + \psi_x\right)^2 \Bigg] dxdy \end{aligned} \tag{4.63}$$

Considering a single load P uniformly distributed over the area of the rectangle shown in Figure 4.15, the potential energy for this case is give as

$$V = \int_{\xi-\frac{\tilde{u}}{2}}^{\xi+\frac{\tilde{u}}{2}} \int_{\eta-\frac{\tilde{v}}{2}}^{\eta+\frac{\tilde{v}}{2}} \frac{P}{\tilde{u}\tilde{v}} w_0 dxdy \tag{4.64}$$

where $\tilde{u}, \tilde{v}$ are the length of the rectangular uniformly distributed area in x- and y-direction respectively; and ξ, η are the coordinates of the centre of the rectangular area where the load is applied (see Figure 4.15). In particular, if $\xi = a/2$, $\eta = b/2$, $\tilde{u} = a$ and $\tilde{v} = b$, then the potential energy for a plate under uniformly distributed load is obtained. Furthermore, by letting $\tilde{u}$ and $\tilde{v}$ tend to zero, another interesting case of a point load at any given point $x = \xi$, $y = \eta$ of the plate is derived. The boundary conditions for the simply supported plate are given by

$$\begin{aligned} & \psi_x(x, 0) = \psi_x(x, b) = 0, \quad \psi_y(0, y) = \psi_y(a, y) = 0 \\ & w_0(x, 0) = w_0(x, b) = w_0(0, y) = w_0(a, y) = 0 \end{aligned} \tag{4.65a}$$

$$M_x(0, y) = M_x(a, y) = 0, \quad M_y(x, 0) = M_y(x, b) = 0 \tag{4.65b}$$

The following displacement fields with double trigonometric series satisfies the essential boundary condition (4.65a).

$$w_0(x, y) = \sum_{m=1}^{\infty}\sum_{n=1}^{\infty} W_{mn} \sin\alpha x \sin\beta y \tag{4.66a}$$

$$\psi_x(x, y) = \sum_{m=1}^{\infty}\sum_{n=1}^{\infty} X_{mn} \cos\alpha x \sin\beta y \tag{4.66b}$$

$$\psi_y(x, y) = \sum_{m=1}^{\infty}\sum_{n=1}^{\infty} Y_{mn} \sin\alpha x \cos\beta y \tag{4.66c}$$

where $\alpha = \dfrac{m\pi}{a}$ and $\beta = \dfrac{n\pi}{b}$. Substitution of Eqs. (4.63), (4.64) and (4.66a~c) into Eq. (4.48) and using the following formulas (Timoshenko and Woinowsky-Krieger 1959)

$$\int_0^a\int_0^b \sin^2\frac{m\pi x}{a}\sin^2\frac{n\pi y}{b}dxdy = \int_0^a\int_0^b \cos^2\frac{m\pi x}{a}\cos^2\frac{n\pi y}{b}dxdy = \frac{ab}{4} \tag{4.67a}$$

$$\int_0^a\int_0^b \sin^2\frac{m\pi x}{a}\cos^2\frac{n\pi y}{b}dxdy = \int_0^a\int_0^b \cos^2\frac{m\pi x}{a}\sin^2\frac{n\pi y}{b}dxdy = \frac{ab}{4} \tag{4.67b}$$

$$\int_0^a\int_0^b \sin\frac{m\pi x}{a}\cos\frac{m\pi x}{a}\sin\frac{n\pi y}{b}\cos\frac{n\pi y}{b}dxdy = 0 \tag{4.67c}$$

$$\begin{aligned}&\int_{\xi-\frac{\tilde{u}}{2}}^{\xi+\frac{\tilde{u}}{2}}\int_{\eta-\frac{\tilde{v}}{2}}^{\eta+\frac{\tilde{v}}{2}}\sin\frac{m\pi x}{a}\sin\frac{n\pi y}{b}dxdy\\ &= \begin{cases}\dfrac{4ab}{\pi^2 mn}\sin\dfrac{m\pi\xi}{a}\sin\dfrac{n\pi\eta}{b}\sin\dfrac{m\pi\tilde{u}}{2a}\sin\dfrac{n\pi\tilde{v}}{2b}, & (m, n = 1, 3, 5,\ldots)\\ 0, & (m, n = 2, 4, 6,\ldots)\end{cases}\end{aligned} \tag{4.67d}$$

the total energy Π for the plate bending problem then can be written as

$$\begin{aligned}\Pi &= U + V\\ &= \frac{ab}{8}\sum_{m=1}^{\infty}\sum_{n=1}^{\infty}\Big[(D_{11}\alpha^2 + D_{66}\beta^2 + KA_{55})X_{mn}^2 + 2(D_{12}\alpha\beta + D_{66}\alpha\beta)X_{mn}Y_{mn}\\ &\qquad + (D_{22}\beta^2 + D_{66}\alpha^2 + KA_{44})Y_{mn}^2 + (KA_{44}\beta^2 + KA_{55}\alpha^2)W_{mn}^2\\ &\qquad + 2KA_{44}\beta W_{mn}Y_{mn} + 2KA_{55}\alpha W_{mn}X_{mn}\Big]\\ &\quad - \sum_{m=1}^{\infty}\sum_{n=1}^{\infty}\frac{4Pab}{\pi^2 mn\tilde{u}\tilde{v}}\sin\frac{m\pi\xi}{a}\sin\frac{n\pi\eta}{b}\sin\frac{m\pi\tilde{u}}{2a}\sin\frac{n\pi\eta}{2b}W_{mn}\end{aligned} \tag{4.68}$$

where m and n are both odd integers. If the system is in equilibrium, its total energy is a minimum, which results in the following equations

$$\delta \Pi = \frac{\partial \Pi}{\partial W_{mn}} \delta W_{mn} + \frac{\partial \Pi}{\partial X_{mn}} \delta X_{mn} + \frac{\partial \Pi}{\partial Y_{mn}} \delta Y_{mn} = 0 \tag{4.69}$$

Since the variations $\delta W_{mn}, \delta X_{mn}, \delta Y_{mn}$ are arbitrary and independent, it follows that

$$\frac{\partial \Pi}{\partial W_{mn}} = 0, \quad \frac{\partial \Pi}{\partial X_{mn}} = 0, \quad \frac{\partial \Pi}{\partial Y_{mn}} = 0 \tag{4.70}$$

Thus, the coefficients (W_{mn}, X_{mn}, Y_{mn}) can be calculated from the following equations

$$\begin{bmatrix} \hat{s}_{33} & \hat{s}_{34} & \hat{s}_{35} \\ \hat{s}_{34} & \hat{s}_{44} & \hat{s}_{45} \\ \hat{s}_{35} & \hat{s}_{45} & \hat{s}_{55} \end{bmatrix} \begin{Bmatrix} W_{mn} \\ X_{mn} \\ Y_{mn} \end{Bmatrix} = \begin{Bmatrix} F_{mn} \\ 0 \\ 0 \end{Bmatrix} \tag{4.71}$$

where

$$\begin{aligned} &\hat{s}_{33} = K(A_{44}\beta^2 + A_{55}\alpha^2), \quad \hat{s}_{34} = KA_{55}\alpha, \quad \hat{s}_{35} = KA_{44}\beta \\ &\hat{s}_{44} = (D_{11}\alpha^2 + D_{66}\beta^2 + KA_{55}), \quad \hat{s}_{45} = (D_{12} + D_{66})\alpha\beta \\ &\hat{s}_{55} = (D_{22}\beta^2 + D_{66}\alpha^2 + KA_{44}) \end{aligned} \tag{4.72a}$$

and

$$F_{mn} = \frac{16P}{\pi^2 mn\tilde{u}\tilde{v}} \sin\frac{m\pi\xi}{a} \sin\frac{n\pi\eta}{b} \sin\frac{m\pi\tilde{u}}{2a} \sin\frac{n\pi\tilde{v}}{2b}, \quad (m, n = 1, 3, 5, \ldots) \tag{4.72b}$$

By solving the Eq. (4.72), the quantities of these coefficients are obtained as

$$\begin{aligned} W_{mn} &= \frac{F_{mn}(\hat{s}_{45}^2 - \hat{s}_{44}\hat{s}_{55})}{\Delta} \\ X_{mn} &= \frac{F_{mn}(\hat{s}_{34}\hat{s}_{55} - \hat{s}_{35}\hat{s}_{45})}{\Delta} \\ Y_{mn} &= \frac{F_{mn}(\hat{s}_{35}\hat{s}_{44} - \hat{s}_{34}\hat{s}_{45})}{\Delta} \end{aligned} \tag{4.73}$$

where

$$\Delta = \hat{s}_{35}^2\hat{s}_{44} - 2\hat{s}_{34}\hat{s}_{35}\hat{s}_{45} + \hat{s}_{34}^2\hat{s}_{55} + \hat{s}_{33}(\hat{s}_{45}^2 - \hat{s}_{44}\hat{s}_{55}) \tag{4.74}$$

By using these basic functions in the Ritz formulation, a Ritz solution for the bending problem of the transformed plate with all edges simply supported is obtained for the case of rectangular patch loading. This solution can also be extended for the case of a uniformly distributed load and a point load as mentioned earlier.

Three load cases were considered in this part of the verification study: a uniformly distributed load, a central point load and a central rectangular patch load. The magnitude of the uniformly distributed load and the central rectangular patch load are 0.0401 N/mm^2 and 3.086N /mm^2 (over the area of 180×180 mm^2) respectively, which is equivalent to 100 kN on the complete slab model. The point load is chosen as P = 100 kN at $\xi = 0.5a$ and $\eta = 0.5b$.

The figures used to verify the Ritz solution are normalized with respect to the vertical central displacement of the slab obtained from the detailed 3D finite element analysis (refer Chapter 5). In order to eliminate the local deformation underneath the applied load, all deflections were extracted from the bottom surface of the 3D finite element model. The software package – Mathematica (version 3.0) was used to conduct all parameter and numerical calculations.

In dealing with a series solution, the convergence of the solution for the different cases of loading was investigated. Figure 4.16 shows the convergence of the rectangular patch loaded plate, and the convergence of the uniform distributed and central point load are depicted in Figures 4.17 and 4.18. The results show that the solution converged when using $m_{\max} = n_{\max} = 7$ for uniformly distributed load, $m_{\max} = n_{\max} = 9$ for rectangular patch load and $m_{\max} = n_{\max} = 11$ for central point load, respectively.

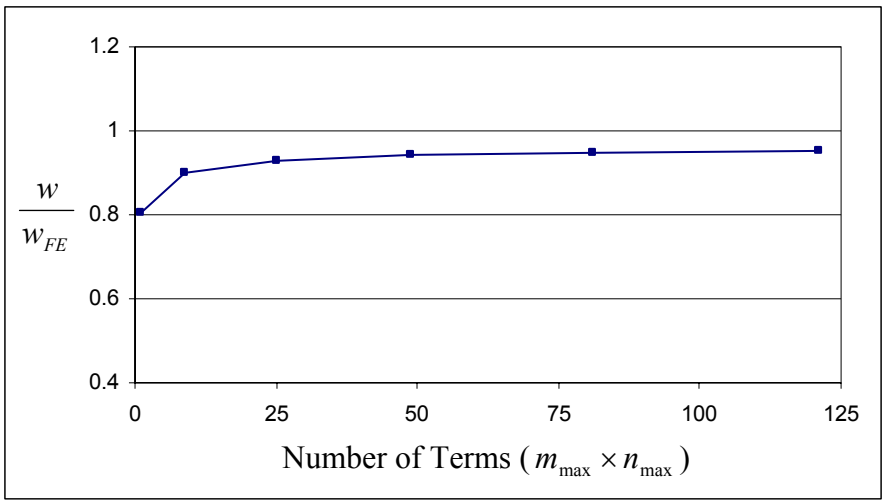

Figure 4.16 Convergence of Ritz series solution for a central rectangular patch load

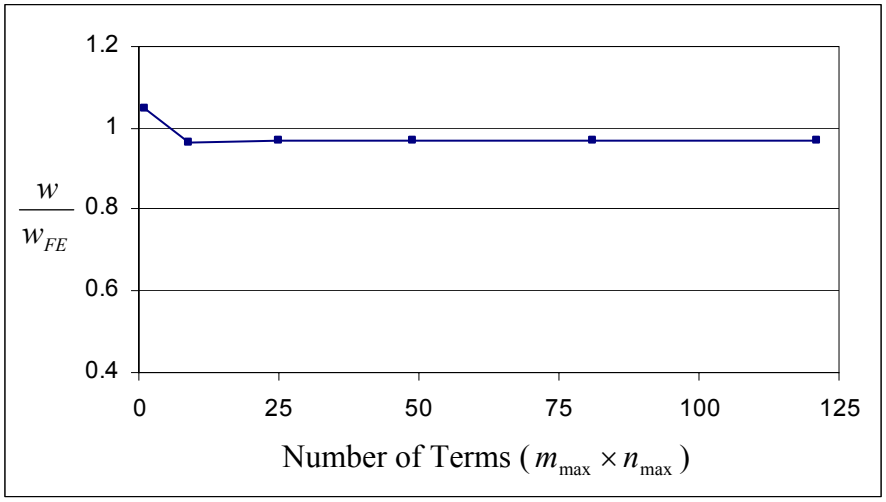

Figure 4.17 Convergence of a Ritz series solution for a uniformly distributed load

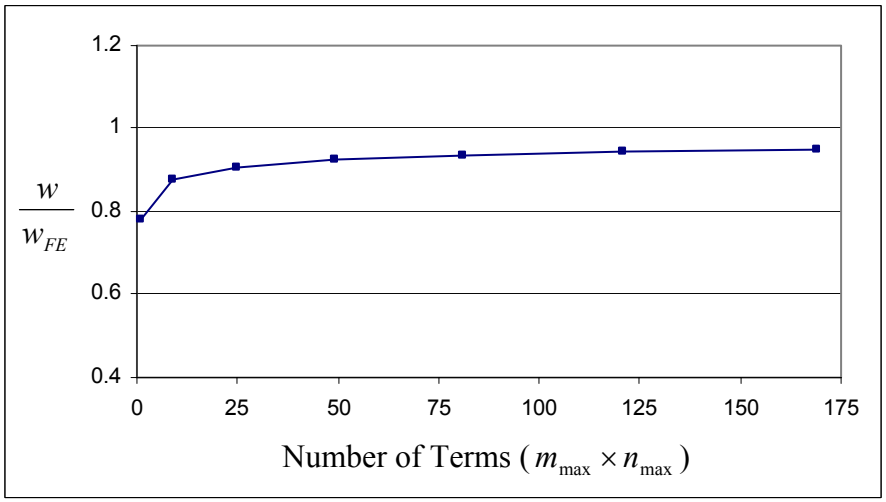

Figure 4.18 Convergence of Ritz series solution
for a point load at (0.5*a*, 0.5*b*)

Figure 4.19 shows the convergence plots of the three loading cases. As expected the Ritz solution for the uniformly distributed load converges faster than both patch and point loads.

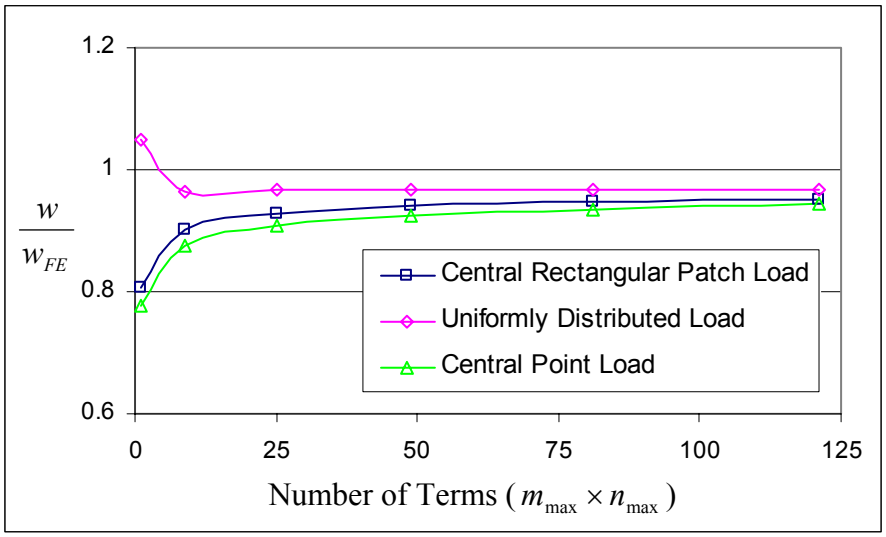

Figure 4.19 Convergence of Ritz series solution for three loading cases

Figures 4.20 and 4.21 show the plots of the vertical displacements along the *x*- and *y*-axes for the Ritz solution and 3D FEA result (including the top and bottom surfaces) under uniformly distributed loads. In these figures, the Ritz solution agrees very well with the finite element results for the both top and bottom surfaces with only about 3.4% difference.

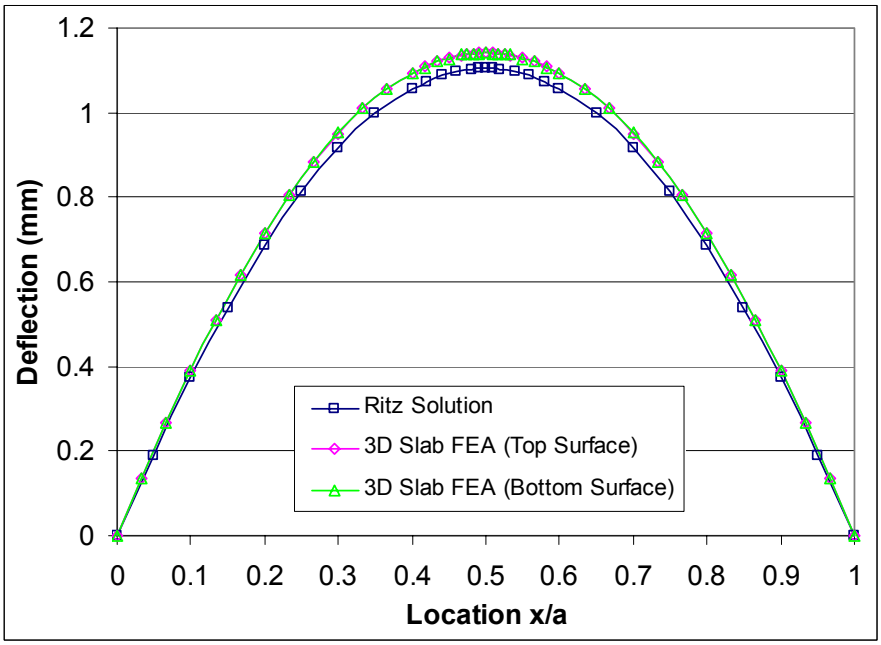

Figure 4.20 Vertical displacement for a uniformly distributed load along *x* at $y = 0.5b$ for Ritz solution ($m_{\max} = n_{\max} = 7$) and 3D FEA results

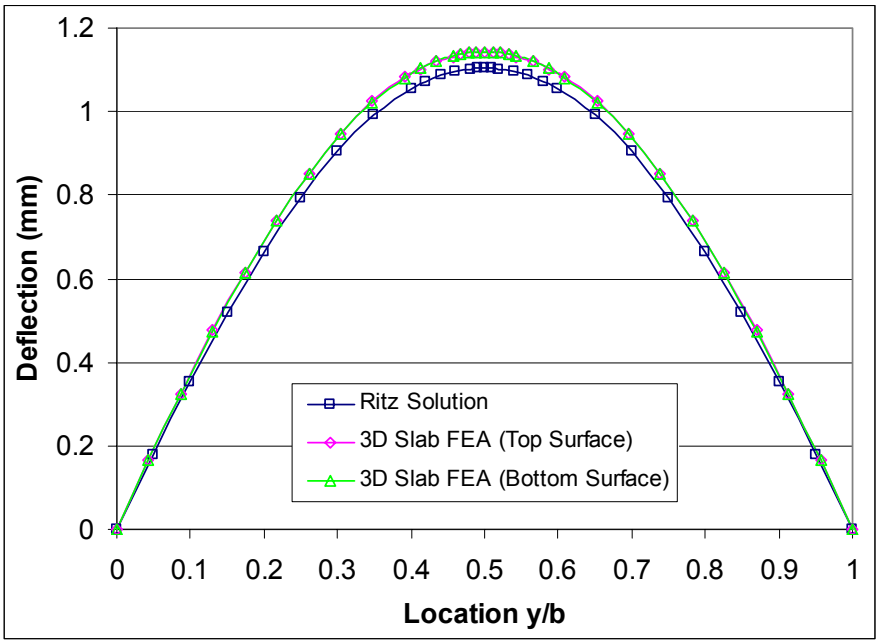

Figure 4.21 Vertical displacement for a uniformly distributed load along y at $x = 0.5a$ for Ritzl solution ($m_{\max} = n_{\max} = 7$) and 3D FEA results

The plots of the vertical displacement along x- and y-axes for the Ritz solution and 3D FEA result for a central rectangular patch load and central point load at ($0.5a$, $0.5b$) are shown in Figures 4.22 ~ 4.25.

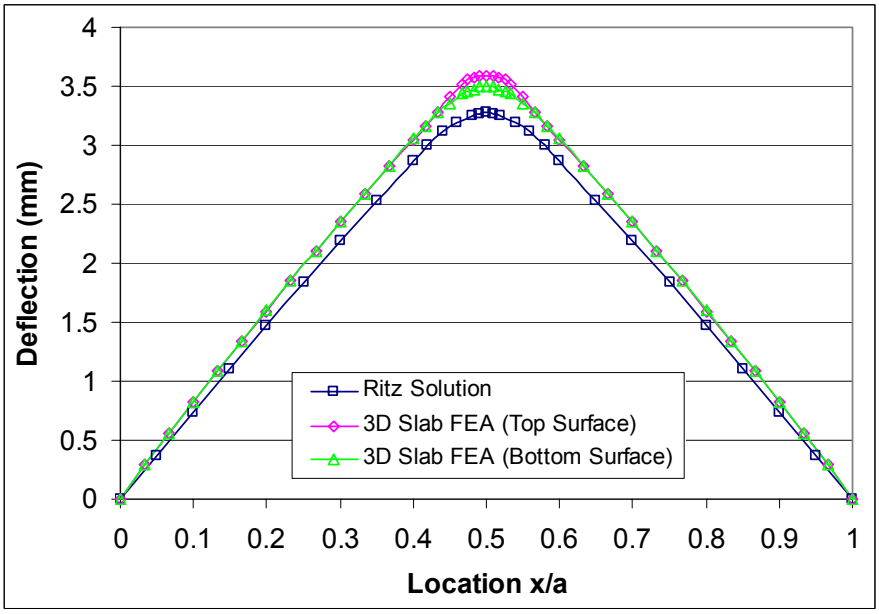

Figure 4.22 Vertical displacement for a central rectangular patch load along x at $y = 0.5b$ for Ritz solution ($m_{\max} = n_{\max} = 9$) and 3D FEA results

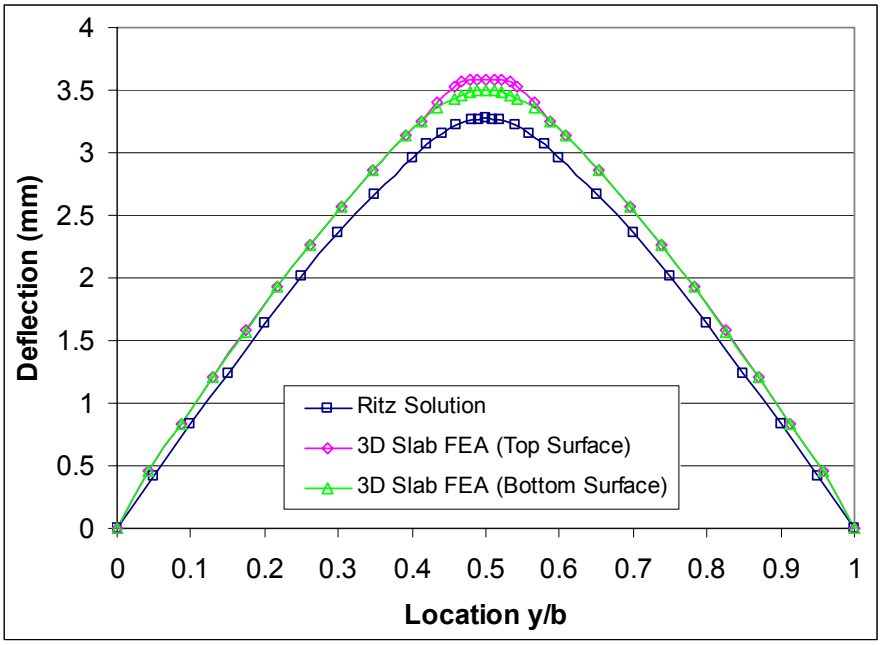

Figure 4.23 Vertical displacement for a central rectangular patch load along y at $x = 0.5a$ for Ritz solution ($m_{\max} = n_{\max} = 9$) and 3D FEA results

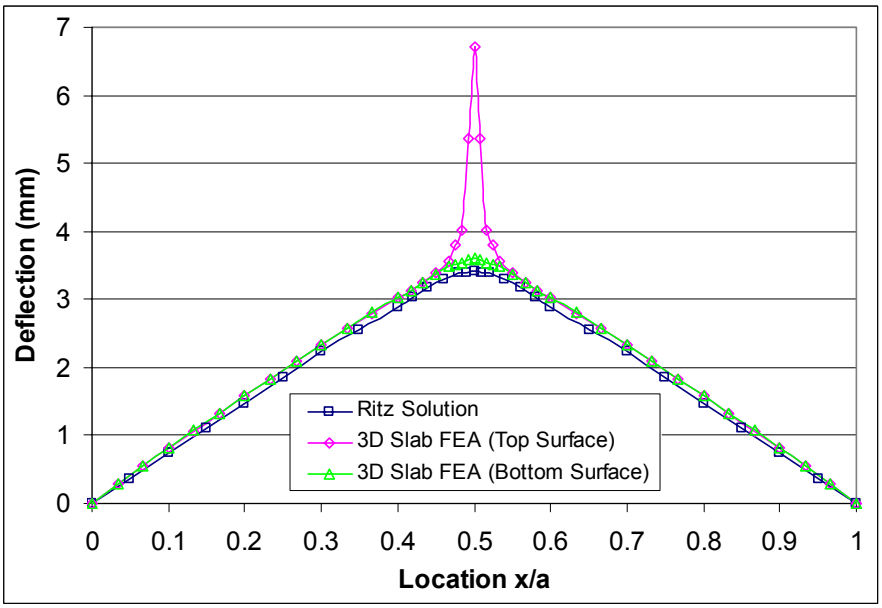

Figure 4.24 Vertical displacement for a point load at (0.5a, 0.5b) along x at $y = 0.5b$ for Ritz solution ($m_{\max} = n_{\max} = 11$) and 3D FEA results

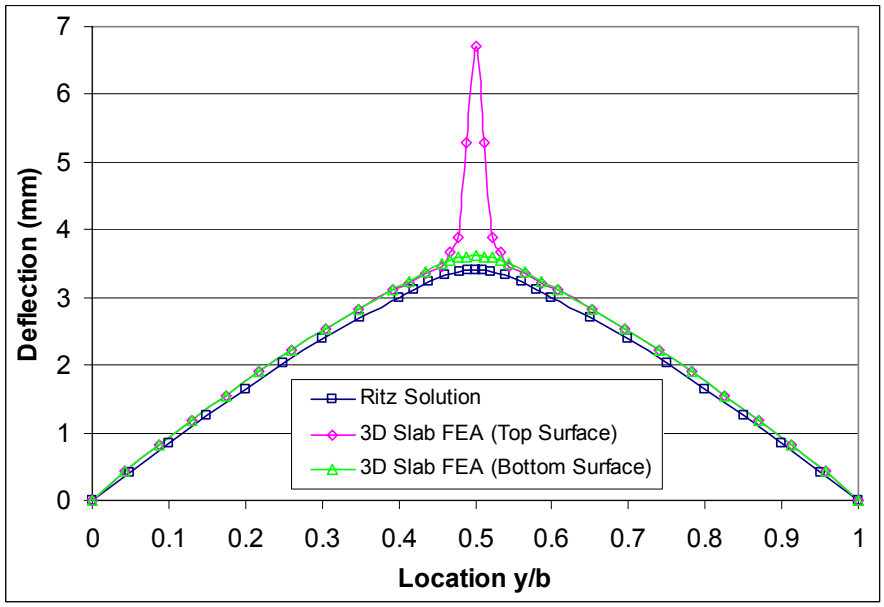

Figure 4.25 Vertical displacement for a point load at (0.5a, 0.5b) along y at $x = 0.5a$ for Ritz solution ($m_{\max} = n_{\max} = 11$) and 3D FEA results

In these load cases, a good correlation and accuracy is clearly observed again when comparing with the deflection at the bottom surface of the 3D finite element model. The discrepancy between the Ritz solution and the 3D FEA result is about 5.8% for the central rectangular patch load case and 6.7% for the central point load case. However, the top surface exhibits significant local deformations which are not captured by the analytical (Ritz) solution. Under the patch and point loads, the analytical (Ritz) solution for the equivalent transformed plate shows no local effects, whereas the detailed 3D finite element model exhibits local deformation under these loads, particularly for the point load case.

4.4.2 Finite Element Solution of Equivalent Transformed Plate

Alternatively, the equivalent transformed plate can be also analysed by incorporating the stiffness matrices into a standard 2D finite element model. In this section, the 2D finite element analysis of this plate model is conducted using the commercial finite element package – Strand 7, and the results are compared with the 3D slab FEA results.

The 2D finite element model of the equivalent transformed plate is shown in Figure 4.14. The generated transformed stiffness matrices (Eqs. 4.63) were input into "User Defined Plate Element Property" of Strand 7 (refer G+D Computing 2000) to define the stiffness properties of the equivalent transformed plate. The density (ρ_{equiv}) and thickness (t_{equiv}) of the equivalent transformed plate was determined as follows:

$$\rho_{equiv} = \frac{\sum_{i=I}^{III} \rho_i v_i}{\sum_{i=I}^{III} v_i} \tag{4.77}$$

$$t_{equiv} = \frac{\sum_{i=I}^{III} \rho_i v_i}{\rho_{equiv}\, ab} \tag{4.78}$$

where ρ_I, ρ_{II} and ρ_{III} are the material densities of the outer shell (I), circular cell (II) and PFR core (III) respectively. Similarly, v_I, v_{II} and v_{III} are the total material volumes of the outer shell (I), circular cell (II) and PFR core (III) of the two-way FRP slab respectively. The symbols *a* and *b* represent the longitudinal and transverse spans of the actual slab determined in Chapter 3.

Three types of the boundary conditions were considered in this part of the verification study: all edges simply supported (SSSS), all edge clamped (CCCC), two opposite edges simply supported and the other two edges clamped (CCSS). The applied load was a central rectangular patch load with the magnitude of 3.086 N/mm^2 (over the area of 180×180 mm^2), which is equivalent to 100 kN on the complete slab model.

Figures 4.26 ~ 4.31 show the plots of the vertical displacements along the *x*- and *y*-axes for the 2D and 3D FEA results (including the top and bottom surfaces) with three different boundary conditions.

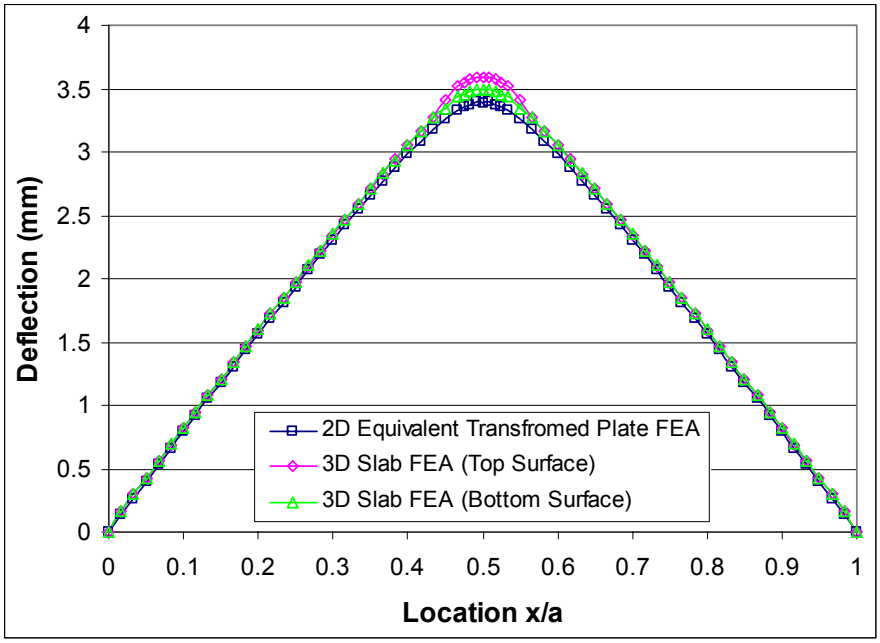

Figure 4.26 Vertical displacement for SSSS along x at $y = 0.5b$ for 2D and 3D FEA results

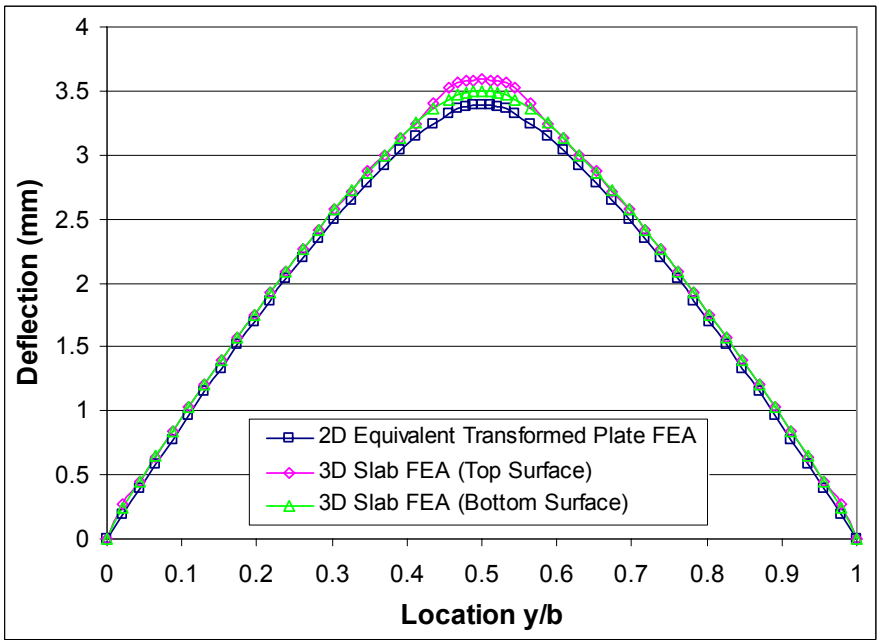

Figure 4.27 Vertical displacement for SSSS along y at $x = 0.5a$ for 2D and 3D FEA results

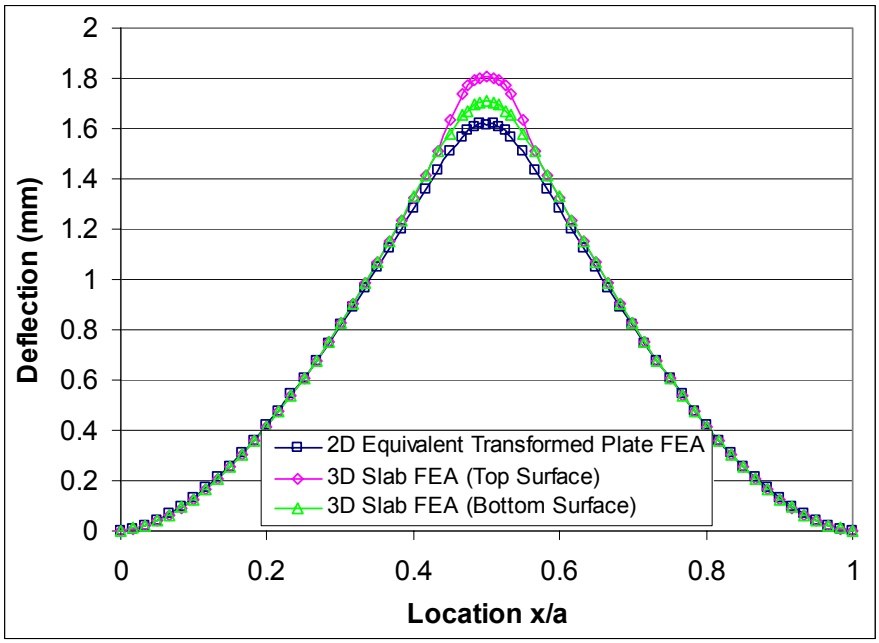

Figure 4.28 Vertical displacement for CCCC along x at $y = 0.5b$ for 2D and 3D FEA results

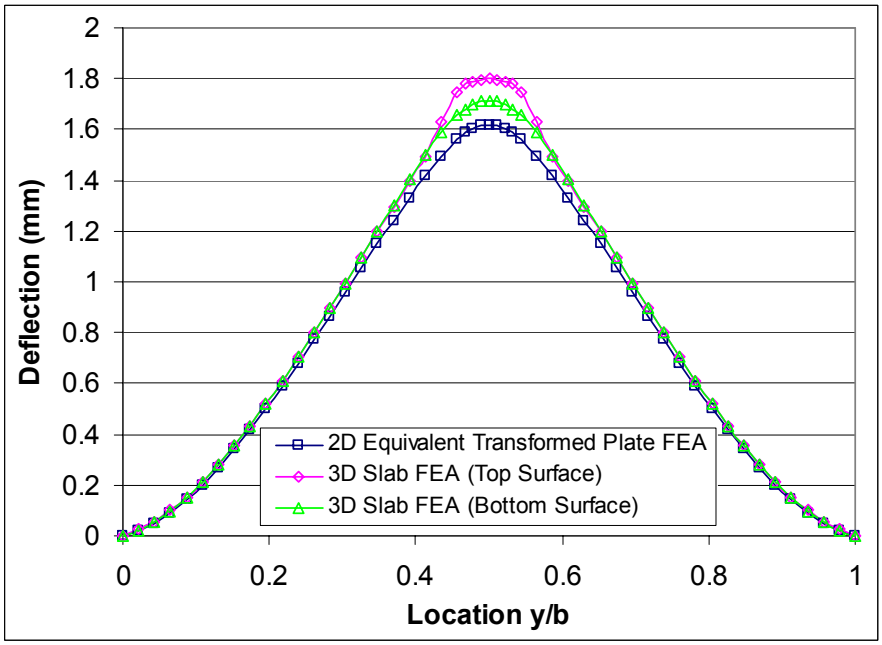

Figure 4.29 Vertical displacement for CCCC along y at $x = 0.5a$ for 2D and 3D FEA results

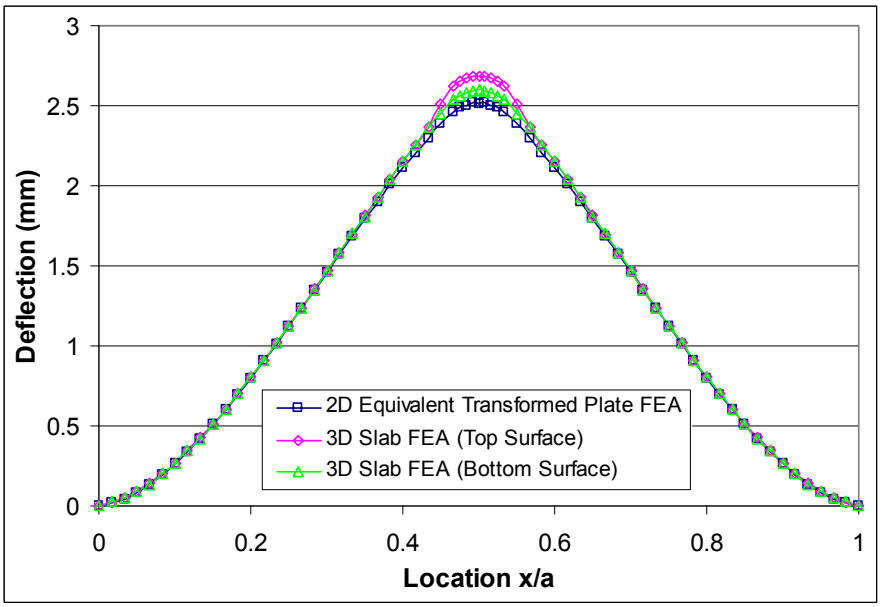

Figure 4.30 Vertical displacement for CCSS along x at $y = 0.5b$ for 2D and 3D FEA results

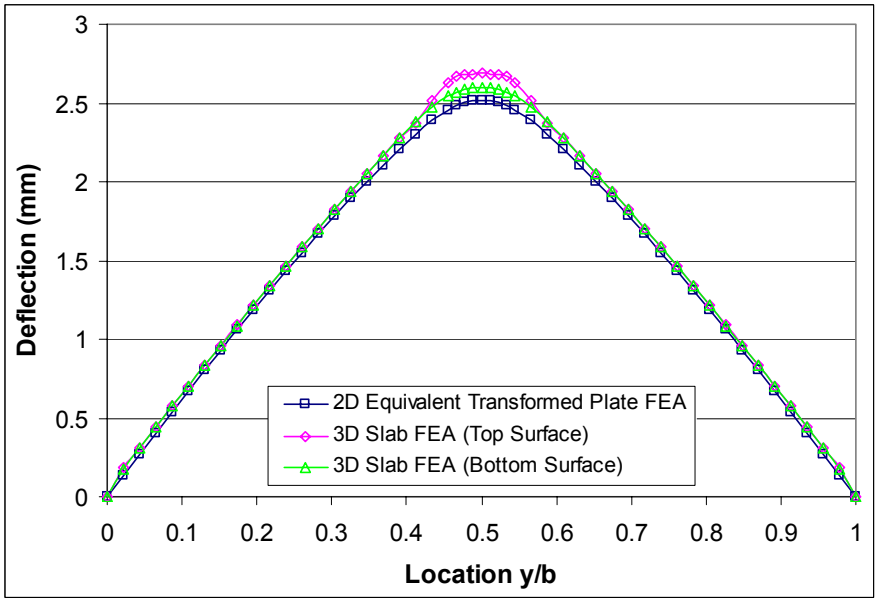

Figure 4.31 Vertical displacement for CCSS along y at $x = 0.5a$ for 2D and 3D FEA results

From these figures, an excellent agreement is clearly observed between the 2D equivalent transformed plate FEA result and the 3D slab FEA result at the bottom surface with the discrepancy of about 3.1%, 5.8% and 3.4% for the boundary condition of SSSS, CCCC and CCSS respectively. However, the local deformations shown at the top surface of the 3D finite element model for all three boundary conditions were not captured by the 2D plate model, particularly for the boundary condition of CCCC.

In this section, the 2D finite element solution of the equivalent transformed plate was compared with the 3D slab finite element model to further verify the simplified transformed plate approach. The results from these comparisons have indicated that the transformed plate formulations associated with 2D finite element solution is capable to produce relatively accurate results when compared with the 3D slab FEA results.

4.5 Conclusions

This chapter has focused on the development of a simplified transformed plate approach for the analysis of the two-way FRP slab. A brief review of various laminated plate theories was presented, and the appropriate laminated plate theory for the analysis of the proposed new composite slab structure was identified. The simplified analysis procedure is based on the first-order shear laminate deformation theory to develop the equivalent transformed anisotropic plate. This transformed plate is a homogeneous, orthotropic Mindlin plate that has the same global stiffness characteristics that relate the section forces and moments to the midsurface strains and curvatures of the two-way FRP slab system. Using this transformed plate approach, the governing equation of the equivalent transformed plate was derived, and the mathematical model of the two-way FRP composite slab was established. Consequently, both the Ritz solution associated with three loading cases and 2D finite element solution associated with three boundary conditions of the equivalent transformed plate were developed, and compared with the detailed 3D slab FEA results obtained in the next chapter to verify this newly developed simplified approach. The verification studies showed that high level of the accuracy is achieved

for both Ritz and 2D FE solutions based on the transformed plate approach. Despite the fact that both Ritz and 2D FE solutions of the equivalent transformed plate failed to predict any local deformations, it can be concluded that the transformed plate formulation with the Ritz or 2D finite element solution produce conservative yet accurate results.

The simplified transformed plate approach is a good analysis tool for preliminary structural design and analysis proposes. It allows engineers to use this tool to perform quick calculation to get preliminary design and overall behaviour of structures without requiring any detailed finite element analysis. Moreover, the philosophy of this simplified approach can be extended to more general applications of fibre reinforced sandwich composite structures.

Chapter 5

3D FINITE ELEMENT ANALYSIS OF THE TWO-WAY FRP SLAB

5.1 Introduction

Chapter 4 described the development of a simplified transformed plate approach for the analysis of the two-way FRP slab, which addressed the primary objective of this PhD study. Chapter 5 and 6 primarily deal with the 2nd main objective of this PhD study, i.e. conduct numerical and experimental investigations to obtain a more detailed insight into the structural behaviour of this new two-way FRP slab structure (Section 1.3).

This chapter describes the range of detailed 3D finite element analyses conducted for the two-way FRP slab. The main aims of these numerical analyses were to:

- verify the simplified transformed plate approach presented in the previous chapter,
- provide more insight into the localised structural behaviour of the two-way FRP slab, and
- model the experimental test of the two-way FRP slab presented in the following chapter.

The objectives of this chapter are a sub-set of the above objectives, and are more limited as follows:

(a) Verification of the simplified transformed plate approach using the results of 3D finite element analysis was described in Chapter 4, however the modelling

techniques and model construction were not discussed in Chapter 4. **The first objective of this chapter is to describe in detail how the results in Chapter 4 were obtained using commercially available finite element software**.

(b) The value obtained from experimental investigations can be significantly enhanced if relatively sophisticated numerical investigations have first been undertaken. This assists the experimental process, particularly with respect to testing and instrumentation planning, and provides the basis to compare experimental and numerical results which informs both processes. **The second objective of this chapter is therefore to describe the numerical analysis techniques used to investigate experimental behaviour of the slab and present summaries of the results of these analyses for later use in Chapter 6**. Only limited discussions regarding the implications of these results are discussed in this chapter, with the majority of discussion being presented in Chapter 6 and 7.

(c) As with most structures, engineering focus is greater in specific parts of the structure once its global behaviour is understood. **The third objective of this chapter is to describe the parts of the structure of greater interest, how modelling techniques were modified to reveal more detail in these areas, and discuss the limitations of such modelling**. Again, while the results are presented in this chapter, more detailed discussion is presented in subsequent chapters with the benefit of experimental results.

The analysis of a fibre reinforced composite sandwich structure requires finite element software capable of modelling anisotropic material types and laminated composites. The finite element software package, Strand7 (Release 1.05.6)[44], fulfilled these requirements and was used to complete the numerical analysis. In this study, the following types of 3D FEA analyses were preformed for the two-way FRP slab with three different boundary conditions:

1. Static analysis,
2. Natural frequency analysis, and
3. Buckling analysis;

and these are described individually in the remainder of this chapter.

5.2 Static Analysis

5.2.1 Development of Finite Element Model

- Use of Symmetry

For static analysis, the size of finite element models can be reduced significantly through the use of symmetry, resulting in substantial computational savings. In order to make use of symmetry, both loading and structural configuration must be symmetric.

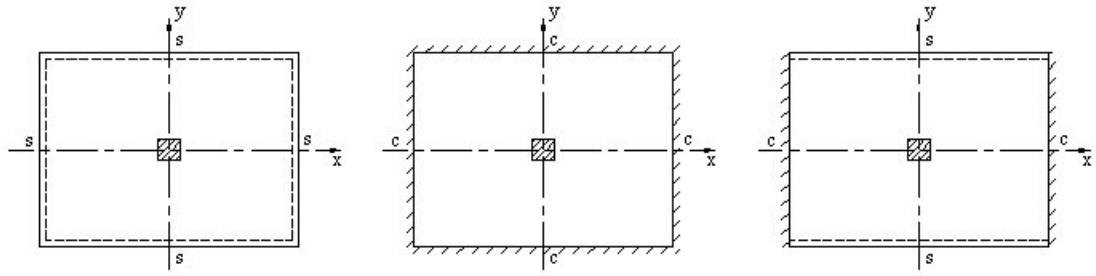

(a) (b) (c)

Figure 5.1 Slab with symmetric axis system: (a) All edges simply support; (b) All edges clamped; (c) Two opposite edges simply supported and the other two edges clamped

Three different boundary conditions were considered in the static analysis, namely, all edges simply supported (SSSS), all edges clamped (CCCC), and two opposite edges simply supported and the other two edges clamped (CCSS) (Figure 5.1). As shown in these figures, there is symmetry along both the length (the longitudinal axis, or *x*-axis) and width (the transverse axis, or *y*-axis) of the slab. The central patch loading that was used in the experiments (Chapter 6) is also symmetric about both *x*- and *y*-axis. Thus, the entire slab structure can be modelled as a quadrant, which significantly reduces the number of elements without sacrificing accuracy.

- Choice of Element Type and Mesh Details

A four-node quadrilateral plate/shell laminate element was used to model the fibre composite laminates. The element has six degrees of freedom at each node: translations in the nodal x, y, and z directions and rotations about the nodal x, y, and z-axes. Figure 5.2 shows a typical finite element mesh of the laminate skins and

circular tubes. The PFR core is modelled using 3-dimensional eight nodes hexahedra brick elements that have only three translational degrees of freedom at each node. A typical finite element mesh of the PFR core is shown in Figure 5.3.

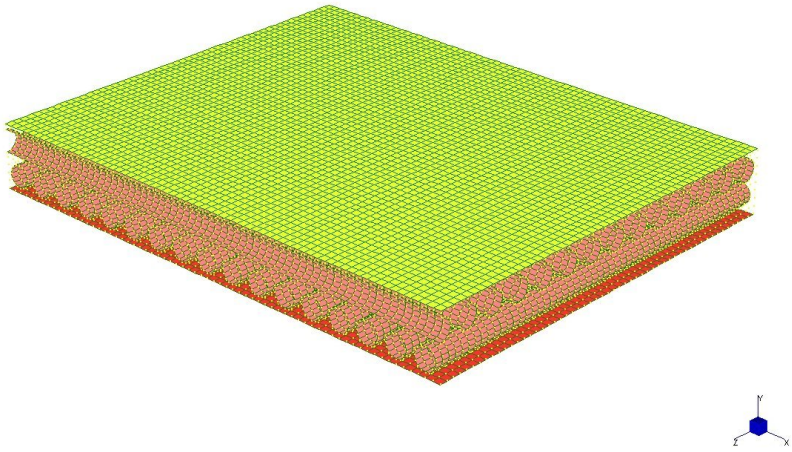

Figure 5.2 3D FE model of fibre laminate skins and circular tubes using four nodes plate elements

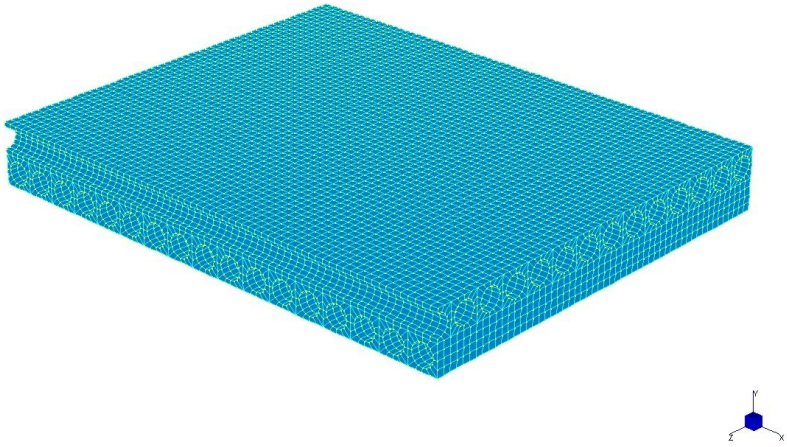

Figure 5.3 3D FE model of the PFR core using eight nodes brick elements

Since the fibre laminate skins and circular tubes are bonded to the core in the sandwich slab structure, the plate and brick elements used in the analysis for modelling the laminate and core have coincidental nodes. However, due to the lack of three rotational degrees of freedom at the nodes of brick elements, it is possible to cause discontinuous displacement between two coincidental nodes that are shared by both plate and brick elements. This problem can be overcome by using a relatively refined mesh during the finite element modelling. An investigation conducted as part

of this research indicated that combining 4-node plate/shell elements and 8-node brick elements was computationally more economical, taking less time to analyse the relatively complicated finite element model (compared with choosing 8-node plate/shell and 16-node brick elements) while still obtaining reasonably accurate results.

A typical mesh of the 3D finite element model with appropriate symmetrical conditions applied along the cross-sections of symmetry used in the static analysis is shown in Figure 5.4. A convergence investigation conducted at the start of the modelling exercise showed that this mesh provides a relatively high level of accuracy for the overall stress and strain distribution in the model.

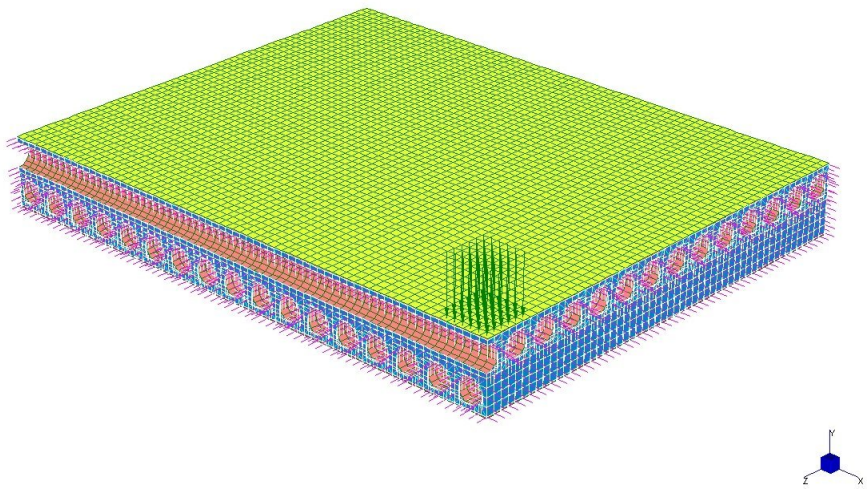

Figure 5.4 Typical mesh used for the two-way FRP slab

Relatively high stress concentrations appeared in certain regions of the model during the course of the analysis. This required the use of a sub-modelling technique to further investigate these regions with high mesh refinements. The sub-modelling technique confined the more intense meshing to the area of interest, thus reducing the computational time while maintaining a high level of accuracy. Details of this technique will be described in the following section.

- Material Properties

Due to the considerably different properties of the fibre composite laminate and PFR core materials (Chapter 3) in tension and compression, separate elements associated

with different material properties were used above and below the assumed neutral axis of the slab for the static analysis (Figure 5.5). Details of the coupon tests and the material properties obtained from these tests are presented in Appendix C.

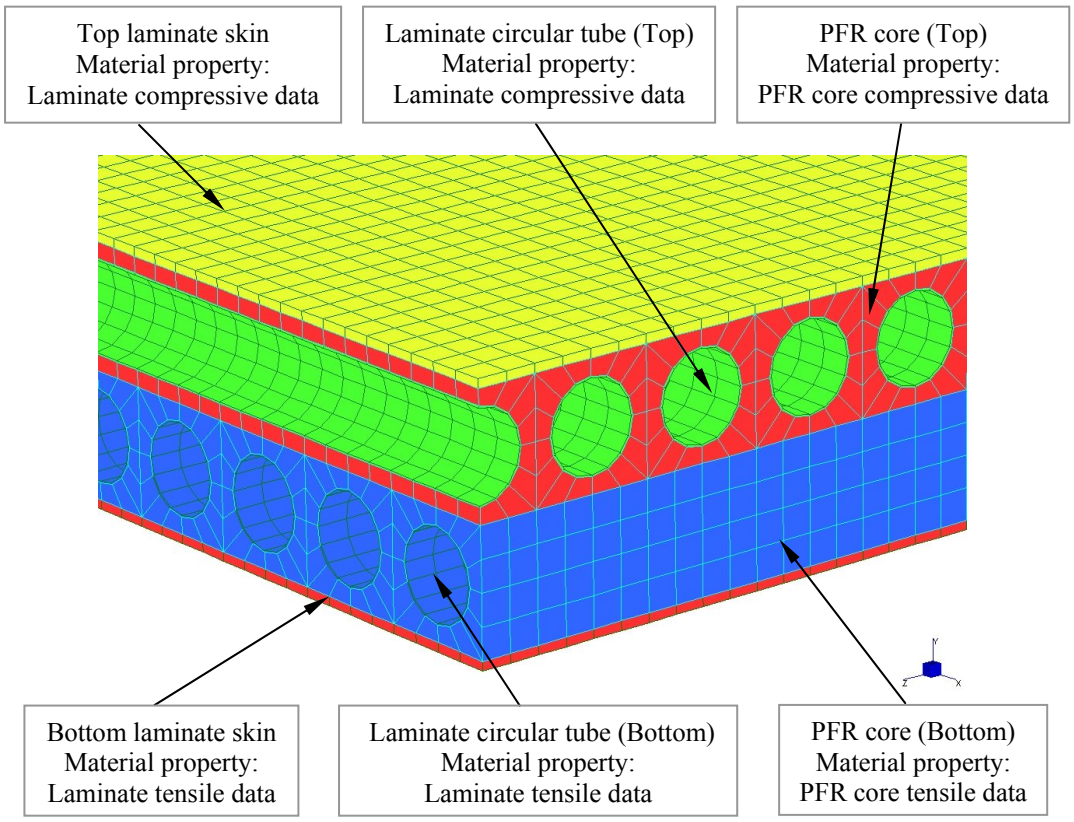

Figure 5.5 Separate parts of the two-way FRP slab with different material properties for the static analysis

The following material properties, taken from Appendix C, were input into the 3D finite element model for the static analysis:

1. Compressive properties of E-glass Uni-directional laminates:

Density,	ρ:	1825 kg/m^3
Young's Modulus,	E_{1c}:	28221 MPa
	E_{2c}:	12052 MPa
Poisson's Ratio,	ν_{12}:	0.253
Shear Modulus,	G_{12}:	3074 MPa
Thickness per layer,	t_{UD}:	0.542 mm (Unidirectional Fabric 450g/m^2)
Thickness per layer,	t_{DB}:	2 × 0.362 mm (Double Bias Fabric 600g/m^2)

2. Tensile properties of E-glass Uni-directional laminates:

Density,	ρ:	1825 kg/m^3
Young's Modulus,	E_{1t}:	21222 MPa
	E_{2t}:	9207 MPa
Poisson's Ratio,	ν_{12}:	0.253
Shear Modulus,	G_{12}:	3074 MPa
Thickness per layer,	t_{UD}:	0.542 mm (Unidirectional Fabric 450g/m^2)
Thickness per layer,	t_{DB}:	2×0.362 mm (Double Bias Fabric 600g/m^2)

3. Compressive properties of PFR core:

Density,	ρ:	924 kg/m^3
Young's Modulus,	E_c:	6127 MPa
Poisson's Ratio,	ν:	0.316

4. Tensile properties of PFR core:

Density,	ρ:	924 kg/m^3
Young's Modulus,	E_t:	4925 MPa
Poisson's Ratio,	ν:	0.316

The double bias reinforcement was modelled as two layers of unidirectional reinforcement at $\pm 45°$. It is noted that the input layup sequences in the finite element model replicated the laminate stacking sequences in the actual testing slab (refer Chapter 3).

- Simulation of Boundary Conditions

Figure 5.6 shows the CCSS boundary condition imposed on the finite element model, which illustrates the simulations of both the simply supported edge and clamped edge. As can be seen in the figure, only the nodes at the bottom line of the simply supported edge were restrained in the global *y*-direction translation, and all translations and rotations were restrained for the nodes at the clamped edge. However, the upward displacements at the four edges of the slab were not restricted in the actual prototype test (refer Chapter 6). As a result, uplifting can occur at the corners of the prototype slab when it is subjected to a relative high concentrated load

(Figure 5.7). This effect is known to be worse if the slab has relatively low stiffness (Timoshenko and Woinowsky-Krieger 1959). Thus, the SSSS boundary condition does not accurately replicate the edge conditions of the test slab.

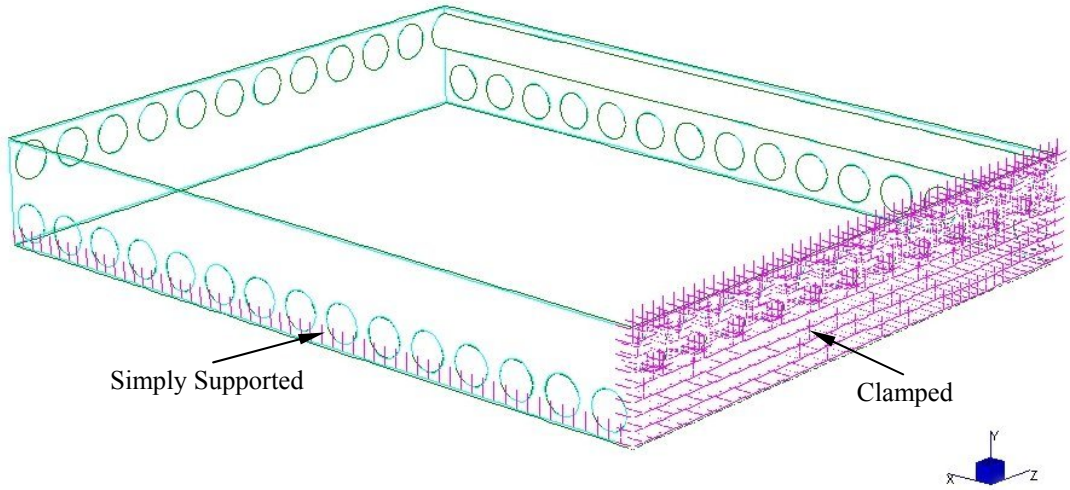

Figure 5.6 The boundary condition of CCSS imposed on the model

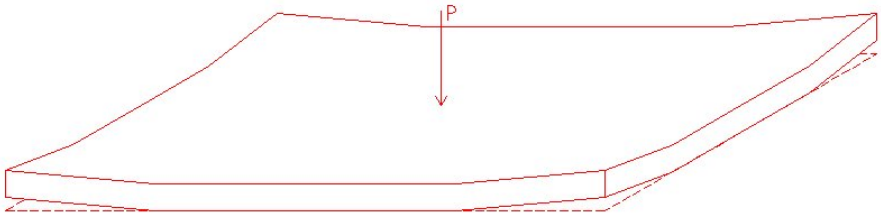

Figure 5.7 Uplifting at the four corners of the slab

In order to accurately predict the behaviour of the two-way FRP slab under the actual prototype test configuration, the experimental supported edge condition of the slab was simulated using additional 2-node beam elements. The nodes at one end of the beam elements were connected to the node at the bottom line of the simply supported slab edge, and the nodes at the other end of the beam elements were restrained in the global *y*-direction. As shown in Figure 5.8, these beam elements were defined as point contact elements with zero gaps (G+D Computing 1999). This type of point contact element is only active when the gap is closed and provides stiffness only in compression. The relative high value of initial stiffness (an initial estimate of the stiffness required to enforce the contact condition) was input into the point contact

element to improve the convergence by limiting the movement in the first iteration during the computational analysis. The modelling also utilised the "Dynamic Stiffness" option that allows the solver to increase and/or decrease the stiffness dynamically during the analysis to better enforce the contact conditions. In addition, Master-Slave links with only freedom of vertical translation were created, sharing the same nodes as the point contact elements to ensure consistent translations and rotations between both nodes of the elements with the exception of vertical deformation.

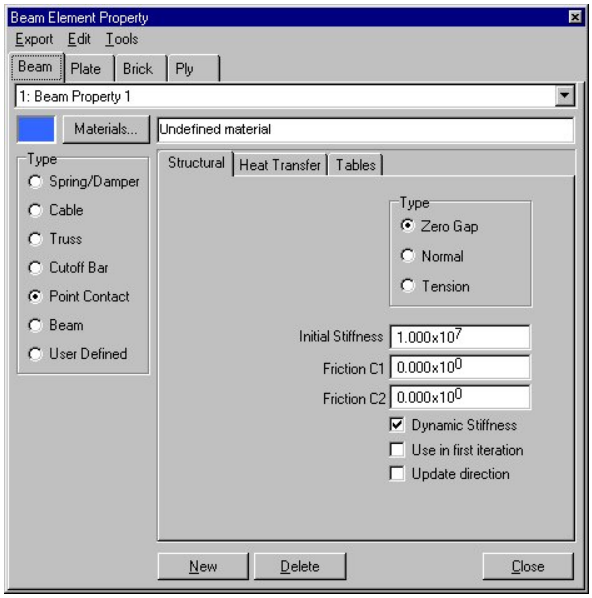

Figure 5.8 Definition of the point contact type beam element

Compared to the FE model using the SSSS boundary condition, the model including the point contact elements allows for the vertical deformation of the nodes at the bottom line of the simply supported edge.

The nonlinear static solver was used to conduct the computational analysis of the model with the point contact elements (G+D Computing 1999). Material nonlinearities were not incorporated into this analysis. The linear static analysis was performed for the model without the point contact elements as well.

Figure 5.9 shows the load deflection diagrams for the FE models with and without point contact elements. All values of the centre deflection were extracted from the

bottom surface of the slab. Comparison of the centre deflection (Figure 5.9) shows good agreement between the two models (approximately 2.5% difference) indicating that the actual support condition has only a small effect on the central region of the slab. Similar results were also obtained for the deflection comparison at the corners of the slab suggesting that the prototype slab is relatively stiff. These results indicate that using a SSSS boundary condition for the simulation of the supported edge condition in the actual prototype test is an appropriate simplification for the purpose of this study. Due to the extremely time consuming computing effort associated with of using a non-linear static solver, the SSSS boundary condition was used in subsequent finite element analyses to simulate the supported edge condition of the slab experiments.

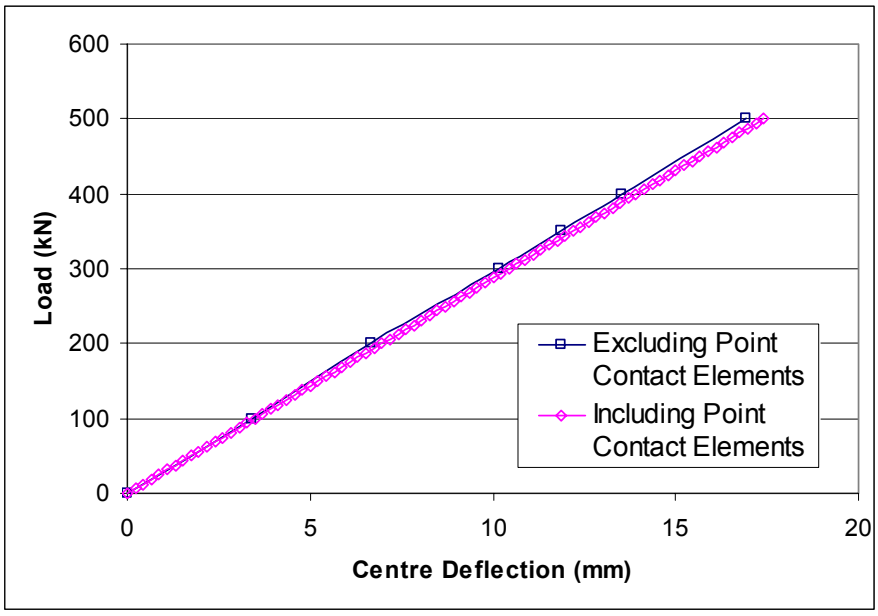

Figure 5.9 Plot of load-deflection diagram for FE model of the slab with SSSS including and excluding point contact elements

- Simulation of Loading Condition

The method of loading adopted in the analysis simulated the experimental conditions as much as possible. In the actual static loading test, the central patch load was applied to the top of the two-way FRP slab through a 180×180mm steel loading patch (described in Chapter 6). In the finite element modelling, this was modelled using a plate surface pressure (Figure 5.4) with a magnitude of 3.086 N/mm^2 over a 90×90 mm^2 area for the quarter model (equivalent to 100 kN on full model).

5.2.2 Results and Discussions

A linear static analysis was performed to investigate the fundamental structural behaviour of the two-way FRP slab under static loading. Linear elastic material characteristics were assumed, and geometric non-linearity was not considered.

The deflected shapes of the two-way FRP slab for three different boundary conditions are shown in Figures 5.10, while Figure 5.11 through 5.14 show the strain distribution in the fibre laminates and the PFR core throughout the slab.

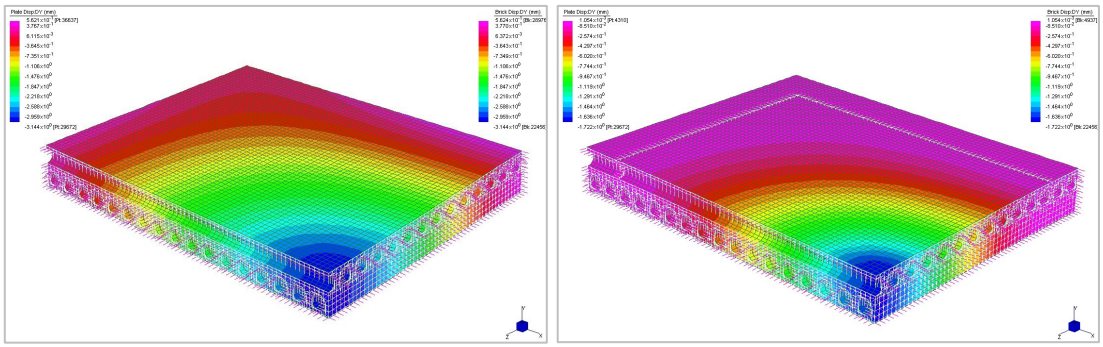

(a) (b)

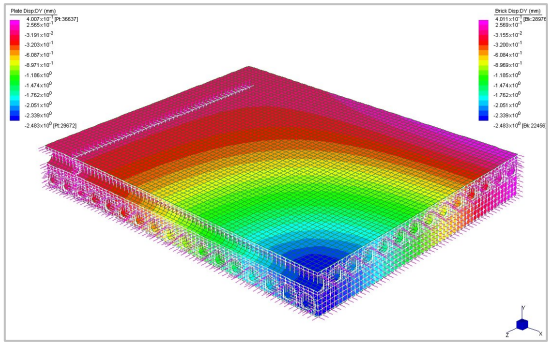

(c)

Figure 5.10 Deflection shape of the two-way FRP slab:
(a) SSSS; (b) CCCC; (c) CCSS

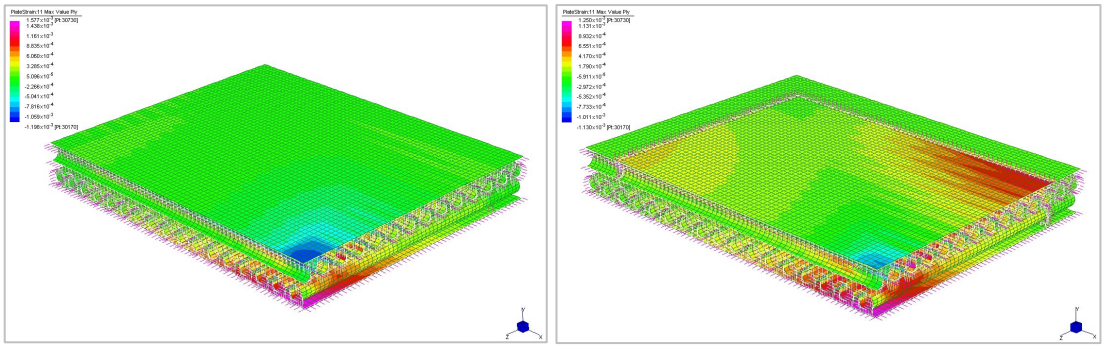

(a) (b)

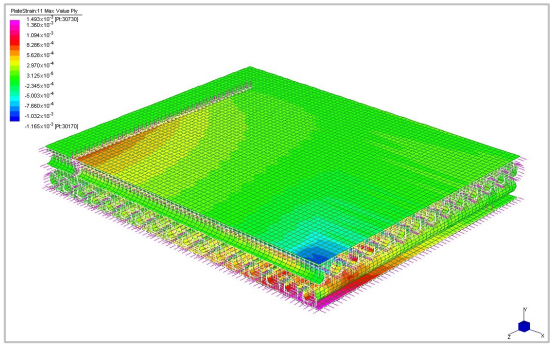

(c)

Figure 5.11 Ply strain at fibre direction in laminates:
(a) SSSS; (b) CCCC; (c) CCSS

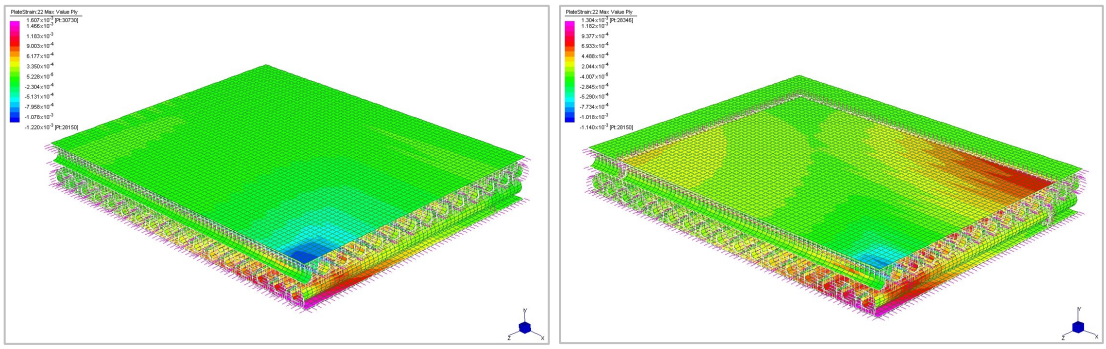

(a) (b)

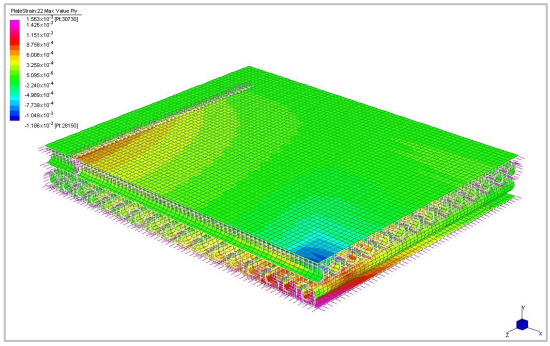

(c)

Figure 5.12 Ply strain at normal to fibre direction in laminates:
(a) SSSS; (b) CCCC; (c) CCSS

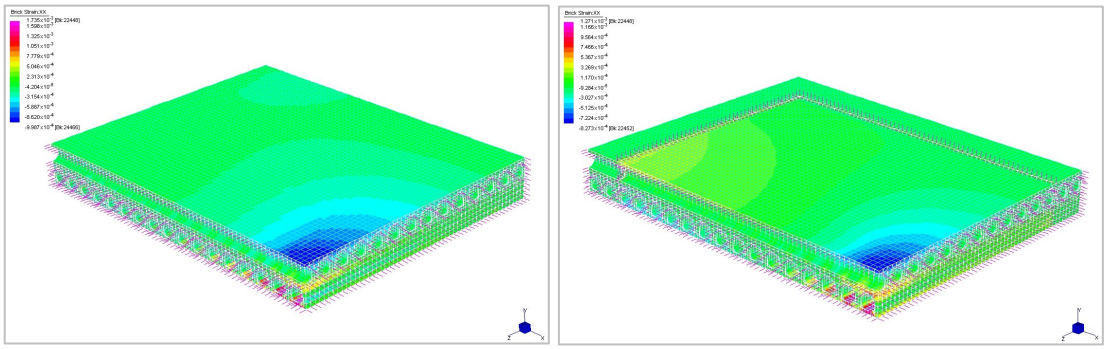

(a) (b)

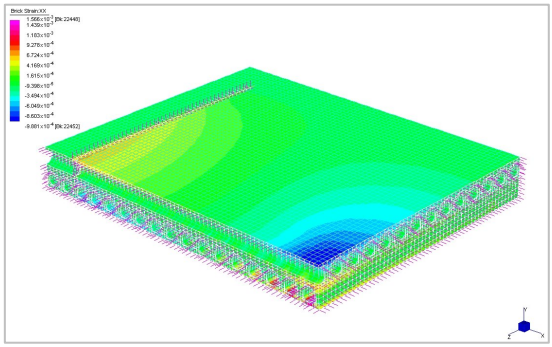

(c)

Figure 5.13 Strain at X-direction in PFR core: (a) SSSS; (b) CCCC; (c) CCSS

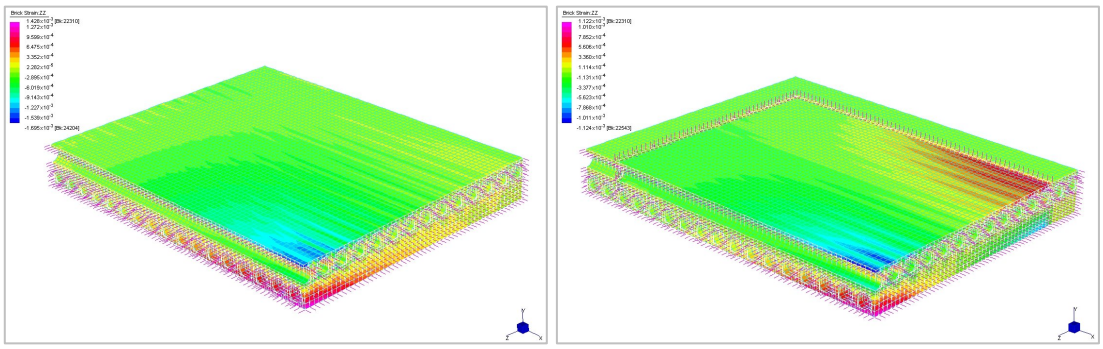

(a) (b)

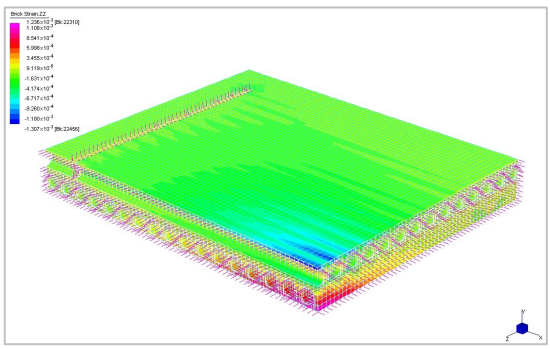

(c)

Figure 5.14 Strain at Z-direction in PFR core: (a) SSSS; (b) CCCC; (c) CCSS

From the above figures, it is clear that the greater strain gradients occur in the centre of the slab under the patch loading. The maximum tensile and compressive strains in both laminates and core occurred at the centre of the bottom and top parts of the composite slab (under the loading region), respectively. While the strain concentrations also appear at the supported edges for the CCCC and CCSS boundary conditions. The magnitude of the strain (including both tension and compression) at the support edge is significantly lower than those at the centre of the slab, which was to be expected. Furthermore, the region of greatest strain gradient occurs in an area approximately 300 mm from centre of the quarter model back towards the supports on both faces of symmetry. Consequently, this is the region of the greatest interest with respect to detailed materials behaviour. Thus, only the central region of the slab was further subdivided using the sub-modelling technique in order to gain a more thorough understanding of the slab behaviour. The sub-model of the centre part of the slab with a refined finite element mesh is shown in Figure 5.15. The displacements on the cut boundaries of the original model are applied as prescribed displacements to the sub-model.

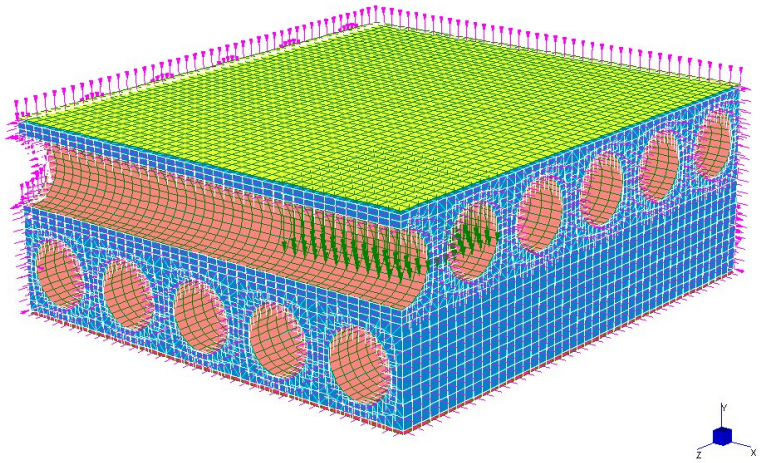

Figure 5.15 Sub-model of the centre part of the two-way FRP slab

The centre deflection of the two-way FRP slab for the three different boundary conditions is shown in Figure 5.16. Due to the localised compressive effects of the loading platen on the top of the slab, all values of the centre deflection were extracted at the bottom of the slab. As expected, Figure 5.16 indicates that the stiffness of the slab is significantly affected by the different boundary conditions.

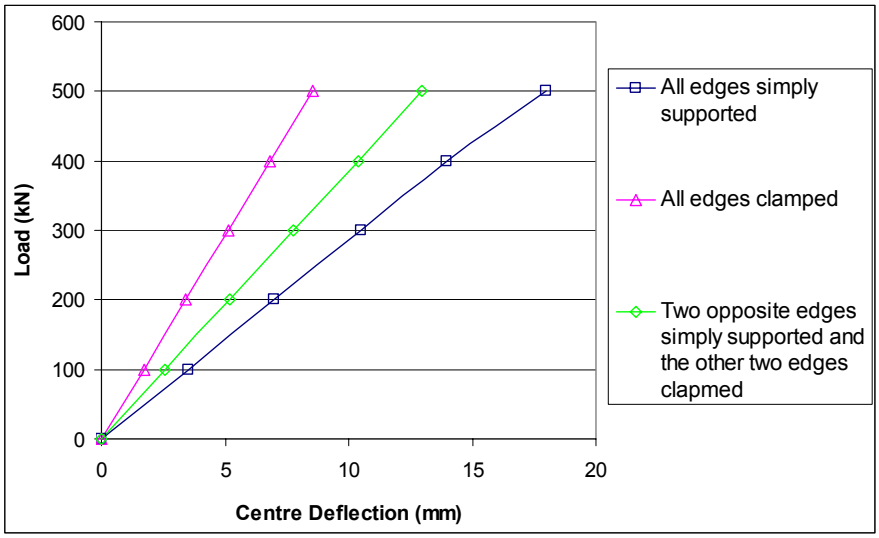

Figure 5.16 Comparison of the two-way FRP slab stiffness for three boundary conditions

Figure 5.17 and 5.18 show the ply strain distribution at both fibre and normal to fibre directions in the sub-model of the centre regions of the slab at 100 kN load, respectively.

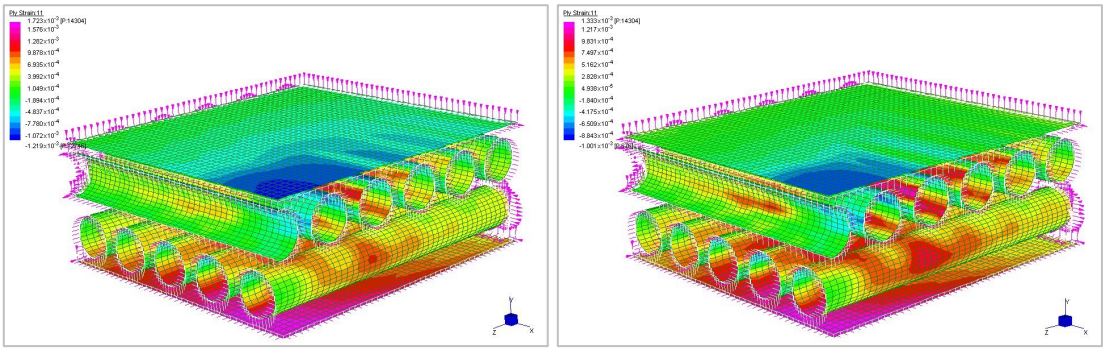

(a) (b)

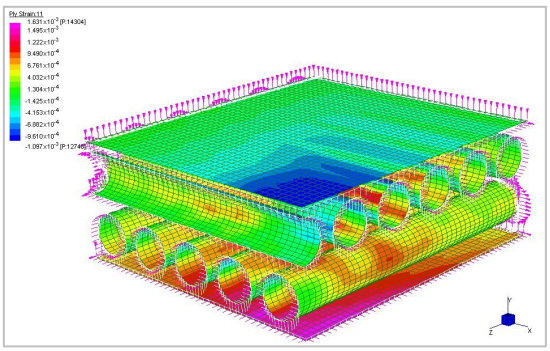

(c)

Figure 5.17 Ply strain at fibre direction in the sub-model: (a) SSSS; (b) CCCC; (c) CCSS

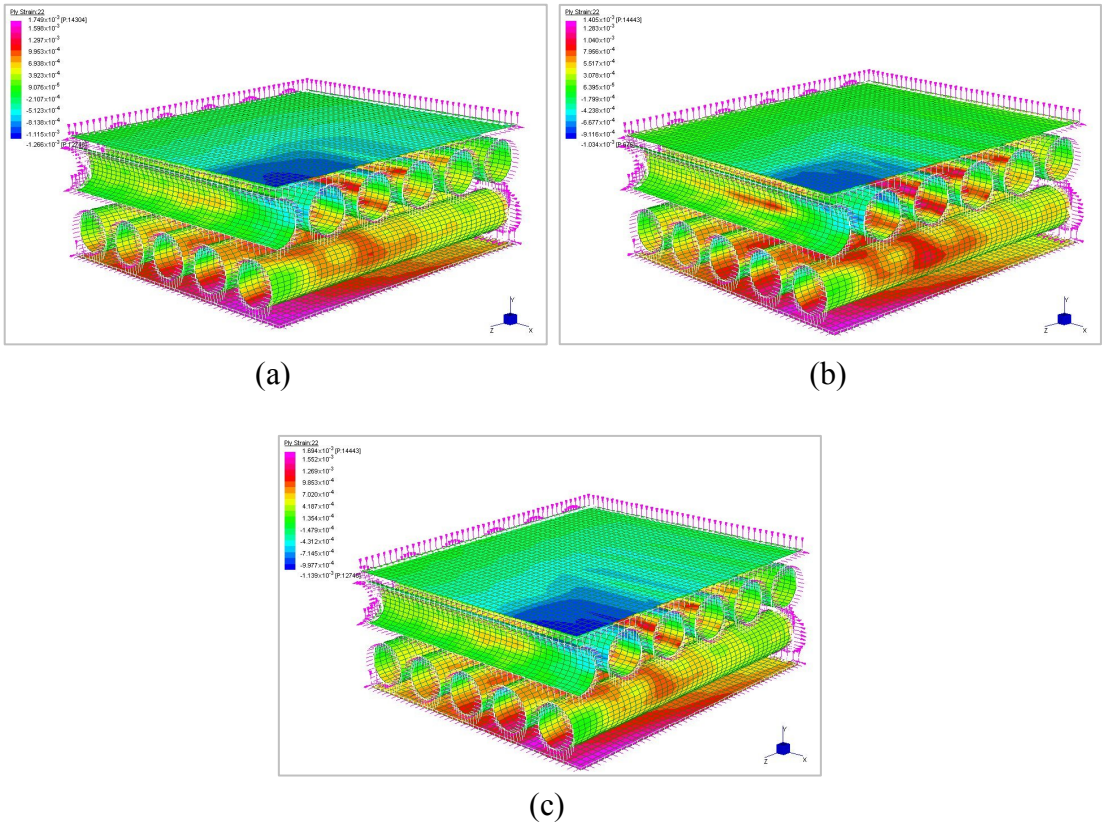

Figure 5.18 Ply strain at normal to the fibre direction in the sub-model: (a) SSSS; (b) CCCC; (c) CCSS

The finite element program (Strand 7) provides several multi-axial failure criteria for estimating the strength of individual laminae under in-plane stresses including maximum stress, maximum strain, Tsai-Hill, Hoffman and Tsai-Wu failure theories. Such strength criteria can be used on a ply-by-ply basis for a laminate to determine the load level of the failure of the first ply. This load is called the first ply failure load. In this static analysis, the Tsai-Hill criterion was used to predict first ply failure and its corresponding failure load. Details of the Tsai-Hill criterion and the comparison with other failure criteria are presented in Appendix E.

It should be noted that the loads corresponding to first ply failure are not necessarily the laminate failure loads since a laminate generally has plies at several orientations. That is, there will usually be a sequence of ply failures at different loads culminating in ultimate failure when all plies have failed. The load at which all the plies in the laminate have failed is called the last ply failure load. However, due to the significant lower failure strain of PFR core materials compared with glass fibre laminates (refer

Appendix C), cracking in the PFR core occurs long before the last ply failure load is reached. Once the PFR core cracks, the current finite element analysis fails to accurately simulate post-failure behaviour of the two-way FRP slab since Strand 7 is unable to model cracking. Thus, a prediction of the last ply failure load was not considered in the analysis.

Table 5.1 provides the stiffness and strength results for the first ply failure prediction of the two-way FRP slab for three boundary conditions. The results indicate that the slab for all three boundary conditions failed in tension at the bottom laminate skin. The first ply to fail was the ply at the outer surface of the laminate.

Table 5.1 Summary of 3D FEA results for the first ply failure prediction

	SSSS	CCCC	CCSS
Predicted first ply failure load (kN)	310	400	340
Centre deflection at the first ply failure load (mm)*	10.84	6.84	8.83
Ply strain ε_{11} in the element of first ply failure ($\mu\varepsilon^{\dagger}$)	5490	5207	4880
Ply strain ε_{22} in the element of first ply failure ($\mu\varepsilon$)	5594	5563	5764
Max tensile strain ε_{xx} in PFR core at the first ply failure load ($\mu\varepsilon$)	5338	5115	5419
Max tensile strain ε_{zz} in PFR core at the first ply failure load ($\mu\varepsilon$)	4559	4272	4037
Max compressive strain ε_{xx} in PFR core at the first ply failure load ($\mu\varepsilon$)	3216	3190	3338
Max compressive strain ε_{zz} in PFR core at the first ply failure load ($\mu\varepsilon$)	5461	5010	4936

* All values of centre deflections were extracted from the bottom of the slab.
† $\mu\varepsilon$ - microstrain

Figure 5.19 and 5.20 show the ply strain in both fibre and normal to fibre directions in the sub-model at the first ply failure load and the location at which it occurred.

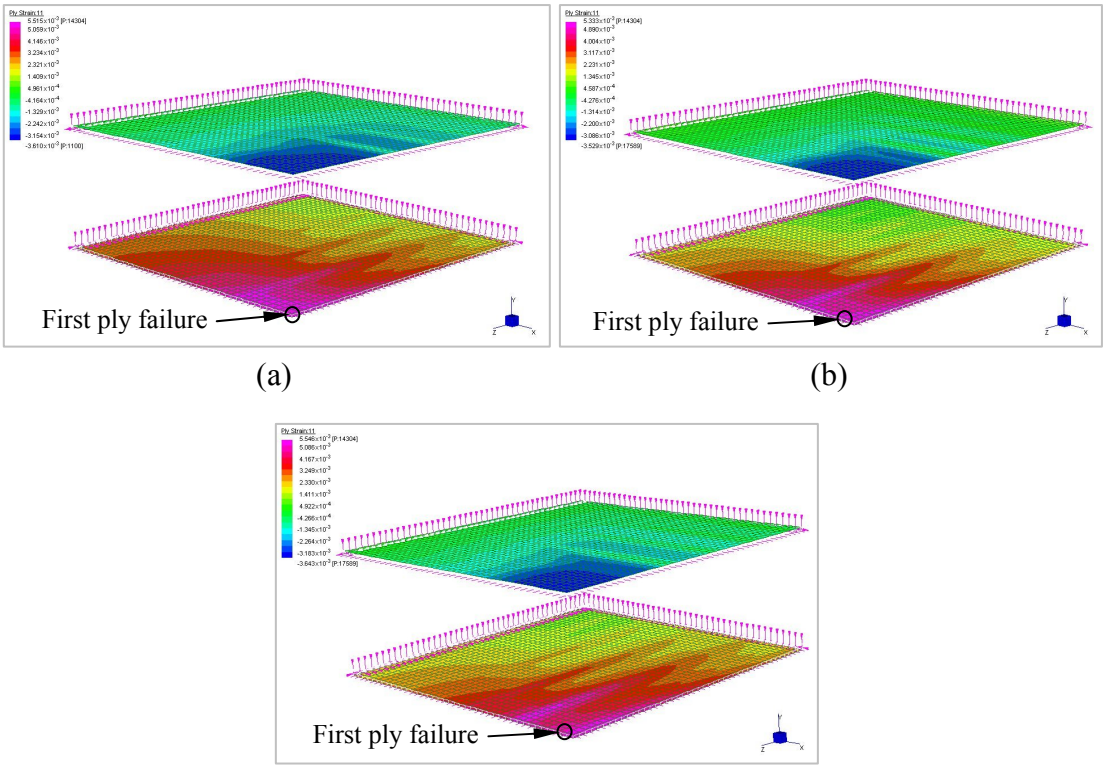

(a) (b)

(c)

Figure 5.19 Ply strain in fibre direction and location of the first ply failure: (a) SSSS (at failure load 320 kN); (b) CCCC (at failure load 400 kN); (c) CCSS (at failure load 340 kN)

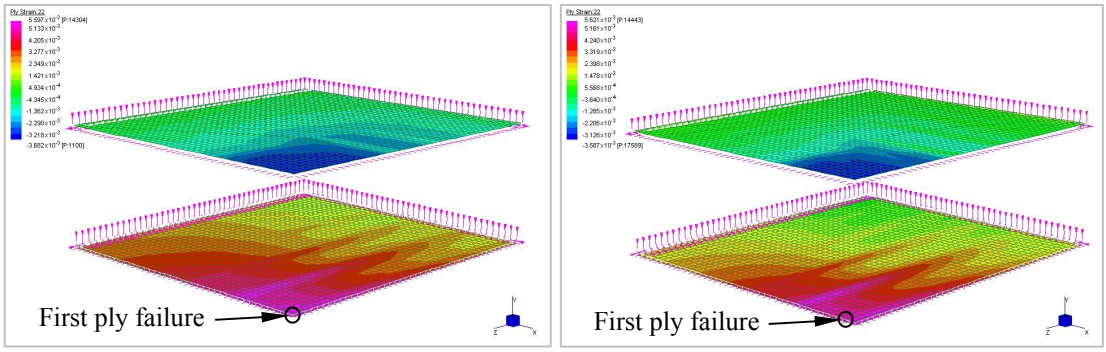

(a) (b)

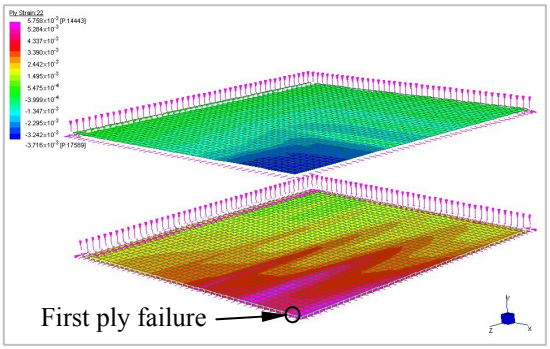

(c)

Figure 5.20 Ply strain normal to fibre direction and location of the first ply failure: (a) SSSS (at failure load 320 kN); (b) CCCC (at failure load 400 kN); (c) CCSS (at failure load 340 kN)

The similar ply strain distribution in the fibre direction and normal to fibre direction shown in Figure 5.19 and 5.20 indicates that the load is relatively evenly distributed in both longitudinal and transverse direction of the slab.

The first ply failure occurred at the bottom laminate skin rather than in the circular laminate tubes that were made of double bias fabric. This result indicates that the shear reinforcement in the two-way FRP slab is adequate at the first ply failure load. However, due to the relatively low shear strength of the PFR core compared with the glass fibre reinforcements (Appendix C), it is important to evaluate the shear magnitude of the stresses in the PFR core at first ply failure. It should be noted that only out-of-plane shear (through the thickness) of PFR core was considered in this analysis since it is more critical than in-plane shear of PFR core, due to the relatively high concentrated load imposed on the slab.

The shear strain distributions in the PFR core in global XY- and YZ-direction in the sub-model of the centre part of the slab under 100 kN load are shown in Figure 5.21 and 5.22. As shown in these figures, a high shear strain concentration is observed in the PFR core beneath the region of the applied patch load for each of the three boundary conditions.

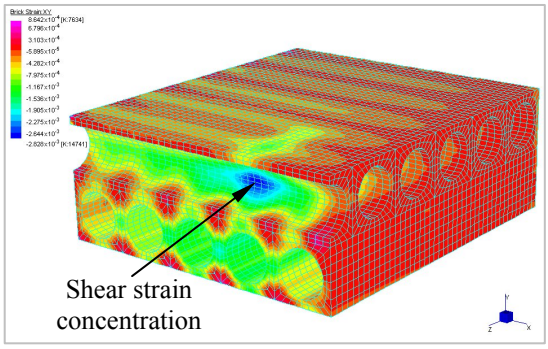

(a)

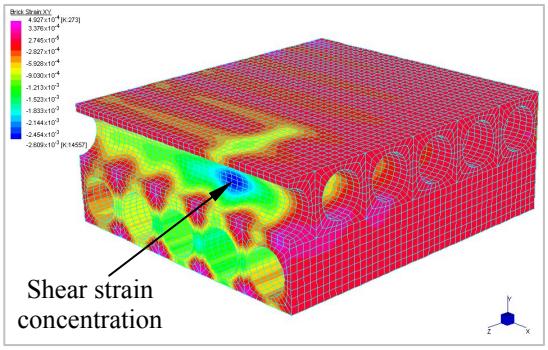

(b)

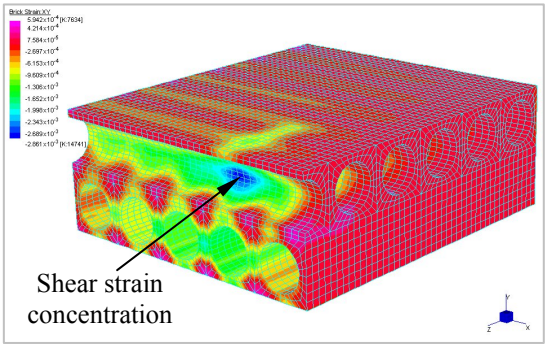

(c)

Figure 5.21 PFR core shear strain in XY-direction:
(a) SSSS; (b) CCCC; (c) CCSS

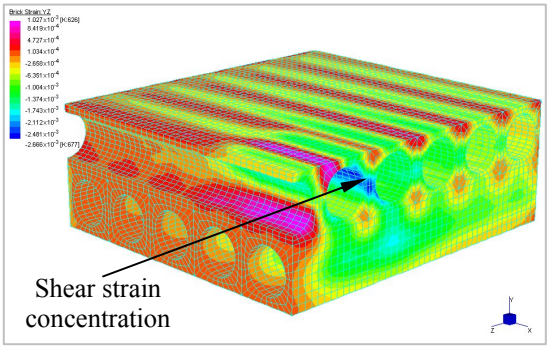

(a)

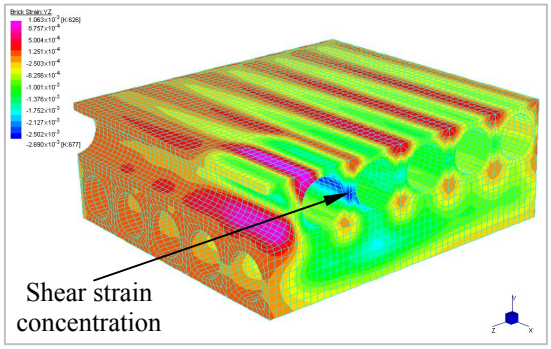

(b)

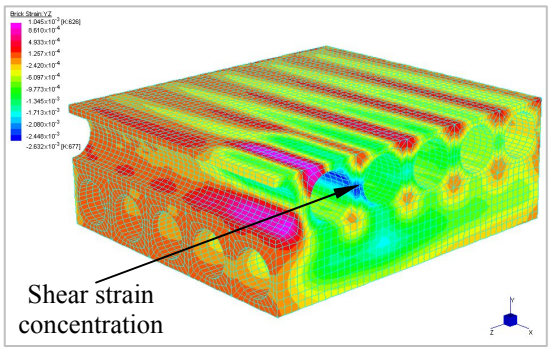

(c)

Figure 5.22 PFR core shear strain in YZ-direction:
(a) SSSS; (b) CCCC; (c) CCSS

The maximum out-of-plane shear strains in the PFR core versus the load for three boundary conditions are shown in Figure 5.23 through 5.25.

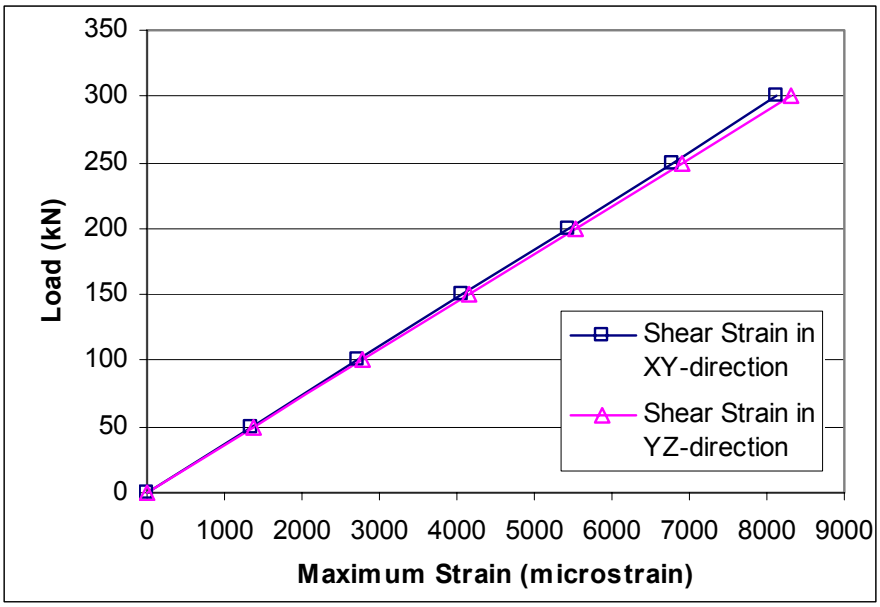

Figure 5.23 Maximum shear strain in the PFR core versus load for SSSS

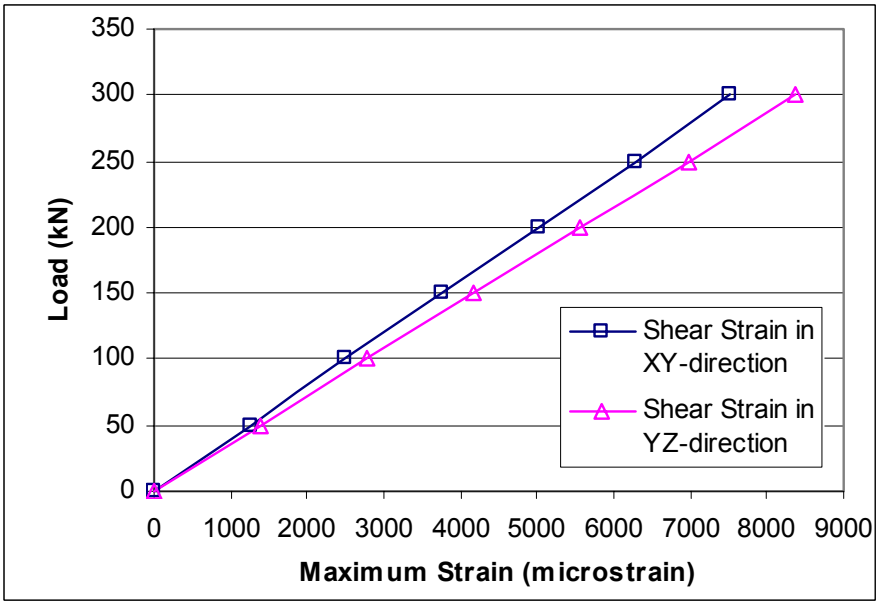

Figure 5.24 Maximum shear strain in the PFR core versus load for CCCC

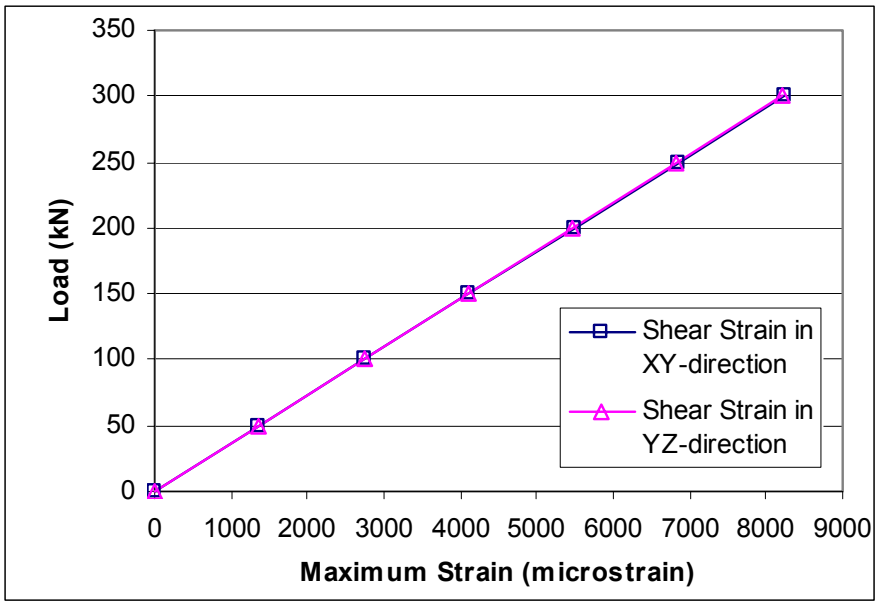

Figure 5.25 Maximum shear strain in PFR core versus load for CCSS

Based on these figures, the values of the PFR core cracking load were calculated corresponding to the average shear failure strain of 7924 microstrain that was obtained from the linear relationship between shear strength and shear modulus of the PFR core (refer Appendix C). Table 5.2 summarizes the predicted PFR core cracking load of the slab for three different boundary conditions. The listed values correspond to:

- shear strain in YZ-direction for the slab with SSSS and CCCC,
- shear strain in XY-direction for the slab with CCSS.

The centre deflections extracted from the bottom of the slab at these loads and the corresponding maximum tensile ply strain in the fibre (ε_{11}) and normal to the fibre (ε_{22}) direction are also included in the table.

Table 5.2 Summary of 3D FEA results for PFR cracking load prediction

Boundary conditions	SSSS	CCCC	CCSS
Predicted PFR core cracking load (kN)	284	286	289
Centre deflection at the predicted PFR core cracking load (mm)	9.93	4.89	7.51
Max Tensile Ply Strain ε_{11} at the predicted PFR core cracking load ($\mu\varepsilon$)	4872	3811	4712
Max Tensile Ply Strain ε_{22} at the predicted PFR core cracking load ($\mu\varepsilon$)	4989	4081	4954

In comparison with the first ply failure load (Table 5.1), the lower PFR core cracking load predicted for all three boundary conditions indicates that the initial failure of the slab will occur in the PFR core due to the out-of-plane shear rather than rupture of the bottom fibre reinforced laminate. As shown in Table 5.2, the predicted PFR core cracking load for each of the three boundary conditions is almost identical. This indicates that the boundary condition has little influence on the out-of-plane shear response of the slab under the concentrated load. Considering the location of the maximum shear strain generated as indicated in Figures 5.21 and 5.22, the initial failure mode of the slab is most likely to be a punching shear type of failure.

It should be noted that the two-way FRP slab may continue to carry the load after the initial cracking of PFR core until the last ply failure of the laminate has occurred. However, as described previously, the current finite element analysis is unable to accurately simulate structural responses after PFR core cracking. The post-failure (after PFR core cracking) behaviour of the slab will be discussed in Chapter 6.

5.3 Natural Frequency Analysis

Analysis of structures subjected to a static load provides a sound understanding of the behaviour of most structures. However, seldom in real life is a structure only subjected to static loads. More often, structures are subjected to various dynamic loads such as vehicular and earthquake loads. Hence, a calculation of the fundamental natural frequencies is of importance to the study of structural vibrations.

In this research, a natural frequency (eigenvalue) analysis of the two-way FRP slab was performed using Strand 7 in order to predict the fundamental natural frequencies.

5.3.1 Development of Finite Element Model

- Use of Symmetry

In contrast with the static analysis, the full finite element model is often required for natural frequency analyses in order to determine all natural frequencies and corresponding modes. However, the limited computational resources available in this project did not allow the solution of a full 3D FE model of the slab. Thus, a quarter model of the slab was used in the natural frequency analysis. As a result, the analysis will only determine natural frequencies with corresponding symmetric modes. Thus, only the first fundamental natural frequency and corresponding mode of the slab for three boundary conditions was determined in this study.

- Choice of Element Type and Mesh Details

As with the static analysis, the four-node quadrilateral plate/shell laminate element and eight-node hexahedral brick elements were used in the natural frequency analysis. Due to the reasonably uniformly stiffness distribution throughout the two-way FRP slab, a uniform finite element mesh shown in Figure 5.4 was used to investigate the natural frequencies of the slab. For a dynamic analysis, the stress distribution is often less important than knowing the natural frequencies or the displacements associated with the dynamic response. Moreover, a dynamic analysis generally can have a coarser mesh than a static analysis because the response tends to be controlled by the low frequency behaviour (Hitchings 1992). Initial investigation found that rapid convergence can be achieved with the coarse mesh arrangement shown in Figure 5.4. Thus, no further mesh refinement was used in the analysis.

- Material Properties

As described previously, different properties of the fibre composite laminate and PFR core materials in tension and compression were assigned to various parts of the model in the static analysis (Figure 5.5). However, this is not the case for the dynamic analysis since the compressive and tensile components swap position during

the structural vibration. Due to this nature of dynamic behaviour, the average of the tensile and compressive properties of the fibre laminate and PFR core were used in the natural frequency analysis (Figure 5.26).

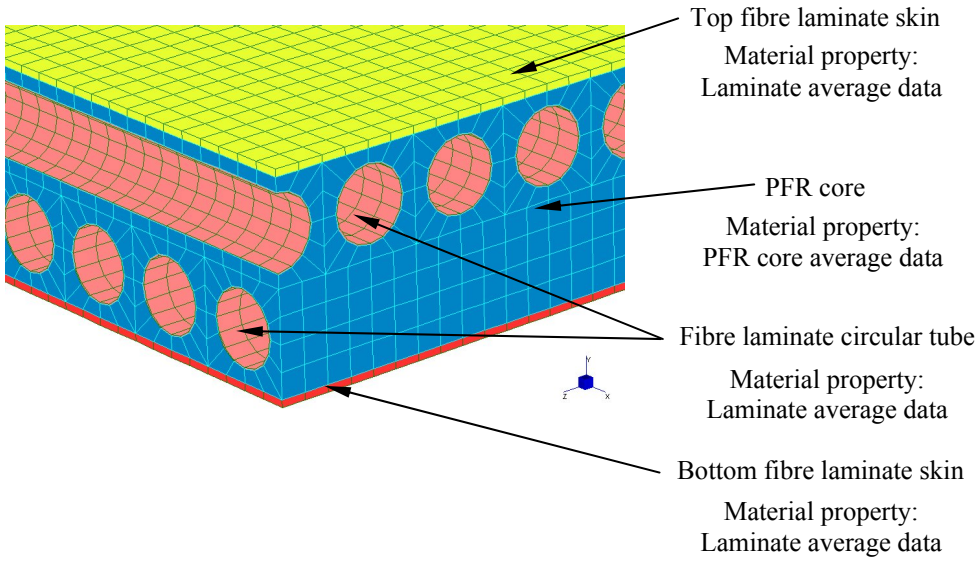

Figure 5.26 Separate parts of the two-way FRP slab with average material properties for the natural frequency analysis

The material properties were input into the 3D finite element model for the natural frequency analysis as follows:

1. Average properties of E-glass Uni-directional laminates:

Density,	ρ:	1825 kg/m^3
Young's Modulus,	E_{1a}:	24721 MPa
	E_{2a}:	10629 MPa
Poisson's Ratio,	ν_{12}:	0.253
Shear Modulus,	G_{12}:	3074 MPa
Thickness per layer,	t_{UD}:	0.542 mm (Unidirectional Fabric 450g/m^2)
Thickness per layer,	t_{DB}:	2 × 0.362 mm (Double Bias Fabric 600g/m^2)

2. Average properties of PFR core:

Density,	ρ:	924 kg/m^3
Young's Modulus,	E_a:	5526 MPa
Poisson's Ratio,	ν:	0.316

- Simulation of Boundary Conditions

As with the static analysis, the same simulation of boundary conditions were used in the natural frequency analysis, i.e. the nodes at the bottom line of the simply supported edge were restrained in global *y*-direction translation, and all translations and rotations were restrained for the nodes at the clamped edge.

- Simulation of Loading Condition

In the natural frequency analysis, no external load was applied to the 3D finite element model.

5.3.2 Results and Discussions

Figure 5.27 shows the deflected shapes of the first vibration mode of the slab for three boundary conditions. The first fundamental natural frequency of the slab for the three different boundary conditions are summarised in Table 5.3.

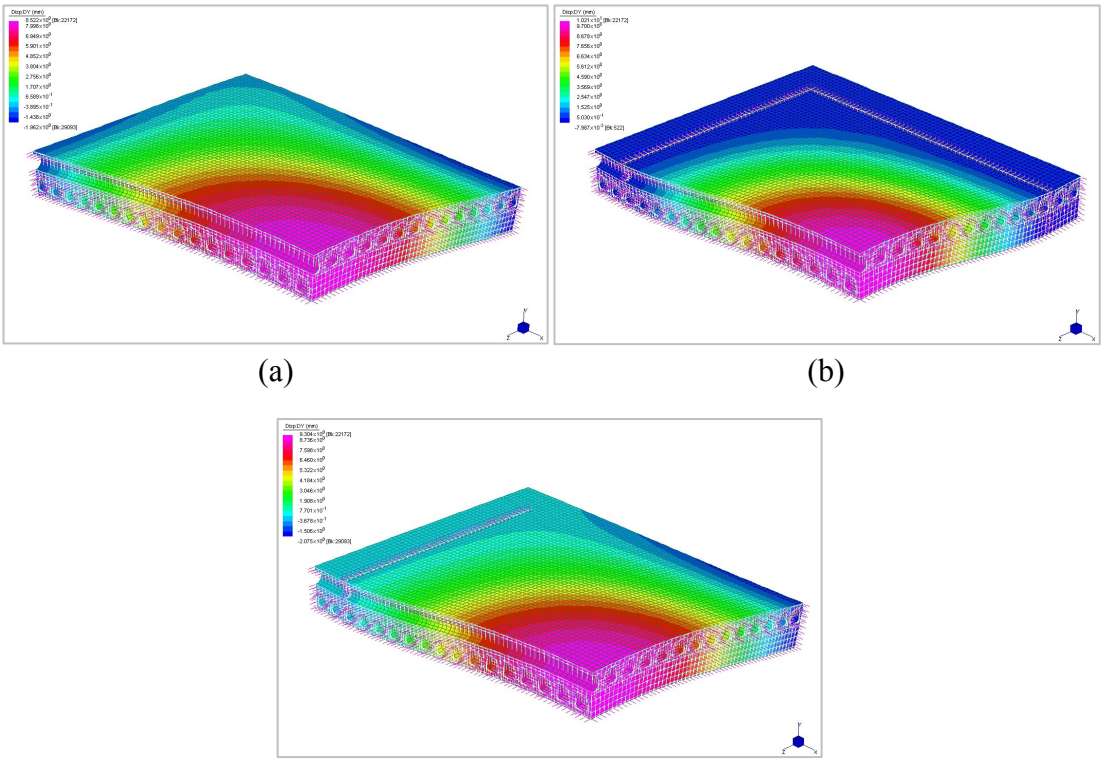

(a) (b)

(c)

Figure 5.27 First vibrational mode of the two-way FRP slab:
(a) SSSS; (b) CCCC; (c) CCSS

Table 5.3 First natural frequency of the two-way FRP slab

Boundary conditions	1st Fundamental Natural Frequency (Hz)
SSSS	133.49
CCCC	228.08
CCSS	166.27

As illustrated in the figure, the shape of the first vibrational mode of the slab is relatively similar for the three boundary conditions. However, the first natural frequency differs significantly for three boundary conditions (Table 5.3). As expected, the highest frequency occurred in the slab with CCCC and the lowest frequency occurred in the slab with SSSS. Given that the mass of the slab is constant, the configuration with the highest stiffness results in the highest natural frequency.

5.4 Buckling Analysis

In general, global buckling is unlikely for a floor slab structure when the slab is subjected to an out-of-plane (along the slab thickness) load. This is also true for the two-way FRP slab since the fibre reinforced laminate outer skins and circular tubes are well bonded to the PFR core. However, local buckling is possible within the composite slab in the thin walls between the circular voids. Thus, a finite element buckling analysis was performed in this study to provide an indication of the local buckling sensitivity of this two-way FRP slab. It should be noted that the results obtained from this buckling analysis provide a guide to the significance of local buckling rather than an accurate estimation of the buckling load.

5.4.1 Development of Finite Element Model

- Use of Symmetry

Generally, the lowest eigenvalue is of most interest from a buckling analysis for a given dimension, material, boundary condition, and a given load type. Thus, only the first buckling mode was considered in this analysis and consequently a quarter model of the slab was used.

- Choice of Element Type and Mesh Details

As with the static analysis, the four-node quadrilateral plate/shell laminate element and eight-node hexahedra brick elements were used in the buckling analysis. Due to considerable computational effort and time required for this analysis, only a simple mode with relatively coarse mesh could be solved. The typical mesh used in the buckling analysis is shown in Figure 5.4.

- Material Properties

As with the static analysis, different properties of the fibre composite laminate and PFR core materials in tension and compression were assigned to various parts of the model in the buckling analysis (Figure 5.5).

- Simulation of Boundary Conditions

As with the static analysis, the same simulation of boundary conditions were used in the buckling analysis, i.e. the nodes at the bottom line of the simply supported edge were restrained in global *y*-direction translation, and all translations and rotations were restrained for the nodes at the clamped edge.

- Simulation of Loading Condition

The load condition was modelled using a plate surface pressure (Figure 5.4) with the magnitude of 3.086 N/mm^2 over a 90×90 mm^2 area for the quarter model (equivalent to 100 kN on full model).

5.4.2 Results and Discussions

A linear eigenvalue analysis was performed to obtain a fist indication of the buckling behaviour of the test slab. Figure 5.28 through 5.30 show the first buckling mode of the laminates within the two-way FRP slab for the three boundary conditions.

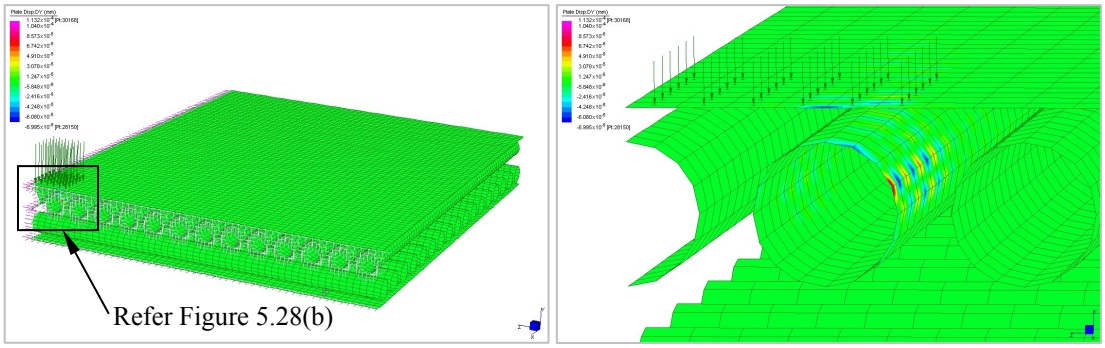

(a) (b)

Figure 5.28 First local buckling occurred in the fibre laminate of the two-way FRP slab with SSSS

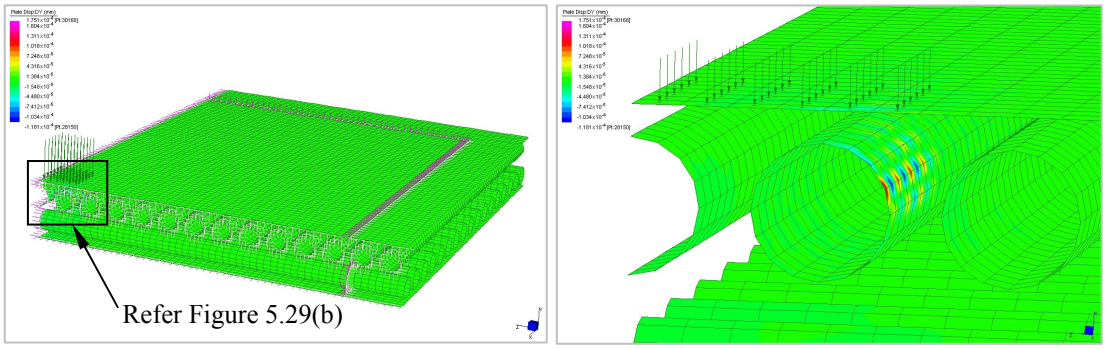

(a) (b)

Figure 5.29 First local buckling occurred in the fibre laminate of the two-way FRP slab with CCCC

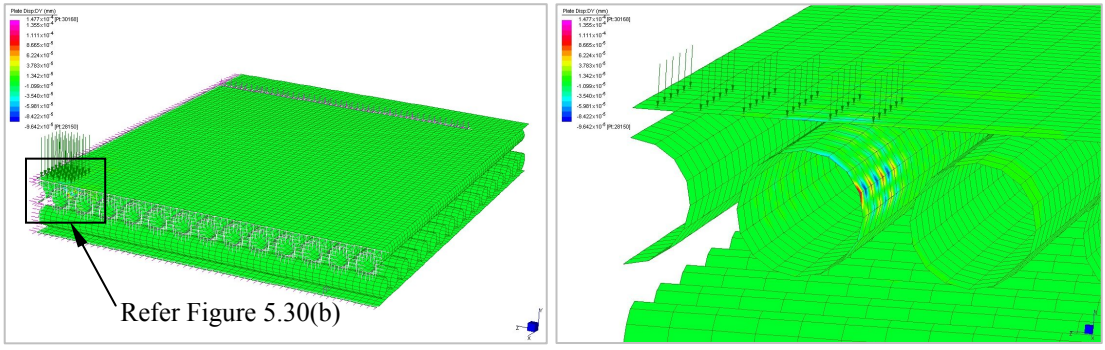

(a) (b)

Figure 5.30 First local buckling occurred in the fibre laminate of the two-way FRP slab with CCSS

Local buckling rather than global buckling was observed for all three boundary conditions. However, closer examination of the buckling modes revealed that these buckling modes are most likely a result of the FE modelling technique rather than actual physical buckling modes. More accurate modelling of the buckling behaviour is required and this would almost certainly result in a higher buckling load. The first eigenvalue calculated using the current model only represent a lower bound estimation of the buckling load.

Table 5.4 Calculated buckling factors

Boundary conditions	λ_{cr}
SSSS	3.35
CCCC	3.95
CCSS	3.64

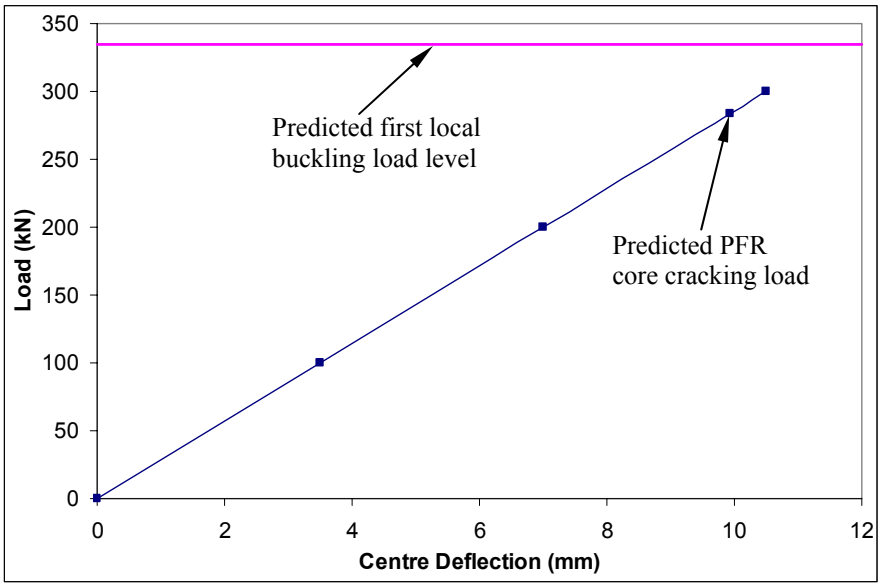

Figure 5.31 Predicted first local buckling load in comparison with predicted PFR core cracking load for the two-way FRP slab with SSSS

The first eigenvalues for the different boundary conditions are shown in Table 5.4. The associated buckling load is obtained by multiplying the initial applied load (100 kN) with the factors shown in this table. All the buckling loads are higher than the predicted PFR core cracking load (refer Table 5.2), as shown in Figure 5.31. Hence,

local buckling does not seem to be a crucial issue for the test slab under the present loading conditions. Nevertheless, it is advisable that detailed buckling investigations of this slab concept are the subject of future research.

5.5 Conclusions

This chapter has described detailed 3D finite element analyses of the two-way FRP slab. The main aim of the analysis was to verify the simplified analytical approach (presented in the previous chapter), and to establish any trends in the structural behaviour of the two-way FRP slab that could predict, simulate and supplement the experimental study discussed in the following chapter.

Three types of finite element analysis, namely, static, natural frequency and buckling, were conducted to investigate the structural behaviour of the slab with three different boundary conditions. A number of responses of the slab were predicted during the analysis, which includes:

- first ply failure load of the laminate,
- PFR core cracking load with failure mode of the slab,
- first fundamental natural frequency with the corresponding mode, and
- first buckling mode with the corresponding buckling load.

Numerical results show that a relatively high and comparable load carrying capacity in longitudinal and transverse directions was achieved in this two-way FRP slab, with the initial failure resulting from shear failure of the PFR core. The failure condition was similar to a punching shear failure mode.

The first fundamental natural frequency obtained from the finite element analysis indicates the high stiffness characteristic of the slab. The numerical results also show the notable influence of boundary condition types on structural behaviours of the slab. Although the simple FE linear buckling analysis has captured an indication of the local buckling sensitivity, it shows the lower bound of the first eigenvalue and does not affect the prediction of strength and stiffness behaviours of the slab.

Finite element analysis provides a relatively inexpensive, and time efficient alternative to physical experiments. However, it is vital to have a sound set of experimental data upon which to calibrate a finite element model. It is then possible to investigate a wide range of parameters within the FE model. Thus, the experimental investigations of the prototype two-way FRP slab will be presented in the next chapter.

Chapter 6

EXPERIMENTAL INVESTIGATION OF THE TWO-WAY FRP SLAB

6.1 Introduction

The models and analytical procedures developed in Chapters 4 and 5 for the structural analysis of the two-way FRP slab are evaluated and verified experimentally in this chapter. Details of the experimental procedures used to characterise the behaviour of the slab are presented. While the main interest was in determining the flexural strength and stiffness of the slab under static loading, the fundamental natural frequency, indication of fatigue behaviour and failure mode of the slab are also discussed in this chapter.

In this experimental program, the prototype two-way FRP slab was subjected to the following series of tests:

- Test 1: Natural frequency test;
- Test 2: Static loading up to 25% of 3D FEA predicted PFR cracking load test;
- Test 3: Static loading up to 70% of 3D FEA predicted PFR cracking load test;
- Test 4: Fatigue indication test;
- Test 5: Failure load test;
- Test 6: Post failure behaviour test.

Following a brief description of the fabrication of the prototype two-way FRP slab, the static tests of the slab including Test 2, Test 3, Test 5 and Test 6 are described first in this chapter, followed by the dynamic tests including Test 1 and Test 4.

6.2 Fabrication of the Prototype Two-way FRP Slab

As described previously, the two-way FRP slab was created as a sandwich structure with a central core being formed by orienting a number of PFR based modules in both longitudinal and transverse directions. The glass fibre reinforced skins were then laminated on the top and bottom of the assembled modules to complete this sandwich slab system. The fabrication of the prototype slab was carried out as follows:

1. Pre-fabricated standard single modules were connected using the dowel-type joint technique (refer Chapter 3 and Appendix B).
2. The first layer of modules was assembled on a flat table. Several small pieces of double bias mat were randomly placed on the surface of the modules to act as spacers to control the glue line thickness between two bonded modules. A low clamping pressure was then applied to the glued modules to ensure the removal of voids and squeeze the adhesive evenly.
3. After allowing the adhesive to cure, the first layer of modules was sanded using a belt sander to remove any excess glue at the joints and to create a flat surface on which to bond the second layer of modules. The assembly of the second layer of modules oriented at 90° to the first layer of modules was then carried out following the same procedure as described in step 2. Additional pressure in the vertical direction was applied during the assembly to ensure sufficient adhesive bonding between two layers of the assembled modules, as shown in Figure 6.1.
4. Following atmospheric cure of the adhesive, the surfaces on both side of the assembled modules were sanded and cleaned prior to lamination of the reinforcement. Eight layers of unidirectional E-glass reinforcement were laminated on each side of the assembled core using the sequence $[0°/90°]_4$ (Figure 6.2).
5. Subsequent to the lamination of the fibre reinforcement, the slab was allowed to cure at room temperature for a period of 24 hours, followed by a post cure at 80°C for 8 hours. The edges of the slab were then trimmed where necessary. Figure 6.3 shows the completed prototype two-way FRP slab ready for the testing.

Figure 6.1 Modules assembly of the slab

Figure 6.2 Reinforcement lamination of the slab

Figure 6.3 Completed prototype two-way FRP slab

The E-glass reinforcement and matrix types used in the slab were described in Chapter 3. A vinylester based adhesive (SPV 500) was used to assemble the modules.

6.3 Test Arrangement and Instrumentation

The primary intent of the instrumentation layout was to measure deflection and strain responses under loading in order to quantify strain and deflection profiles within the slab. Similar test arrangements were used for both the static and dynamic tests performed in this study. Figure 6.4 shows the prototype slab under the testing configuration. The slab was simply supported at all edges by four steel universal beams which were bolted together to minimise deformation on the steel beam supports during the test. Solid steel block strips were then welded on top of the universal beams to create the span of 1800 mm in longitudinal direction and 1380

mm transversely (Figure 6.5). Rubber matting was placed on the top of the solid steel blocks to prevent local stress concentrations at the simply supported reaction line of the slab. Load was applied at the centre of the slab through a 180×180 mm steel loading patch by an Instron hydraulic actuator mounted on a loading frame (Figure 6.4). A combination of steel plates and rubber matting was placed between the loading platen and the slab specimen to ensure even distribution of load into the slab, and to prevent local stress concentration (Figure 6.6). Load was measured using a 222 kN or 444 kN capacity load cell (for different tests), and the midspan deflection of the slab was measured using a 100mm stroke LVDT (linear voltage displacement transducer).

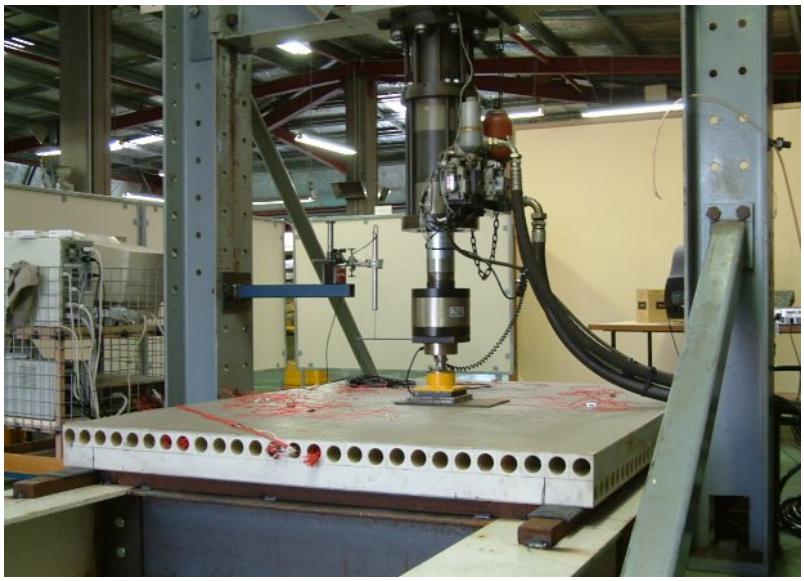

Figure 6.4 View of the prototype two-way FRP slab in test configuration

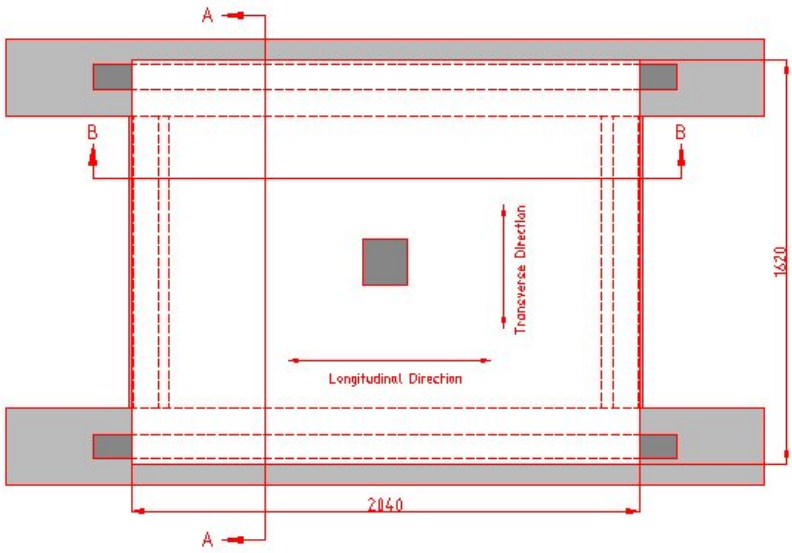

(a)

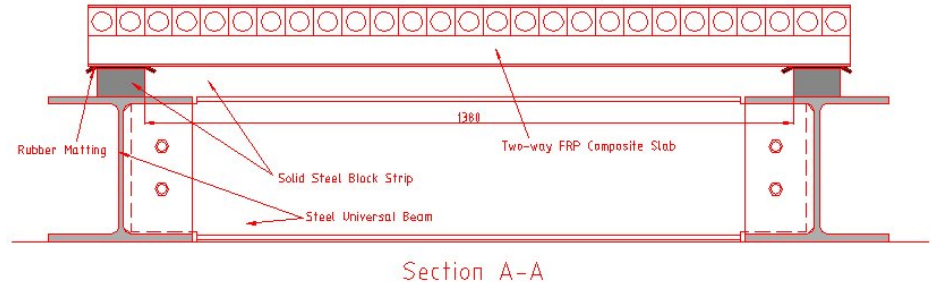

(b)

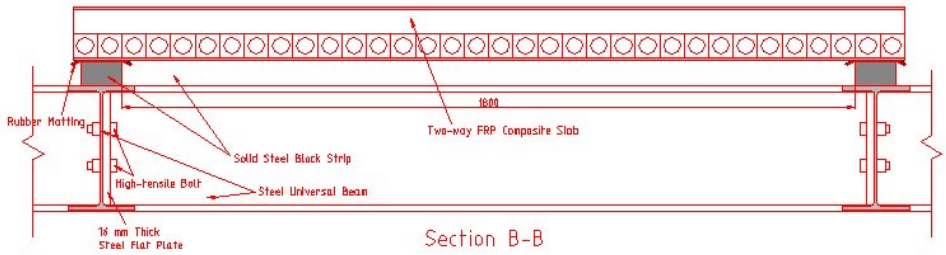

(c)

Figure 6.5 Detailed test setup configuration for the prototype two-way FRP slab: (a) Top view; (b) Section A-A; (c) Section B-B

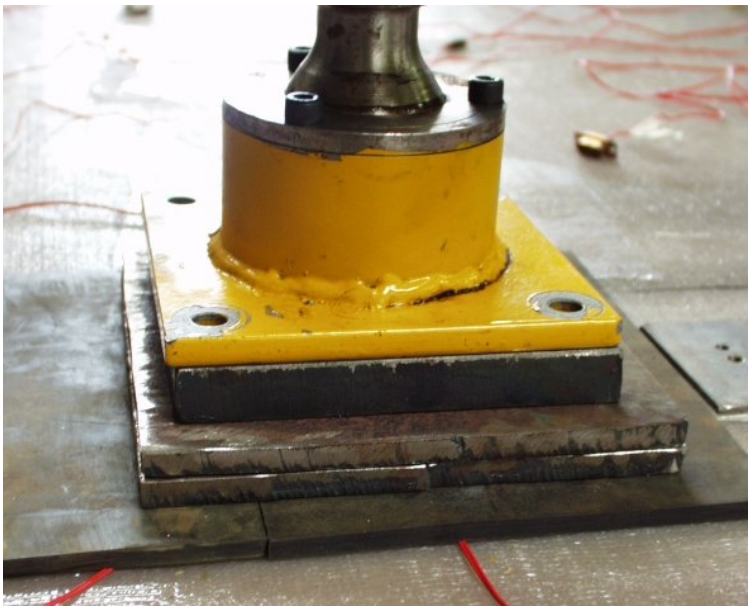

Figure 6.6 Combination of steel plates and rubber matting underneath the loading platen

Figure 6.7 shows the comparison of 3D FEA results for the centre deflection at the top and bottom surface of the slab. This result indicates that the centre deflection at

the top surface is marginally higher (approximately 2%) than that at bottom surface of the slab. Due to difficulties associated with measuring the deflection of underside of the slab, it decided that the centre deflection would be measured at the top surface of the slab throughout the experimental investigation (Figure 6.4).

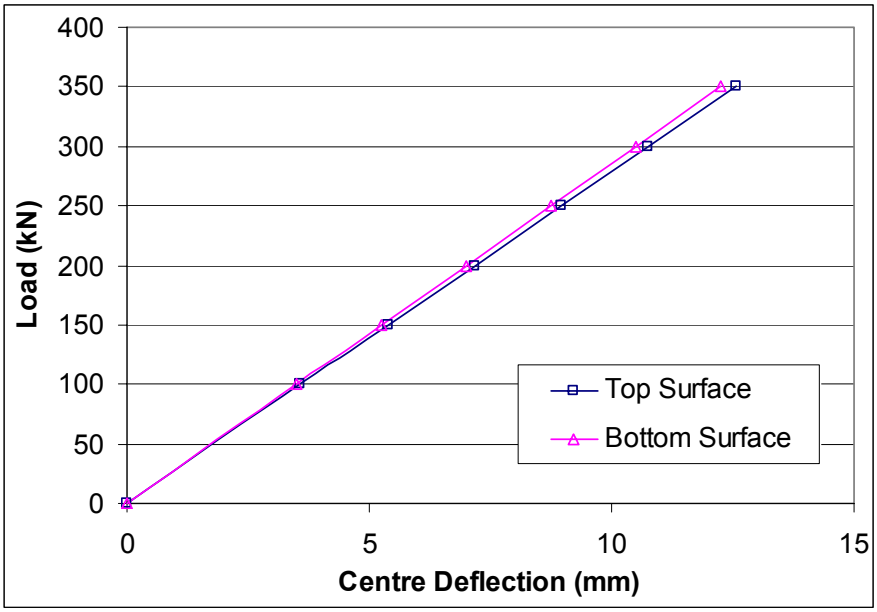

Figure 6.7 Comparison of the centre deflection at between top and bottom surface of the slab

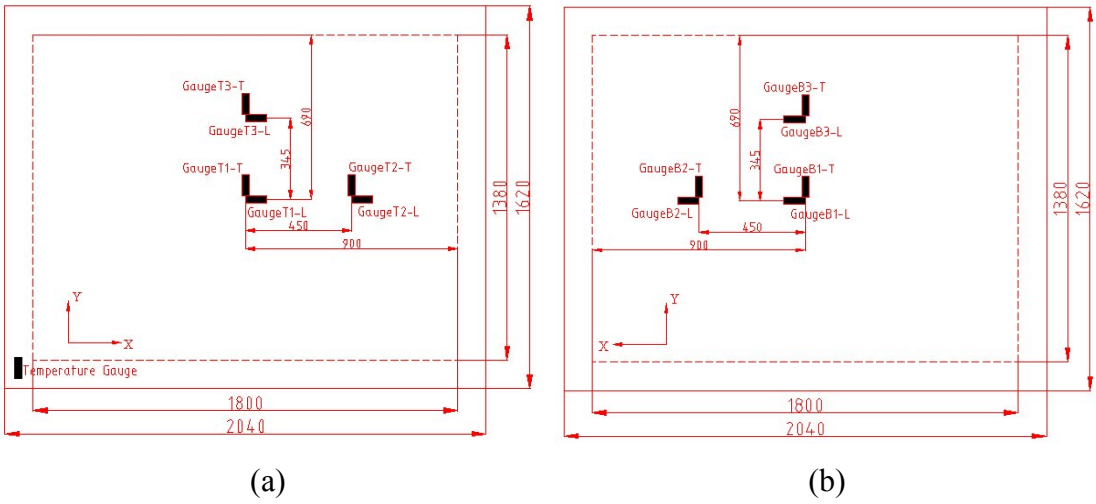

(a) (b)

Figure 6.8 Location of strain gauges on: (a) Top surface of the slab; (b) Bottom surface of the slab

A number of unidirectional strain gauges were bonded to the top and bottom surfaces of the slab to measure longitudinal strains (length direction) and transverse strains (width direction) at the locations shown in Figure 6.8. T1-L refers to the gauge at the top middle surface of the slab measuring longitudinal strain and T1-T refers to the gauge at the same position but measuring transverse strain. The digits "2" and "3" refer to the gauge position along longitudinal and transverse direction respectively. Measurement of the centre compressive strain of the slab was not possible due to the presence of the loading platen, and the difficulties associated with the accurate measurement of the complex stress field in the immediate vicinity of the concentrated load. Hence, no strain data at the middle of the top slab surface was recorded throughout the testing programs.

All data obtained from testing of the prototype two-way FRP slab was measured electronically. Data signals from the instrumentation were fed into a 15-channel data acquisition system (HP System 5000), which was linked to a compatible computer for storage in unformatted data files. These were later formatted and analysed using Microsoft Excel 2000.

6.4 Static Tests

In this section, four different static tests are described (refer Section 6.1), namely

- Test 2: Static loading up to 25% of 3D FEA predicted PFR cracking load test;
- Test 3: Static loading up to 70% of 3D FEA predicted PFR cracking load test;
- Test 5: Failure load test;
- Test 6: Post failure behaviour test.

The objective of conducting these tests was to verify the simplified approach and 3D finite element modelling discussed in the previous chapters, to investigate the flexure strength and stiffness of the slab experimentally, and understand the failure mode of the slab.

6.4.1 Static Loading up to 25% of 3D FEA Predicted PFR Cracking Load Test

The first static test (Test 2) investigated the static behaviour of the two-way FRP slab up to a load of 75 kN (approximately 25% of the 3D FEA predicted PFR cracking load). The reason for choosing a load limit of 75 kN (corresponding to maximum strain level of about 1332 microstrain at the bottom surface of the slab obtained from 3D complete slab FEA) was to retain the test in the linear elastic range, and to avoid damaging the slab.

Due to the anti-symmetric nature of the slab cross-section associated with the different spans in longitudinal and transverse direction (Chapter 3), the prototype two-way FRP slab may exhibit different behaviour when loaded in different cross-section orientations. In order to understand this behaviour better, two different tests were conducted in the experimental program of Test 2. In the first test, the slab was loaded in the original orientation, denoted as Orientation 1, which is shown in Figure 6.9(a). While in the second test the slab was loaded in the inverted direction to Orientation 1 which is denoted as Orientation 2, as shown in Figure 6.9(b). Note particularly that the test arrangements for both cross-section orientations are identical, however, the circular voids that were on the top of cross-section (Figure 6.9(a)) are at the bottom of cross-section (Figure 6.9(b)). Both tests were conducted to the same load level. It should be noted that all subsequent tests were conducted by loading the prototype slab in Orientation 1 unless otherwise specified.

(a) (b)

Figure 6.9 View of the two-way FRP slab loaded in different cross-section orientations: (a) Orientation 1; (b) Orientation 2

The load was applied at a rate of 2 mm/minute, with the load, centre deflection (at the load point) and strains recorded at the intervals of 0.1s during the testing.

6.4.1.1 Slab Loaded in Orientation 1

The load-deflection diagram for the first test together with the Ritz and FE results are provided in Figure 6.10. As expected, the load versus deflection behaviour was linear elastic throughout the test.

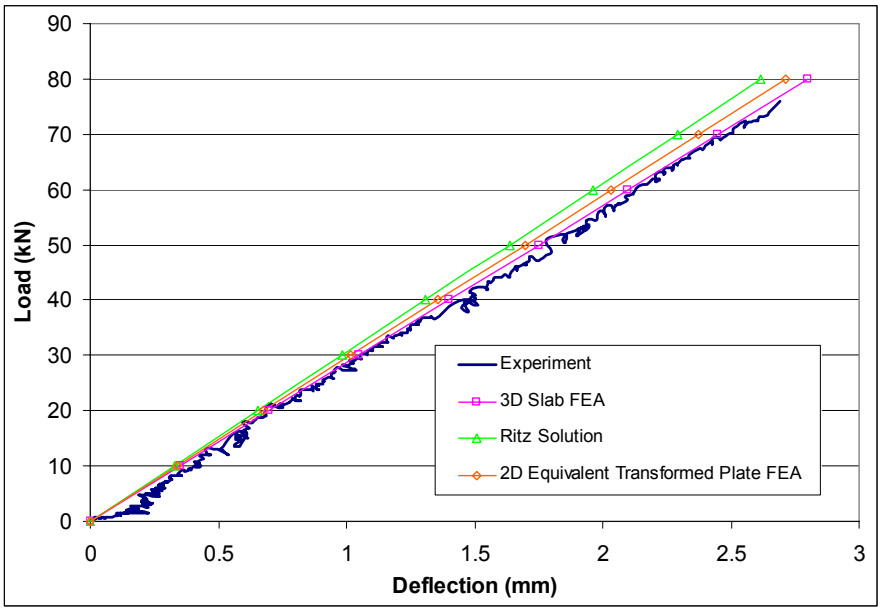

Figure 6.10 Load-deflection behaviour for the first test of the Test 2

The deflection comparison in the figure shows good agreement between experimental and analytical results in the linear elastic range. Considering experimental variability, there is no significant difference between 3D slab FEA and experimental results. However, the Ritz solution and 2D equivalent transformed plate FEA result indicate a difference of about 5.7% and 2.4% respectively when compared with experimental results. This is probably due to the effect of the localized loading condition imposed on the test, which is not accurately captured by the equivalent transformed plate model (refer Chapter 4).

Comparison between the strains predicted by the 3D slab FEA and those measured by the strain gauges on the test slab also yield favourable results. As shown in

Figures 6.11(a) through 6.11(j), the strains calculated by the 3D FE analysis are relatively accurate, with a typical variation of 6%. Eliminating possible uncertainties caused by experimental variability and convergence of the finite element results, this correlation is quite good.

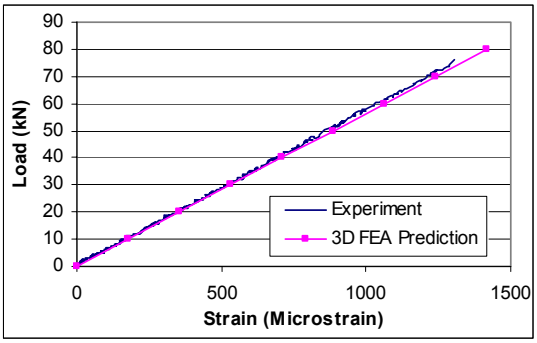

Figure 6.11(a) Strain from strain gauge B1-L for the first test of Test 2 compared with 3D FEA prediction

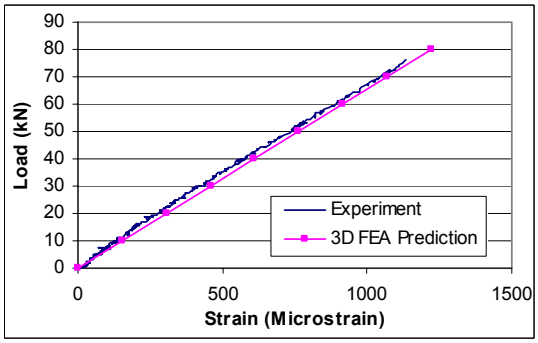

Figure 6.11(b) Strain from strain gauge B1-T for the first test of Test 2 compared with 3D FEA prediction

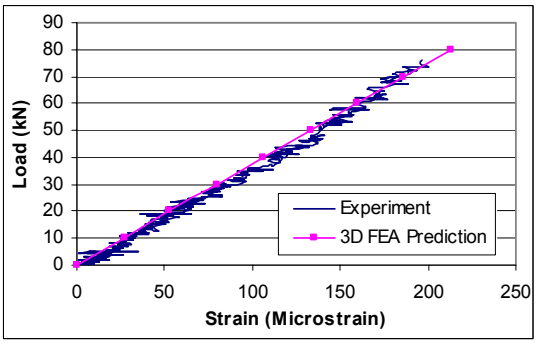

Figure 6.11(c) Strain from strain gauge B2-L for the first test of Test 2 compared with 3D FEA prediction

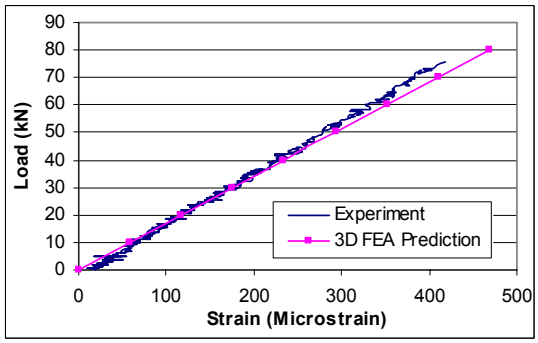

Figure 6.11(d) Strain from strain gauge B2-T for the first test of Test 2 compared with 3D FEA prediction

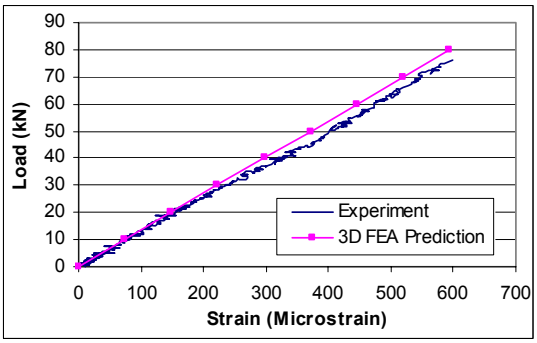

Figure 6.11(e) Strain from strain gauge B3-L for the first test of Test 2 compared with 3D FEA prediction

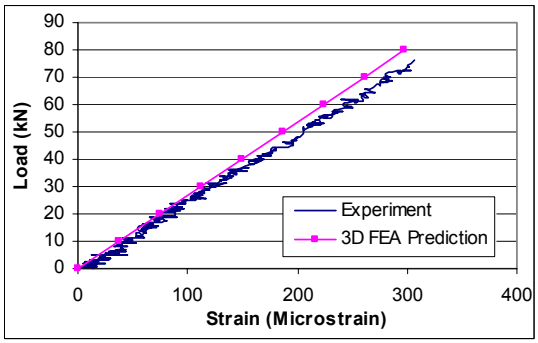

Figure 6.11(f) Strain from strain gauge B3-T for the first test of Test 2 compared with 3D FEA prediction

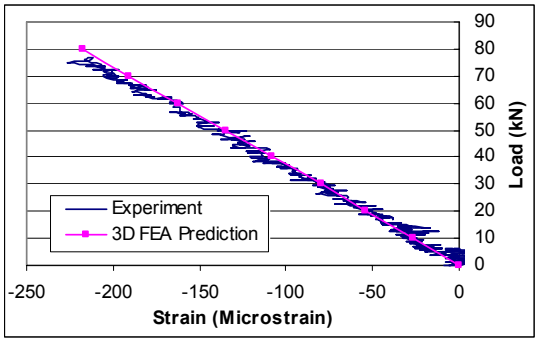

Figure 6.11(g) Strain from strain gauge T2-L for the first test of Test 2 compared with 3D FEA prediction

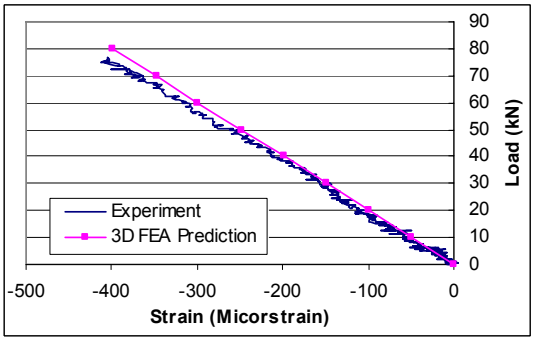

Figure 6.11(h) Strain from strain gauge T2-T for the first test of Test 2 compared with 3D FEA prediction

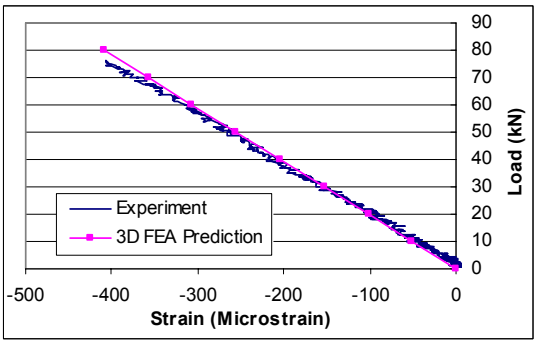

Figure 6.11(i) Strain from strain gauge T3-L for the first test of Test 2 compared with 3D FEA prediction

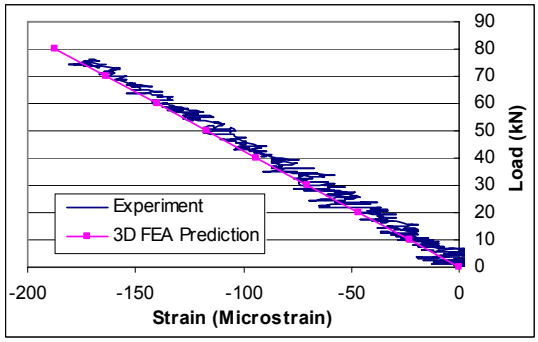

Figure 6.11(j) Strain from strain gauge T3-T for the first test of Test 2 compared with 3D FEA prediction

6.4.1.2 Slab Loaded in Orientation 2

This section describes the second test of the Test 2 series that was conducted to investigate the structural response of the two-way FRP slab when loaded in orientation 2. This test provided an additional opportunity to evaluate the accuracy of both 2D equivalent transformed plate and 3D slab models presented in the previous chapters.

The same mesh details, input material properties, and analysis procedures as presented in Chapter 5 were used to perform the linear static finite element analysis of the fibre composite floor slab with all edges simply supported while loaded in

Orientation 2. The load-deflection diagram for the second test and the comparison with analytical and numerical results are shown in Figure 6.12.

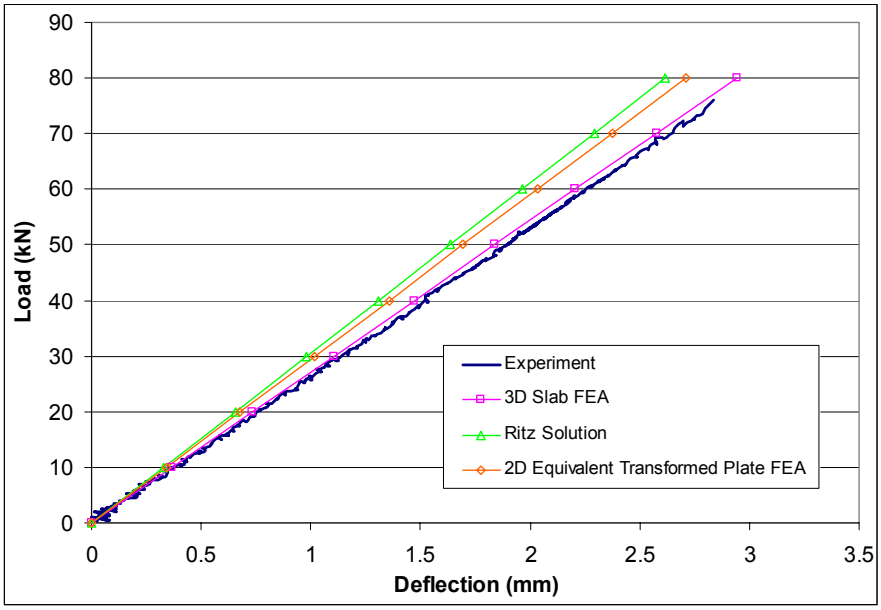

Figure 6.12 Load-deflection behaviour for the second test of the Test 2

Again, linear load-deflection behaviour was observed throughout the test. Similar to the observation obtained for the slab loaded in Orientation 1, the comparison in Figure 6.12 shows no significant difference between the 3D slab FEA and the experiment. However, considerable discrepancy was observed (about 12% and 8.9% for the Ritz solution and 2D equivalent transformed plate FEA respectively when compared with experimental results. This is probably due to the same reason described for the slab loaded in Orientation 1. Nevertheless, the overall agreement is reasonably satisfactory.

Figure 6.13(a) through 6.13(j) depicts the bottom and top strains resulting from the finite element analysis and experiment. It should be noted that the label of the top and bottom strain gauges defined in Figure 6.8 remained constant in the second test of the Test 2, but actual locations of these strain gauges were revised when compared with first test of the Test 2. Again, relatively good agreement between experimental and 3D slab FEA results was obtained with typical variation of approximately 6%.

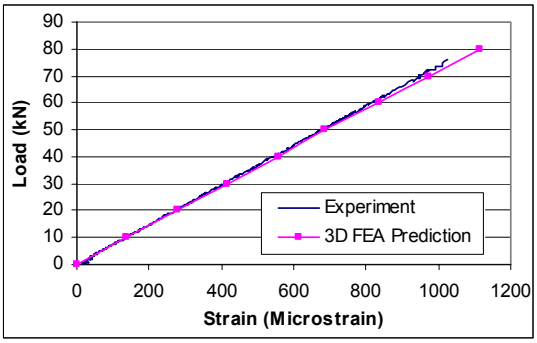

Figure 6.13(a) Strain from strain gauge T1-L for the second test of Test 2 compared with 3D FEA prediction

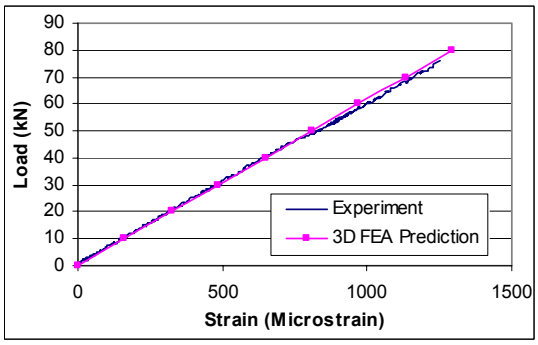

Figure 6.13(b) Strain from strain gauge T1-T for the second test of Test 2 compared with 3D FEA prediction

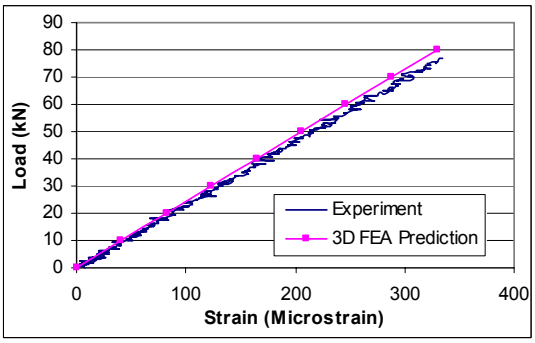

Figure 6.13(c) Strain from strain gauge T2-L for the second test of Test 2 compared with 3D FEA prediction

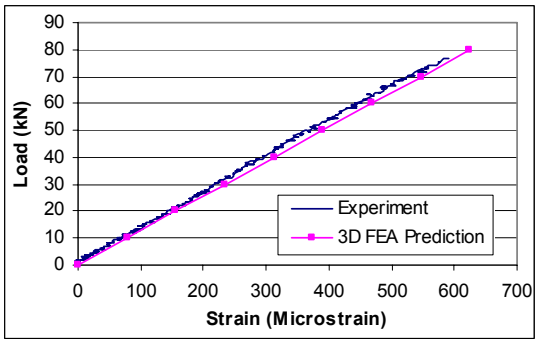

Figure 6.13(d) Strain from strain gauge T2-T for the second test of Test 2 compared with 3D FEA prediction

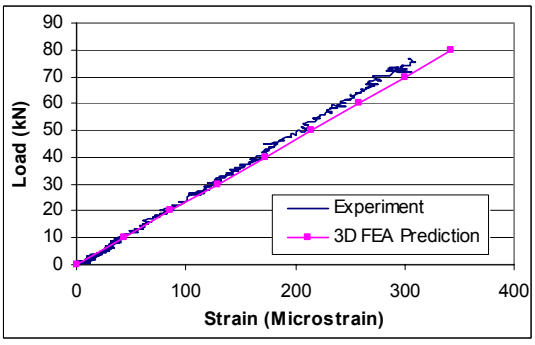

Figure 6.13(e) Strain from strain gauge T3-L for the second test of Test 2 compared with 3D FEA prediction

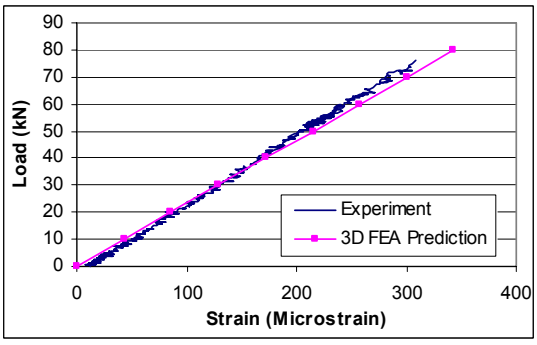

Figure 6.13(f) Strain from strain gauge T3-T for the second test of Test 2 compared with 3D FEA prediction

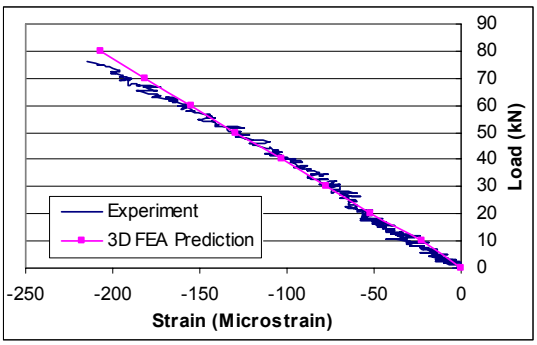

Figure 6.13(g) Strain from strain gauge B2-L for the second test of Test 2 compared with 3D FEA prediction

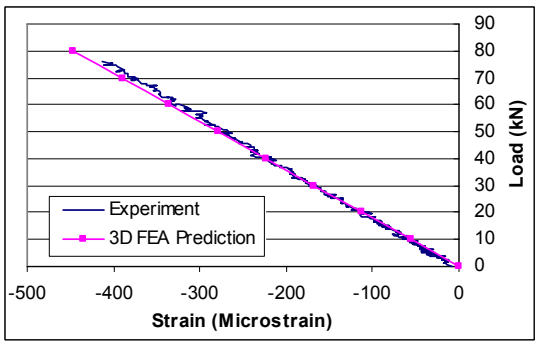

Figure 6.13(h) Strain from strain gauge B2-T for the second test of Test 2 compared with 3D FEA prediction

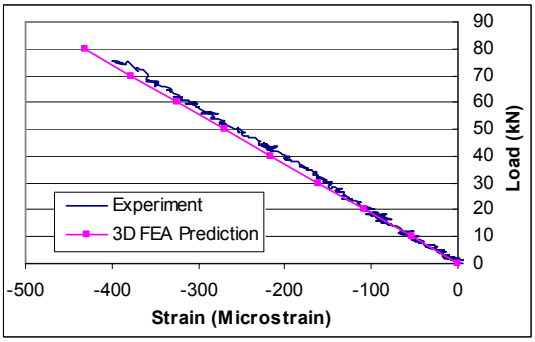

Figure 6.13(i) Strain from strain gauge B3-L for the second test of Test 2 compared with 3D FEA prediction

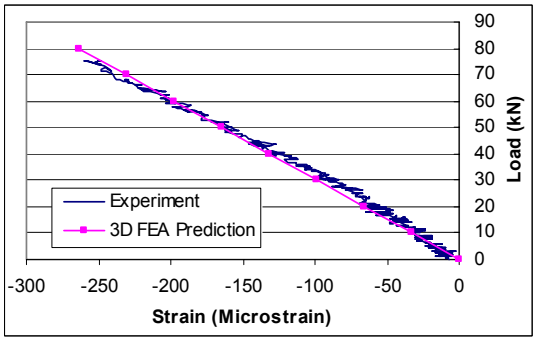

Figure 6.13(j) Strain from strain gauge B3-T for the second test of Test 2 compared with 3D FEA prediction

6.4.1.3 Comparisons and Discussions

The comparison of the load-deflection response between two loading orientations for different results is given in Figures 6.14(a) to 6.14(d). It is seen that the slab loaded in orientation 1 gives a somewhat stiffer response than the slab loaded in orientation 2 for the case of experiment and 3D slab FEA. The discrepancy of orientation 1 in comparison with orientation 2 is obtained at about 6.4% for the experiment, 4.9% for the 3D slab FEA. This result indicates that the difference in stiffness behaviour of the slab between two orientations is detectable but relatively insignificant. Considering experimental variability, the difference predicted by 3D slab FEA is also consistent with the experimental results. However, such difference was not captured by the Ritz solution and 2D equivalent transformed plate FEA,

which indicates that the simplified transformed approach is unable to identify the difference in the behaviour of the slab between the two orientations.

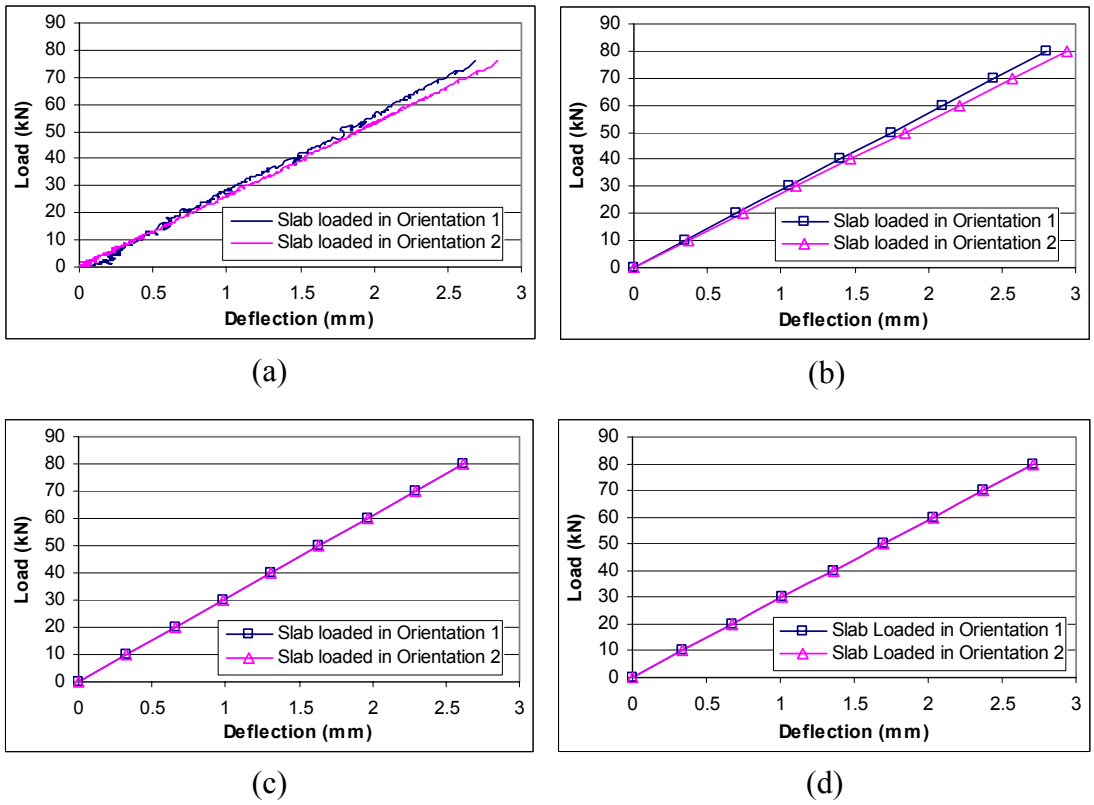

Figure 6.14 Stiffness comparisons for the slab loaded in two different cross-section orientations: (a) Experiment; (b) 3D slab FEA; (c) Ritz solution; (d) 2D equivalent transformed plate FEA

Table 6.1 Strain comparison for the slab loaded in two different orientations

	Experiment	3D FEA
Longitudinal strain for slab loaded in orientation 1 (microstrain)	1307	1332
Longitudinal strain for slab loaded in orientation 2 (microstrain)	1024	1045
Transverse strain for slab loaded in orientation 1 (microstrain)	1135	1147
Transverse strain for slab loaded in orientation 2 (microstrain)	1255	1214

Table 6.1 shows the comparison of the bottom longitudinal and transverse strains at the middle of the slab for two loading orientations at a load of 75 kN. Both

experimental and 3D FEA results show considerable difference of fibre strain between two loading orientations with the maximum discrepancy of 28% for longitudinal strain and 9.6% for transverse strain.

Based on Test 2 presented in this section, several conclusions can be drawn as follows:

- 3D slab FEA predicts the linear elastic behaviour of the slab very accurately (within bounds of experimental variability).
- Transformed plate approach produces reasonably accurate results of the slab stiffness when compared with the experiment. However, a maximum discrepancy of 12% exists, which consists of effects of the local deformation, cross-section orientation and assumption made during the analytical procedure.
- Structural behaviour of the proposed two-way FRP composite slab varies between orientation 1 and 2 with insignificant influence on slab stiffness and considerable influence on slab strain, which are only captured by the 3D slab FEA and experiment.
- Transformed plate approach was unable to reveal the difference in stiffness behaviour of the slab between orientation 1 and 2 because its formulation does not include sufficient geometric parameters.

Despite the variations mentioned above, it can be concluded that both 2D equivalent transformed plate and 3D slab models successfully replicated the slab behaviour in the lower portion of the linear elastic range, and can be used to justify the assumptions and simplifications used in the analyses.

6.4.2 Static Loading up to 70% of 3D FEA Predicted PFR Cracking Load Test

The second static test (Test 3) extended the investigation described in Section 6.4.1 to observe static behaviour of the proposed two-way FRP composite slab system up to a load of 200 kN (70% of 3D FEA predicted PFR cracking load). The aim of this test was to investigate the stiffness and strength characteristics of the slab at

relatively high load level prior to fatigue indication test (Test 4, described in Section 6.5.2) without any significant damage to the slab specimen.

The load was applied at a rate of 2 mm/minute, with the load, centre deflection (at the load point) and strains recorded during the testing at the intervals of 0.1s.

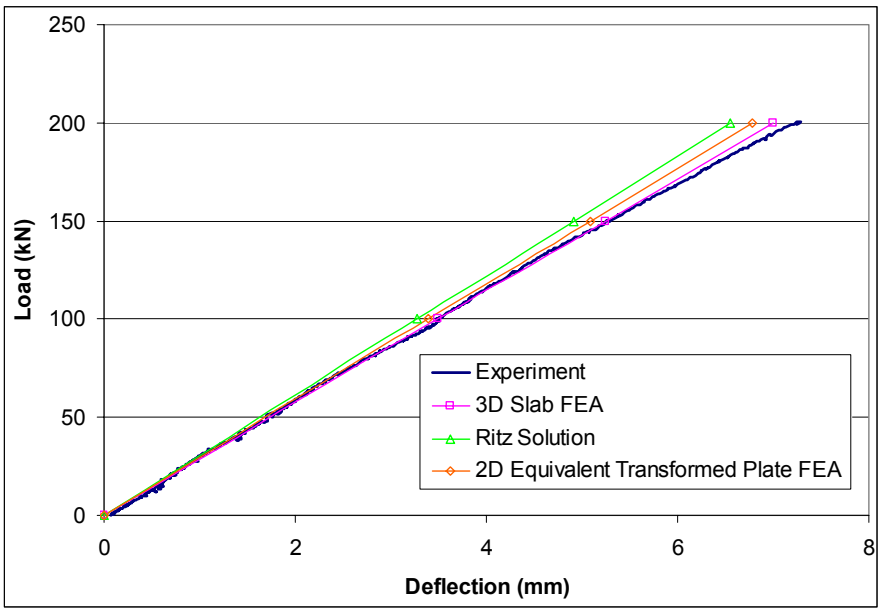

Figure 6.15 Load-deflection curve for static loading up to 200kN

The results gained from the test data yield linear load-deflection behaviour up to 200 kN, as shown in Figure 6.15. The comparison in the figure shows relatively good agreement between experiment and analyses, and indicates that both simplified 2D plate and 3D slab models can accurately predict the load-deflection behaviour up to a load of 200 kN. The 3D FE model gives more accurate prediction than the equivalent transformed plate model due to the reasons summarised in Section 6.4.1.1.

During the load cycle up to 200 kN, audible noises firstly occurred at a load of about 88 kN, and then again at about 163 kN. Minor reductions in stiffness at these loads were observed in the load-deflection curve (Figure 6.15). Despite these observations, the results indicate that there was no significant loss in overall stiffness of the slab specimen. Consequently, the noise was possibly caused by small cracks in the adhesive between adjacent modules at the bottom middle of the slab instead of PFR core itself. As a result, these tiny cracks would not significantly detract from overall stiffness characteristics of the slab.

Figure 6.16(a) through 6.16(j) shows the strain data recorded from the test in comparison with 3D slab FEA results (Chapter 5). Reasonably good agreement was obtained between the experiment and 3D FEA prediction with typical variation of approximately 5%. This indicates that satisfactory 3D finite element prediction of strength characteristic of the slab can be achieved for static loading up to 200 kN. As expected, the overall largest longitudinal and transverse strains of 3662 microstrain and 3497 microstrain were recorded at 200 kN from the strain gauges B1-L and B1-T respectively, located on the bottom surface of the slab, directly underneath the loading patch. The comparable longitudinal and transverse strains also further verified the 3D slab FEA findings presented in Section 5.3.1 which showed that the load was reasonably evenly distributed in both directions demonstrating the typical characteristic of two-way slab structures.

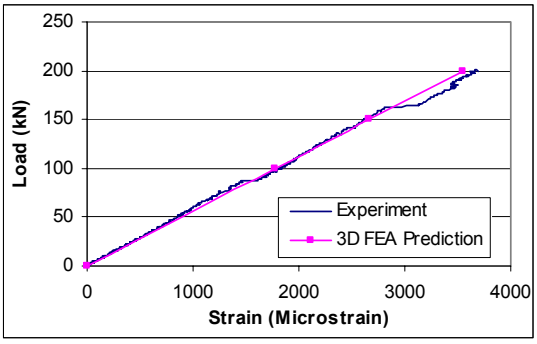

Figure 6.16(a) Strain from strain gauge B1-L for static loading up to 200kN test compared with 3D FEA prediction

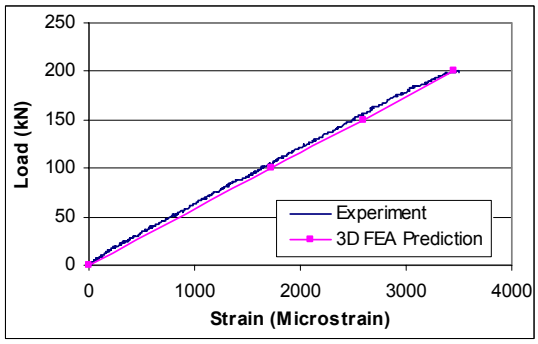

Figure 6.16(b) Strain from strain gauge B1-T for static loading up to 200kN test compared with 3D FEA prediction

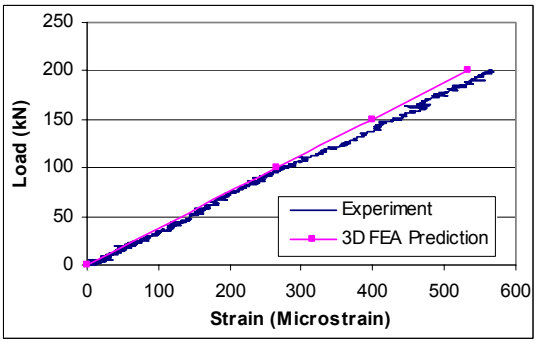

Figure 6.16(c) Strain from strain gauge B2-L for static loading up to 200kN test compared with 3D FEA prediction

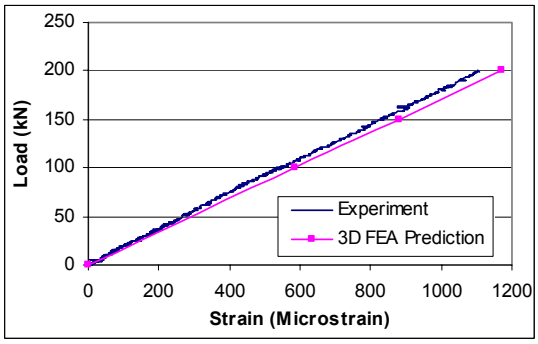

Figure 6.16(d) Strain from strain gauge B2-T for static loading up to 200kN test compared with 3D FEA prediction

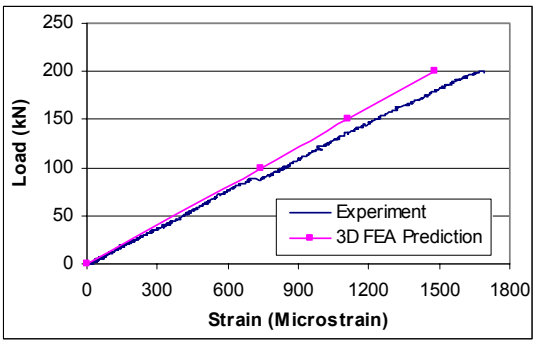

Figure 6.16(e) Strain from strain gauge B3-L for static loading up to 200kN test compared with 3D FEA prediction

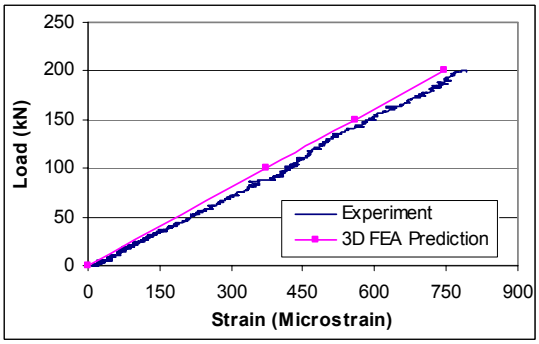

Figure 6.16(f) Strain from strain gauge B3-T for static loading up to 200kN test compared with 3D FEA prediction

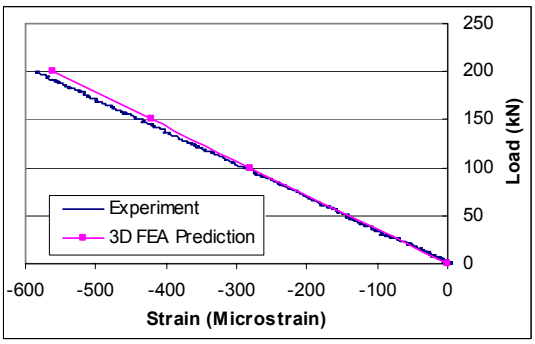

Figure 6.16(g) Strain from strain gauge T2-L for static loading up to 200kN test compared with 3D FEA prediction

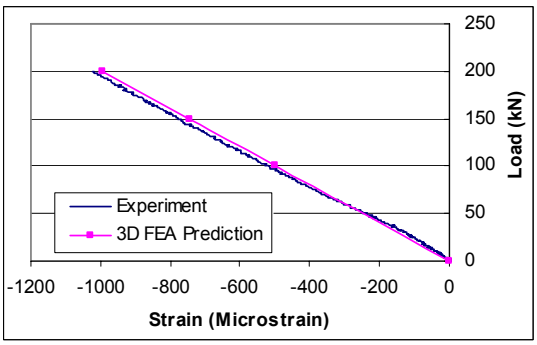

Figure 6.16(h) Strain from strain gauge T2-T for static loading up to 200kN test compared with 3D FEA prediction

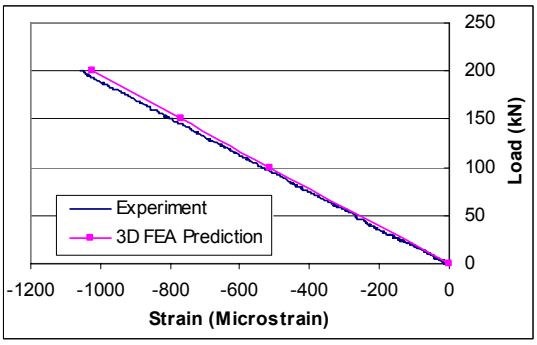

Figure 6.16(i) Strain from strain gauge T3-L for static loading up to 200kN test compared with 3D FEA prediction

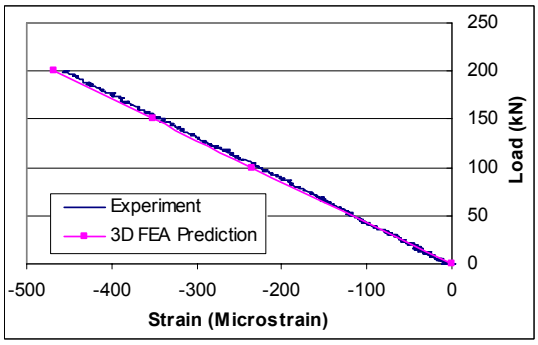

Figure 6.16(j) Strain from strain gauge T3-T for static loading up to 200kN test compared with 3D FEA prediction

Despite the cracking that possibly occurred in the adhesive between adjacent modules, the strain results indicated no significant loss in strain of the slab up to a load of 200 kN. From these strain results, it also can be seen that the response to the

audible noise at load of 88 kN and 163 kN during the test were captured in load-strain curves for bottom strain gauges B1-L, B1-T, B3-L and B3-T, respectively. No similar response was observed in the diagrams for the bottom strain gauge B2-L and B2-T and all strain gauges at the top surface of the slab specimen. This is further evident that small localized cracks most likely occurred in the adhesive between the two modules at the bottom middle of the slab (considering the locations of the strain gauges B3-L and B3-T) rather than in the PFR core. Moreover, a careful inspection of the test piece (particularly the area of the bottom surface across midspan of the slab along the transverse direction) was conducted at the conclusion of this load cycle, and revealed no visible sign of damage to the glass fibre laminate.

6.4.3 Failure Load Test

For the third static test, the slab specimen was tested to failure under a static loading after Test 4 – fatigue indication test (described in Section 6.5.2) had been completed. The intention of conducting this test was to determine the ultimate load capacity of the two-way FRP composite slab and evaluate the mode of the failure.

The load was applied at a rate of 2 mm/minute, with the load, centre deflection (at the load point) and strains recorded throughout the duration of the test at the intervals of 0.1s.

The load-deflection diagram for the failure test of the two-way FRP composite floor slab is provided in Figure 6.17 and indicates a fairly linear and consistent response up to a load level of approximately 250 kN. The first considerable noise (possibly initial cracking in PFR core) occurred at a load of 238 kN with centre deflection of 8.60 mm, subsequently three relatively loud noises were heard at loads of 284 kN, 316 kN and 338 kN respectively accompanied by the load drops, as shown in the load-deflection curve. The load of 238 kN will be referred to as “first PFR core cracking” load. After this load, the slab clearly demonstrated a loss in stiffness. When the load reached 347 kN, a loud noise was heard, and the load was promptly removed due to the automatic unloading caused by the hydraulic actuator of Instron testing machine. This is a safety feature of the Instron system. The large load drop at the load of 347 kN exceeded the limit of sudden load change of the load control

system of the testing machine and resulted in activating the emergency stop to ensure no damage to the hydraulic actuator.

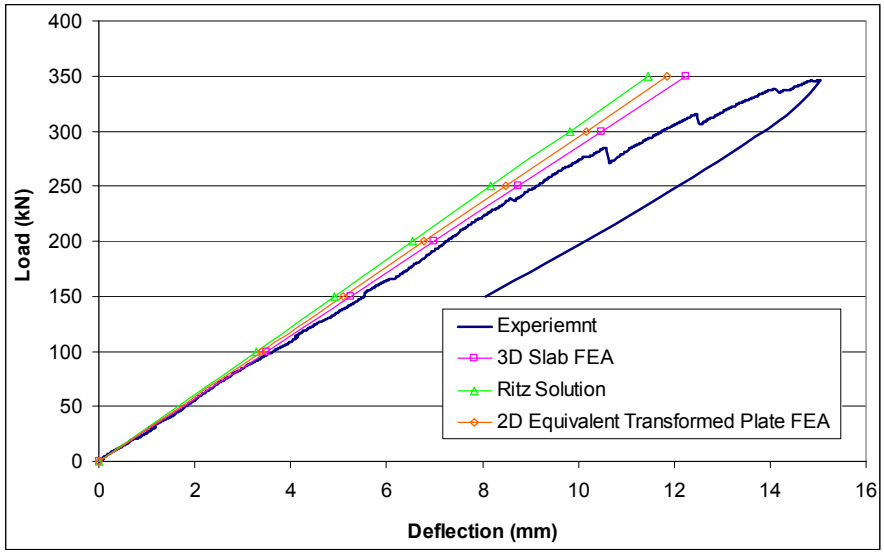

Figure 6.17 Load-deflection curve for the failure test of the slab

The deflection comparison in Figure 6.17 shows reasonably good agreement between analytical, finite element and experimental results until the first PFR core cracking occurred. This finding also indicates that both simplified approach (Chapter 4) and 3D finite element analysis (Chapter 5) are able to predict the load-deflection behaviour of the two-way FRP composite slab up to the first PFR cracking load. However, this failure test was unable to determine the maximum failure load of the slab due to the automatic unloading feature of the Instron testing machine. Since the large load reduction occurred at a load of 347 kN (that resulted in automatic unloading), it is reasonable to assume that the maximum failure load was close to 347 kN.

Figure 6.18(a) through 6.18(j) shows the strain data recorded from the test in comparison with 3D slab FEA results. Reasonably good agreement was obtained between the experiment and 3D FEA prediction in the initial region up to 238 kN with typical variation of approximately 5%. This indicates that a satisfactory finite element prediction of strength characteristic of the slab was achieved until the first PFR core cracking occurred. The overall largest strains of 4623 microstrain in the longitudinal direction and 4556 microstrain in the transverse direction were recorded at 238 kN from the strain gauges B1-L and B1-T respectively. Again, the comparable

longitudinal and transverse strains recorded on the bottom middle surface of the slab during the test verifies the 3D FEA findings presented in Section 5.3.1, and indicate that the two-way FRP slab evenly distributes the load in both directions in a predictable manner.

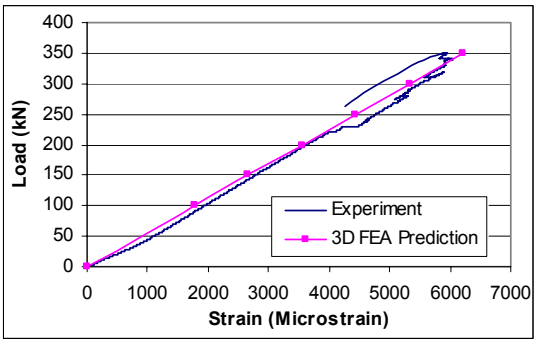

Figure 6.18(a) Strain from strain gauge B1-L for the failure test compared with 3D FEA prediction

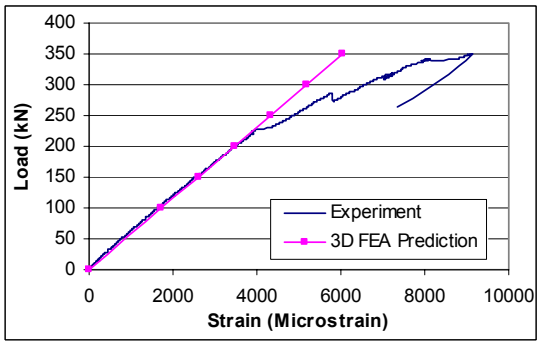

Figure 6.18(b) Strain from strain gauge B1-T for the failure test compared with 3D FEA prediction

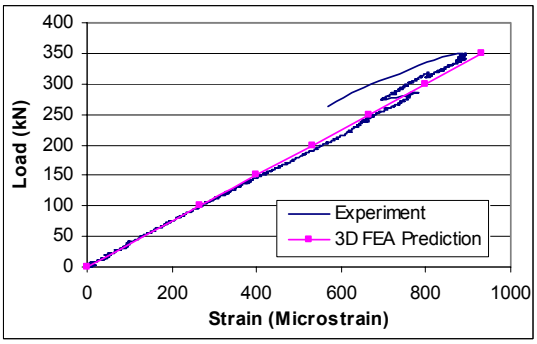

Figure 6.18(c) Strain from strain gauge B2-L for the failure test compared with 3D FEA prediction

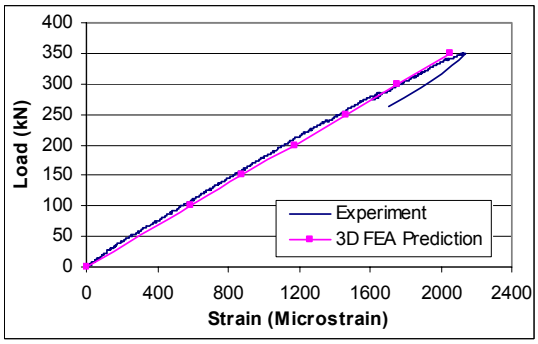

Figure 6.18(d) Strain from strain gauge B2-T for the failure test compared with 3D FEA prediction

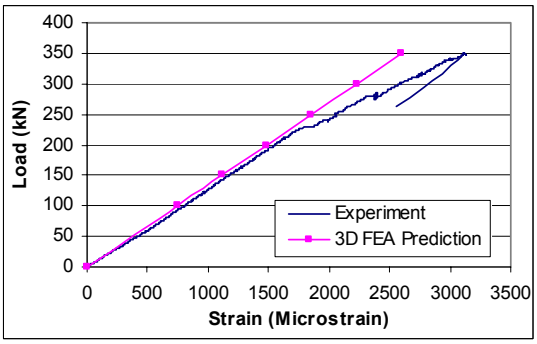

Figure 6.18(e) Strain from strain gauge B3-L for the failure test compared with 3D FEA prediction

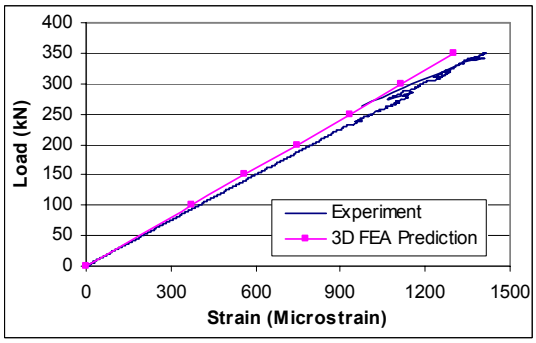

Figure 6.18(f) Strain from strain gauge B3-T for the failure test compared with 3D FEA prediction

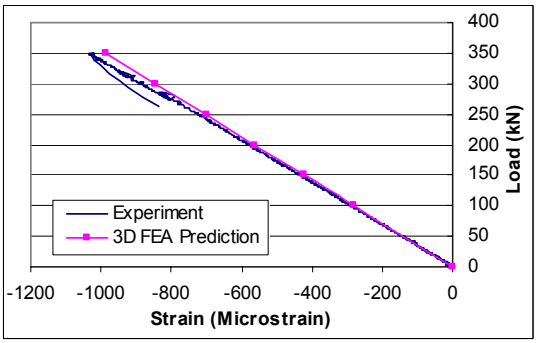

Figure 6.18(g) Strain from strain gauge T2-L for the failure test compared with 3D FEA prediction

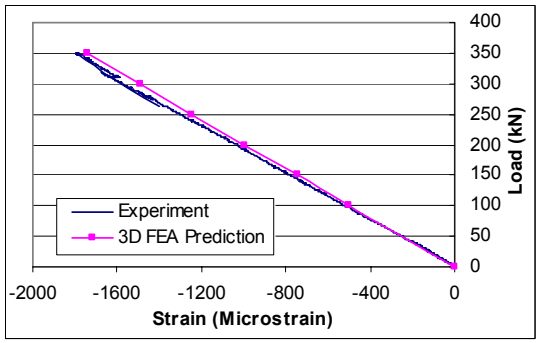

Figure 6.18(h) Strain from strain gauge T2-T for the failure test compared with 3D FEA prediction

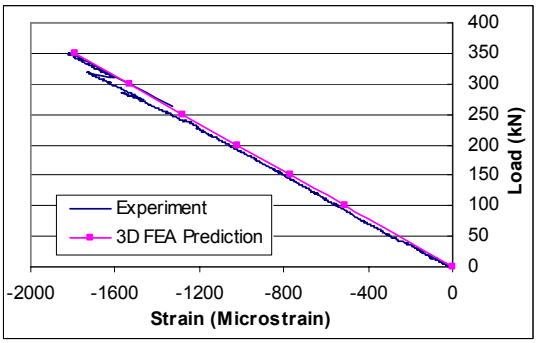

Figure 6.18(i) Strain from strain gauge T3-L for the failure test compared with 3D FEA prediction

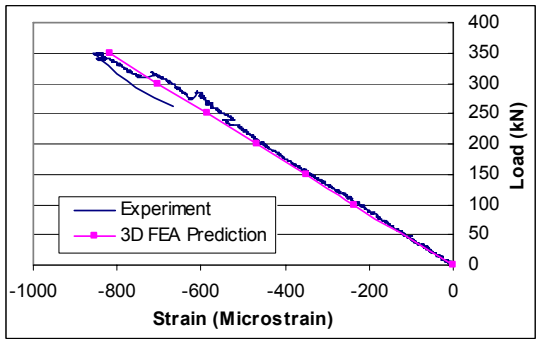

Figure 6.18(j) Strain from strain gauge T3-T for the failure test compared with 3D FEA prediction

At the end of this load cycle to failure (Test 5), a large localized deformation around the edge of the loading patch on the top surface of the slab was clearly observed. Inspection of the slab at the conclusion of this load cycle also revealed local debonding between bottom laminate skin and modular core assembly at the bottom surface of the slab, directly underneath the loading patch. However no rupture of glass fibre laminates was found. Such observations would be consistent with punching shear failure (out-of-plane shear failure of the composite slab) due to the shear cracking of PFR core, which agreed with 3D FEA predicted failure mode (refer Chapter 5). However, the first PFR core cracking load of 238 kN due to punching shear was lower than the FEA prediction (280 kN). This difference could be explained by the fact that a relatively simple unidirectional failure criterion was used to predict the FRP core cracking load in the 3D finite element analysis (Chapter 5) instead of more sophisticated multi-directional failure criterion.

Table 6.2 Comparison of test results between two tests of the two-way FRP slab

Static testing stage	Experimental values at a load of 200kN		
	Centre deflection (mm)	Longitudinal strain at gauge B1-L (microstrain)	Transverse strain at gauge B1-T (microstrain)
Test 3 (static test up to 200kN before 1,000,000 cycles)	7.27	3662	3497
Test 5 (static test to failure after 1,000,000 cycles)	7.29	3649	3511

A comparison of strain and deflection measurements at a load of 200 kN for the Test 3 (static loading up to 70% 3D FEA predicted PFR cracking load test) and Test 5 (failure load test) conducted after 1,000,000 fatigue cycles are shown in Table 6.2 (refer Section 6.1). The centre deflection at 200 kN of load for the failure test after fatigue cycles was 7.29 mm, and the measured strains were 3649 microstrain in longitudinal direction and 3511 microstrain in the transverse direction from the strain gauges B1-L and B1-T respectively. These values show good agreement with those measured during the second static test up to a load of 200 kN (Table 6.2), which indicates no significant loss in stiffness or strength as a result of cyclic loading (detailed in Section 6.4.2). Furthermore, the result of this comparison also suggests that the small cracking that occurred in Test 3 (static loading up to 200 kN) did not cause deterioration of the overall stiffness or strength characteristics of the slab.

6.4.4 Post Failure Behaviour Test

Since no rupture of glass fibre laminates was found after the failure load test (Test 5), it was reasonable to assume that the slab specimen may not have completely failed and may still have been capable of sustaining a greater post failure load. Thus, the unscheduled Test 6 (post failure behaviour test) including several static load cycles was conducted to further investigate the load carry capacity of the prototype two-way FRP slab after the occurrence of punching shear failure. A relatively large steel loading patch (370×290 mm) was used during these static load tests to prevent the progression of cracks caused by nominal punching shear from the previous failure

test. Load was measured using a 444 kN capacity load cell, and no strain was recorded since some of the strain gauges were found to be unserviceable after the previous failure test. For each load cycle, the load was applied at a rate of 2 mm/minute until the automatic unloading occurred due to the safety issue previously described. Load and centre deflection (at the load point) were recorded during the test at the intervals of 0.1s.

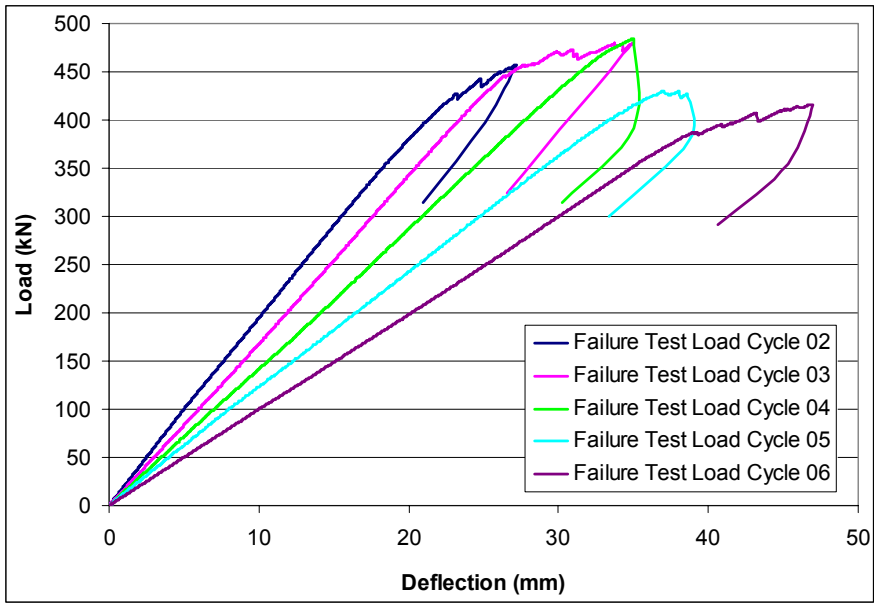

Figure 6.19 Load-deflection curve for the post failure behaviour test of the slab

Figure 6.19 depicts the load-deflection behaviour for these static load cycles of the Test 6. For each load cycle up to the unloading point, the deflection and load data indicate a fairly linear and consistent response. The significant loss in stiffness of the slab for each load cycle is clearly illustrated in Figure 6.19 due to the serious PFR core cracking that occurred during each reloading. The result from "failure test load cycle 02" also indicate that the large size of the steel loading patch (370×290 mm) successfully prevented the further cracking progression due to punching shear failure that occurred in the previous failure test, and the slab was able to sustain load up to 457 kN. The highest load recorded among these static load cycles was 484 kN. The mode of failure was again a punching shear failure, with significant localized deformation on the top surface of the slab and the relatively large debonding area at bottom surface of the slab, as shown in Figure 6.20. This was observed during the

inspection of the slab at the conclusion of all load cycles. Subsequently, the slab specimen was dissected after the failure test to further investigate the failure mode. Transverse and longitudinal sections through the slab in the damaged areas were cut using a circular saw with a diamond tipped blade.

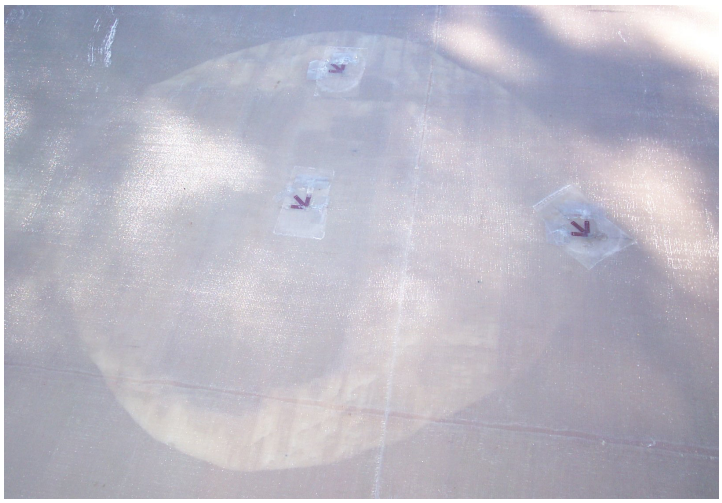

Figure 6.20 Debonding between fibre laminate skins and PFR core at the bottom surface of the slab

The location of the transverse cut and related damage is shown in Figure 6.21. The typical punching shear damage on the transverse section is clearly visible. Further demonstration of the shear failure through the section can be seen in Figure 6.22, which are magnified views from Figure 6.21. For both punching shear failures (using different size of load patches), the initial crack occurred in the PFR core of the upper assembled modules adjacent to the edge of loading patch. As load increased, the cracking progressed at 45° throughout the thickness of the assembled modules at the transverse section of the slab. Note that failure was accompanied by debonding between adjacent modules or upper and lower modular core assemblies, and rupture of glass fibre shear reinforcements (double bias circular tubes). This observation does not agree with the 3D FEA prediction that indicated no double bias shear reinforcement failure at the load level resulting in punching shear failure (Chapter 5). This could be explained by the high stress concentrations that may have been generated in the double bias circular tubes adjacent to these cracks as cracking in the PFR core progressed, and resulted in the earlier rupture of the shear reinforcement.

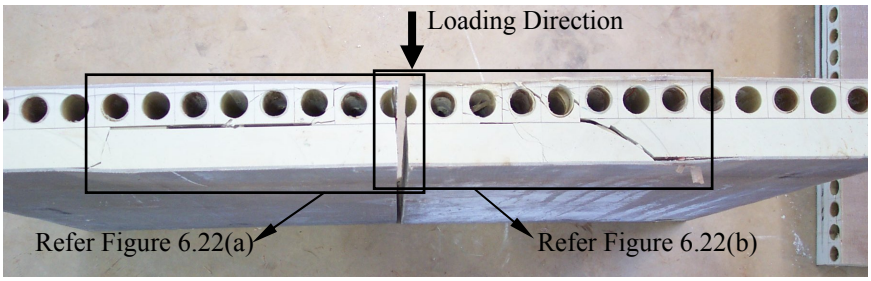

Figure 6.21 Transverse slab section after punching shear failure

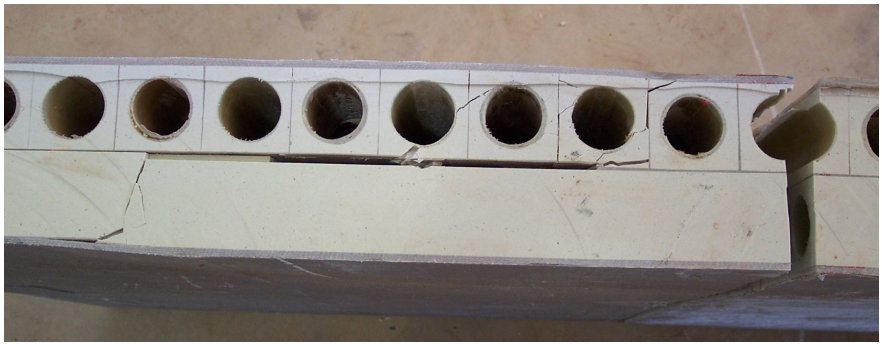

(a)

(b)

Figure 6.22 Magnified views of the transverse slab section after punching shear failure

In addition to the transverse section described above, the longitudinal section was cut through the middle of the module that is under the load patch from the damage area of the slab, as shown in Figure 6.23 with further magnified views in Figure 6.24. Typical punching shear damage on longitudinal section is again clearly visible. All the considerations described during the discussion of the transverse section also

apply here. In comparison with the view from the transverse section cut, the rupture of double bias shear reinforcement can be clearly seen from the cut through the longitudinal section.

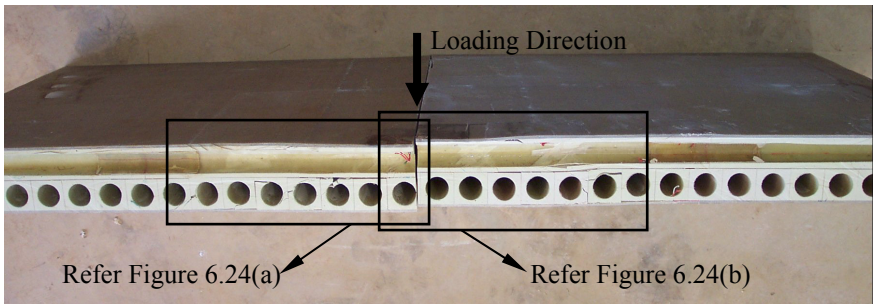

Figure 6.23 Longitudinal slab section after punching shear failure

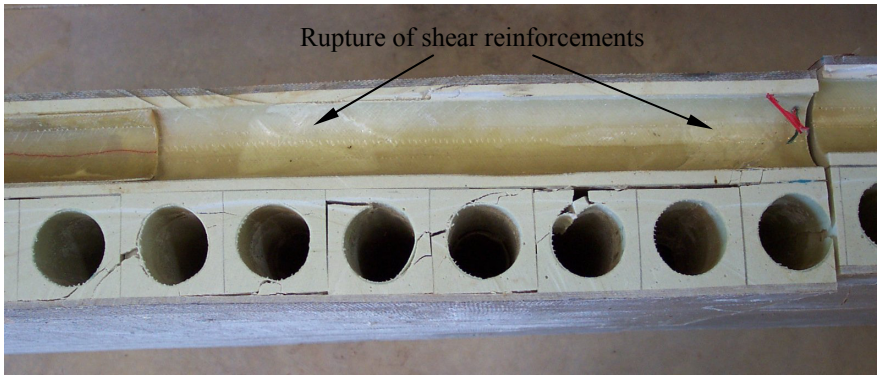

(a)

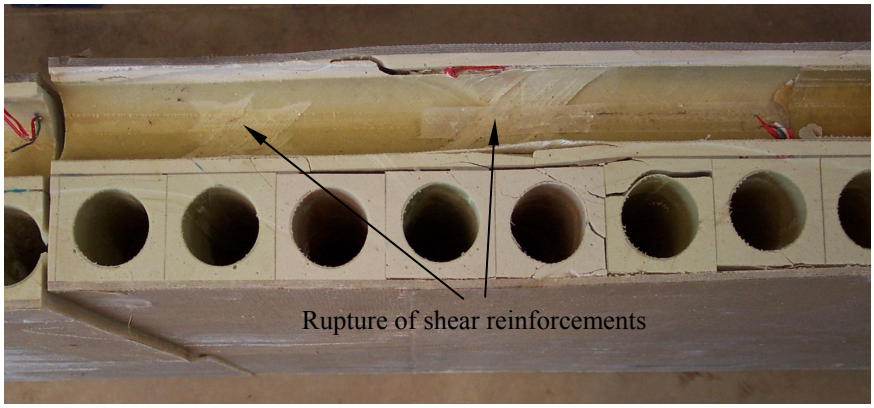

(b)

Figure 6.24 Magnified views of the longitudinal slab section after punching shear failure

6.5 Dynamic Test

In this section, the dynamic test of the two-way FRP composite slab including natural frequency test (Test 1) and fatigue indication test (Test 4) are described. The objective of this test program was to verify 3D FE dynamic analysis presented in Section 5.3.2, and to gain an initial indication of fatigue performance of the two-way FRP slab.

6.5.1 Natural Frequency Test

In this test, responses to excitation were measured with the slab unloaded as shown in Figure 6.24. The random test technique was used, such that the slab response was measured at a single location with excitation given at a number of locations on the slab specimen. A rubber mallet was used to excite the slab and an accelerometer (PCB Share Model 353B33 with 100 mV/g sensitivity) attached to the slab (as shown in Figure 6.25) was used to measure the slab response. Only vertical vibration response perpendicular to the plane of the composite slab was measured. A computer based data acquisition card (Model No. DAQCard 1200 manufactured by National Instruments) combined with a data acquisition system programmed using LabView (Version 5.1) software package were used to record the test data and store an unformatted data file through a linked compatible laptop computer (Figure 6.25). It was later formatted and the data analysed using Microsoft Excel 2000.

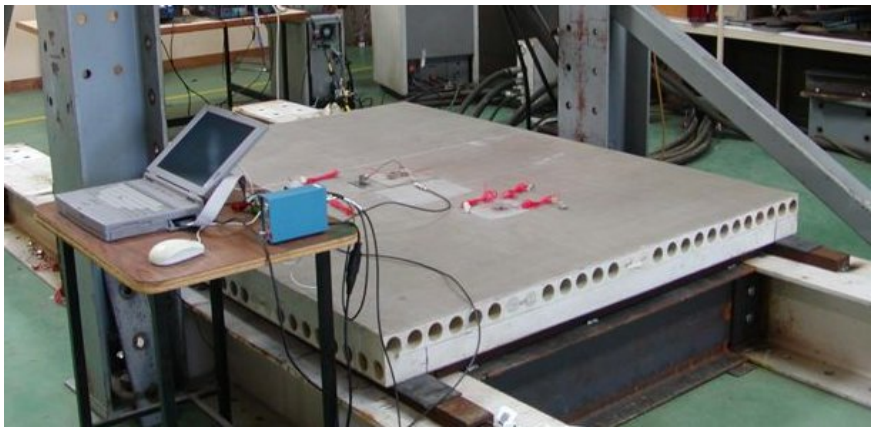

Figure 6.25 Test setup and instrumentation for natural frequency test of the slab

Figure 6.26 Accelerometer attached to the testing slab

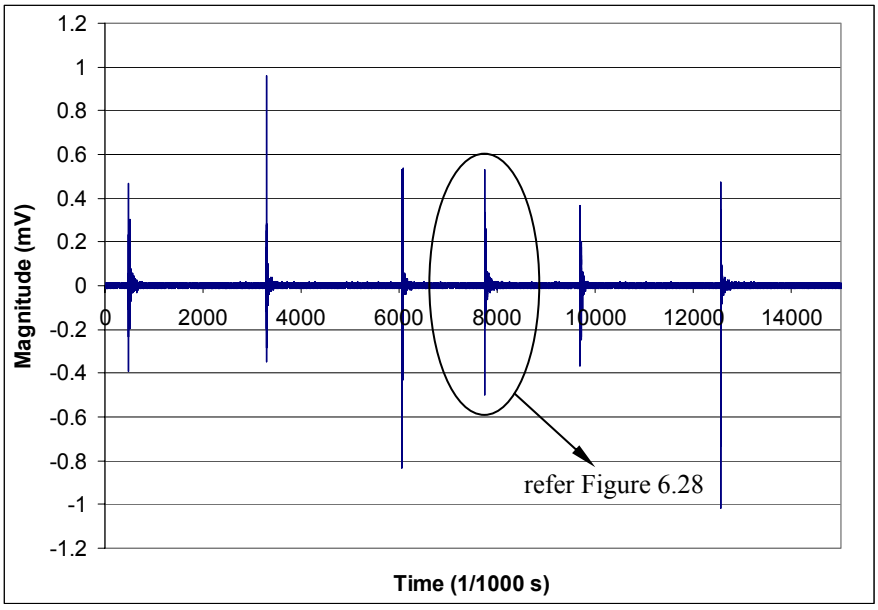

Figure 6.27 Electrical responses recorded from attached accelerometer for a number of excitations

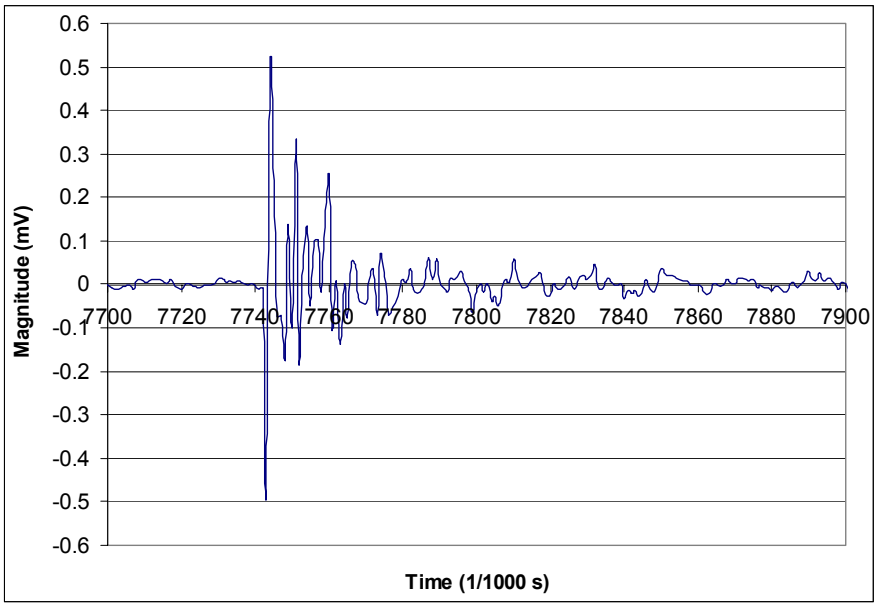

Figure 6.28 Part of electrical responses recorded from attached accelerometer for one excitation

Figure 6.27 depict the electrical responses measured from attached accelerometer for a number of excitations impacted by the rubber mallet. Based on these signals, the fundamental natural frequency of the slab was determined by conducting power spectral density (PSD) analysis using LabView. For the excitation shown in Figure 6.28, the result of PSD analysis (Figure 6.29) shows a number of pecks at different levels of frequency, in particular 50 Hz and 140 Hz. Based on these peak values, signal in narrow frequency bands (peak value ±5 Hz) were extracted from the raw signal (Figure 6.28) using a bandpass filter. The frequency band centred on 50 Hz was extracted and identified as electrical interference. The form of the signal filtered with bandpass 135 to 145 Hz (shown in Figure 6.30) was clearly identified as a structural response due to impact. Hence, it was concluded that the 140 Hz signal on Figure 4.29 resulted from the first fundamental natural frequency of the slab system. This result (140 Hz) was found consistently for the other excitations shown in Figure 6.27. While several peaks at frequency levels higher than 140 Hz were observed (Figure 6.29), studies on higher vibrational modes of the slab are beyond the scope of this PhD project for both numerical and experimental investigations.

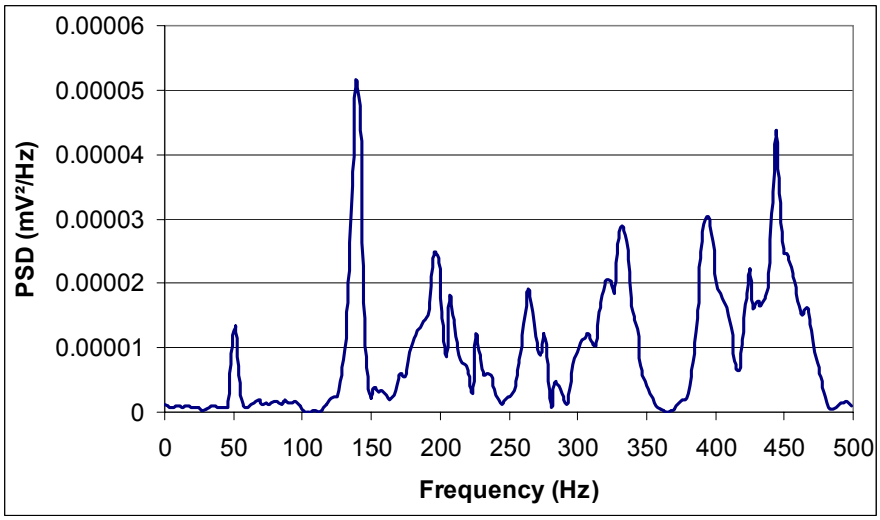

Figure 6.29 Results of power spectral density analysis for the signal shown in Figure 6.27

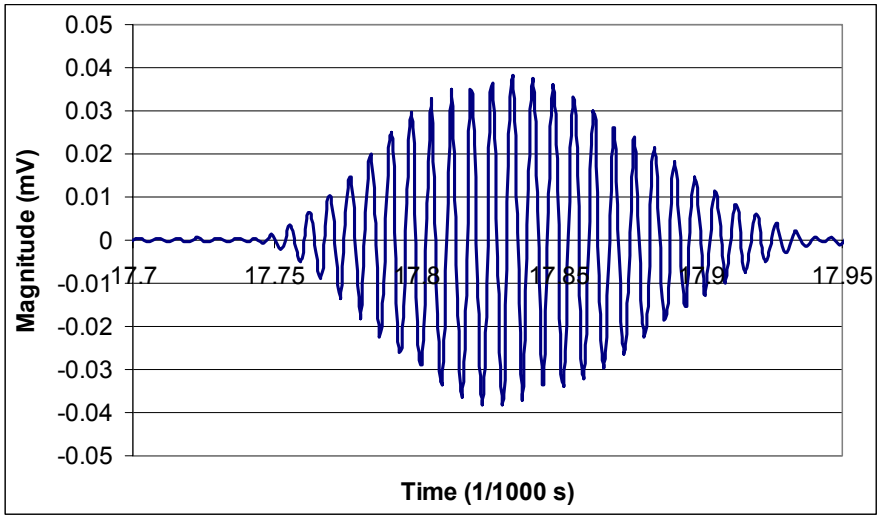

Figure 6.30 An identified structural response for the excitation shown in Figure 6.27 with the filtering bandpass of 135 Hz to 145 Hz

The fundamental natural frequency of the slab obtained from the experiment is in relatively close agreement with 3D FEA predication of 133.49 Hz (refer Chapter 5). The variation between experimental and numerical results could be explained by the fact that the accelerometer used in the test has the capability to capture only vertical motion (thickness direction); however the free vibrational responses captured by

finite element analyses also include effects of deformations in longitudinal and transverse directions (in-plane direction) and thus produced more conservative results. Nevertheless, the 3D finite element analyses reasonably predicted the fundamental natural frequency of the two-way FRP slab.

6.5.2 Fatigue Indication Test

Fatigue performance is often an important criterion, particularly for structures subjected to dynamic, long-term loading. As one of the most common structural elements, slab structures have been widely used in civil infrastructure including building floors, roof structures and bridge decks. In particular, most of research in FRP composite slab structures has so far concentrated on bridge deck applications (refer Chapter 3). Hence, it is essential to evaluate the fatigue response of the proposed two-way FRP slab. However, a detailed investigation on fatigue behaviour of this slab was beyond the scope of this PhD project. Rather, this section provides a preliminary indication of the fatigue performance of the two-way FRP slab, with the anticipation that this would form the foundation for further research into this topic.

The initial indication of fatigue performance of the slab can be quantified by determining the degradation of stiffness and strength with the number of load cycles. The test setup and instrumentation of this test are similar to the static tests, but cycling loading is used. The fatigue indication test was conducted using load control with the slab cycled through a load range from approximately 10 kN to 70 kN at a constant frequency range of 1.5 Hz. The reason of choosing a minimum load limit of 10 kN instead of 0 kN was to ensure complete contact between hydraulic actuator and the slab specimen throughout the test. A maximum load limit of 70 kN was chosen because a maximum strain of 1210 microstrain at this load level recorded from Test 2 was about 25% of strain value at the 3D FEA predicted core cracking load (refer Chapter 5). Although the 3D FEA predicted core cracking load is not the ultimate failure load of the slab, it was used as a reference to determine the maximum load limit of Test 4 since the 3D finite element analysis was unable to predict the ultimate load capacity of the prototype slab.

An arbitrary value of 1,000,000 cycles was chosen to provide an initial indication of fatigue performance of the slab system. As with the static tests discussed in the previous sections, no strain gauge was used to measure the compressive strain at the top middle surface of the slab due to the presence of loading platen. A temperature compensation strain gauge was attached to the top fibre reinforced laminate skin at the end of the slab (as shown in Figure 6.4), positioned such that no strain was imposed upon the gauge during the static test loading. This gauge was inserted to compensate for the change of ambient temperature during the test and to automatically adjust the readings of other strain gauges by pre-programming the data acquisition system mentioned previously. Both deflection (at the load point) and load were measured using a LVDT and a 222 kN capacity load cell respectively.

Preceding the commencement of cycling loading, the slab specimen was subjected to a static load test. This test was used to establish the initial slab stiffness and strength, thereby forming a reference point to assess the magnitude of the stiffness or strength loss associated with fatigue damage. The slab was loaded at a rate of 2 mm/min up to a load of 75 kN, and then the load was removed and the data retrieved. This process was also performed between each periodically interrupted fatigue cycles, to determine the extent of any loss of slab stiffness or strength resulting from fatigue damage. Due to the quantity of data acquired throughout the fatigue test, the data acquisition system was programmed to record signals continuously for the initial half hour and then for 30 seconds every half hour at a sampling rate of 50 Hz. To ensure that any notable incidents that may have occurred between the 30 seconds were recorded, the data acquisition system was also configured to automatically begin continuous sampling in the event that any of the load, deflection or strain levels deviated from specified limits. The fatigue tests were sub-divided into blocks of about 24-hour duration. This enabled the download of data from the recording equipment, and provided an opportunity for the periodical static tests described above.

A sample of the applied load, centre deflection (at the load point) and the corresponding strains recorded at both the longitudinal and transverse gauges at the bottom middle surface of the slab is shown in Figure 6.31 through 6.34, respectively.

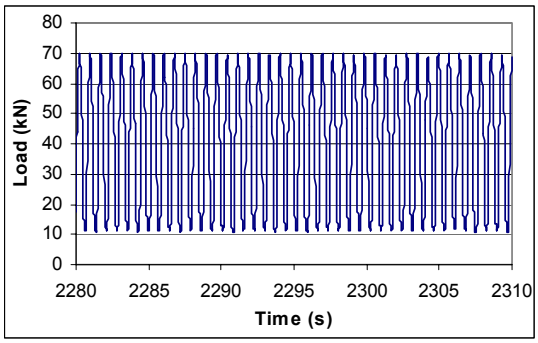

Figure 6.31 Sample of the two-way FRP slab fatigue loading

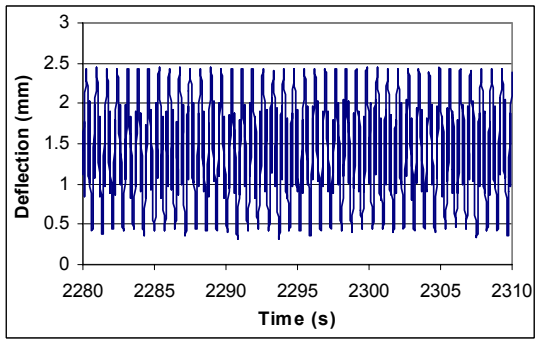

Figure 6.32 Sample of the deflection at the centre of the slab

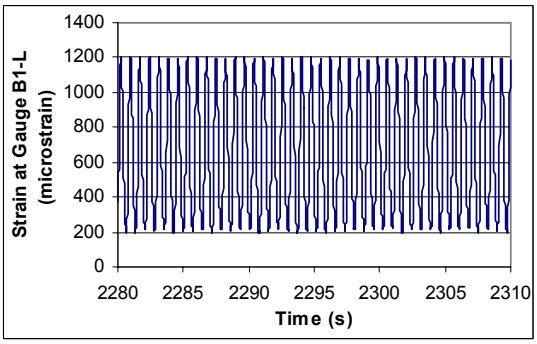

Figure 6.33 Sample of longitudinal strain at gauge B1-L

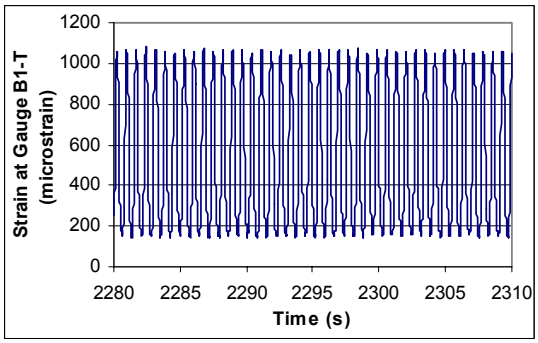

Figure 6.34 Sample of transverse strain at gauge B1-T

The results from deflection measurements and strain measurements taken during the static tests after 250,000, 500,000, and 1,000,000 cycles are shown in Figure 6.35 and Figure 6.36(a) through 6.36(j), respectively. The deflection and strain response remained fairly constant for all of the static load tests, and the slab demonstrated no apparent loss in stiffness or strength. These results suggest that cyclic load of 1,000,000 cycles does not cause significant deterioration in performance of the slab. Consequently, it is reasonable to assume that the two-way FRP slab can be arranged to have robust fatigue performance. However, further investigation into the fatigue performance of this slab structure is required to confirm this early finding.

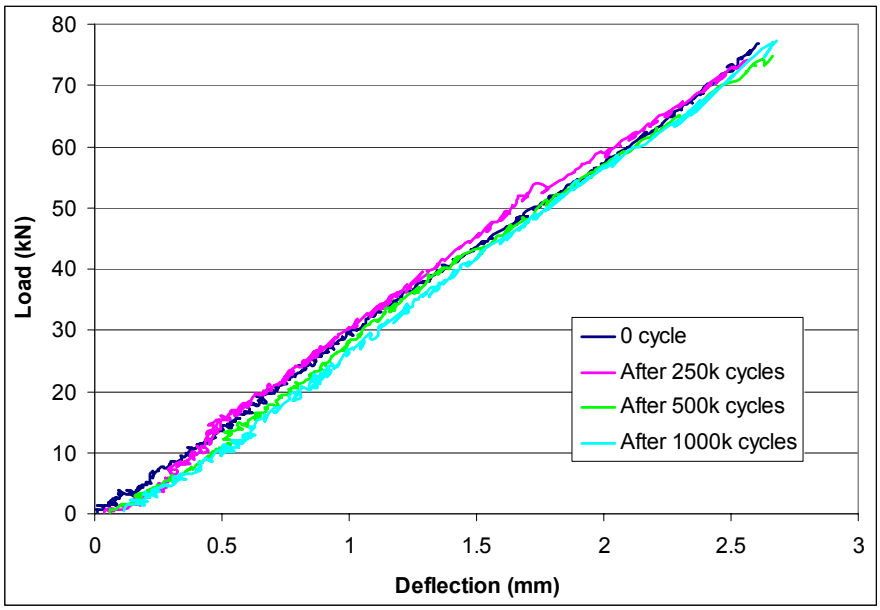

Figure 6.35 Load-deflection curves from interrupted fatigue cycling

.

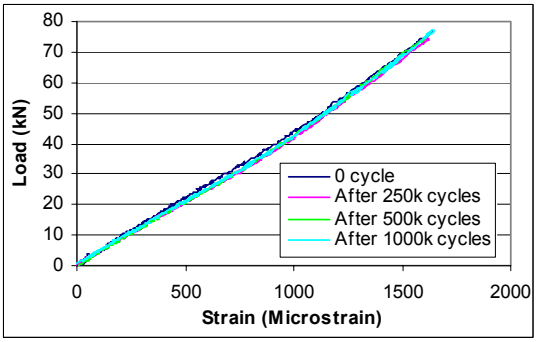

Figure 6.36(a) Strain at gauge B1-L from interrupted fatigue cycling

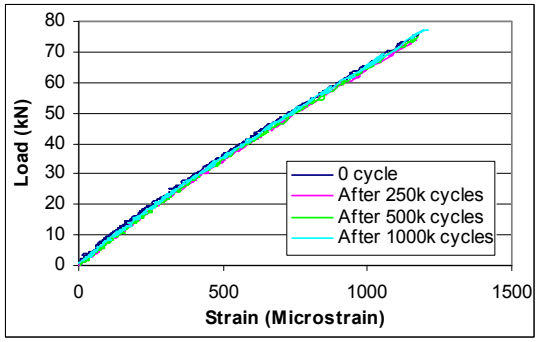

Figure 6.36(b) Strain at gauge B1-T from interrupted fatigue cycling

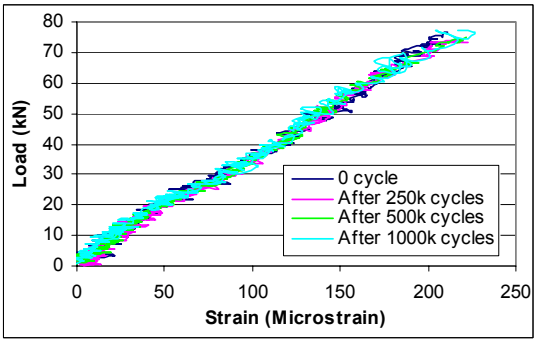

Figure 6.36(c) Strain at gauge B2-L from interrupted fatigue cycling

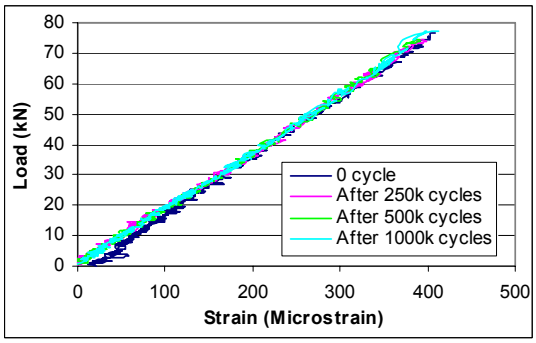

Figure 6.36(d) Strain at gauge B2-T from interrupted fatigue cycling

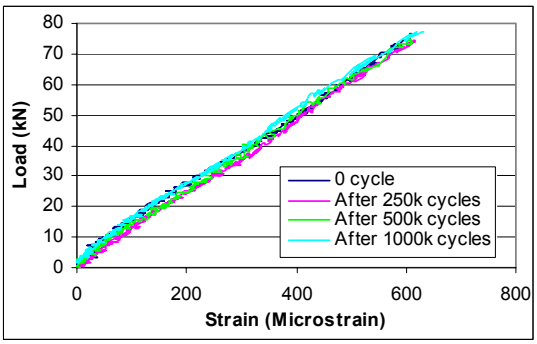

Figure 6.36(e) Strain at gauge B3-L from interrupted fatigue cycling

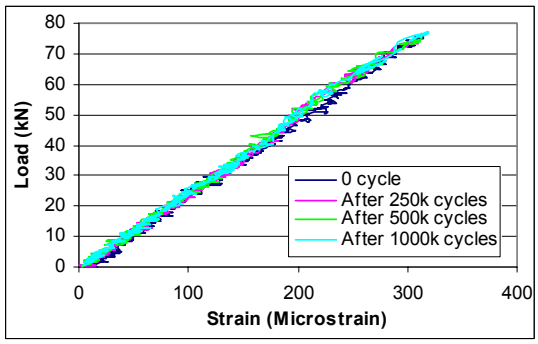

Figure 6.36(f) Strain at gauge B3-T from interrupted fatigue cycling

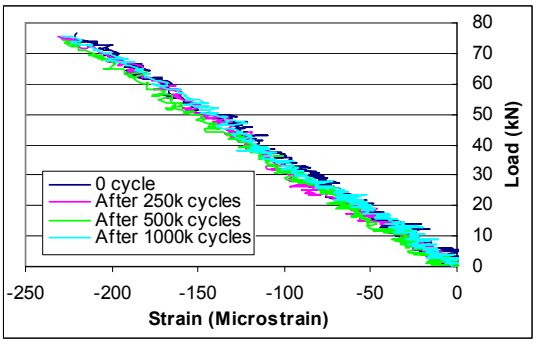

Figure 6.36(g) Strain at gauge T2-L from interrupted fatigue cycling

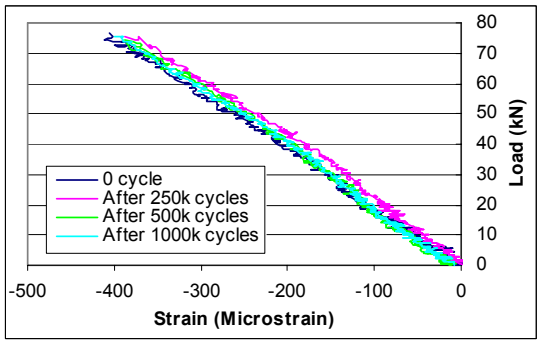

Figure 6.36(h) Strain at gauge T2-T from interrupted fatigue cycling

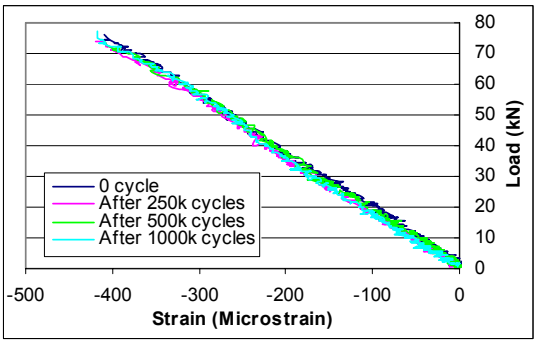

Figure 6.36(i) Strain at gauge T3-L from interrupted fatigue cycling

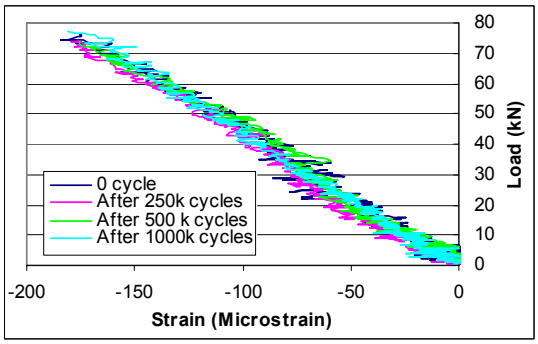

Figure 6.36(j) Strain at gauge T3-T from interrupted fatigue cycling

6.6 Conclusions

This chapter described the experimental investigation of the prototype two-way FRP composite slab through an extensive testing program including both static and dynamic experiments. The comparison between the results from the experimental program and simplified 2D plate and detailed 3D slab models developed earlier yielded excellent correlation. The accuracy of the analyses demonstrates that the analytical and numerical models are capable of predicting the behaviour of the two-way FRP slab in the linear elastic range.

The ultimate mode of failure of the prototype slab was punching shear. A typical shear failure across the thickness of the slab was observed. The slab exhibited fully linear elastic behaviour up to the point where the shear cracking failure of PFR core occurred. The initial shear cracking load of the slab was reasonably predicted by the 3D finite element analysis. Transverse strains were almost as large as longitudinal strains at the bottom middle of the slab. This indicates the ability of the two-way FRP composite slab to distribute the load in both directions. Preliminary fatigue response was also evaluated experimentally, and the results indicate that no significant change in stiffness and strength of the slab seem to occur after 1,000,000 cycles of loading.

Chapter 7

FINDINGS AND CONCLUSIONS

7.1 Review of Research

Fibre reinforced polymer (FRP) composites are increasingly being used for a variety of civil engineering applications, and new applications are continually being found. As one of the major structural components in civil engineering applications, floor slab structures are used widely in civil infrastructure including bridge decks and building slabs. Significant research has already been undertaken into the development of FRP slabs and decks. Although a range of technical solutions on such floor system has been generated, none have developed into a dominant commercial solution.

One form of composite construction that has been very successful in aviation and marine industries is FRP sandwich panels. However, only limited attempts have been made to extend FRP sandwich panels into civil engineering applications. One of the reasons for this limited activity has been the lack of a suitable core material. Davey et al (2001) identified an FRP sandwich panel form of construction using a newly developed PFR core that may be suitable for a board range of civil engineering applications. The two-way FRP slab proposed in this research is the extension of the one-way slab concept and is based on the similar philosophy as that proposed by Davey et al (2001). Further development of this slab concept requires considerable research such as extensive parametric studies to understand behaviour in a range of practical situations. However, there have only been limited analysis tools available to undertake such an investigation.

The primary objective of this research was to develop an appropriate efficient analysis tool to facilitate parametric investigations into slab configurations to further develop the proposed two-way FRP slab. As a secondary objective, this research also served as the first major investigation into structural behaviour of this slab concept. Product development was beyond the scope of this PhD project, however this study revealed a series of important findings that have implications for product development in addition to future research.

In meeting the above objectives a number of major outcomes and key findings have been achieved, and these are summarised in the following section.

7.2 Major Outcomes and Key Findings

7.2.1 FRP Composites in Civil Engineering

The background and context for this PhD study were examined in Chapter 2. A brief review of FRP composite materials and their usage in various civil constructions has demonstrated that FRP composites are structurally capable materials and exhibit significant potential in a wide range of civil engineering applications. However, the majority of FRP composites in civil applications are still in the realm of demonstrations rather than in fully commercialised products and technologies. Fibre composite research conducted in civil engineering applications is occurring in the context of a relatively immature industry.

7.2.2 Development of A Prototype Two-way FRP Slab

The review of FRP composite floor slab structures demonstrated that the use of FRP composites in these fundamental structural components is a promising application. Within these developments, a new one-way FRP slab proposed by Davey et al (2001) showed significant potential in terms of both structural performance and manufacturing process. Such potential therefore prompted the extension of the one-way slab concept into a two-way FRP slab using similar structural philosophy. Suitable FRP composite materials for the construction of the prototype slab were

selected mainly based on previous investigations at FCDD into the combination of cost and performance. The uncertainty associated with existing material properties prompted the testing of each of the material types used within this study to provide reliable data for FE modelling and interpretation of the prototype tests. A modular approach for the slab construction was used to overcome the relative high volumetric shrinkage behaviour of the selected matrix system. The experimental investigations on both single module and small-scale slab tests demonstrated the feasibility of the modular approach for both small and large slab structures.

7.2.3 Development of A Novel Simplified Approach

Investigations into this new two-way FRP slab should include a thorough parametric study; however a suitable analysis tool was not available at the commencement of the present research. Chapter 4 focused on the development of this analysis tool, a simplified transformed plate approach, for the analysis of the two-way FRP slab.

Following a brief review of three common laminated plate theories a first-order shear deformation theory was chosen to develop the simplified transformed plate approach. The simplified analysis procedure developed was based on computing the transformed properties of the actual slab geometry. By developing these transformed plate formulations, the 3D two-way FRP slab structure was reduced to an equivalent 2D transformed anisotropic plate that has same global stiffness characteristics as the slab. This equivalent transformed plate was combined with both the Ritz and finite element methods, to obtain the response of the slab for various loading cases and boundary conditions. The accuracy of the simplified transformed plate approach in predicting the maximum deflection of the slab was good compared with detailed 3D slab FEA results. As expected, the comparison also indicated that the simplified transformed plate approach is less accurate in predicting localized deformations. Nevertheless, it can be concluded that the simplified transformed plate approach is capable of providing sufficient accuracy for the preliminary structural analysis of a slab structure. The Ritz and 2D FE solutions presented in this study focused on static analysis. The simplified approach can be extended to investigate the basic dynamic behaviour of the two-way FRP slab.

7.2.4 Detailed 3D Finite Element Analyses of the Two-way FRP Slab

The main aim of the detailed 3D finite element analysis was to verify the simplified transformed plate approach (presented in Chapter 4), and to establish any trends in the structural behaviour of the two-way FRP slab that could predict, simulate and supplement the experimental investigations discussed in Chapter 6.

Three types of finite element analyses were performed in this study, namely, static, natural frequency and linear eigenvalue. Numerical results show that the prototype two-way FRP slab exhibited a relatively high load carrying capacity which was predictably distributed in longitudinal and transverse directions. The high first fundamental natural frequency obtained from the finite element analysis also confirms the relatively high stiffness of the slab. While the investigation of the failure mechanism of the prototype slab was not the primary objective of this numerical analysis, a failure sequence of the prototype slab was predicted by the 3D finite element analysis based on simple failure criteria including:

(1) cracking of the PFR core,
(2) first ply failure of the laminate skin,
(3) local buckling of the laminate circular tube.

The predicted failure sequence of the slab listed above is not exhaustive because it does not include interaction between these effects. However, it does provide an indication of possible failure modes within this prototype slab. The predicted initial failure of the slab was shear failure of the PFR core corresponding to a punching shear failure mode. This initial PFR core cracking load was used as a reference load in subsequent experimental investigations.

Punching shear failure is an unusual failure mode for slabs unless loads are highly concentrated. The fact that a punching shear failure mode was predicted for the prototype slab is probably due to the relative low span/depth ratio (approximately 10) used in dimensions of the prototype slab. A different span/depth ratio could result in the change of the failure sequence (i.e., first ply failure of the laminate skin may occur first instead of cracking of the PFR core). Thus, the effect of different

span/depth ratios on the structural behaviour of the two-way FRP slab warrants future research.

7.2.5 Experimental Investigations of the Two-way FRP Slab

Chapter 6 presented details of the testing program, data analysis and interpretation of the experimental results, which formed the basis for calibrating both the simplified 2D plate and detailed 3D slab models developed earlier, and provided more detailed insight into the structural behaviour of the prototype slab.

The good correlation between the experimental results and those obtained from the simplified 2D plate and detailed 3D slab models demonstrates that both the simplified transformed plate approach and detailed 3D finite element modelling are capable of accurately predicting the actual behaviour of the prototype slab in the linear elastic range. This finding also confirms that the simplified approach provides sufficient accuracy for preliminary investigations and parametric studies of this two-way FRP slab concept. Moreover, the assumptions made throughout the analytical and numerical procedures were largely verified. However, the experimental results also indicated that the actual behaviour of the prototype slab is sensitive to cross-section orientations of the applied load, which was captured by the detailed 3D slab model but not by the simplified 2D plate model. Thus, use of the transformed plate approach should be limited to predicting global behaviour rather than analysing local behaviour. For more accurate local analysis, the 3D finite element analysis should be conducted.

The experimental results demonstrate that the slab exhibits full linear elastic behaviour up to the point where the cracking of the PFR core occurred. The ultimate mode of failure was typical of a punching shear failure as predicted by the 3D finite element analysis. Although a simplistic material failure criterion was used in the 3D FE model, it was able to provide a reasonable prediction of the initial shear cracking load with the corresponding failure mode of the prototype slab. Further research into the analysis of material failure mechanism using more sophisticated failure criteria for this type of slab structures are recommended.

Even though the failure mode was brittle in nature (punching shear type failure), secondary post failure mechanisms were engaged once primary failure had occurred. The experimental results showed that the post failure ultimate load carrying capacity exceeded the primary failure load by approximately 50%, which suggests that the prototype slab is quite robust. Furthermore, preliminary findings obtained from the fatigue indication test also suggest that this prototype slab is likely to have very robust fatigue performance. However, further detailed investigations into fatigue behaviour of the two-way FRP slab are highly recommended.

7.3 Conclusions and Recommendations

7.3.1 Conclusions

1. The simplified analysis technique (transformed plate approach) is capable of analysing the global structural behaviour of the new two-way FRP slab.
2. The detailed 3D finite element analyses and a series of experimental investigations let to the following conclusions regarding to the structural behaviour of the slab:
   - Elastic behaviour of the slab is predicted very accurately using a conventional finite element modelling technique.
   - Failure behaviour of the slab is reasonably well predicted using relatively simple failure criteria.
   - The proposed two-way FRP slab concept is sensitive to cross-section orientation of circular voids, which can be predicted by a conventional finite element modelling technique.
   - Local effects of the slab can be significant. These can be predicted by a conventional 3D finite element modelling technique.
   - The proposed two-way FRP slab concept demonstrates significant post failure capacity.
   - Evidence suggests that the fatigue performance of the proposed slab concept will be quite robust.
3. The investigations conducted within this PhD study demonstrate the significant potential of the proposed two-way FRP slab concept. Further detailed research

into this slab concept is warranted, including extensive parametric studies to produce optimised behaviour suitable for a range of practical applications.

7.3.2 Recommendations for Future Research

The research contained in this study forms part of a major investigation into the structural behaviour of the new two-way FRP slab structure, which requires extension with respect to a number of structural design and analysis issues. Key topics that have been identified for future research and study are:

1. An extensive parametric study of the slab concept in order to produce optimised structural solutions in terms of performance, cost, and suitability for specific practical applications.
2. A detailed investigation into the post failure behaviour and failure mechanism of the two-way FRP slab using more sophisticated failure criteria.
3. An investigation into the effect of different span/depth and aspect ratios on the structural behaviour of the two-way FRP slab.
4. A detailed investigation into fatigue performance of the two-way FRP slab.
5. Research into the proposed two-way slab concept hybrid composite systems (i.e., a hybrid FRP/concrete slab system).
6. Investigation into fire issues of the proposed slab system. For example, the effect of using a phenolic resin to increase the fire resistant capability of the slab.

REFERENCES

[1] Anon, Carbon fibre strands prestress Calgary span, Engineering News Rec. 18 October, P. 21, 1993.

[2] Aref, A.J. and Parsons, I.D., Design and performance of a modular fibre reinforced plastic bridge, *Composites Part B*: *engineering*, 31(6-7), 619-628, 2000.

[3] Aref, A.J. and Parsons, I.D., Design optimisation procedure for fibre reinforced plastic bridges, *Journal of Engineering mechanics*, 125(9), 1040-1047, 1999.

[4] Aref, A.J., A novel fibre reinforced composite bridge structural system, *PhD Thesis*, The University of Illinois at Urbana-Champaign, USA, 1997.

[5] Aref, A.J., Alampalli, S. and He Y., Ritz-based static analysis method for fibre reinforced plastic rib core skew bridge superstructure, *Journal of Engineering mechanics*, 127(5), 450-458, 2001.

[6] ASTM D5379/D5379M:1998, Standard test method for shear properties of composite materials by the V-notched beam method, American Society for Testing and Materials.

[7] Åström, B.T., Manufacturing of polymer composites, Chapman & Hall, 1997.

[8] Auricchio, F. and Sacco, E., Partial-mixed formulation and refined models for the analysis of composite laminates within an FSDT, *Composite Structures*, 46(2), 103-113, 1999.

[9] Ayers, S.R. and Van Erp, G.M., Development of a new structural material for composites in civil engineering, in *Proceedings of 16th Australian Conference on the Mechanics of Structures and Materials, Sydney, Australia*, 367-372, 1999.

[10] Ayers, S.R., Material foundations for application of fibre composite materials in civil and structural engineering, *PhD Thesis*, The University of Southern Queensland, Australia, 2001.

[11] Bakis, C.E., Bank, L.C., Brown, V.L., Cosenza, E., Davalos, J.F., Lesko, J.J., Machida, A., Rizkalla, S.H. and Triantafillou, T.C., Fibre-reinforced polymer composites for construction – State-of-the-art review, *Journal of Composite for Construction*, 6(2), 73-87, 2002.

[12] Ball F., Manufacturing process, in *Handbook of Polymer Composites for Engineers* (L. Hollaway ed.), Woodhead Publishing, 73-98, 1994.

[13] Bank, L.C. and Gentry, T.R., Composite materials for roadside safety structures, in *Proceedings of the ACUN-2 International Composites Conference*: *Composites in the Transportation Industry*, *Sydney*, *Australia*, 68-77, 2000.

[14] Bank, L.C., Russell Gentry, T., Nuss, K.H., Hurd, S.H., Lamanna, A.J., Duich, S.J. and Oh, B., Construction of a pultruded composite structure: Case study, *Journal of Composites for Construction*, 4(3), 112-119, 2000.

[15] Barbero, E.J., Introduction to composite materials design, Taylor & Francis, 1999.

[16] Berglund L.A., Thermoplastic resins, in *Handbook of Composite* (S.T. Peters, ed.), Chapman & Hall, 115-130, 1998.

[17] Bert, C.W., Simplified analysis of static shear correction factors for beams of non-homogeneous cross section, *Journal of Composite Materials*, 7, 525-529, 1973.

[18] Bridge superstructures and deck system components and applications, viewed 15 November 2001, <*www.strongwell.com*>.

[19] Brown, R.T. and Zureick, A., Truss section fibreglass reinforced composite causeway deck, in *Proceedings of 30th International SAMPE Technical Conference*, 303-315, 1998.

[20] Burgoyne C.J., Advanced composites in civil engineering in Europe, *Structural Engineering International*, 9(4), 267-273, 1999.

[21] Casas, J.R. and Aparicio, A.C., A full-scale experiment on a prestressed concrete structure with high strength fibres: the North ring road in Barcelona, FIP-XI International Congr., Hamburg, paper T15, 1990.

[22] Cassity P., Richards, D. and Gillespie, J., Compositely acting FRP deck and girder system, *Structural Engineering International*, 12(2), 71-75, 2002.

[23] Cattell, C.L., The design and manufacture of a modular fibre-reinforced composite beam, *Bachelor Thesis*, University of Southern Queensland, Australia, 2000.

[24] Chajes, A., Principles of structural stability theory, Prentice-Hall, 1974.

[25] Clarke, J.L., FRP material for reinforcing and strengthening concrete structures, *Proceedings of Conference of Composites and Plastic in Construction*, *Watford*, *UK*, Paper 17, 1999.

[26] Coker, R.A., An investigation into the feasibility and application of fibre composites to flatbed semi-trailers, *PhD Thesis*, The University of Southern Queensland, Australia, 2002.

[27] Composites in infrastructure – Building new markets (First Edition), Elsevier Advanced Technology, 2000.

[28] Crews, K.I., Behaviour and critical limit states of transversely laminated timber cellular bridge decks, *PhD Thesis*, The University of Technology, Sydney, Australia, 2002.

[29] Cripps, A., Fibre-reinforced polymer composite in construction, CIRIA, 2002.

[30] Data Sheets – ProBalsa from DIAB, viewed 8 August 2002, <*www.diabgroup.com*>.

[31] Davalos, J.F., Qiao, P.Z., Xu, X.F., Robinson, J. and Barth, K.E., Modelling and characterization of fibre-reinforced plastic honeycomb sandwich panels for highway bridge application, *Composite structures*, 52(3-4), 441-452, 2001.

[32] Davey, S.W., The fabrication of a fibre composite floor slab, *Technical Report*, University of Southern Queensland, Australia, 1999.

[33] Davey, S.W., Van Erp, G.M. and Marsh R., Fibre composite bridge decks an alternative approach, *Composites Part A: applied science and manufacturing*, 32, 1339-1343, 2001.

[34] Deskovic, N. and Triantafillou, T.C., Innovative design of FRP combined with concrete: short-term behaviour, *Journal of Structural Engineering*, 121(7), 1069-1078, 1995a.

[35] Deskovic, N. and Triantafillou, T.C., Innovative design of FRP combined with concrete: long-term behaviour, *Journal of Structural Engineering*, 121(7), 1079-1089, 1995b.

[36] Deskovic, N., Innovative design of FRP composite members combined with concrete, *PhD Thesis*, Massachusetts Institute of Technology, USA, 1993.

[37] Dong, S.B., Pister, K.S. and Taylor, R.L., On the theory of laminated anisotropic shells and plates, *Journal of Aeronautical Science*, 29(8), 969-975, 1962.

[38] Duranovic, N., Pilakoutas, K. and Waldron, FRP reinforcement for concrete structures: design considerations, in *Proceedings of Third International Symposium on Non-metallic* (*FRP*) *Reinforcement for Concrete Structures*, Vol.2, Japan Concrete Institute, 527-534, 1997.

[39] El-Ghandour, A.W., Pilakoutas, K. and Waldron, P., Punching shear behaviour of fibre reinforced polymers reinforced concrete flat slabs: experimental study, *Journal of Composites for Construction*, 7(3), 258-265, 2003.

[40] Europe's first advanced composite public highway bridge lowered ready for official opening, October 2002, viewed 5 December 2003, <*www.mouchelparkman.com*>.

[41] Fardis, M.N. and Khalili, H., Concrete encased in fibreglass-reinforced plastic, *Journal of American Concrete Institute*, 78(6), 440-446, 1981.

[42] Fertis, D.G., Dynamics and vibration of structures, John Wiley & Sons, 1973.

[43] Foster, D.C., Richards, D. and Bogner, B.R., Design and installation of fibre-reinforced polymer composite bridge, *Journal of Composites for Construction*, 4(1), 33-37, 2000.

[44] G+D Computing, Strand7 Release 1.05.6 online manual, 2000.

[45] GangaRao, H.V.S. and Craigo II, C.A., Fibre-reinforced composite bridge decks in the USA, *Structural Engineering International*, 9(4), 286-288, 1999.

[46] GangaRao, H.V.S., and Siva, H.R.V., Advances in fibre-reinforced polymer composite bridge decks, *Progress of Structural engineering and Materials*, 4, 161-168, 2002.

[47] Gibson, R.F., Principles of composite materials mechanics, McGraw-Hill Inc., 1994.

[48] Hambly, E.C., Bridge deck behaviour (Second Edition), E & FN Spon, 1991.

[49] Handbook for infrastructure applications of composite materials, Beavercreek, Ohio, AdTech Systems Research, Inc., 1998.

[50] Hartman, D.R., Greenwood, M.E. and Miller, D.M., High strength glass fibres, Owens-Corning Fiberglas Corporation Technical Paper, Toledo, Ohio, 1994.

[51] Hastak, M. and Halpin D.W., Assessment of life-cycle benefit-cost of composites in construction, *Journal of Composites for Construction*, 4(3), 103-111, 2000.

[52] Hayes, M.D., Lesko, J.J., Haramis, J., Cousins, T.E., Gomez, J. and Masarelli, P., Laboratory and field testing of composite bridge superstructure, *Journal of Composites for Construction*, 4(3), 120-128, 2000.

[53] Hayes, M.D., Ohanehi, D., Lesko, J.J., Cousins, T.E. and Witcher, D., Performance of tube and plate fibreglass composite bridge deck, *Journal of Composites for Construction*, 4(2), 48-55, 2000.

[54] Henry, J., Deck-girder systems for highway bridges using fibre-reinforced plastics, MS thesis, North Carolina State University, Raleigh, N.C., 1985.

[55] Herakovich, C.T., Mechanics of fibrous composites, John Wiley & Sons Inc., 1998.

[56] Hill, R., The mathematical theory of plasticity, Oxford University Press, London, 1950.

[57] Hitchings, D., A finite element dynamics primer, NAFEMS, 1992.

[58] Hodgkinson, J.M., Mechanical testing of advanced fibre composites, Woodhead Publishing, 2000.

[59] Hodgson, J.A., Development of an advanced composite decking system for new build applications, in *Proceedings of the 8th International Conference on Fibre Reinforced Composite* (*FRC 2000*), *Newcastle, UK*, Woodhead Publishing, 11-18, 2000.

[60] Hollaway, L.C. and Cadei, J., Progress in the technique of upgrading metallic structures with advanced polymer composites, *Progress of Structural engineering and Materials*, 4, 131-148, 2002.

[61] Hollaway, L.C. and Head, P.R., Advanced polymer composites and polymers in the civil infrastructure, Elsevier Science, 2001.

[62] Hollaway, L.C. and Leeming, M.B., Strengthening of reinforced concrete structures using externally bonded FRP composites, in *Structural and Civil Engineering* (L.C. Hollaway and M.B. Leeming, eds.), Woodhead Publishing, Cambridge, 1999.

[63] Hollaway, L.C., The evolution of and the way forward for advanced polymer composites in the civil infrastructure, in *Proceedings of International Conference on FRP Composites in Civil Engineering* (*CICE 2001*), *Hong Kong, P.R. China*, Elsevier Science, Vol. 1, 27-40, 2001.

[64] Huang, D., Van Erp, G.M., Heldt, T.J. and Ayers, S.R., Development of a new two-way fibre composite slab – Modular approach, in *Proceedings of 17th Australian Conference on the Mechanics of Structures and Materials* (*ACMSM 17*), *Gold Coast, Australia*, Griffith University, 25-30, 2002.

[65] Hull, D. and Clyne, T.W., An introduction to composite materials (Second Edition), Cambridge University Press, 1996.

[66] Introduction to core materials, viewed 15 November 2001, <*www.spsystems.com*>.

[67] ISO 1172:1996, Textile-glass-reinforced plastics – Prepregs, moulding compounds and laminates – Determination of the textile-glass and mineral-filler content – Calcination methods.

[68] ISO 14126:1999, Fibre-reinforced plastic composites – Determination of compressive properties in the in-plane direction.

[69] ISO 14129:1997, Fibre-reinforced plastic composites – Determination of the in-plane shear stress/shear strain response, including in-plane shear modulus and strength, by the ±45° tension test method.

[70] ISO 527-2:1993, Plastics – Determination of tensile properties – Part 2: Test conditions for moulding and extrusion plastics.

[71] ISO 527-5:1997, Plastics – Determination of tensile properties – Part 5: Test conditions for unidirectional fibre-reinforced plastic composites.

[72] Iyer, S.L., Advanced composite demonstration bridge deck, in *Fibre Reinforced Plastic Reinforcement for Concrete Structures* (A. Nanni and C.W. Dolan, eds.), SP 138, American Concrete Institute, Detroit, P. 83, 1993.

[73] Jones, R.M., Mechanics of composite materials (Second Edition), Taylor & Francis, 1999.

[74] Juska T.D. and Puckett P.M., Matrix resins and fiber/matrix adhesion, in *Composite Engineering Handbook* (P.K. Mallick, ed.), Marcel Dekker, Inc., 101-165, 1997.

[75] Karbhari, V.M. and Seible, F., Fibre reinforced composites – advanced materials for the renewal of civil infrastructure, *Applied Composite Materials*, 7, 95-124, 2000.

[76] Karbhari, V.M., Fibre Reinforced composite decks for infrastructure renewal, in *Proceedings of the 2nd International Conference on Advanced Composites in bridges and Structures* (*ACMBS-2*), *Montreal*, *Canada*, 759-766, 1996.

[77] Karbhari, V.M., Seible, F., Burgueño, R., Davol, A., Wernli, M. and Zhao, L., Structural characterization of fibre-reinforced composite short- and medium-span bridge systems, *Applied Composite Materials*, 7, 151-182, 2000.

[78] Kaw, A.K., Mechanics of composite materials, CRC Press, 1997.

[79] Keller, T., Overview of fibre-reinforced polymers in bridge construction, *Structural Engineering International*, 12(2), 66-70, 2002.

[80] Keller, T., Recent all-composite and hybrid fibre-reinforced polymer bridges and buildings, *Progress of Structural engineering and Materials*, 3, 132-140, 2001.

[81] Keller, T., Towards structural forms for composite fibre materials, *Structural Engineering International*, 9(4), 297-300, 1999.

[82] Kim, D.H., Composite structures for civil and architectural engineering, E & FN Spon, 1995.

[83] Knox, C.E., Fiberglass reinforcement, in *Handbook of Composite* (G. Lubin, ed.), Van Nostrand Reinhold, New York, 1982.

[84] Kumar S. and Wang Y, Fibers, fabrics, and fillers, in *Composite Engineering Handbook* (P.K. Mallick, ed.), Marcel Dekker, Inc., 51-100, 1997.

[85] Lam, K.Y. and Qian W, Free vibration of symmetric angle-ply thick laminated composite cylindrical shells, *Composites Part B*: *engineering*, 31(4), 345-354, 2000.

[86] Leeming, M.B., UK experience of plate bonding with advanced composite materials, in Recent Advances in Bridge Engineering, Evaluation Management and Repair, *Proceedings of US-Europe Workshop on Bridge Engineering, Barcelona, Spain*, CIMNE, 1996.

[87] Lopez-Anido, R., GangaRao, H., Trovillion, J. and Busel, J., Development and demonstration of a modular FRP deck for bridge construction and replacement, in *Proceedings of the 1997 International Composites Expo, Nashville, Tennessee, USA*, 16D/1-16D/6, 1997a.

[88] Lopez-Anido, R., GangaRao, H., Vedam, V. and Overby, N., Design and evaluation of a modular FRP bridge deck, in *Proceedings of the 1997 International Composites Expo, Nashville, Tennessee, USA*, 3E/1-3E/6, 1997b.

[89] Luke, S., Darby, J. and Skwarski, A., Using stressed and unstressed composite plates for strengthening existing structures, in *Proceedings of the 8th International Conference on Fibre Reinforced Composite* (*FRC 2000*), *Newcastle, UK*, Woodhead Publishing, 35-40, 2000.

[90] Luke, S., Lee, C., Collins, S., Knudsen, E., Brown, P., Taljsten, B. and Olofsson, I., Advanced composite bridge decking system – Project ASSET, *Structural Engineering International*, 12(2), 76-79, 2002.

[91] Marshall, A.C., Sandwich construction, in *Handbook of Composite* (S.T. Peters, ed.), Chapman & Hall, 254-290, 1998.

[92] Marzullo A., Boron, high silica, quartz and ceramic fibers, in *Handbook of Composite* (S.T. Peters, ed.), Chapman & Hall, 156-168, 1998.

[93] Matthews, F.L. and Rawlings, R.D., Composite materials: engineering and science, Chapman & Hall, 1994.

[94] McCormac, J.C., Design of reinforced concrete (Fifth Edition), John Wiley & Sons, 2001.

[95] Meier U., Composite materials in bridge repair, *Applied Composite Materials*, 7, 74-94, 2000.

[96] Mindlin, R.D., Influence of rotatory inertia and shear on flexural motions of isotropic, elastic plates, *Journal of Applied Mechanics*, 18, 31-38, 1951.

[97] Munipalle, U.M., Analysis and testing of wood-glass fibre reinforced plastic adhesive interface, *M.S. Thesis*, West Virginia University, USA, 1992.

[98] Neale, K.W., FRPs for structural rehabilitation: a survey of recent progress, *Progress of Structural engineering and Materials*, 2, 133-138, 2000.

[99] Noritke, K., Practical Applications of aramid FRP rods to prestressed concrete structures, in *Fibre Reinforced Plastic Reinforcement for Concrete Structures* (A. Nanni and C.W. Dolan, eds.), SP 138, American Concrete Institute, Detroit, p. 853, 1993.

[100] Norton, M.P., Fundamentals of noise and vibration analysis for engineers, Cambridge University Press, 1989.

[101] Norwood L., Fibre reinforced polymers, in *Handbook of Polymer Composites for Engineers* (L.C. Hollaway, ed.), Woodhead Publishing, 3-69, 1994.

[102] Park, R. and Gamble, W.L., Reinforced concrete slabs (Second Edition), John Wiley & Sons, 2000.

[103] Penn, L.S. and Wang H., Epoxy resins, in *Handbook of Composite* (S.T. Peters, ed.), Chapman & Hall, 48-74, 1998.

[104] Plantema, F.J., Sandwich Construction, John Wiley & Sons, 1966.

[105] Plecnik, J. and Azar, W., Structural components, highway bridge deck applications, *International Encyclopedia of Composites*, 6, 430-445, 1991.

[106] Rahman, A.H., Kingsley, C.Y. and Kobayashi, K., Service and ultimate load behaviour of bridge deck reinforced with carbon FRP grid, *Journal of Composites for Construction*, 4(1), 16-23, 2000.

[107] Reddy J.N., A refined nonlinear theory of plates and transverse shear deformation, *International Journal of Solids and Structures*, 20(9/10), 881-906, 1984b.

[108] Reddy, J.N. and Miravete, A., Practical Analysis of Composite Laminates, CRC Press, Inc., 1995.

[109] Reddy, J.N., A simple higher-order theory for laminated composite plates, *Journal of Applied Mechanics*, 51, 745-752, 1984a.

[110] Reddy, J.N., Energy and variational methods in applied mechanics, John Wiley & Sons, 1984.

[111] Reddy, J.N., Mechanics of laminated composite plates - theory and analysis, CRC Press, Inc., 1997.

[112] Reissner, E. and Stavsky, Y., Bending and stretching of certain types of aeolotropic elastic plates, *Journal of Applied Mechanics*, 28, 402-408, 1961.

[113] Reissner, E., Note on the effect of transverse shear deformation in laminated anisotropic plates, *Computer Methods in Applied Mechanics and Engineering*, 20, 203-209, 1979.

[114] Reissner, E., The effect of transverse shear deformation on the bending of elastic plates, *Journal of Applied Mechanics*, 12, 60-77, 1945.

[115] Rostasy, F.S., Hankers, C. and Ranisch, E-H., Strengthening of R/C- and P/C-structures with bonded FRP plates, in *Advanced Composite Materials in Bridges and Structures*, (K.W. Neale and P. Labossiere, eds.), The Canadian Society for Civil Engineering, Montreal, Canada, 253-263, 1992.

[116] Schwartz, M.M., Composite materials - Vol 1, Properties, nondestructive testing, and repair, Prentice-Hall, Inc., 1997a.

[117] Schwartz, M.M., Composite materials - Vol 2, Processing, fabrication, and application, Prentice-Hall, Inc., 1997b.

[118] Seible, F., Design with FRP composites in the civil engineering environment, in *Proceedings of International Conference on FRP Composites in Civil Engineering* (*CICE 2001*), *Hong Kong, P.R. China*, Elsevier Science, Vol. 1, 73-84, 2001.

[119] Seible, F., Priestley, M.J.N., Hegemier, G.A. and Innamorato, D., Seismic retrofit of RC columns with continuous carbon fibre jackets, *Journal of Composites for Construction*, 1(2), 40-52, 1997.

[120] Shaw, M.A. and Drewett, J.F., Case studies of carbon fibre bonding worldwide, in *Strengthening of Reinforced Concrete Structures – using externally-bonded FRP composites in structural and civil engineering* (L.C. Hollaway and M.B. Leeming, eds.), Woodhead Publishing, 288-324, 2000.

[121] Simpson, P.E. and Van Erp, G.M., Composite materials? The 3000 Mpa question, in *Proceedings of 16th Australian Conference on the Mechanics of Structures and Materials* (*ACMSM 16*), *Sydney, Australia*, A.A. Balkema Publishers, 531-536, 1999.

[122] Tarnopol'skii, Tu.M., Peters, S.T. and Bell', A.I., Filament winding, in *Handbook of Composite* (S.T. Peters, ed.), Chapman & Hall, 456-475, 1998.

[123] Thomson, W.T., Theory of vibration with applications (Third Edition), Unwin Hyman, 1988.

[124] Timoshenko, S. and Woinowsky-Krieger, S., Theory of plates and shells (Second Edition), McGraw-Hill, 1959.

[125] Trahair, N.S., Flexural-torsional buckling of structures, E & FN Spon, 1993.

[126] Triantafillou, T.C. and Meier, U., Innovative design of FRP combined with concrete, in *Proceeding of 1st International Conference on Advanced Composite Materials for Bridges and Structures* (*ACMBS-1*), *Sherbrooke, Canada*, 492-499, 1992.

[127] Triantafillou, T.C., Seismic retrofitting of structures with fibre-reinforced polymers, *Progress of Structural engineering and Materials*, 3, 57-65, 2001.

[128] Tsai, S.W., Strength theories of filamentary structures, in *Fundamentals Aspects of Fibre Reinforced Plastic Composites* (R.T. Schwartz and H.S. Schwartz, eds.), Wiley Inter-science, New York, 3-11, 1968.

[129] Tsuji, Y., Kanda, M. and Tamura, T., Applications of FRP materials to prestressed concrete bridges and other structures in Japan, PCI Journal, July-August, 50, 1993.

[130] Van Erp, G. and Ayers, S., A fair dinkum approach to fibre composites in civil engineering, in *Proceedings of the Second International Conference on Advanced Polymer Composites for Structural Applications in Construction, Guildford, UK*, Woodhead Publishing, 101-113, 2004.

[131] Van Erp, G.M., Heldt, T., Cattell, C.L. and Marsh, R., A new approach to fibre composite bridge structures, in *Proceedings of 17th Australian Conference on the Mechanics of Structures and Materials* (*ACMSM 17*), *Gold Coast, Australia*, Griffith University, Supplementary Volume, 37-45, 2002.

[132] Vinson J.R., The behaviour of sandwich structures of isotropic and composite materials, Technomic Publishing Company, 1999.

[133] Warner, R.F., Rangan, B.V., Hall, A.S. and Faulkes, K.A., Concrete structures, Addison Wesley Longman Australia Pty Limited, 1998.

[134] Weavwe, A., Composites: world markets and opportunities, viewed 15 November 2001, <*www.spsystems.com*>.

[135] Whelam, A., Reinforcement of mouldings, in *Plastics and Resin Compositions* (W.G. Simpson, ed.), The Royal Society of Chemistry, 26-53, 1995.

[136] Whitney, J.M. and Leissa, A.W., Analysis of heterogeneous anisotropic plates, *Journal of Applied Mechanics*, 36(2), 261-266, 1969a.

[137] Whitney, J.M. The effect of transverse shear deformation in the bending of laminated plates, *Journal of Composite Materials*, 3, 534-547, 1969b.

[138] Whitney, J.M., Shear correction factors for orthotropic laminates under static load, *Journal of Applied Mechanics*, 40(1), 302-304, 1973.

[139] Wilkinson, T., The plastic behaviour of cold-formed rectangular hollow sections, *PhD Thesis*, The University of Sydney, Australia, 1999.

[140] Williams, B., Shehata, E. and Rizkalla, S.H., Filament-wound glass fibre reinforced polymer bridge deck modules, *Journal of Composites for Construction*, 7(3), 266-273, 2003.

[141] Wittrick, W.H., Analytical three-dimensional elasticity solutions to some plate problem and some observations on Mindlin's plate theory, *International Journal of Solids and Structures*, 23, 441-464, 1987.

[142] Wolff, R. and Meisseler, H.J., Glass fibre prestressing system, in *Alternative Materials for the Reinforcement and Prestressing of Concrete* (J.L. Clarke, ed), Blackie, Glasgow, 127-152, 1993.

[143] Yang, P.C., Norris, C.H. and Stavsky, Y., Elastic wave propagation in heterogeneous plates, *International Journal of Solids and Structures*, 2, 665-684, 1966.

[144] Yu, Y.Y., Vibration of elastic plates, Springer-Verlag, 1996.

[145] Zureick, A., Shih, B. and Munley, E., Fibre-reinforced polymeric bridge decks, *Structural Engineering Review*, 7(3), 257-266, 1995.

Appendix A

FRP COMPOSITES IN BRIEF

This appendix presents more detailed background of FRP composites to supplement the discussion in Chapter 2. It contains discussions of three main constituent materials of FRP composites and introductions of most common manufacturing processes for FRP composites.

A.1 Reinforcing Fibres

A.1.1 Fibre Types

Three most commonly used fibres in civil engineering applications are glass, carbon and aramid fibres, which are discussed in the remainder of this section.

(a) Glass Fibres

Glass fibres are one of the most economical reinforcing fibres available today. They account for the major share of the market for reinforcement fibres for use in the fibre reinforced polymers industry. Glass fibre is made by melting the raw materials in a high-temperature furnace, then drawing the molten material into filaments. It is a capital-intensive process (Schwartz 1997a). There are two main categories of glass fibre: E-glass and S-glass. Anther type, known as C-glass, is used in chemical applications requiring greater resistance to acid attack than is provided by E-glass. E-glass (E is an abbreviation for electrical) has the lowest cost of all commercially available reinforcing fibres, which is the reason for its widespread use in the fibre

reinforced polymers industry. E-glass is available as continuous filament, chopped staple, and random fibre mats suitable for most methods of resin impregnation and composite fabrication. S-glass, originally developed for aircraft components and missile casings, has a higher stiffness and strength (hence the designation S) than E-glass (Matthews et al 1994). However, the compositional difference and higher manufacturing cost make it more expensive then E-glass. S-glass fibres are still used for some specialist applications but they have been largely superseded by fibres such as carbon and aramid, which have superior mechanical properties.

Glass fibre composites provide high levels of engineering properties (refer Table 2.1). They are strong, low in cost, nonflammable, nonconductive (electrically), and corrosion-resistant. The disadvantages are low tensile modulus, relatively high specific gravity (compared with other commercial fibres), and relatively low fatigue resistance (in comparison with carbon fibres).

(b) Carbon Fibres

Glass fibres have excellent high strength, are relatively low cost materials (refer Table 2.1) and currently provide the majority of structural composite components in construction industry. However, particular structural requirements may need materials which have a higher modulus and a high fatigue strength value then those which can be provided by glass fibres. For such cases high performance fibres will be used although the cost is higher. The most commonly used high performance fibres in civil engineering applications are carbon fibres.

Carbon fibres are manufactured by controlled pyrolysis and crystallization of certain organic precursors. The manufacturing process consists of a sequence of procedures which are stabilization, carbonisation, graphitisation and surface treatment. The precursors commonly used in the production of carbon fibre reinforcement include polyacrylonitrile (PAN), mesophase pitch, and rayon. Polyacrylonitrile (PAN) is the most common precursor currently used for carbon fibres. PAN carbon fibres are generally categorized into high strength (HS), high modulus (HM), and ultra high modulus (UHM) types. The high strength PAN carbon fibres, such as T-300 and AS-4, have the lowest modulus, whereas the ultra high modulus PAN carbon fibres, such

as GY-70, have the lowest tensile strength as well as the lowest tensile strain to failure. Recently, a number of intermediate modulus, high-strength PAN carbon fibres have been developed that possess the highest strain to failure of all carbon fibres (Schwartz 1997a). Pitch is a lower-cost precursor than PAN. The pitch carbon fibres have very high modulus values, but their tensile strength and strain to failure are lower than those of PAN carbon fibres. Rayon precursors were among the earliest precursors used to make carbon fibres. The significant disadvantage is that only a small part (typically 25%) of the initial fibre mass remains after carbonisation, resulting in expensive fibres (Kim 1995). In recent years, less costly PAN based fibres have been taken most of the rayon based fibre market.

Carbon fibres are commercially available with a variety of tensile moduli ranging from 207 GPa to 1035 GPa (Schwartz 1997a). In general, low-modulus fibres have lower specific gravities, lower cost, higher tensile strength, and higher tensile strain to failure than higher-modulus fibres. Carbon fibre has the highest specific stiffness of any commercially available fibre, very high strength in both tension and compression and a high resistance to corrosion, creep and fatigue. The major disadvantage of carbon fibres is their high cost, which has so far limited them in widespread applications. The cost (by weight) of the most inexpensive carbon fibre is still around ten times than that of glass fibres. Additionally, carbon fibre is incompatible with some matrix systems, and is typically combined with more expensive epoxy and high-performance vinyl ester resin systems. They are still used mostly in the aerospace industry, where weight saving is considered more critical then cost. However, the exceptional combination of high strength and stiffness, low weight, and excellent long term performance offered by carbon fibres also makes them of interested in other applications such as ground transportation and infrastructure. The usage of carbon fibre is continuing to increase, and the increased demand may eventually be accompanied by a reduction in price. The development of new inexpensive precursors will also assist in reducing the price of carbon fibres.

(c) Aramid Fibres

Aramid fibre is a generic term for the class of aromatic-polyamide fibres produced using para-phenylene terephthalamide. These fibres were first introduced on a

commercial basis by DuPont in the early 1970s. A number of commercially available aramid fibres, e.g., Kevlar (DuPont), Twaron (Akzo) and Technora (Teijin); of these Kevlar is the most well known. The Kevlar range covers a spectrum of strength and modulus values, from low-modulus Kevlar 29, through high-modulus Kevlar 49, to very high-modulus Kevlar 149 and very high-strength Kevlar 129. Kevlar 49 is the grade used more extensively in structural composites.

In general, aramid fibres have the lowest specific gravity and the highest tensile strength-to-weight ratio of current reinforcing fibres. They possess a density, typically 1.44 g/cm^3, which is lower than that of both glass fibre (by about 40%) and carbon fibre (by about 20%), and this result in the fibres having high specific strength values (refer Table 2.1). Aramid fibre also exhibits reasonably high levels of elongation to break. Other advantageous properties of aramid fibres are excellent fatigue and wear resistance, good electrical insulation, high toughness, and good chemical resistance. However, aramid fibre responds elastically in tension but it exhibits nonlinear behaviour under compression. The compressive strength of aramid fibres is only about 20% of the tensile strength (Schwartz 1997a), and special attention is necessary when application of aramid fibre involves high strain compression or flexural loads. Other disadvantages of aramid fibres include moisture absorption by the fibre, relatively low adhesion to most resin matrix materials, and difficult machining compared to other composites.

A.1.2 Reinforcement Forms

Although essentially all reinforcing fibres are produced as continuous reinforcement strands, this is often not the form in which it is finally used. Reinforcement in strand forms limits its use in fibre reinforced polymers to specific process such as filament winding and pultrusion. It is the ease with which reinforcement strands can be converted into various fabrics that has brought about the growth its use in many other fabrication processes. There are a multitude of different reinforcement forms available in today's market. The following sections describe the most common reinforcement forms used in civil engineering applications.

(a) Woven Fabrics

Woven fabrics are among the most widely used forms for composite reinforcement. The longitudinal direction (i.e., in the 0° direction) of the fabric is called warp and the transverse direction (i.e., in the 90° direction) weft or fill (Figure A.1). Warp yarns are also referred to as "ends", and weft yarns as "picks".

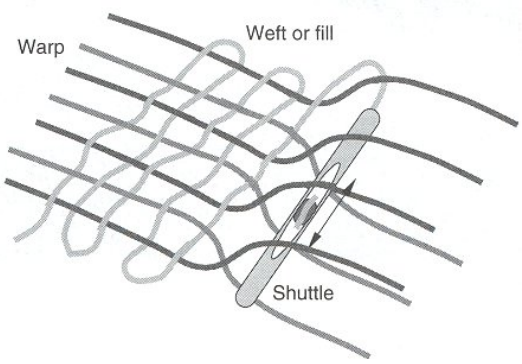

Figure A.1 Schematic of weaving[7]

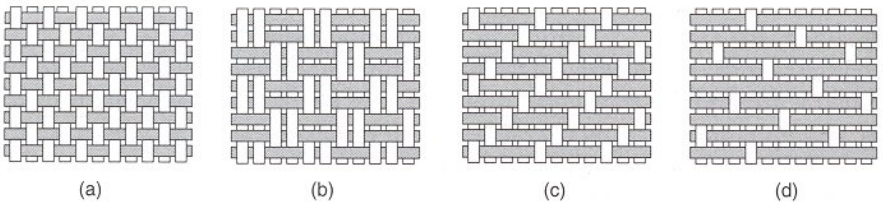

Figure A.2 Example of woven fabric forms (a) plain weave; (b) Basket weave; (c) twill; (d) eight-harness satin weave[7]

Woven fabrics have a number of different weaves. Some examples of woven fabric forms are shown in Figure A.2. The most common and simplest weave is plain weave, which contains two ends and two picks. This weave is made by interlacing yarns in an alternating over-and-under pattern. The plain weave provides the maximum fabric stability and firmness with minimum yarns slippage. It has good strength in the two yarns direction. Plain weave fabrics are used commonly for flat laminates and printed circuit boards. The basket weave is a variation of the plain weave. Multiple ends and multiple picks are woven in a manner analogous to the plain weave interlacement scheme. The basket weave offers improved drapeability

over the plain weave, while the twill weave offers even greater drapeability. The satin weaves are a family of weaves categorized by the number of yarns in the repeating unit. The detailed discussion of different woven fabric forms can be found in Norwood (1994), Kumar et al (1997), and Åström (1997).

Uni-directional (UD) fabrics are the most widely used form of reinforcement in civil engineering applications. These materials are a cloth type product wherein all the fibres are aligned along one primary axis (mostly in warp direction). UD woven is a typically plain weave with densely packed warp yarns composed of reinforcing fibres and sparsely space filling yarns that are thin filaments. The fibre weight in the weft direction is commonly less than 10% of the normal fabric weight. Maximum tensile properties are obtained in the warp direction with these fabrics. An example of UD plain weave fabrics is shown in Figure A.3. Other methods of fibre alignment of UD fabric creation include stitched and heatset (Ayers 2001). The UD fabric form also results in laminates to be fabricated with highly orthotropic mechanical properties.

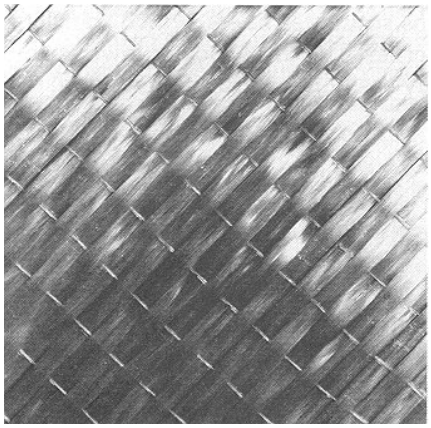

Figure A.3 Plain weave of a UD fabric[7]

(b) Multi-axial Fabrics

Multiaxial fabrics have received a lot of attention within the composite industry in recently years. In this fibre form, yarns are placed parallel to each other in separate layers of different orientation which are then stitched together to form a single cloth type product (Figure A.4).

Biaxial (0°/90°) and double bias (+45°/-45°) fabrics are the most common muliaxial fabric forms in composite industry. Biaxial fabric is similar to plain weaves, expect that two UD fibre layers are overlaid on each other and stitch together at 0° and 90° to the warp direction, rather than woven. Double bias (DB) fabric is produced by overlaying two layers of UD fibres and stitched at +45° and -45° to the warp direction. This form of reinforcement is often used to resist the shear force, as the fibres are generally oriented in the direction of principal stress. Recent developments have also seen the availability of triaxial (0°/+45°/-45°) and quadraxial (0°/90°/+45°/-45°) fabric forms (Kumar et al 1997 and Ayers 2001).

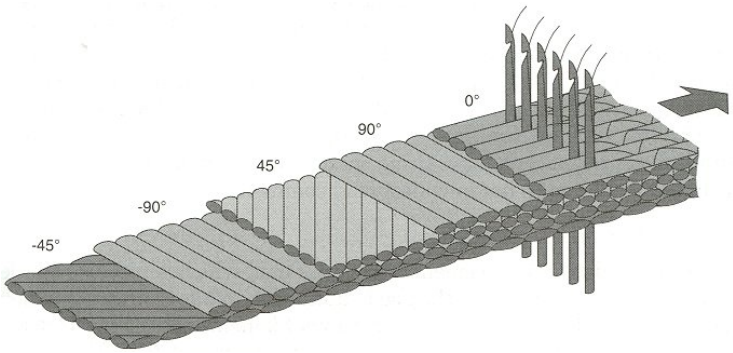

Figure A.4 Stitched multi-axial fabrics[7]

(c) Knitted Fabrics

An alternative to weaving is knitting which produces a looser and more flexible fabric (Figure A.5). Unlike weaving, knitting requires a minimum of one yarn set, not two. There are two general categories of knitting: weft knitting and warp knitting (Kumar et al 1997). Knitted fabrics containing high modulus yarns offer a wide range of form and behaviour. Due to the highly curved fibre configuration in knitted preforms and the high fabric bulk, knitted composite normally exhibit lower strength and modulus than woven structures (Wang et al 1995). However, knitted fabrics do offer some unique advantages, especially in conformability, for making complex-shaped parts. Additionally, the absence of waste fibre in the knitting process and ease of processing using conventional textile machines are particular interest to the manufacturers of composite materials. Currently the use of knitted composites is limited and is primarily for non-structural applications requiring complex shapes.

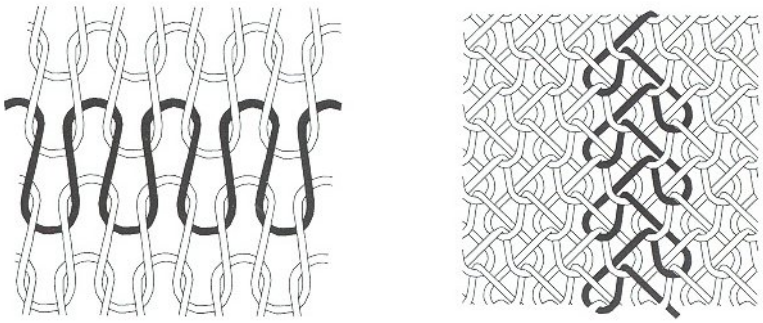

(a) (b)

Figure A.5 Knitted structures: (a) weft knit; (b) warp knit[61]

(d) Chopped Strand Mat (CSM) Fabrics

Chopped strand mat (CSM) has been used for many years in a wide range of non-structural composite components. CSM fabrics are produced by randomly depositing chopped fibres onto a carrier film and then applying a binder. CSM are widely used in lightly stressed applications since they allow significant draping and provide a certain degree of in-plane isotropy (Åström 1997).

(e) Combination Fabrics

It is common that different types of fabrics are stitched or needled together to facilitate both handing and reinforcement orientation. The most common combination is probably that of CSMs and woven fabrics, which are widely used in for example boat building to save time and money in reinforcement cutting and placement operations. More details on this type of reinforcement forms can be found in Åström (1997).

A.2 Polymer Matrix Resins

A.2.1 Polyester Resins

Unsaturated polyester resins, usually simply referred to as polyester resins, are one of the most frequently used resins for the manufacture of FRP. They are syrups consisting of polymer chains dissolved in reactive organic solvent (monomer).

Addition of a suitable catalyst and accelerator causes the syrup to undergo a chemical reaction in the cold state and, without pressure, to form a solid, three-dimensional structure (Norwood 1994). Polyester resins are cured via a free radical co-polymerisation reaction, which can be initiated at room temperature with organic peroxides. It is the ability to cold-cure polyester resins from liquid that makes them more suitable than any other resin system for the manufacture of very large structures. The catalyst systems consist of organic peroxides (initiators) activated by accelerators or promoters. The most common initiator used for curing polyester resins is methyl ethyl ketone peroxide (MEKP). MEKP is not a true catalyst because it is consumed in the reaction, although it is sometimes referred to as "the catalyst". The curing time for polyester resins depends on the decomposition rate of the catalyst, which can be increased by increasing the curing temperature. Amount of typical catalyst for curing is typically 1-2 percent by weight. Other commonly used initiators such as acetyl acetone peroxide, cyclohexanone peroxide and benzoyl peroxide can be found in references of Norwood (1994) and Juska et al (1997).

Polyester resins can be formulated with a variety of properties ranging from hard and brittle to soft and flexible to suit a wide variety of applications. Their advantages include good mechanical properties, low viscosity, fast cure time, and low cost, but their mechanical properties are generally lower than those for epoxy resins (refer Table 2.2). Polyester resins also have good resistance to chemical attack and have been used for many corrosion-resistant structures. The principal disadvantage of polyester resins is their high volumetric shrinkage during cure (4 - 8%). Polyester resins also do not bond well to carbon fibre reinforcements. These disadvantages may affect their widespread use in composite applications. However, for civil and architectural structures, polyester resins are still the commonly used because of their low cost and ease of processing, coupled with their ability to make good quality composites. Their usage will increase through the ongoing development of polyester resins.

A.2.2 Epoxy Resins

Epoxy resins are often used due to their significant superiority where mechanical properties and temperature tolerance of unsaturated polyesters no longer suffice.

However, these improved properties come at a higher price and epoxy resins are therefore often seen in the fields where the cost tolerance is highest, e.g. aerospace, defence, and sports applications.

Epoxy resins are a series of products with a common epoxy ring consisting of two carbon atoms single bonded to an oxygen atom (Kim 1995). The most common epoxy is based on condensation polymerisation of epichlorohydrin and bisphenol A creating diglycidylether of bisphenol A (DGEBPA or DGEBA) epoxy (Åström 1997). Epoxy resins are usually two-part systems, consisting of an epoxy and a curing agent, often referred as catalysts or hardeners. The epoxy largely dictates the properties of the resin and the curing agent determines the cure temperature. Two main types of curing agents are amines and anhydrides. The most common system used to cure epoxy resins in civil engineering application is the amine curing agent. Although some of epoxies are formulated to crosslink at room temperature, most epoxies used in composite applications also require subsequent postcuring to completely crosslink and to achieve optimum properties. Generally, the curing times required by epoxy resins significantly exceed those of polyester resins.

A wide variety of properties of epoxy resins can be formulated to suit a range of applications due to a large number of epoxies and curing agents available (Juska et al 1997, Penn at al 1998). Mechanical properties of epoxy resins are nevertheless between good and excellent (refer Table 2.2), which explains their extensive usage in a wide range of applications. Other advantages of epoxy resins include low viscosity, low shrinkage, excellent resistance to chemicals and solvents, improved resistance to creep and fatigue, good electrical properties, and excellent adhesion to a wide variety of reinforcement fibres, such as glass, carbon, aramid and other fibres. In addition, epoxy resins also exhibit low shrinkage comparing with polyester resins, typically 1 – 5% (Matthews et al 1994). The major drawbacks of epoxy resins are high price, long cure time, and complex processing requirements, which often include elevated temperature and consolidation pressure, thus translating into costly manufacturing operations.

A.2.3 Vinylester Resins

Vinylester resins are the most recent addition to the family of thermosetting polymers. The technology is still relatively new and emerging. These resins are chemically closely related to both usaturated polyesters and epoxies and in most respects represent a compromise between the two, which can be termed as unsaturated esters of epoxy resins (Kim 1995). Vinylesters were developed in an attempt to combine the fast and simple crosslinking of unsaturated polyesters with the mechanical and thermal properties of epoxies. They are produced by reacting an epoxy with an unsaturated acid, and cure via a free radical reaction initiated in the same way as the cure mechanism for polyester resins. Thus, the same curing agents used for polyester resins can be used for curing vinylester resins. The most common curing system used for vinyl ester resins is that of an MEKP initiator in combination with a cobalt accelerator. Being based on epoxies, vinylesters are also typically classified by the epoxy type used. Being a compromise between unsaturated polyesters and epoxies, vinylesters are available for room-temperature curing or may require elevated temperature for postcuring to achieve optimum properties.

Vinylester resins have similar properties to epoxies and processibility of a polyester due to their chemical structures. These resins are often identified as a class of unsaturated polyester thermosetting resins because of the curing and processing similarities. Vinylester resins possess the good characteristics of epoxy resins, such as excellent chemical resistance and tensile strength, combined with those of polyester resins such as low viscosity, fast curing and low cost (refer Table 2.2). However, the volumetric shrinkage of vinylester resins is similar to polyester resins, which is higher than that of the parent epoxy resins. The outstanding balance of properties provide by vinylester resins is obvious and their usage are still continuing strong growth in wide range of civil engineering applications.

A.2.4 Other Thermosetting Resin Systems

There are other resins besides polyesters, vinylesters and epoxy resins which are used for laminating and moulding applications. These include furane resins, polyimide resins, silicone resins, phenolics, melamine and urea-formaldehyde resins. These

resins are primarily formulated as specialty matrices for specific purposes. For example, phenolic resins are utilised in applications where low flammability and low smoke production are required, while polymides are often utilised in high service temperature environments (Matthews et al 1994). More detailed discussions of these resin systems are included in the references of Norwood (1994), Åström (1997), Juska (1997) and Schwartz (1997a).

A.3 Core Materials

The following discussion will outline the commonly used sandwich core materials, their characteristics and applications.

A.3.1 Wood

The wood core is the oldest of core materials used in sandwich structures. The most commonly used wood core is end-grain balsa, in which the grain direction of the core blocks is perpendicular to the plane of the skins in a sandwich structure. Balsa wood cores first appeared in the 1940's in flying boat hulls and clearly dominates the wood core category. The balsa wood is sawed into slices transverse to the grain direction and is then machined into rectangles which are adhesively bonded together side by side to form a large core block. Apart from its high compressive properties in the direction of the grain, end-grain balsa also possesses good thermal insulator and acoustic absorption, and is easily worked simple tools and equipment.

Balsa cores are available as contoured end-grain sheets 3 to 50mm think on a backing fabric, and rigid end-grain sheets up to 100mm thick. These sheets can be provided ready to be resin-coated for vacuum-bagging, prepreg or pressure-based manufacturing processes. However, all wood cores are susceptible to moisture attack and will rot if not well surrounded by laminate or resin. Another disadvantage of balsa is that it can absorb large quantities of resin during lamination if not pre-sealed. Despite this, due to ease use and good durability of the end product, balsa has led to substantially increased usage, particularly of the carefully selected grades of end-grain balsa, in application such as boat hulls, large tanks and airborne pallets and containers.

A.3.2 Foam

Foams are one of the most common forms of core materials. It has been used as a structural core for some time, and extensive development of various foam types has increased the use of these materials. Any polymer (thermoset and thermoplastic) may be expanded in different manners and density ranges. They can be manufactured from variety of synthetic polymers including more common types such as polystyrene (PS), polyurethane (PU), polyvinyl chloride (PVC) and styreneacrylonitrile (SAN). Foams for structural sandwich applications usually have densities in the range from 40 to 200 kg/m^3 and are available in variety of thicknesses, typically from 5mm to 50mm (Ref. [66]).

PS foams are used extensively in sail and surf board manufacture due to their light weight (40kg/m^3), low cost and easy of machining characteristics. However, their low mechanical properties exclude them from a large number of structural applications. PS foams are also not compatible with polyester and vinylester resin systems because they will be dissolved by the styrene present in the resin.

PU foams exhibit only moderate mechanical properties and have a tendency for the foam surface at the resin/core interface to deteriorate with age, leading to skin delamination. Their structural applications are therefore normally limited to the production of formers to create frames and the use of lightly loaded sandwich panels. Polyurethane foams can also be cut and machined readily to required shapes or profiles.

PVC foams are one of the most commonly used core materials for the construction of high performance sandwich structures. They offer a balanced combination of static and dynamic properties and good resistance to water absorption. PVC foams also have a large operating temperature range and are resistant to many chemicals. This foam can be used safely with polyester and vinylester resin systems because of its reasonable resistance to styrene and it is therefore popular in many sandwich structural applications. PVC foams are available in two main types: crosslinked and uncrosslinked with the uncrosslinked foams sometimes being referred to as “linear”. While the uncrosslinked PVC foams have some lower mechanical properties than an

equivalent density of cross-linked PVC, they possess greater toughness and are inherently less brittle. However, PVC foams are one of the most expensive foam cores available, thus limiting their use in civil structures.

SAN foams behave in a similar way to toughened cross-linked PVC foams. They have most of the static properties of cross-linked PVC cores, yet have much higher elongations and toughness. They are therefore able to absorb impact levels that would fracture both conventional and even the toughened PVC foams. However, unlike the toughened PVC's, which use plasticizers to toughen the polymer, the toughness properties of SAN are inherent in the polymer itself, and so do not change appreciably with age. As a result, SAN foams are replacing PVC foams in many applications. The primary disadvantage of SAN foams is its high cost which restricts usage in most civil applications.

A.3.3 Honeycomb

The name honeycomb core stems from this core type's normally hexagonal cellular structure, which strongly resembles the beeswax honeycomb. Honeycomb core are widely used in the aerospace industry where their high price is acceptable to achieve the high specific stiffness and strength uniquely offered by this core type. While numerous different material combinations are used in honeycombs, the most common are aluminium and aramid-fibre paper impregnated with a phenolic resin, the latter having the (Du Pont) trade name Nomex. The characteristics of a honeycomb core significantly depend on its constituents, but also on cell configuration and wall thickness. The predominant advantage of honeycomb cores is their excellent specific mechanical properties since their density is so low. Disadvantages include moisture sensitivity, difficult machining, difficult bonding of faces, and high price. Due to high price and difficult processing requirements, honeycomb cores are mostly limited to applications where cost is not the prime concern and their use in civil structures is unlikely. Further information on manufacturing processes and honeycomb materials properties can be found in references of Åström 1997, Marshall 1998 and Ref. [66].

A.4 Manufacturing Processes of FRP Composites

This section will discuss the more common manufacturing processes of FRP laminate fabrication which have potential for applications in civil structures. Moreover, in term of commercial usage, thermosets clearly dominate in structural composite applications. Therefore, the fabrication techniques described in this section will be restricted to thermosetting resins.

A.4.1 Wet Layup

The wet layup manufacturing techniques refer to processes where the resin is applied in liquid form and the reinforcement is impregnated as part of the layup. The layup may either be performed by hand, herein referred to as hand layup, or in a partially automated procedure, referred to as spray-up.

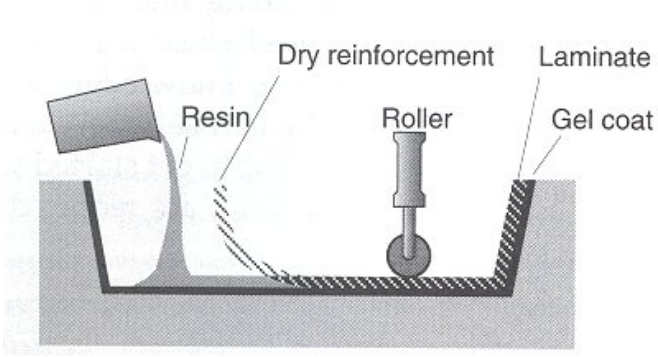

Figure A.6 Hand layup[7]

Despite being one of the first techniques used, the hand layup is the simplest and most versatile of all composite manufacturing techniques. Basically, it involves placement of the dry reinforcements in the mould and subsequent application of the resin (Figure A.6). Then, the wet composite is rolled using hand rollers to facilitate uniform resin distribution and removal of air pockets. The layered structure is then cured. Due to the extremely low capital equipment costs and versatility, hand layup is widely used for all kinds of prototypes as well as for products manufactured in short series. However, the hand layup process is labour-intensive and only has low production rate. The quality of product depends on the skill of workers and product uniformity is also difficult to maintain.

Spray-up is a process in which both resin and chopped reinforced fibre are sprayed onto the mould simultaneously. An air-driven chopper unit is mounted on a resin spray gun. The chopper devours strands of continuous reinforcement, cut them and spits them out in short lengths. The chopped fibre is carried to the mould by the resin stream so that reinforcement and resin are dispensed and positioned simultaneously. Consolidation is by hand rolling as in hand laminating, but is easier as the reinforcement contains no binder and the fibre content is more uniform. The spray-up technique is demonstrated in Figure A.7. The spray gun is normally hand-held, but for longer production runs it may prove economically feasible to mount it on a robot to reduce labour costs. If spraying is performed manually, the quality of component also depends on the skill of operator. Spray-up can be used to manufacture geometrically complex components and applications are similar to those for hand layup, but it is incapable to manufacture the product with continuous fibres. However, with spray-up the resin-reinforcement ratio is well controlled by the spray gun, which leads to more uniform component properties than obtained in hand layup.

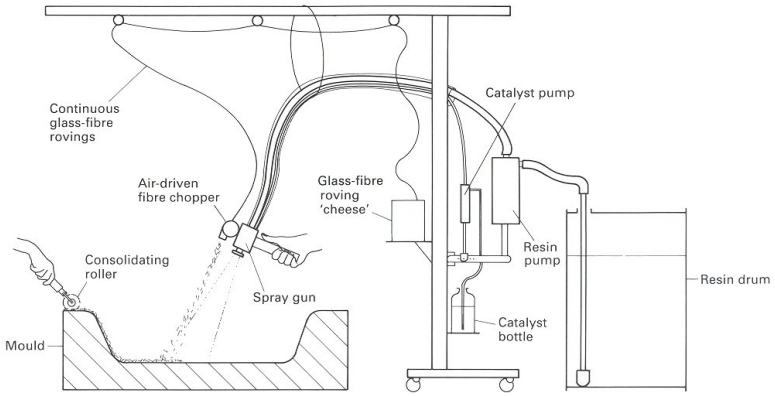

Figure A.7 Spray-up process[12]

A.4.2 Bag Moulding

A uniform pressure applied to the laminate before it is cured improves consolidation of the fibres and removes excess resin, air and volatiles from the matrix. Pressure is applied with the aid of a flexible diaphragm or bag. There are three basic methods of applying pressure to the laminate: pressure bag, vacuum bag, and autoclave processing, the latter two being the most popular methods. Reinforcement and resin

are applied by hand laminating to a simple open mould. Release film or release agent is used on both sides of the laminate to prevent it from sticking to the mould or to the breather. The laminate is then covered with a flexible bag, which is perfectly sealed to the mould. By applying vacuum under the bag, the laminate is cured and consolidated with heat and uniformed atmospheric pressure. The vacuum helps withdraw excess volatile compounds, such as residual solvent, trapped air, or low molecular weight components of the resins.

Vacuum bag moulding, shown in Figure A.8, allows for the production of large, high quality, lower cost composite parts. The main advantages of vacuum bagging are that the vacuuming and curing equipment can be used for a variety of parts. It is also a very effective method for bonding sandwich laminates together. However, vacuum bagging is still labour-intensive, so that the quality of the product is largely dependent on the worker's skill. Thus, this method is only suitable for low production rate processing.

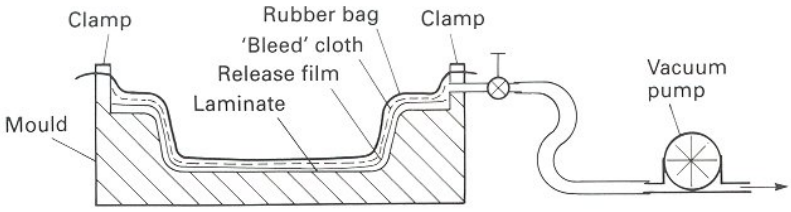

Figure A.8 Vacuum bag moulding[12]

Autoclaves are pressure vessels that contain compressed gas during the processing of the composite. This process is an extension of the vacuum bag technique, providing higher pressure than available with vacuum and giving greater compression and void elimination. The composite part is laid up and enclosed in a vacuum bag. Full or partial vacuum is drawn within the bag, and gas pressure greater than atmospheric is applied on the exterior of the bag. The part temperature is then raised to cure off the laminate. Autoclave processing is commonly used for the production of high quality, complex parts. The method is good for large parts and moderate production quantities. However, autoclave operations consume large amounts of energy and materials including industrial gases and bagging materials, which is very expensive as it often uses vacuum bag moulding techniques. Autoclave processing is also

labour intensive and time consuming. The curing cycle and consolidation of a laminate in an autoclave is long and intensive. The curing cycle may have to be repeated several times to complete curing if the laminate is very thick.

A.4.3 Resin Transfer Moulding

Resin transfer moulding (RTM) is one of the most common liquid moulding technique for manufacturing of fibre-reinforced composites. It is a closed mould process in which the fibre reinforcement is placed dry in the mould. The liquid resin is then pumped into the mould through the inlet, soaking the fibre, filling the mould cavity, and outlet that allow air to escape (Figure A.9). When the mould is full, the inlets and outlets are sealed, and heat is applied until the curing is completed.

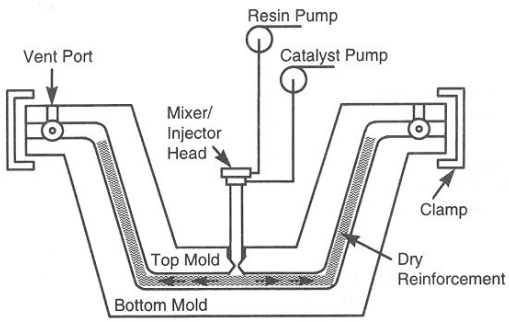

Figure A.9 Resin transfer moulding[15]

The RTM process can produce large continuous fibre reinforced composites with complicated shapes and relatively short cure cycle times. The process is differentiated from other moulding processes in that all the reinforcement is place dry in the mould before any resin is applied. This allows for better control over the orientation of the fibres, thus improving materials properties. However, the cost and time to build a preform for resin transfer moulding are reasonably high. The application of RTM process to civil engineering include large runs of structural components which would then be assembled on site. This process is most commonly used in automobile, aerospace and marine industries.

A.4.4 Filament Winding

Filament winding is a high efficient and automated process in which a filamentary yarn or tow is first wetted by a resin and then uniformly and regularly wound about a rotating mandrel (Figure A.10). In filament winding, continuous reinforcements are fed via a resin bath, then drawn through a delivery eye that controls the angle at which the fibres are applied around the mandrel. The mandrel rotates continuously while the delivery eye moves back and forth. The rotational speed of the mandrel and the linear speed of the delivery eye can be controlled (typically computer controlled) to produce any fibre orientation between 5° and 90° to the axis of rotation, and with up to six degrees of freedom between the mandrel and the delivery eye in typical advanced winding machine (Barbero 1999, Tarnopol'skii 1998). There are two basic types of winding machines: helical and polar. More details of different types of reinforcement configurations in filament winding process can be found in Barbero (1999), Åström (1997), Schwartz (1997b) and Tarnopol'skii (1998).

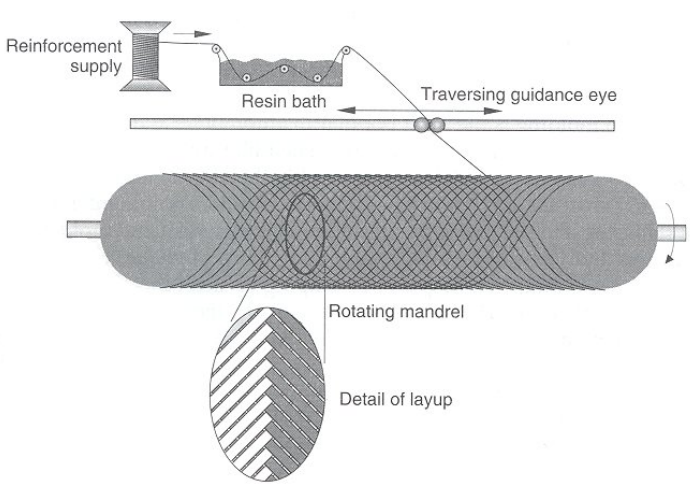

Figure A.10 Schematic of filament winding[7]

The principal advantages of filament winding over other composite material fabrication methods are its low material and labour cost and its reproducibility due to the robotic motions. The major limitations of filament winding are size restrictions, geometric possibilities, the orientation of the fibres, and the surface finish of the final product. Despite the limitation of the process, filament winding has been used in an impressive array of applications courtesy of repeatable and very high mechanical properties in combination with relatively low component cost. Common applications

of filament winding process includes pressure vessels, pipes, launch tubes, and other rotationally symmetric components.

A.4.5 Pultrusion

Pultrusion is a continuous manufacturing process used to produce high-fibre-content reinforced components with constant cross-section shapes of any length. Pultrusion is a low-cost process because it achieves direct conversion of continuous fibres and resin into a finished product. In the basic pultrusion process (Figure A.11), continuous fibrous reinforcement is pulled from packages in creels and is then gradually brought together and pulled into open resin bath wherein the reinforcement is impregnated. Following resin impregnation, the impregnated reinforcements are drawn into the heated die. The cross section of the die gives final shape of the product and the heat that is transferred to the wet reinforcement initiates and completes the curing. The hot finished product from the die is then allowed to cool off before being pulled by the pulling mechanism, which is followed by a moving cut off saw to continuously cut the product to desired length.

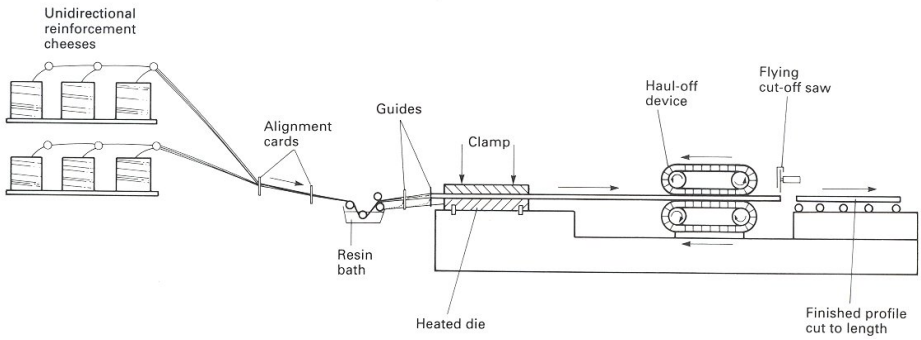

Figure A.11 Schematic of pultrusion[12]

In comparison with filament winding process, pultrusion has the primary reinforcement in the longitudinal direction whereas filament winding places the primary reinforcement in the circumferential (hoop) direction. Accordingly, while good mechanical properties can be achieved in pultrusion in the transverse (crosswise) direction by using special reinforcements, the primary strength exists in the longitudinal direction. Being the common continuous composite manufacturing technique, pultrusion is the most cost-effective of all methods for mass-producing

composites. Significant variations in reinforcement types and orientations can be used in combination with polyester, vinylester and epoxy resins in this process. The primary limitation of the pultrusion process is that the cross-section of the pultruded products must be constant. Although operational costs of pultrusion are low, the capital equipment costs of the process including the chrome plate dies and the guiding system are relatively high (more than AU$ 0.5 million). For these reasons, pultrusion process is ideally suited for high volume applications. Despite essentially being limited to components with constant cross-section, pultrusion is a fast-growing manufacturing technique and pultruded composite products are used in a wide variety of fields spanning every conceivable application from electrical and civil engineering to sports and medicine.

Appendix B

MODULAR MANUFACTURING APPROACH

This appendix provides details of the modular manufacturing approach that was used to construct the prototype two-way FRP slab discussed in Chapter 3 and 6.

B.1 Introduction

Vinylester resins possess a number of advantages such as excellent chemical resistance, low viscosity, fast curing, and a good balance between mechanical properties and cost. However, the volumetric shrinkage of vinylester resin is in the range of 5-10%, which may cause cracking during the manufacturing process if the volume of PFR core in the structure is large. Thus, in consideration of the actual size of the prototype composite slab, a modular manufacturing approach was adopted to overcome such exotherm problem (Huang et al. 2002). In this manufacturing approach, the shrinkage can be controlled by first fabricating small element (modules) which are later combined into large assemblies. Due to the smaller volume of material involved in the modules, shrinkage is normally restricted to an acceptable level and does not result in cracking.

The slab examined in this study was constructed as a sandwich structure with a central core being formed by adhesively bonding individual modules together into the required geometry. Glass fibre reinforced laminates were then bonded on the top and bottom of the assembled modules. The two-way action was created by orienting modules in both longitudinal and transverse directions (see Figure 3.10). In addition to the efficient control of the exotherm and shrinkage, the advantages of this modular

approach also include cost effectiveness, flexibility of section shapes and suitability for both small and large structures.

B.2 Single Modules

In this section, the manufacturing process of single modules is described in detail, which involves the fabrication of the double bias circular tubes, mould assembly, and PFR pouring and curing. A series of tests on single modules was then conducted with the dowel-type joint technique for connecting the single modules examined to investigate behaviour of the single module and evaluate the feasibility of the modular approach.

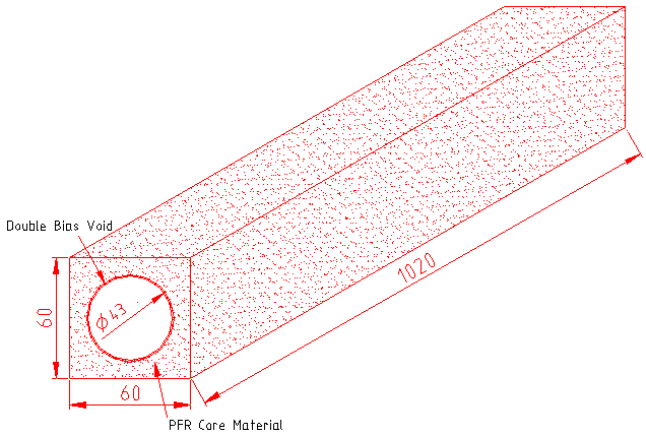

Figure B.1 Typical cross-section and dimensions of single modules

A typical cross-section and dimensions of a single module used in this research is shown in Figure B.1. The length of the modules was designed as 1020 mm, in accordance with the dimensions of the proposed prototype slab (refer Section 3.3.1) and controlled level of shrinkage. The main body of the modules was formed from PFR core with the central circular void created by the double bias tube as described earlier. A casting process was used in conjunction with the PFR core material.

(a) Manufacture of Single Modules

- **Fabrication of Double Bias Circular Tubes**

The PVC pipe with outer dimeter 43 mm (2 mm thickness) was used as a mandrel to create the double bias tubes. First, the PVC pipe with length of 1500 mm was slipped

onto an aluminium pipe to keep it straight during the fabrication. Second, prior to lamination, the surface of the PVC pipe was cleaned and waxed with a release agent – standard wax was used to avoid the adhesion of the laminates to the pipe. The E-glass double bias cloth infused with vinylester resin was then wrapped around the pipe with approximate 20 mm overlapping to ensure the sufficient connection, as shown in Figure B.2. The laminates were allowed to cure at room temperature for about 3 hours (to ensure the sufficient initial curing). Finally, the PVC pipe was pulled out from the circular laminates, then cleaned and waxed for the next fabrication. The finished product of the double bias circular tubes is shown in Figure B.3.

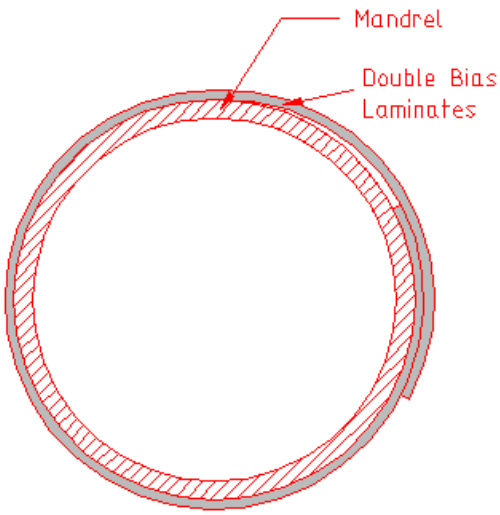

Figure B.2 Double bias tubes lay-up

Figure B.3 A finished double bias circular tube

As discussed in Chapter 2, the disadvantages of the hand layup technique used in the fabrication of double bias circular tubes include being labour-intensive, having low production rate and poor product uniformity, however this technique is suitable for prototype structural components. Highly efficient and automated processes such as filament winding (Refer Appendix A) can be adopted if the large scale production of double bias circular tubes is required.

- **Mould Assembly**

In this study, a steel mould was selected to manufacture the modules due to a number of drawbacks associated with timber mould experienced in previous studies (Davey

1999 and Cattell 2000). This steel mould was constructed from four pieces of 10 mm thick flat mild steel including two sidewalls and top and bottom plates (Figure B.4). Two steel end dams with 43 mm diameter hole were also constructed to seal off the mould and locate the circular double bias tube. In order to restrain the tube at the correct position in the mould, a PVC pipe (outer diameter 43 mm) with approximate 50 mm length was inserted through both holes of end dams and the circular tube at each side of the mould, as shown in Figure B.4b. Prior to the assembly, both steel mould and end dams were cleaned and waxed to avoid the adhesion of PFR to the mould. The steel mould was then assembled by using clamps and set on a flat steel beam base with which three "L" shape steel pieces were bolted at the side edge to keep the sidewall of mould straight (see Figure B.4b). This method of mould assembly has the following desirable characteristics:

- convenience in repeated assembly and disassembly of the mould,
- ease of quality control, and
- suitability for manufacturing prototype structural components.

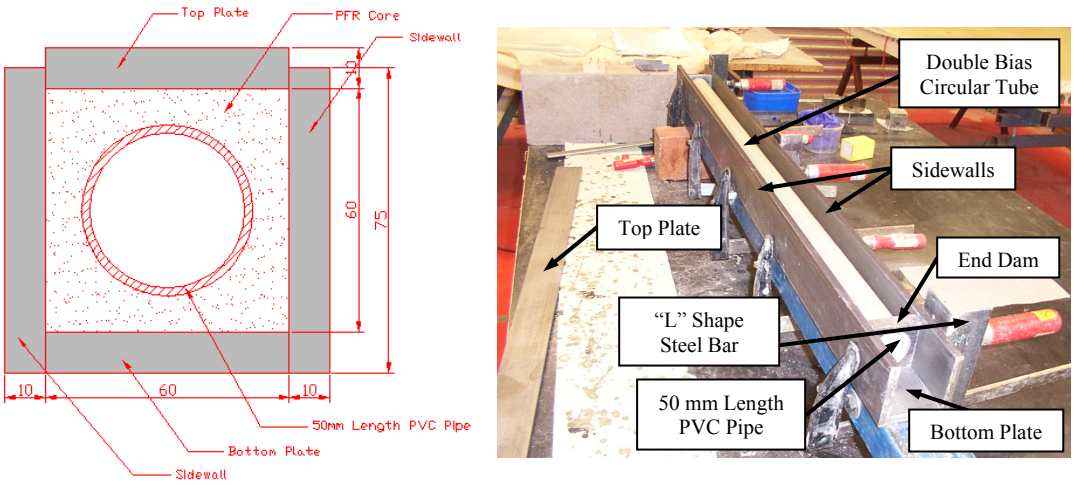

(a) (b)

Figure B.4 Steel mould for manufacturing modules

- **PFR Pouring and Curing**

Pre-calculated mass of vinylester resin, SLG filler and initiator (collectively, PFR) were prepared for each single module pour. The PFR was thoroughly mixed to ensure consistent distribution of the filler, and then poured manually from one side of the mould (see Figure B.5). The consistency of the PFR allowed it to flow up and

around the double bias tubes, and to level itself. This technique minimised air entrapment during the PFR pouring. For the large scale of commercial production, injection moulding could be used rather than manually pouring to pump the PFR in the mould. After PFR pouring, the mould was fully closed by covering with the top plate to allow the casting to cure at room temperature for about 4 hours. This technique was found to offer good control of exotherm temperatures because all four exposed surfaces were available to dissipate heat evenly. Following the ambient curing, the module was removed from the mould (Figure B.6), and cut and finished to final size. The steel mould was then cleaned, waxed and reassembled for the next casting. All completed modules were post-cured for 8 hours at 80°C after ambient curing.

Figure B.5 Pouring PFR into the steel mould

Figure B.6 The ambient cured module removed from the mould

(b) Testing of Single Modules

As a basic structural element of the proposed two-way FRP composite slab system, it was essential to understand the fundamental behaviour of single modules prior to investigating the overall behaviour of the slab. Thus, a small-scale testing program was conducted to investigate the strength and typical characteristics of single modules. The joint technique used in the construction of the composite slab was also examined in this experimental program.

Four-point bending tests were performed on single modules using a 900 mm supported span and 300 mm loading span, which provided the constant bending moments and zero shear force between the two loading points as illustrated schematically in Figure B.7. Two types of signal modules were tested in this program, namely, standard continuous modules and centre joint modules (as shown in Figure B.8). The centre joint was constructed using a double bias laminated tubular insert which acted as a dowel between the two module portions (Figure B.8b). The adhesion was provided by using SPV 500 vinylester based adhesive (Fibre Glass International Pty Ltd). The joint length was chosen at the approximate 10% of the length of the one module portion. The fabrication of the centre joint was similar to that of double bias circular tubes, except that a slightly smaller size of PVC pipe mandrel was used.

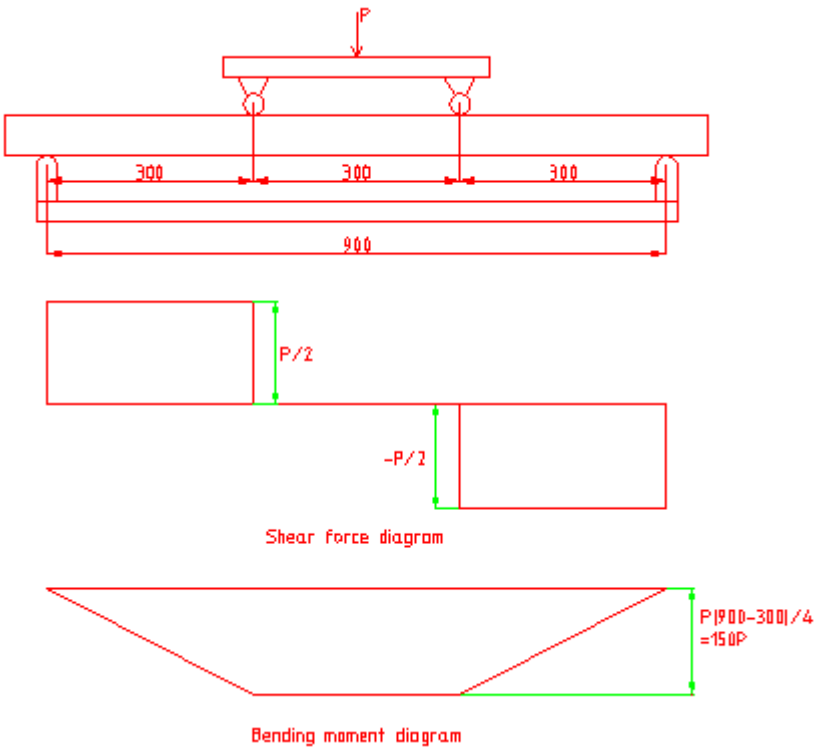

Figure B.7 Schematic of four-point bending test, together with shear force and bending moment diagrams

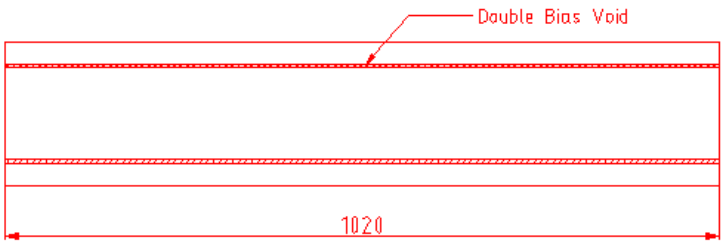

(a)

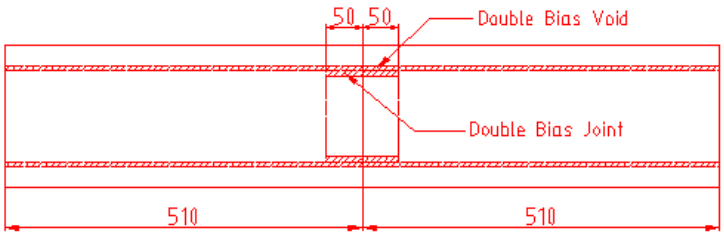

(b)

Figure B.8 Configuration of the tested single modules: (a) Continuous module type A; (b) Jointed module type

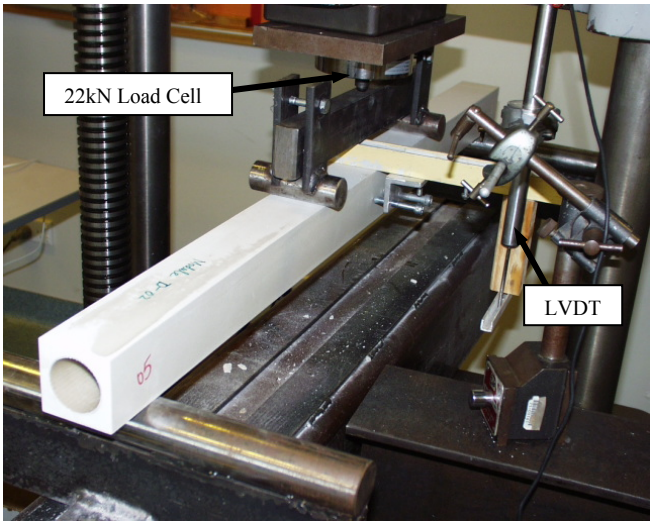

Figure B.9 Single module in test configuration

A total of five test specimens were produced for each configuration. The single module test was conducted on Shimadzu Universal Testing Machine (see Figure 3.12b). Load was measured using a 22 kN capacity load cell, while deflection was measured at the centre of the module using a LVDT (linear voltage differential transducer). Strains along the length of the module were also measured on the bottom surface of the module at critical location using strain gauges. Load, deflection, and

strains were continuously recorded during testing using an electrical data acquisition system (HP System 5000). Figure B.9 shows a photograph of a module under test. The testing results are summarised in Table B.1, and the load deflection diagrams for both module types are shown in Figure B.10.

Table B.1 The results of four-point bending test on single modules

Continuous Module Type A				Jointed Module Type B			
Specimen Number	Peak Load (N)	Centre Deflection (mm)	Strain at Peak (%)	Specimen Number	Peak Load (N)	Centre Deflection (mm)	Strain at Peak (%)
A-01	5535	13.73	0.56	B-01	6007	16.46	0.60
A-02	5361	13.92	0.56	B-02	6125	17.06	0.62
A-03	5847	16.19	0.64	B-03	5789	15.35	0.56
A-04	5477	14.70	0.59	B-04	5520	15.15	0.56
A-05	5779	15.58	0.62	B-05	5373	15.50	0.57
Average	5600	14.82	0.59	**Average**	5763	15.90	0.58

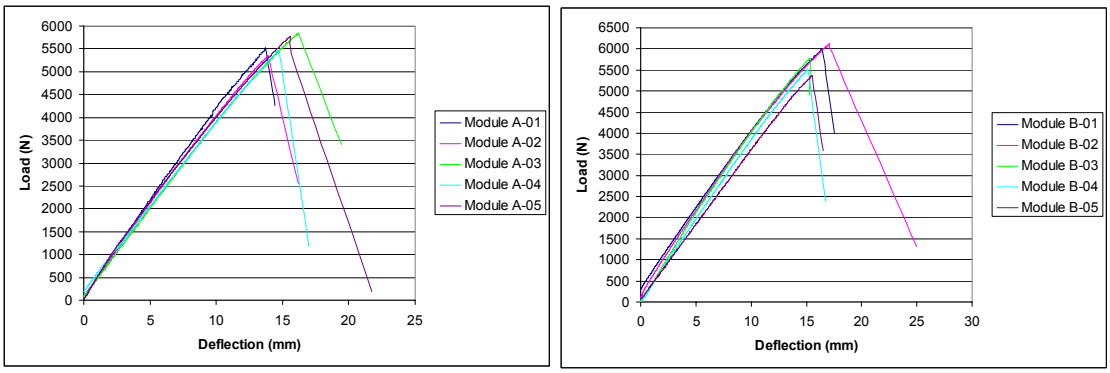

(a) (b)

Figure B.10 Load-deflection behaviour of single modules:
(a) Continuous module type A; (b) Jointed module type B

All specimens failed through tensile cracking of the PFR on the bottom of the module. The average failure load and strain were calculated as 5.60 kN and 0.59%

respectively for continuous modules and 5.76 kN and 0.58% respectively for jointed modules (Table B.1). These values are not significantly different to each other.

The results gained from the test data yielded a relative linear load-displacement relationship of single modules prior to PFR failure as shown in Figure B.10. The average recorded tensile failure strain was approximately 0.6% which is in good agreement with the PFR standard coupon testing results (see Appendix C). The results also indicate that both types of modules displayed similar behaviour (Figure B.10), and that the connection in the jointed module does not detract from overall stiffness or strength characteristics. Consequently, the proposed dowel-type connection technique can be utilized in construction of larger slabs without loss of structural capacity. No further research on optimisation of joint length was undertaken within this testing program. The joint length chosen as 10% of total length of the jointed module portion was used throughout the construction of the two-way FRP composite slab.

B.3 Small-scale Slab Testing

In order to further evaluate the feasibility of the modular construction technique for large-scale slabs, two relatively small-scale slabs were tested. Both slabs were constructed by bonding six standard modules together using SPV 500 vinylester based adhesive. Slab-2 had two extra modules running in transverse direction, as shown in Figure B.11. This testing was only concerned with the behaviour of the central core of the slab, and thus the laminated skins were omitted from test specimens.

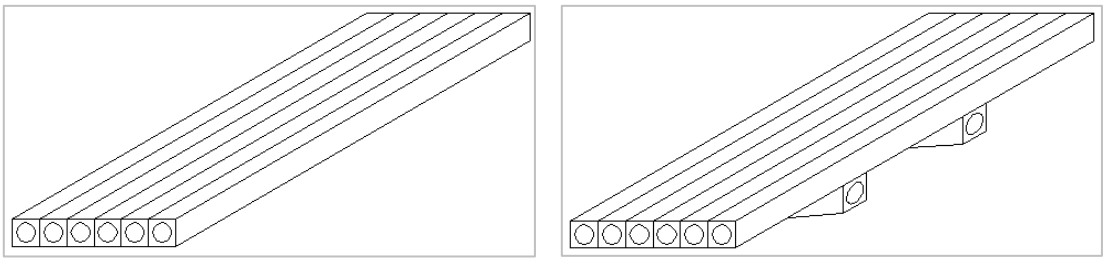

(a) (b)

Figure B.11 Configuration of small-scale test slab: (a) Slab-1; (b) Slab-2

Again, both samples were post-cured for 8 hours at 80°C piror to the testing. The small-scale slabs were tested in bending with a supported span of 900 mm. Load was applied at the centre of the slab through 60×60 mm steel loading patch (Figure B.12). Longitudinal and transverse strains were measured at critical locations on the bottom surface of the slabs using strain gauges. Load, deflection and strains were continuously recorded during testing.

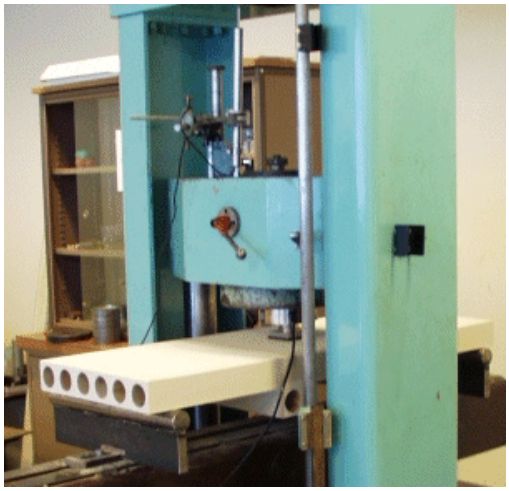

Figure B.12 Side view of a small-scale slab in test configuration

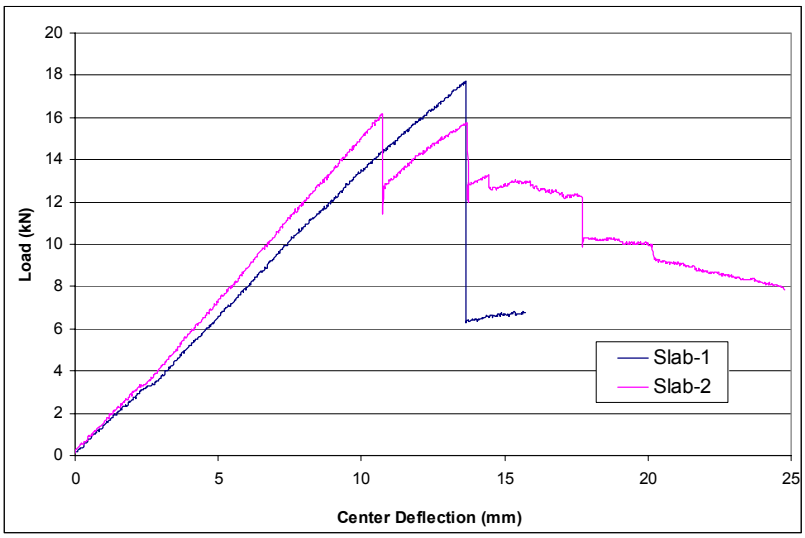

Figure B.13 Load-deflection behaviour of small-scale slabs

The results show that both test slabs exhibited linear load-displacement relationship piror to the PFR failure (Figure B.13). Slab-1 failed at 17.7 kN with a corresponding deflection of 13.7 mm. Slab-2 failed at 16.2 kN and a deflection of 10.7 mm. The relative high stiffness observed in Slab-2 appeared to be due to the two extra transverse modules. Both samples failed through tensile cracking of the PFR. Cracks were initiated on the bottom surface and developed over almost the full depth of the slabs (Figure B.14). Neither slab exhibited punching shear problems despite the highly concentrated loading arrangement. Moreover, no adhesion failure was observed in the specimens prior to the PFR cracking. This was a favourable outcome with respect to the practicability of the proposed modular construction technique.

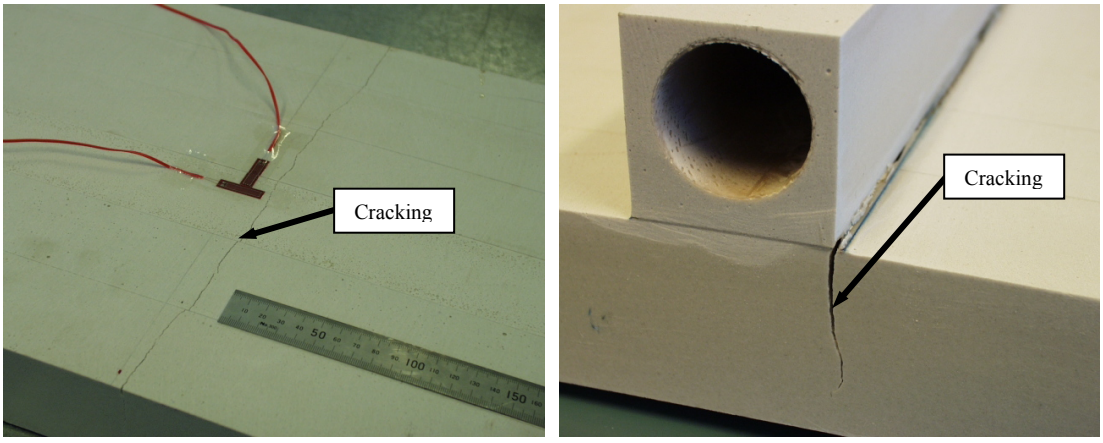

(a) (b)

Figure B.14 Cracking in small-scale slabs: (a) Slab-1; (b) Slab-2

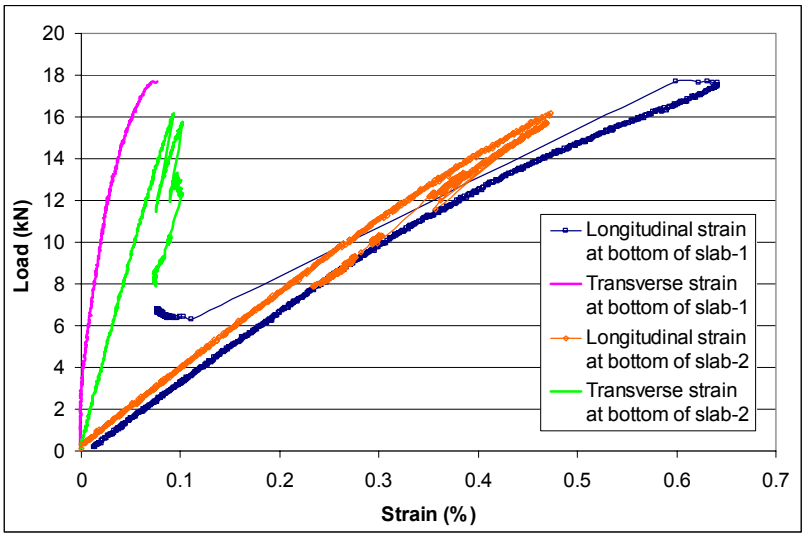

Figure B.15 Load-strain behaviour of small-scale slabs

Figure B.15 shows the recorded strains from both slabs. A longitudinal failure strain of 0.63% with a corresponding transverse strain of 0.076% were measured for Slab-1. The longitudinal failure strain which is very closed to PFR tensile failure strain of 0.66% obtained from the standard coupon test (Appendix C). Slab-2 exhibited a longitudinal failure strain of 0.48% with a corresponding transverse strain of 0.094%. A relative low failure strain in Slab-2 was recorded when compared with Slab-1. This was due to the stress concentration at the sharp corner of Slab-2 where the cracking first initiated (Figure B.14b), which resulted in the earlier tensile failure before the ultimate tensile strain of PFR was reached. In spite of this, a degree of two-way action can be obtained by orientating two layers of modules at 90° to each other. The higher transverse strain recorded in Slab-2 when compared with Slab-1 also indicates that the transverse modules used in Slab-2 were successful in distributing a portion of the load across the width of the slab.

Based on the findings of the single module and small-scale slab tests, it was concluded that the modular manufacturing approach was suitable for production of a prototype slab, and had attributes that may be useful for large-scale slab structures.

Appendix C

DETERMINATION OF FRP COMPOSITE MATERIAL PROPERTIES

C.1 Determination of Laminate Properties

Teat Description: Fibre Fraction Tests

Test Method: ISO 1172:1996

Test Equipment: Muffle Furnace, Analytical Balance

Fibre Type: Unidirectional E-Glass (MU4500)

Resin: Vinyl Ester (Hetron 922)

Initiator: Butanox M60 MEKP

Specimen Description: Laminate Test Panel

Specimen Mass: 7 grams approximate

Calcination Temperature: 575°C ± 20°C

Table C.1 Results of Fibre Fraction Tests

Specimen No.	Dry Crucible Mass (g)	Initial Dry Mass Crucible & Specimen (g)	Final Calcinated Mass Crucible & Specimen (g)	Glass Content (%)
1	20.43	27.55	24.19	52.79
2	21.27	29.12	25.45	53.24
3	21.25	27.95	24.76	52.35
Average	20.98	28.21	24.80	52.79
Std Dev	0.48	0.82	0.63	0.45

Teat Description: Laminate Tensile Tests (for longitudinal direction)

Test Method: ISO 527-5:1997 (Type A Specimen)

Test Equipment: MTS 810 Material Testing System Machine

Fibre Type: Unidirectional E-Glass (MU4500)

Resin: Vinyl Ester (Hetron 922)

Initiator: Butanox M60 MEKP

Layup Sequence: [0°/0°]

Table C.2 Results of Laminate Tensile Tests (Type A Specimen)

Specimen No.	Width (mm)	Thickness (mm)	Area (mm²)	Peak Load (N)	Peak Stress (MPa)	Strain at Peak (%)	Tensile Modulus (E_1) (MPa)
1	15.02	1.35	20.28	10957	540.37	2.72	22301
2	15.30	1.30	19.89	11023	554.20	2.81	21086
3	15.26	1.32	20.14	10504	521.47	2.73	20911
4	15.36	1.35	20.74	10059	485.10	2.67	20119
5	15.59	1.30	20.27	11460	565.45	2.98	21625
6	15.20	1.28	19.46	10558	542.66	2.88	21289
Average	15.29	1.32	20.13	10760	534.87	2.80	21222
Std Dev	0.19	0.03	0.43	489	28.48	0.12	730

Table C.3 Results of Laminate Tensile Tests – Poisson's Ratio (Type A Specimen)

Specimen No.	Width (mm)	Thickness (mm)	Area (mm²)	Peak Load (N)	Peak Stress (MPa)	Axial Strain at Peak (%)	Transverse Strain at Peak (%)	Poisson's Ratio (v_{12}) (mm/mm)
1	15.58	1.32	20.57	1281	62.27	0.30	0.073	0.242
2	15.04	1.32	19.85	1268	63.70	0.30	0.076	0.248
3	15.07	1.34	20.19	1280	63.54	0.30	0.076	0.247
4	15.29	1.35	20.64	1298	62.73	0.30	0.080	0.262
5	15.17	1.38	20.93	1301	62.00	0.30	0.077	0.259
6	15.12	1.38	20.87	1319	63.08	0.30	0.078	0.261
Average	15.21	1.35	20.51	1291	62.89	0.30	0.077	0.253
Std Dev	0.20	0.03	0.41	18	0.68	0.00	0.002	0.009

Test Description: Laminate Tensile Tests (for transverse direction)

Test Method: ISO 527-5:1997 (Type B Specimen)

Test Equipment: MTS 810 Material Testing System Machine

Fibre Type: Unidirectional E-Glass (MU4500)

Resin: Vinyl Ester (Hetron 922)

Initiator: Butanox M60 MEKP

Layup Sequence: $[90°/90°]_2$

Table C.4 Results of Laminate Tensile Tests (Type B Specimen)

Specimen No.	Width (mm)	Thickness (mm)	Area (mm²)	Peak Load (N)	Peak Stress (MPa)	Strain at Peak (%)	Tensile Modulus (E_2) (MPa)
1	25.17	2.57	64.69	2623	40.55	0.51	8719
2	25.22	2.26	57.00	2437	42.76	0.53	9377
3	25.18	2.15	54.14	2182	40.31	0.50	8949
4	25.01	2.25	56.27	2427	43.13	0.57	9274
5	25.00	2.20	55.00	2599	47.25	0.61	9620
6	25.22	2.32	58.51	2618	44.74	0.57	9305
Average	25.13	2.29	57.60	2481	43.12	0.55	9207
Std Dev	0.10	0.15	3.79	172	2.62	0.04	322

Table C.5 Results of Laminate Tensile Tests – Poisson's Ratio (Type B Specimen)

Specimen No.	Width (mm)	Thickness (mm)	Area (mm²)	Peak Load (N)	Peak Stress (MPa)	Axial Strain at Peak (%)	Transverse Strain at Peak (%)	Poisson's Ratio (v_{23}) (mm/mm)
1	25.18	2.15	54.14	1507	27.79	0.30	0.012	0.038
2	25.34	2.47	62.59	1723	27.56	0.30	0.011	0.035
3	25.25	2.42	61.11	1679	27.48	0.30	0.018	0.058
4	25.05	2.42	60.62	1645	27.19	0.30	0.011	0.036
5	25.19	2.37	59.70	1631	27.37	0.30	0.013	0.042
6	25.00	2.21	55.25	1520	27.52	0.30	0.012	0.038
Average	25.17	2.34	58.90	1618	27.49	0.30	0.013	0.041
Std Dev	0.13	0.13	3.41	87	0.20	0.00	0.003	0.009

Test Description: Laminate Compressive Tests (for longitudinal direction)

Test Method: ISO 14126:1999 (Type A Specimen – dimension modified)

Test Equipment: Shimadzu Universal Testing Machine, Loading Fixture

Fibre Type: Unidirectional E-Glass (MU4500)

Resin: Vinyl Ester (Hetron 922)

Initiator: Butanox M60 MEKP

Layup Sequence: $[0°/0°]_4$

Table C.6 Results of Laminate Compressive Tests (Type A Specimen)

Specimen No.	Width (mm)	Thickness (mm)	Area (mm²)	Peak Load (N)	Peak Stress (MPa)	Strain at Peak (%)	Compressive Modulus (E_1) (MPa)
1	12.43	4.21	52.33	28942	553.06	1.98	28187
2	12.85	4.41	56.67	34953	616.80	2.49	29130
3	12.92	4.42	57.11	30292	530.45	2.09	26946
4	12.66	4.35	55.07	32035	581.70	2.18	30527
5	12.86	4.40	56.58	32512	574.58	2.37	27769
6	12.67	4.55	57.65	32439	562.70	2.35	26766
Average	12.73	4.39	55.90	31862	569.88	2.24	28221
Std Dev	0.18	0.11	1.95	2065	29.16	0.19	1421

Test Description: Laminate Compressive Tests (for transverse direction)

Test Method: ISO 14126:1999 (Type B Specimen – dimension modified)

Test Equipment: Shimadzu Universal Testing Machine, Loading Fixture

Fibre Type: Unidirectional E-Glass (MU4500)

Resin: Vinyl Ester (Hetron 922)

Initiator: Butanox M60 MEKP

Layup Sequence: $[90°/90°]_4$

Table C.7 Results of Laminate Compressive Tests (Type B Specimen)

Specimen No.	Width (mm)	Thickness (mm)	Area (mm²)	Peak Load (N)	Peak Stress (MPa)	Strain at Peak (%)	Compressive Modulus (E_2) (MPa)
1	12.87	4.47	57.53	9293	161.54	1.95	11760
2	12.92	4.54	58.66	8350	142.35	1.58	13134
3	12.89	4.39	56.59	8974	158.59	1.89	12675
4	12.85	4.53	58.21	8655	148.68	1.60	14150
5	12.84	4.35	55.85	8114	145.27	1.78	11229
6	12.65	4.51	57.05	8600	150.73	2.25	9365
Average	12.84	4.47	57.31	8664	151.19	1.84	12052
Std Dev	0.10	0.08	1.04	424	7.50	0.25	1670

Test Description: Laminate Shear Tests

Test Method: ISO 14129:1997

Test Equipment: MTS 810 Material Testing System Machine

Fibre Type: Unidirectional E-Glass (MU4500)

Resin: Vinyl Ester (Hetron 922)

Initiator: Butanox M60 MEKP

Layup Sequence: $[+45°/-45°]_8$

Table C.8 Results of Laminate Shear Tests (Shear Modulus)

Specimen No.	Width (mm)	Thickness (mm)	Area (mm²)	Peak Load (N)	Peak Stress (MPa)	Axial Strain at Peak (%)	Transverse Strain at Peak (%)	Shear Modulus (G_{12}) (MPa)
1	25.08	8.68	217.69	7637	17.55	0.38	0.22	2901
2	25.09	8.41	211.01	7709	18.28	0.38	0.22	3079
3	25.21	8.38	211.26	7891	18.68	0.39	0.21	3126
4	24.96	8.52	212.66	7806	18.34	0.39	0.21	3080
5	25.11	8.52	213.94	8105	18.94	0.39	0.21	3186
Average	25.09	8.50	213.31	7830	18.36	0.39	0.21	3074
Std Dev	0.09	0.12	2.72	182	0.52	0.01	0.01	106

Table C.9 Results of Laminate Shear Tests (Shear Strength)

Specimen No.	Width (mm)	Thickness (mm)	Area (mm²)	Peak Load (N)	Shear Strength (MPa)
1	25.08	8.61	215.94	29736	68.85
2	25.11	8.75	219.71	29821	67.86
3	25.15	8.68	218.30	29998	68.71
4	25.22	8.76	220.93	30007	67.91
5	24.94	8.32	207.50	27656	66.64
Average	25.10	8.62	216.48	29444	68.00
Std Dev	0.10	0.18	5.35	1006	0.88

C.2 Determination of PFR Core Properties

Test Description: PFR Core Tensile Tests

Test Method: ISO 527-2:1993

Test Equipment: MTS 810 Material Testing System Machine

Filler Type: SLG

Resin: Vinyl Ester (Hetron 922)

Initiator: Butanox M60 MEKP

Ratio of Mixture: Resin : Filler = 56% : 44% (by volume)

Table C.10 Results of PFR Core Tensile Tests

Specimen No.	Width (mm)	Thickness (mm)	Area (mm²)	Peak Load (N)	Peak Stress (MPa)	Strain at Peak (%)	Tensile Modulus (MPa)	Poisson's Ratio (mm/mm)
1	9.96	4.10	40.84	1058	25.91	0.64	5022	0.318
2	9.89	4.09	40.45	1110	27.44	0.76	4996	0.312
3	9.95	4.09	40.70	1075	26.42	0.66	5006	0.303
4	9.93	4.07	40.42	1121	27.74	0.74	5063	0.336
5	9.93	4.05	40.22	1001	24.89	0.62	4757	0.311
6	9.92	4.05	40.18	998	24.84	0.72	4742	0.314
7	9.98	4.08	40.72	933	22.91	0.51	4901	0.318
8	9.95	4.03	40.10	973	24.27	0.65	4873	0.314
9	9.92	4.04	40.08	966	24.23	0.67	4999	0.312
10	9.96	4.06	40.44	980	24.23	0.65	4892	0.318
Average	9.94	4.07	40.41	1022	25.29	0.66	4925	0.316
Std Dev	0.03	0.02	0.27	65	1.55	0.07	111	0.008

Test Description: PFR Core Compressive Tests

Test Method: In-house End-loaded Compressive Testing Technique

Test Equipment: Shimadzu Universal Testing Machine, Loading Fixture

Filler Type: SLG

Resin: Vinyl Ester (Hetron 922)

Initiator: Butanox M60 MEKP

Ratio of Mixture: Resin : Filler = 56% : 44% (by volume)

Table C.11 Results of PFR Core Compressive Tests

Specimen No.	Width (mm)	Thickness (mm)	Area (mm^2)	Peak Load (N)	Peak Stress (MPa)	Strain at Peak (%)	Compressive Modulus (MPa)
1	12.66	4.20	53.17	4406	82.86	2.75	5943
2	12.49	4.11	51.33	3981	77.55	2.13	6067
3	12.69	4.08	51.78	4314	83.32	2.78	6809
4	12.46	4.28	53.33	4441	83.28	2.73	5812
5	12.67	4.01	50.81	4228	83.22	2.60	6008
6	12.68	4.06	51.48	4122	80.07	2.76	6122
Average	12.61	4.12	51.98	4249	81.72	2.62	6127
Std Dev	0.10	0.10	1.03	176	2.39	0.25	351

Test Description: PFR Core Shear Tests

Test Method: ASTM D5379/D5379M:1998

Test Equipment: MTS 810 Material Testing System Machine, Loading Fixture

Filler Type: SLG

Resin: Vinyl Ester (Hetron 922)

Initiator: Butanox M60 MEKP

Ratio of Mixture: Resin : Filler = 56% : 44% (by volume)

Table C.12 Results of PFR Core Shear Tests (Shear Strength)

Specimen	Notch Width (mm)	Thickness (mm)	Area mm2	Peak Load (N)	Shear Strength (MPa)
1	11.67	3.47	40.49	581	14.35
2	11.72	3.50	41.02	463	11.29
3	11.84	3.51	41.56	606	14.58
4	11.71	3.55	41.57	573	13.78
5	11.74	3.50	41.09	612	14.89
6	11.74	3.49	40.97	593	14.47
Average	11.74	3.50	41.12	571	13.89
Std Dev	0.06	0.03	0.40	55	1.33

Appendix D

ARBITRARY TRANSFORMATION OF CONSTITUTIVE EQUATIONS

D.1 Constitutive Equations for Out Shell Segments I

The compliance matrix and stress-stain in the principal material coordinate system {1, 2, 3} are given as (Eq. 4.12):

$$\begin{Bmatrix} \sigma_1 \\ \sigma_2 \\ \tau_{23} \\ \tau_{13} \\ \tau_{12} \end{Bmatrix}_k = \begin{bmatrix} C_{11} & C_{12} & 0 & 0 & 0 \\ C_{12} & C_{22} & 0 & 0 & 0 \\ 0 & 0 & C_{44} & 0 & 0 \\ 0 & 0 & 0 & C_{55} & 0 \\ 0 & 0 & 0 & 0 & C_{66} \end{bmatrix}_k \begin{Bmatrix} \varepsilon_1 \\ \varepsilon_2 \\ \gamma_{23} \\ \gamma_{13} \\ \gamma_{12} \end{Bmatrix}_k \tag{D.1}$$

However, laminates are constructed in such a manner that the principal material co-ordinate system do not coincide with the natural co-ordinate system of the reference body. Given the constitutive model, we use the transformation $C_{ij} = e_{im} e_{jn} \overline{C}_{mn}$ to obtain the constitutive model in global coordinate system.

The transformation matrix [T] and Reuter's matrix [R] are given as

$$[T] = \begin{bmatrix} \cos^2\theta & \sin^2\theta & 0 & 0 & 2\cos\theta\sin\theta \\ \sin^2\theta & \cos^2\theta & 0 & 0 & -2\cos\theta\sin\theta \\ 0 & 0 & \cos\theta & -\sin\theta & 0 \\ 0 & 0 & \sin\theta & \cos\theta & 0 \\ -\cos\theta\sin\theta & \cos\theta\sin\theta & 0 & 0 & \cos^2\theta - \sin^2\theta \end{bmatrix}, \quad [T]^{-1} = [T(-\theta)]$$

$$[R]=\begin{bmatrix}1&0&0&0&0\\0&1&0&0&0\\0&0&2&0&0\\0&0&0&2&0\\0&0&0&0&2\end{bmatrix},\quad [R]^{-1}=\begin{bmatrix}1&0&0&0&0\\0&1&0&0&0\\0&0&\frac{1}{2}&0&0\\0&0&0&\frac{1}{2}&0\\0&0&0&0&\frac{1}{2}\end{bmatrix}$$

The transformation of stresses and strains from the lamina principal directions to the global coordinate system is achieved by using the transformation matrix [T]

$$\begin{Bmatrix}\sigma_1\\\sigma_2\\\tau_{23}\\\tau_{31}\\\tau_{12}\end{Bmatrix}=[T]\begin{Bmatrix}\sigma_x\\\sigma_y\\\tau_{yz}\\\tau_{xz}\\\tau_{xy}\end{Bmatrix},\quad \begin{Bmatrix}\varepsilon_1\\\varepsilon_2\\\frac{1}{2}\gamma_{23}\\\frac{1}{2}\gamma_{31}\\\frac{1}{2}\gamma_{12}\end{Bmatrix}=[T]\begin{Bmatrix}\varepsilon_x\\\varepsilon_y\\\frac{1}{2}\gamma_{yz}\\\frac{1}{2}\gamma_{xz}\\\frac{1}{2}\gamma_{xy}\end{Bmatrix} \tag{D.2}$$

Using the Reuter's matrix [R], it has the following relationships

$$\begin{Bmatrix}\varepsilon_1\\\varepsilon_2\\\gamma_{23}\\\gamma_{31}\\\gamma_{12}\end{Bmatrix}=[R]\begin{Bmatrix}\varepsilon_1\\\varepsilon_2\\\frac{1}{2}\gamma_{23}\\\frac{1}{2}\gamma_{31}\\\frac{1}{2}\gamma_{12}\end{Bmatrix},\quad \begin{Bmatrix}\varepsilon_x\\\varepsilon_y\\\gamma_{yz}\\\gamma_{xz}\\\gamma_{xy}\end{Bmatrix}=[R]\begin{Bmatrix}\varepsilon_x\\\varepsilon_y\\\frac{1}{2}\gamma_{yz}\\\frac{1}{2}\gamma_{xz}\\\frac{1}{2}\gamma_{xy}\end{Bmatrix} \tag{D.3}$$

Substituting the expressions (D.2), (D.3) and matrices [T], [R] in Eq. (D.1), it yields

$$\begin{Bmatrix}\sigma_x\\\sigma_y\\\tau_{yz}\\\tau_{xz}\\\tau_{xy}\end{Bmatrix}=[T]^{-1}[C][R][T][R]^{-1}\begin{Bmatrix}\varepsilon_x\\\varepsilon_y\\\gamma_{yz}\\\gamma_{xz}\\\gamma_{xy}\end{Bmatrix}=\left[T^{-1}\right][C][T]^{-T}\begin{Bmatrix}\varepsilon_x\\\varepsilon_y\\\gamma_{yz}\\\gamma_{xz}\\\gamma_{xy}\end{Bmatrix} \tag{D.4}$$

where $[T]^{-T}=[R][T][R]^{-1}$

Expanding Eq. (D.4), the constitutive equations for outer shell segments I as:

$$\begin{Bmatrix}\sigma_x\\\sigma_y\\\tau_{yz}\\\tau_{xz}\\\tau_{xy}\end{Bmatrix}_k^I=\begin{bmatrix}\overline{C}_{11}&\overline{C}_{12}&0&0&\overline{C}_{16}\\\overline{C}_{12}&\overline{C}_{22}&0&0&\overline{C}_{26}\\0&0&\overline{C}_{44}&\overline{C}_{45}&0\\0&0&\overline{C}_{45}&\overline{C}_{55}&0\\\overline{C}_{16}&\overline{C}_{26}&0&0&\overline{C}_{66}\end{bmatrix}_k^I\begin{Bmatrix}\varepsilon_x\\\varepsilon_y\\\gamma_{yz}\\\gamma_{xz}\\\gamma_{xy}\end{Bmatrix}_k^I \tag{D.5}$$

where

$$\overline{C}_{11} = C_{11}\cos^4\theta + 2(C_{12} + 2C_{66})\sin^2\theta\cos^2\theta + C_{22}\sin^4\theta$$
$$\overline{C}_{12} = (C_{11} + C_{22} - 4C_{66})\sin^2\theta\cos^2\theta + C_{12}(\sin^4\theta + \cos^4\theta)$$
$$\overline{C}_{22} = C_{11}\sin^4\theta + 2(C_{12} + 2C_{66})\sin^2\theta\cos^2\theta + C_{22}\cos^4\theta$$
$$\overline{C}_{16} = (C_{11} - C_{12} - 2C_{66})\sin\theta\cos^3\theta + (C_{12} - C_{22} + 2C_{66})\sin^3\theta\cos\theta$$
$$\overline{C}_{26} = (C_{11} - C_{12} - 2C_{66})\sin^3\theta\cos\theta + (C_{12} - C_{22} + 2C_{66})\sin\theta\cos^3\theta$$
$$\overline{C}_{66} = (C_{11} + C_{22} - 2C_{12} - 2C_{66})\sin^2\theta\cos^2\theta + C_{66}(\sin^4\theta + \cos^4\theta)$$
$$\overline{C}_{44} = C_{44}\cos^2\theta + C_{55}\sin^2\theta$$
$$\overline{C}_{45} = (C_{55} - C_{44})\sin\theta\cos\theta$$
$$\overline{C}_{55} = C_{44}\sin^2\theta + C_{55}\cos^2\theta$$

D.2 Constitutive Equations for Circular Cell Segments II

Firstly, the stresses and strains are transformed from the {1, 2, 3} coordinate system (i.e., lamina principal directions) into the shell local coordinate system {*x*, *s*, *r*}. Repeating the steps shown in equations (D.2) and (D.3), the constitutive equations for circular cell segments II in the shell local coordinate system can be obtained as

$$\begin{Bmatrix} \sigma_x \\ \sigma_s \\ \tau_{sr} \\ \tau_{xr} \\ \tau_{xs} \end{Bmatrix}^{II}_{k} = \begin{bmatrix} \overline{C}_{11} & \overline{C}_{12} & 0 & 0 & \overline{C}_{16} \\ \overline{C}_{12} & \overline{C}_{22} & 0 & 0 & \overline{C}_{26} \\ 0 & 0 & \overline{C}_{44} & \overline{C}_{45} & 0 \\ 0 & 0 & \overline{C}_{45} & \overline{C}_{55} & 0 \\ \overline{C}_{16} & \overline{C}_{26} & 0 & 0 & \overline{C}_{66} \end{bmatrix}^{II}_{k} \begin{Bmatrix} \varepsilon_x \\ \varepsilon_s \\ \gamma_{sr} \\ \gamma_{xr} \\ \gamma_{xs} \end{Bmatrix}^{II}_{k} \tag{D.6}$$

where

$$\overline{C}_{11} = C_{11}\cos^4\theta + 2(C_{12} + 2C_{66})\sin^2\theta\cos^2\theta + C_{22}\sin^4\theta$$
$$\overline{C}_{12} = (C_{11} + C_{22} - 4C_{66})\sin^2\theta\cos^2\theta + C_{12}(\sin^4\theta + \cos^4\theta)$$
$$\overline{C}_{22} = C_{11}\sin^4\theta + 2(C_{12} + 2C_{66})\sin^2\theta\cos^2\theta + C_{22}\cos^4\theta$$
$$\overline{C}_{16} = (C_{11} - C_{12} - 2C_{66})\sin\theta\cos^3\theta + (C_{12} - C_{22} + 2C_{66})\sin^3\theta\cos\theta$$
$$\overline{C}_{26} = (C_{11} - C_{12} - 2C_{66})\sin^3\theta\cos\theta + (C_{12} - C_{22} + 2C_{66})\sin\theta\cos^3\theta$$
$$\overline{C}_{66} = (C_{11} + C_{22} - 2C_{12} - 2C_{66})\sin^2\theta\cos^2\theta + C_{66}(\sin^4\theta + \cos^4\theta)$$
$$\overline{C}_{44} = C_{44}\cos^2\theta + C_{55}\sin^2\theta$$
$$\overline{C}_{45} = (C_{55} - C_{44})\sin\theta\cos\theta$$
$$\overline{C}_{55} = C_{44}\sin^2\theta + C_{55}\cos^2\theta$$

Then transform the stresses and strains from the shell local coordinate system into global coordinate system $\{x, y, z\}$. The stresses at top circular cell segment II_t are rotated around x-axis by an angle ϕ. The general from for the transformation in this case is given by

$$\begin{Bmatrix} \sigma_x \\ \sigma_s \\ \sigma_r \\ \tau_{sr} \\ \tau_{xr} \\ \tau_{xs} \end{Bmatrix} = [T_1] \begin{Bmatrix} \sigma_x \\ \sigma_y \\ \sigma_z \\ \tau_{yz} \\ \tau_{xz} \\ \tau_{xy} \end{Bmatrix} = \begin{bmatrix} 1 & 0 & 0 & 0 & 0 & 0 \\ 0 & m^2 & n^2 & 2mn & 0 & 0 \\ 0 & n^2 & m^2 & -2mn & 0 & 0 \\ 0 & -mn & mn & m^2-n^2 & 0 & 0 \\ 0 & 0 & 0 & 0 & m & -n \\ 0 & 0 & 0 & 0 & n & m \end{bmatrix} \begin{Bmatrix} \sigma_x \\ \sigma_y \\ \sigma_z \\ \tau_{yz} \\ \tau_{xz} \\ \tau_{xy} \end{Bmatrix}$$

where $m = \cos\phi, \quad n = \sin\phi$ and $[T_1]^{-1} = [T_1(-\phi)]$.

By neglecting σ_z and ε_z, the transformation matrix reduces to

$$[T_1'] = \begin{bmatrix} 1 & 0 & 0 & 0 & 0 \\ 0 & m^2 & 2mn & 0 & 0 \\ 0 & -mn & m^2-n^2 & 0 & 0 \\ 0 & 0 & 0 & m & -n \\ 0 & 0 & 0 & n & m \end{bmatrix}, \quad [T_1']^{-1} = \begin{bmatrix} 1 & 0 & 0 & 0 & 0 \\ 0 & m^2 & -2mn & 0 & 0 \\ 0 & mn & m^2-n^2 & 0 & 0 \\ 0 & 0 & 0 & m & n \\ 0 & 0 & 0 & -n & m \end{bmatrix}$$

Thus, the transformation from shell local coordinate system $\{x, s, r\}$ into global coordinate system $\{x, y, z\}$ are given by

$$\begin{Bmatrix} \sigma_x \\ \sigma_s \\ \tau_{sr} \\ \tau_{xr} \\ \tau_{xs} \end{Bmatrix} = [T_1'] \begin{Bmatrix} \sigma_x \\ \sigma_y \\ \tau_{yz} \\ \tau_{xz} \\ \tau_{xy} \end{Bmatrix}, \quad \begin{Bmatrix} \varepsilon_x \\ \varepsilon_s \\ \frac{1}{2}\gamma_{sr} \\ \frac{1}{2}\gamma_{xr} \\ \frac{1}{2}\gamma_{xs} \end{Bmatrix} = [T_1'] \begin{Bmatrix} \varepsilon_x \\ \varepsilon_y \\ \frac{1}{2}\gamma_{yz} \\ \frac{1}{2}\gamma_{xz} \\ \frac{1}{2}\gamma_{xy} \end{Bmatrix} \tag{D.7}$$

By using the Reuter's matrix $[R]$, the following relationships can be defined

$$\begin{Bmatrix} \varepsilon_x \\ \varepsilon_s \\ \gamma_{sr} \\ \gamma_{xr} \\ \gamma_{xs} \end{Bmatrix} = [R] \begin{Bmatrix} \varepsilon_x \\ \varepsilon_s \\ \frac{1}{2}\gamma_{sr} \\ \frac{1}{2}\gamma_{xr} \\ \frac{1}{2}\gamma_{xs} \end{Bmatrix}, \quad \begin{Bmatrix} \varepsilon_x \\ \varepsilon_y \\ \gamma_{yz} \\ \gamma_{xz} \\ \gamma_{xy} \end{Bmatrix} = [R] \begin{Bmatrix} \varepsilon_x \\ \varepsilon_y \\ \frac{1}{2}\gamma_{yz} \\ \frac{1}{2}\gamma_{xz} \\ \frac{1}{2}\gamma_{xy} \end{Bmatrix} \tag{D.8}$$

Substituting the expressions (D.7), (D.8) and matrices $[T_1']$, $[R]$ in Eq. (D.6), it produces

$$\begin{Bmatrix}\sigma_x\\ \sigma_y\\ \tau_{yz}\\ \tau_{xz}\\ \tau_{xy}\end{Bmatrix} = [T_1']^{-1}[\overline{C}][R][T_1'][R]^{-1}\begin{Bmatrix}\varepsilon_x\\ \varepsilon_y\\ \gamma_{yz}\\ \gamma_{xz}\\ \gamma_{xy}\end{Bmatrix} = [T_1']^{-1}[\overline{C}][T_1']^{-T}\begin{Bmatrix}\varepsilon_x\\ \varepsilon_y\\ \gamma_{yz}\\ \gamma_{xz}\\ \gamma_{xy}\end{Bmatrix} \tag{D.9}$$

where $[T_1']^{-T} = [R][T_1'][R]^{-1}$

Expanding the Eq. (D.9), the constitutive equations for the top circular cell segments II_t can be obtained as:

$$\begin{Bmatrix}\sigma_x\\ \sigma_y\\ \tau_{yz}\\ \tau_{xz}\\ \tau_{xy}\end{Bmatrix}_k^{II_t} = \begin{bmatrix}\widetilde{C}_{11} & \widetilde{C}_{12} & \widetilde{C}_{14} & \widetilde{C}_{15} & \widetilde{C}_{16}\\ \widetilde{C}_{12} & \widetilde{C}_{22} & \widetilde{C}_{24} & \widetilde{C}_{25} & \widetilde{C}_{26}\\ \widetilde{C}_{14} & \widetilde{C}_{24} & \widetilde{C}_{44} & \widetilde{C}_{45} & \widetilde{C}_{46}\\ \widetilde{C}_{15} & \widetilde{C}_{25} & \widetilde{C}_{45} & \widetilde{C}_{55} & \widetilde{C}_{56}\\ \widetilde{C}_{16} & \widetilde{C}_{26} & \widetilde{C}_{46} & \widetilde{C}_{56} & \widetilde{C}_{66}\end{bmatrix}_k^{II_b}\begin{Bmatrix}\varepsilon_x\\ \varepsilon_y\\ \gamma_{yz}\\ \gamma_{xz}\\ \gamma_{xy}\end{Bmatrix}_k^{II_t} \tag{D.10}$$

where

$$\widetilde{C}_{11} = \overline{C}_{11},\quad \widetilde{C}_{12} = m^2\overline{C}_{12},\quad \widetilde{C}_{14} = mn\overline{C}_{12},\quad \widetilde{C}_{15} = n\overline{C}_{16},\quad \widetilde{C}_{16} = m\overline{C}_{16},$$
$$\widetilde{C}_{22} = m^4\overline{C}_{22} + 4m^2n^2\overline{C}_{44},\quad \widetilde{C}_{24} = m^3n\overline{C}_{22} + 2mn(-m^2+n^2)\overline{C}_{44},$$
$$\widetilde{C}_{25} = m^2n(\overline{C}_{26} - 2\overline{C}_{45}),\quad \widetilde{C}_{26} = m^3\overline{C}_{26} + 2mn^2\overline{C}_{45},$$
$$\overline{C}_{44} = m^2n^2\overline{C}_{22} + (m^2-n^2)\overline{C}_{44},\quad \widetilde{C}_{45} = mn^2\overline{C}_{26} + (m^3-mn^2)\overline{C}_{45},$$
$$\widetilde{C}_{46} = m^2n\overline{C}_{26} + (-m^2n+n^3)\overline{C}_{45},$$
$$\widetilde{C}_{55} = m^2\overline{C}_{55} + n^2\overline{C}_{66},\quad \overline{C}_{56} = mn(-\overline{C}_{55} + \overline{C}_{66}),$$
$$\widetilde{C}_{66} = n^2\overline{C}_{55} + m^2\overline{C}_{66}$$

The stresses at bottom circular cell segment II_b are rotated around y-axis by an angle ϕ. The general from for the transformation in this case is given by

$$\begin{Bmatrix} \sigma_x \\ \sigma_s \\ \sigma_r \\ \tau_{sr} \\ \tau_{xr} \\ \tau_{xs} \end{Bmatrix} = [T_2] \begin{Bmatrix} \sigma_x \\ \sigma_y \\ \sigma_z \\ \tau_{yz} \\ \tau_{xz} \\ \tau_{xy} \end{Bmatrix} = \begin{bmatrix} m^2 & 0 & n^2 & 0 & -2mn & 0 \\ 0 & 1 & 0 & 0 & 0 & 0 \\ n^2 & 0 & m^2 & 0 & 2mn & 0 \\ 0 & 0 & 0 & m & 0 & n \\ mn & 0 & -mn & 0 & m^2 - n^2 & 0 \\ 0 & 0 & 0 & -n & 0 & m \end{bmatrix} \begin{Bmatrix} \sigma_x \\ \sigma_y \\ \sigma_z \\ \tau_{yz} \\ \tau_{xz} \\ \tau_{xy} \end{Bmatrix}$$

where $m = \cos\phi$, $n = \sin\phi$ and $[T_2]^{-1} = [T_2(-\phi)]$. Again neglecting σ_z and ε_z, the transformation matrix reduces to

$$[T_2'] = \begin{bmatrix} m^2 & 0 & 0 & -2mn & 0 \\ 0 & 1 & 0 & 0 & 0 \\ 0 & 0 & m & 0 & n \\ mn & 0 & 0 & m^2 - n^2 & 0 \\ 0 & 0 & -n & 0 & m \end{bmatrix}, \quad [T_2']^{-1} = \begin{bmatrix} m^2 & 0 & 0 & 2mn & 0 \\ 0 & 1 & 0 & 0 & 0 \\ 0 & 0 & m & 0 & -n \\ -mn & 0 & 0 & m^2 - n^2 & 0 \\ 0 & 0 & n & 0 & m \end{bmatrix}$$

Thus, the transformation from shell local coordinate system $\{x, s, r\}$ into global coordinate system $\{x, y, z\}$ are given by

$$\begin{Bmatrix} \sigma_x \\ \sigma_s \\ \tau_{sr} \\ \tau_{xr} \\ \tau_{xs} \end{Bmatrix} = [T_2'] \begin{Bmatrix} \sigma_x \\ \sigma_y \\ \tau_{yz} \\ \tau_{xz} \\ \tau_{xy} \end{Bmatrix}, \quad \begin{Bmatrix} \varepsilon_x \\ \varepsilon_s \\ \frac{1}{2}\gamma_{sr} \\ \frac{1}{2}\gamma_{xr} \\ \frac{1}{2}\gamma_{xs} \end{Bmatrix} = [T_2'] \begin{Bmatrix} \varepsilon_x \\ \varepsilon_y \\ \frac{1}{2}\gamma_{yz} \\ \frac{1}{2}\gamma_{xz} \\ \frac{1}{2}\gamma_{xy} \end{Bmatrix} \tag{D.11}$$

Analogous to Eq. (D.8), the Reuter's matrix $[R]$ produces the following relationships

$$\begin{Bmatrix} \varepsilon_x \\ \varepsilon_s \\ \gamma_{sr} \\ \gamma_{xr} \\ \gamma_{xs} \end{Bmatrix} = [R] \begin{Bmatrix} \varepsilon_x \\ \varepsilon_s \\ \frac{1}{2}\gamma_{sr} \\ \frac{1}{2}\gamma_{xr} \\ \frac{1}{2}\gamma_{xs} \end{Bmatrix}, \quad \begin{Bmatrix} \varepsilon_x \\ \varepsilon_y \\ \gamma_{yz} \\ \gamma_{xz} \\ \gamma_{xy} \end{Bmatrix} = [R] \begin{Bmatrix} \varepsilon_x \\ \varepsilon_y \\ \frac{1}{2}\gamma_{yz} \\ \frac{1}{2}\gamma_{xz} \\ \frac{1}{2}\gamma_{xy} \end{Bmatrix} \tag{D.12}$$

Substituting the Eqs. (D.11), (D.12) and matrices $[T_2']$, $[R]$ in Eq. (D.6), it yields

$$\begin{Bmatrix} \sigma_x \\ \sigma_y \\ \tau_{yz} \\ \tau_{xz} \\ \tau_{xy} \end{Bmatrix} = [T_2']^{-1} [\overline{C}] [R] [T_2'] [R]^{-1} \begin{Bmatrix} \varepsilon_x \\ \varepsilon_y \\ \gamma_{yz} \\ \gamma_{xz} \\ \gamma_{xy} \end{Bmatrix} = [T_2']^{-1} [\overline{C}] [T_2']^{-T} \begin{Bmatrix} \varepsilon_x \\ \varepsilon_y \\ \gamma_{yz} \\ \gamma_{xz} \\ \gamma_{xy} \end{Bmatrix} \tag{D.13}$$

where $[T_2']^{-T} = [R][T_2'][R]^{-1}$

By expanding Eq. (D.13), the constitutive equations for the bottom circular cell segments II_b is of the form

$$\begin{Bmatrix} \sigma_x \\ \sigma_y \\ \tau_{yz} \\ \tau_{xz} \\ \tau_{xy} \end{Bmatrix}^{II_b} = \begin{bmatrix} \widetilde{C}_{11} & \widetilde{C}_{12} & \widetilde{C}_{14} & \widetilde{C}_{15} & \widetilde{C}_{16} \\ \widetilde{C}_{12} & \widetilde{C}_{22} & \widetilde{C}_{24} & \widetilde{C}_{25} & \widetilde{C}_{26} \\ \widetilde{C}_{14} & \widetilde{C}_{24} & \widetilde{C}_{44} & \widetilde{C}_{45} & \widetilde{C}_{46} \\ \widetilde{C}_{15} & \widetilde{C}_{25} & \widetilde{C}_{45} & \widetilde{C}_{55} & \widetilde{C}_{56} \\ \widetilde{C}_{16} & \widetilde{C}_{26} & \widetilde{C}_{46} & \widetilde{C}_{56} & \widetilde{C}_{66} \end{bmatrix}_k^{II_b} \begin{Bmatrix} \varepsilon_x \\ \varepsilon_y \\ \gamma_{yz} \\ \gamma_{xz} \\ \gamma_{xy} \end{Bmatrix}^{II_b} \tag{D.14}$$

where

$$\widetilde{C}_{11} = m^4\overline{C}_{11} + 4m^2n^2\overline{C}_{55}, \quad \widetilde{C}_{12} = m^2\overline{C}_{12}, \quad \widetilde{C}_{14} = -m^2n(\overline{C}_{16} - 2\overline{C}_{45}),$$
$$\widetilde{C}_{15} = -m^3n\overline{C}_{11} + 2mn(m^2 - n^2)\overline{C}_{55}, \quad \widetilde{C}_{16} = m^3\overline{C}_{16} + 2mn^2\overline{C}_{45},$$
$$\widetilde{C}_{22} = \overline{C}_{22}, \quad \widetilde{C}_{24} = -n\overline{C}_{26}, \quad \widetilde{C}_{25} = -mn\overline{C}_{12}, \quad \widetilde{C}_{26} = m\overline{C}_{26},$$
$$\overline{C}_{44} = m^2\overline{C}_{44} + n^2\overline{C}_{66}, \quad \widetilde{C}_{45} = mn^2\overline{C}_{16} + (m^3 - mn^2)\overline{C}_{45}, \quad \widetilde{C}_{46} = mn(\overline{C}_{44} - \overline{C}_{66}),$$
$$\widetilde{C}_{55} = m^2n^2\overline{C}_{11} + (m^2 - n^2)\overline{C}_{55}, \quad \overline{C}_{56} = -m^2n\overline{C}_{16} + (m^2n - n^3)\overline{C}_{45},$$
$$\widetilde{C}_{66} = n^2\overline{C}_{44} + m^2\overline{C}_{66}$$

Appendix E

TSAI-HILL FAILURE CRITERION

Several failure criteria are frequently applied to check the ultimate strength of fibrous composite structures including maximum stress criterion, maximum strain criterion, Tsai-Hill criterion, Hoffman criterion and Tsai-Wu criterion. In this study, the maximum work theory, Tsai-Hill failure criterion, is used to check the onset failure in the structure.

The Maximum Distortional Energy criterion, or von Mises criterion, is the most widely used quadratic interaction criteria for predicting the onset of yielding in isotropic metals (Gibson 1994). In 1948, Hill (1950) suggested that the von Mises criterion could be modified to include the effects of induced anisotropic behaviour in initially isotropic metals during large plastic deformation. After more than a decade, the extension of the Hill criterion to prediction of failure in an orthotropic, transversely isotropic lamina was proposed by Tsai (1968), and is often referred to as the Tsai-Hill criterion in the literature. The relation that describes the failure condition of Tsai-Hill criterion is give as

$$\left(\frac{\sigma_L}{\sigma_{LU}}\right)^2 - \left(\frac{\sigma_L}{\sigma_{LU}}\right)\left(\frac{\sigma_T}{\sigma_{LU}}\right) + \left(\frac{\sigma_T}{\sigma_{TU}}\right)^2 + \left(\frac{\tau_{LT}}{\sigma_{LTU}}\right)^2 < 1 \qquad \text{(E.1)}$$

where σ_{LU} is the longitudinal ultimate strength, σ_{TU} is the transverse ultimate strength and σ_{LTU} is the in-plane ultimate shear strength. Here, the longitudinal direction is assumed to be along the fibre reinforcement direction. When equation (E.1) is violated, the ply under consideration has failed. It should be noted that when

the stress in the lamina for the transverse or the longitudinal direction is compressive, the appropriate ultimate compressive value should be used in Tsai-Hill equation (E.1). More details on the derivation of Tsai-Hill failure criterion can be found in Gibson (1994), Herakovich (1998) and Jones (1999).

In comparison with other failure criteria, for general use the Tsai-Hill failure criterion is the most reliable theory although in some situations it will be conservative and underestimate the actual failure stress. Other advantages of the Tsai-Hill failure criterion include (Aref 1997, Jones 1999):

- The agreement between theory and experimental results is fairly good.
- It takes into account the interaction between the failure strengths which does not exist in maximum stress or strain criteria, thus it produces lower estimate strengths than maximum stress and strain criteria.
- It offers a simple equation with strength parameters that can be determined experimentally without going into elaborate experimental techniques such as Tsai-Wu theory where part of the strength terms require biaxial testing.

Furthermore, the Tsai-Hill criterion does not suffer from the inaccuracies when loaded with biaxial compression. Conversely, the Hoffman and Tsai-Wu failure criteria can become unreliable and sometimes fail to predict failure when a laminate is subjected to large biaxial compressive application. Other failure criteria and their use for each specific application can be found in Gibson (1994), Herakovich (1998) and Jones (1999).